PHOTOACTIVE LAYER MANIPULATION TOWARD HIGHLY EFFICIENT AND STABLE ORGANIC SOLAR CELLS

YONGWEN LANG

PhD

The Hong Kong Polytechnic University

2025

The Hong Kong Polytechnic University

Department of Electrical and Electronic Engineering

Photoactive Layer Manipulation Toward Highly Efficient and Stable Organic Solar Cells

Yongwen Lang

A thesis submitted in partial fulfillment of the requirements for the degree of Doctor of Philosophy

May 2025

CERTIFICATE OF ORIGINALITY

I hereby declare that this thesis is my own work and that, to the best of my knowledge and belief, it reproduces no material previously published or written, nor material that has been accepted for the award of any other degree or diploma, except where due acknowledgement has been made in the text.

_____(Signed)

Yongwen Lang (Name of student)

Abstract

Organic solar cells (OSCs) possess promising merits of transparency, flexibility, low pollution, and roll-to-roll processability, making them a dynamic research area. Currently, the power conversion efficiencies (PCEs) of OSCs have surpassed 20%. However, there are many issues to be addressed for practically used long-term stable high-performance OSCs, for example, the crystallization kinetics and morphological controlling in large-area production, the lagged PCEs for eco-friendly solvent-processed OSCs, and the inferior material and device stability. Therefore, the thesis proposed corresponding strategies to address these issues.

The first work proposed a solubility-tuning strategy by the multi-component approach to address the hard-controllable film aggregation kinetics and morphology issue in upscaling manufacturing (doctor-blade coating). The solubility tuning by incorporating a twisted third component (BTP-4Cl) can induce rapid crystallization behavior and promote fine phase separation in blade-coated blends. As a result, a PCE of 19.67% is obtained in OSCs (0.04 cm2), which is one of the state-of-the-art efficiencies among the reported blade-coated OSCs. This work offered novel insights into the effectiveness of solubility-tuning approaches for achieving highly efficient and stable OSCs under open-air coating conditions and provided a deeper understanding and appraisal of film formation kinetics influenced by coating methods.

The second work synthesized two highly crystalline 2D acceptors ATIC-C11 and ATIC-BO to construct highly efficient and stable halogen-free solvent-processed OSCs. The difference in side chains induces ATIC-C11's crystal structure to be an elliptical framework, and ATIC-BO a rectangular framework. ATIC-BO's strong self-aggregation and immiscibility induce large aggregates and severely impede charge transfer (CT) and dissociation. Conversely, ATIC-C11's suitable crystallinity and compatibility positively regulate the crystalline kinetics during film formation, thus forming much-ordered molecular packing and favorable phase separation size in blend films. As a

result, ATIC-C11-based ternary devices achieve a high efficiency of 19.28% with potential in scalability and stability, which is the top-ranking efficiency among nonhalogenated solvent-processed OSCs. This work not only displays highly efficient and stable halogen-free solvent-processed OSCs but also offers a new thought for material design and selection rule on the third component in highly efficient ternary OSCs.

The third work synthesized two central core-extended acceptors, PhIC-BO and AnIC-BO, regarding synergistic enhancement in efficiency and stability. The improvement in efficiency was ascribed to the suppressed recombination loss, optimized molecular packing, facilitated exciton generation, and higher charge and energy transfer efficiency. The increment in stability was attributed to the suppressed material oxidation degradation, improved domain purity, and impeded molecular interdiffusion. Additionally, the two acceptors' difference in electron-deficient central cores affords their different crystal structures, carrier dynamics, and morphological microstructures. As a result, a high PCE of 19.44% was achieved in the PhIC-BO-based OSCs, along with outstanding operational stability. Therefore, this work not only established a high-performance and long-term stable OSC but also provided deep insight into understanding the correlation between structures and properties.

In summary, these works mainly focus on addressing the problems in achieving highly efficient and stable OSCs towards commercialization and industrialization. We expected that these works would provide valuable guidance for further research.

Publications (First author and co-first author)

1. **Yongwen Lang** et al. Kinetics Manipulation Enabled by Solubility Control Toward 19% Organic Solar Cells via Compatible Air Coating. *Adv. Mater.* **2025**, 2420096. (Chapter 3)

2. **Yongwen Lang** et al. Balanced Miscibility and Crystallinity by 2D Acceptors Enabled Halogen-Free Solvent-Processed Organic Solar Cells to Achieve 19.28% Efficiency. *Adv. Mater.* **2025**, *37*, 2413270. (Chapter 4)

3. **Yongwen Lang** et al. Highly crystalline 2D acceptors enabling highly efficient and stable quasiplanar heterojunction organic solar cells. (Under submission) (Chapter 5)

4. **Yongwen Lang** et al. Isomeric Nonfullerene Acceptors: Planar Conformation Leading to a Higher Efficiency. *ACS Applied Energy Materials*, **2022**, *5(4)*, 4556–4563.

5. Hanjian Lai, **Yongwen Lang** (co-first author) et al. Chlorine-Mediated Dispersion Modulates Packing Arrangement of Asymmetric Acceptors for High-Performance Organic Solar Cells. *Adv. Energy Mater*. **2025**, 2406097.

6. Meihong Ou, **Yongwen Lang** (co-first author) et al. One-Pot Synthesis of Conjugation-Extended Isomeric Dimer Acceptors for High-Performance Q-PHJ Solar Cells. *Adv. Funct. Mater*. **2024**, 2419453.

7. Ying Zhang, **Yongwen Lang** et al. Recent advances of non-fullerene organic solar cells: From materials and morphology to devices and applications. *EcoMat*. **2023**, *5(1)*, e12281.

8. Hanjian Lai, Hui Chen, Ziyi Chen, **Yongwen Lang** (co-first author) et al. Exploring the significance of packing modes and 3D framework sizes and utilizing three

chlorine-mediated acceptors and the “like dissolves like” approach for achieving an efficiency over 19%. *Energy Environ. Sci.*, **2023**,*16*, 5944-5955.

9. Hanjian Lai, Xue Lai, **Yongwen Lang** (co-first author) et al. Molecular Skeletons Modification Induces Distinctive Aggregation Behaviors and Boosts the Efficiency Over 19% in Organic Solar Cells. *CCS Chemistry*, **2024**, 1-14.

10. Mingrui Pu, Chunxian Ke, **Yongwen Lang** (co-first author) et al. Dimerized small molecule donor enables efficient ternary organic solar cells. *Giant*, **2024**, *19*, 100325.

Acknowledgments

Tracking back to my Ph.D period, there are many people and things to be thankful for. I here sincerely thank them and wish them all the best in the future.

First, I would like to sincerely thank my supervisors, Prof. Gang Li, Prof. Feng He, and Prof. Tiangang Yang. They offered me this precious opportunity to take my Ph.D degree and inspired my scientific research.

Prof. Li is knowledgeable, enthusiastic, and conscientious about scientific research and treats students with careful guidance, patience, and friendliness. He strives for excellence, providing students with unique and in-depth insights for their research. Not only deepened my knowledge of device physics but also broadened my insight into other interdisciplinary subjects, providing a solid foundation for this thesis.

Prof. He is rigorous and serious in his work, passionate about scientific research, and has keen insight into research. He has provided careful guidance for my study and scientific research from my undergraduate studies to Ph.D training, developed my learning and cognitive abilities, cultivated my capability in material synthesis, and inspired me to make continuous progress and constantly improve myself.

I would like to thank Prof. Yang provided me with the valuable opportunity to Ph.D studies and help me with my study and graduation issues. I also thank Prof. Yanqing Tian for his recommendation and careful concern.

Second, I heartfully thank the help of two groups, especially, Dr. Hanjian Lai and Dr. Ying Zhang. Dr. Lai enlightened me about organic solar cell research and taught me the skills of material design and synthesis. Additionally, he provided great help with guidance and material synthesis on my projects. He is an excellent mentor, friend, collaborator, and role model. Dr. Zhang well trained my skills in device fabrication and led me to complete my research in the early stage of my PhD. She is very rigorous in research and guides me to think carefully, providing the fundamental basis for the completion of this thesis.

I gratefully thank the guidance and assistance from my group members. They are Dr. Kuan Liu, Dr. Zhiwei Ren, Dr. Patrick Fong, Dr. Hao Xia, Dr. Jiehao Fu, Dr. Ruijie Ma, Dr. Jiaming Huang, Dr. Qiong Liang, Dr. Tao Zhu, Dr. Zhiqi Li, Dr. Rishi, Dr. Jiangsheng Yu, Dr. Jiaqi He, Dr. Chen Ye, Mr. Dongyang Li, Mr. Yu Han, Ms. Menghua Cao, Mr. Zhen Lu, Ms. Lei Cheng, Ms. Xiyun Xie, Ms. Qianyi Li, Mr. Peng Bai, Mr. Zhenrong Wang, Mr. Yu Zhen. Dr. Liang Han, Dr. Hui Chen, Dr. Jianfei Qu, Dr. Chengwei Shan, Dr. Xue Lai, Dr. Waka, Dr. Mingrui Pu, Dr. Heng Li, Dr. Mingpeng Li, Dr. Yafei Ding, Mr. Shilong Xiong, Ms. Xuechun Yang, Mr. Yiwu Zhu, Ms. Ying Qian, Mr. Haonan Lin, Mr. Yunpeng Wang, Ms. Meihong Ou, Mr. Zihao Deng, Mr. Dongsheng Qiu, Ms. Xiangyu Shen, Mr. Fuqing Su, Mr. Chengyu Peng, Mr. Zhiqiang Wang, Mr. Changfeng Xie, Ms. Ruoxi Sun, Ms. Sufang Yu, Ms. Yunyun Wei. I would also thank the support from my co-workers: Mr. Yuang Fu, Dr. Miao Zhang, Prof. Xinhui Lu, and Prof. Wai-Yeung Wong.

Also, I want to express my gratitude to two universities, the Hong Kong Polytechnic University and the Southern University of Science and Technology, and the Research Office and the General Office for their constructive assistance.

Finally, I would sincerely and truthfully thank my family for their selfless love and unconditional support, encouraging me to face the difficulties of work and life.

Table of Contents

List of Figures

List of Tables

Chapter 1 Introduction

The accelerating depletion of finite fossil reserves (petroleum, coal, natural gas) encouraged human beings to look for new energy sources to replace non-renewable resources to supply energy for human activities. As a clean, universal, and long-lasting new type of energy, solar energy contains huge energy. If solar energy can be effectively utilized, the problem of energy depletion faced by humans can be easily solved. Photovoltaic (PV) technology enables direct conversion of sunlight into electricity through the semiconductor-mediated photon-electron conversion. At present, silicon solar cells still dominate the commercial market due to their high-power conversion efficiency (PCE) and highly stable stability. However, they still face problems such as high production costs and complicated production processes. Since then, amorphous silicon-based and second-generation solar cells like CdTe, GaAs, CIS, and CIGS have appeared, but these materials contain many toxic heavy metal elements. The landscape has, therefore, transitioned into the third-generation photovoltaics, including perovskite (PSCs), dye-sensitized (DSSCs), and organic solar cells (OSCs). OSCs distinguish themselves through unique merits, mechanical flexibility, optical transparency, eco-friendly processing, and compatibility with roll-to-roll manufacturing, displaying huge commercial and industrial applications in wearable photonics and built-in photovoltaics (BIPV), including multi-colored and see-through photovoltaic windows. Breakthroughs in molecular engineering and device architecture enabled remarkable progress in OSCs, with the PCEs skyrocketing from 1% to beyond 20% within two decades,[1–5] bridging the gap between laboratory prototypes and industrial scalability. In this chapter, the basic knowledge of semiconductors and photovoltaics (PV) will be first introduced, and then specified to the organic photovoltaics, including the difference between the inorganic and organic semiconductors, working mechanism, and device structures, finally followed by the research motivation and objectives of this thesis.

1.1 Solar energy and solar spectrum

1.1.1 Energy consumption and solar energy

Energy is divided into renewable and non-renewable energy. Fossil fuels like coal, oil, and natural gas, playing an important role in human production and living, however, is belong to non-renewable energy sources with severe problems, for example, limited reserves, uneven distribution, and environmental pollution. The massive use of fossil fuels would lead to the emission of large amounts of carbon dioxide, which will disrupt the carbon cycle in the Earth's atmosphere, leading to global warming and the greenhouse effect. In addition, the emission of atmospheric pollutants such as CO, SO_2, and NO_2 endanger human health and cause acid rain to harm the lives of animals and plants.

First, solar energy is abundant compared with fossil fuels. The amount of solar energy radiated from the sun to the earth's surface is 8.0×10^{13} kW every second, equivalent to burning 6×10^9 tons of coal. The solar energy provided in a year is equivalent to 18.92×10^7 billion tons of standard coal.[6] Therefore, solar energy is considered to be inexhaustible. Second, Solar energy is evenly distributed. The transportation costs caused by uneven energy distribution are huge, for example, several major projects in China, West-to-East Gas Transmission, West-to-East Power Transmission, and South-to-North Water Transfer are designed and constructed to address the problem of uneven energy distribution, consumption of 600 billion CNY.[7] However, solar energy is distributed everywhere on Earth, which can be used locally to solve energy supply problems in remote areas with inconvenient transportation, relieving energy supply/demand and transportation pressures. Additionally, environmental protection is an important prerequisite to achieving sustainable development. The utilization of solar energy does not produce waste, noise, and harmful substances. Solar energy is environmentally friendly and meets the requirements of sustainable development. Finally, the cost of solar power generation is much lower in the long run. The cost of current power plants comes from construction costs, fuel costs,

operation and maintenance, and environmental protection investment, for which solar power generation has few requirements.

1.1.2 Photons and the solar spectrum

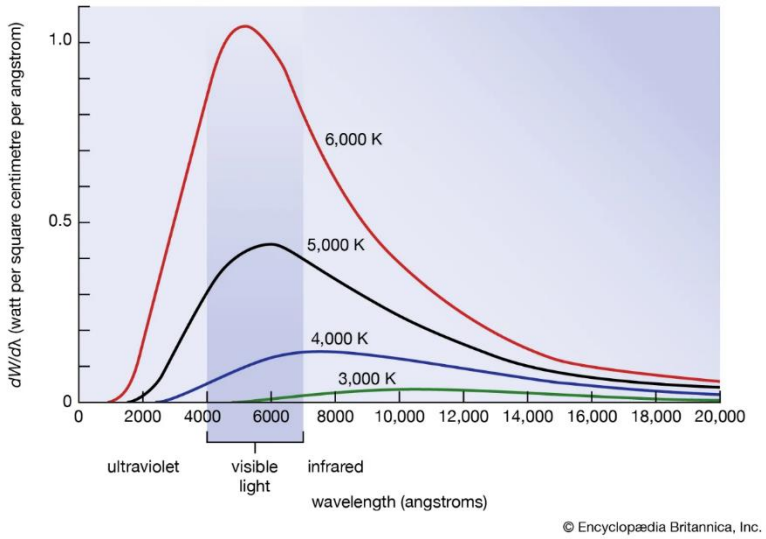

Figure 1.1 The black body radiation at different temperatures.[8]

Objects emit electromagnetic radiation when the temperature is above absolute zero, arising from the thermal movement of atoms and molecules. A black body is an object that can completely absorb all frequencies of electromagnetic radiation that irradiate it. The spectral characteristics of such radiation are governed by Planck's law of blackbody radiation, mathematically expressed as:

$$M(\lambda, T) = \varepsilon(\lambda, T)\frac{2\pi hc^2}{\lambda^5}\frac{1}{\exp\left(\frac{hc}{k_B \pi T}\right) - 1} \qquad 1\text{-}1$$

Where c is the vacuum light speed, λ denotes the wavelength, h represents the Planck constant, and k_B the Boltzmann constant. The spectral emissivity ε(λ, T) equals unity for a perfect blackbody. The features of the black body irradiation (Figure 1.1) include: 1) The radiation intensity among the whole spectrum increases with the increasing temperature of the heat source. 2) The increasing rate of energy output is very fast in the short wavelength. 3) The higher the temperature of a black body, the bluer the spectrum will be. Thermal emission, fundamentally arising from electronic transitions

between quantized energy states, manifests as electromagnetic wave propagation driven by thermal gradients, which aligns with black body radiation principles. The solar spectrum (Figure 1.2) is close to a 5250 ℃ blackbody radiator. The sun is therefore usually treated as a blackbody and can be described by blackbody radiation characteristics.

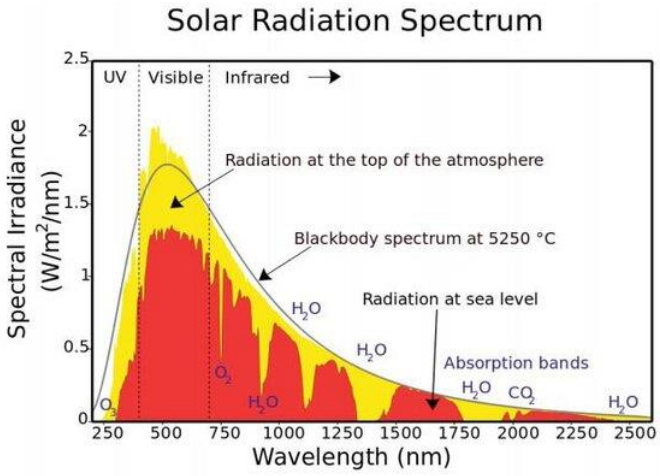

Figure 1.2 Solar radiation spectrum. [9]

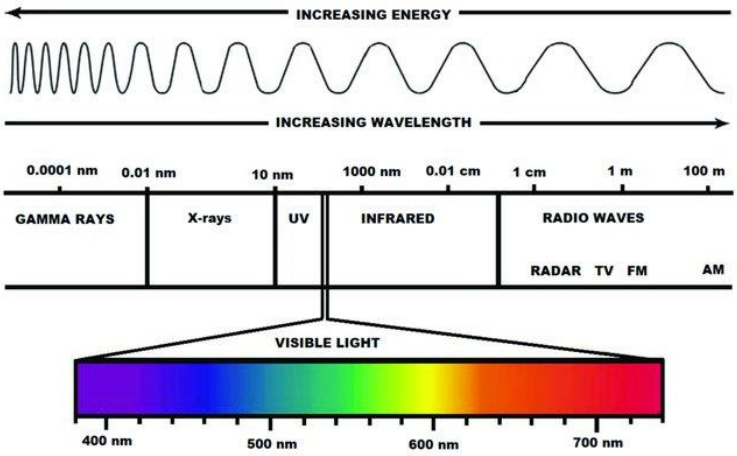

Figure 1.3 The electromagnetic radiation spectrum.

When the sunlight passes through a prism and radiates on a white screen, colored light bands appear, which are called solar spectra (Figure 1.3). The visible spectrum accounts for a small part of the solar spectrum. The wavelengths longer than the visible light wavelength include infrared light, microwaves, radio waves, etc., and the wavelengths shorter than the visible light wavelength include ultraviolet light, X-rays,

etc. Notably, the solar continuum exhibits characteristic absorption lines (Fraunhofer lines) caused by atmospheric elements selectively absorbing specific wavelengths during photon transmission through the Sun's chromosphere. The solar radiation above the Earth's atmosphere is mainly located in the wavelength range of 150~4000 nm (> 99%), among which ~50% of solar radiation is in the visible region (400~760 nm), 7% is in the ultraviolet region (< 400 nm), and 43% is in the infrared region (> 760 nm). The maximum energy is at the wavelength of 475 nm. The change in the distance between the sun and the Earth and the solar activity would influence the solar radiation energy on Earth.

1.1.3 Air mass

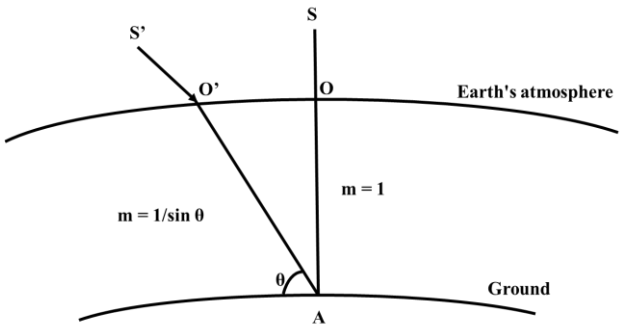

Figure 1.4 The schematic diagram for air mass.

The solar radiation on the ground is influenced by Earth's atmospheric absorption. The measured sunlight is related to the testing place, time, and weather. To quantify their impacts, the air mass (AM) parameter was introduced. One air mass (AM1) is defined as the solar light's shortest path length when the sun is at the zenith of the sea level. The air mass of the sun at any position on the sea level refers to the ratio of sunlight's actual atmospheric path length (O'A) to its minimal zenith-path length (OA) at sea level (Figure 1.4), AM is expressed dimensionlessly as:

$$AM = \frac{\mathrm{O'A}}{\mathrm{OA}} = \frac{1}{\sin\theta} \qquad 1\text{-}2$$

Where θ is the solar altitude angle referring to the angle between the sunlight and the horizontal level. Due to the different atmospheric pressures in different places, the formula needs correction:

$$AM = \frac{P}{P_0} \cdot \frac{1}{\sin\theta} \quad 1\text{-}3$$

Here, P_0 represents standard atmospheric pressure (101.3 kPa), while P corresponds to local barometric pressure.

AM1 refers to the atmospheric mass at sea level is 1 when the sun is at its zenith. AM0 means that the atmospheric mass is 0 in outer space where it does not pass through the atmosphere. The AM0 spectrum is mainly used to evaluate space-used photovoltaic cells and modules. AM 1.5 is selected as the standard spectrum to evaluate the performance of ground-used solar cells and modules as AM1.5 is closer to human living conditions with a solar altitude angle of ~ 48.20°.

1.2 Photovoltaic Technology

1.2.1 Brief introduction to quantum mechanics

In 1901, Planck derived a theoretical formula to precisely describe the experimentally observed spectrum of black-body radiation:

$$B_v(v,T) = \frac{2hv^3}{c^2} \cdot \frac{1}{e^{\frac{hv}{k_B T}} - 1} \quad 1\text{-}4$$

Where B_v is spectral radiance, h is the Planck constant, k_B is the Boltzmann constant, and c is the speed of light. This was based on the concept of "quanta". He hypothesis that a charged oscillator in the cavity of a black-body and its energy increment is based on a minimum amount of E, proportional to the frequency of the electromagnetic wave, which is the fundamental concept of quantum theory.

$$E = hv \quad 1\text{-}5$$

Later in 1905, Einstein explained the photoelectric effect, stating that light is not continuous but composed of discrete photons and that the energy of photons (E_{photon}) is proportional to the electromagnetic wave frequency (v). As shown in Figure 1.5, where Φ is the work function of the metal, E_{kin} is the kinetic energy of the photoelectron. This theory deepens the understanding of the particle nature of light and is the foundation of quantum mechanics. Einstein, therefore, won the Nobel Prize for Physics in 1921.

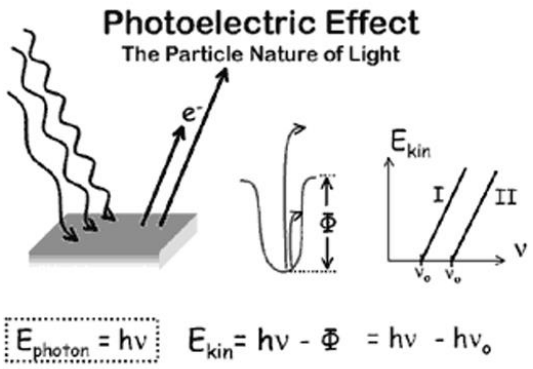

Figure 1.5 The explanation for the photoelectric effect.

In 1925, de Broglie showed that matter such as electrons and atoms exhibited a wave-like property as well as the standard particle-like property, which is the wave–particle duality, and any matter possesses this property.

$$p = \frac{h}{\lambda} = \hbar k \tag{1-6}$$

$$k = \frac{2\pi}{\lambda}, \hbar = \frac{h}{2\pi} \tag{1-7}$$

where p is the momentum, λ is the wavelength, and k is the wavenumber.

Based on the wave–particle duality, Schrodinger gave the wave equation for particles/systems in 1926, which described the particle information like position, momentum, and energy.

$$i\hbar \frac{\partial}{\partial t}\Psi(\mathrm{r},\mathrm{t}) = \hat{\mathrm{H}}\Psi(\mathrm{r},\mathrm{t}) \tag{1-8}$$

Here $\hat{\mathrm{H}}$ denotes the Hamiltonian operator, i the imaginary unit. The solution to the wave equation is the wave function (Ψ), and the square of its absolute value refers to the probability density of a particle ($|\Psi|^2$), for example, the electron cloud, which describes the probability of an electron appearing somewhere outside the nucleus.

Additionally, in 1913, Bohr assumed that electrons move around atoms and the atomic orbital was quantized, which explained the spectra of the hydrogen atom. In 1922, Compton showed that electrons can radiate photons. Later in 1924, Pauli raised the "Pauli exclusion principle", which states that electrons cannot stay in the same state. The two electrons in an atomic orbital must have the opposite spin direction. In 1927,

Heisenberg raised the "Heisenberg uncertainty principle", which showed that the momentum/position of a particle cannot be measured precisely at the same time.

$$\Delta x \Delta p \geq \frac{\hbar}{2} \tag{1-9}$$

Quantum mechanics reveals the motion laws of microscopic particles, well explaining the atomic structure and spectra, element properties, and light absorption and radiation, etc. Heisenberg and Bloch first applied quantum mechanics to solid physics, especially the band theory, which helps people to understand the laws of electron motion in the lattice and the conductive property of semiconductors. It is a successful and important application of quantum mechanics in solid physics.

1.2.2 Semiconductors

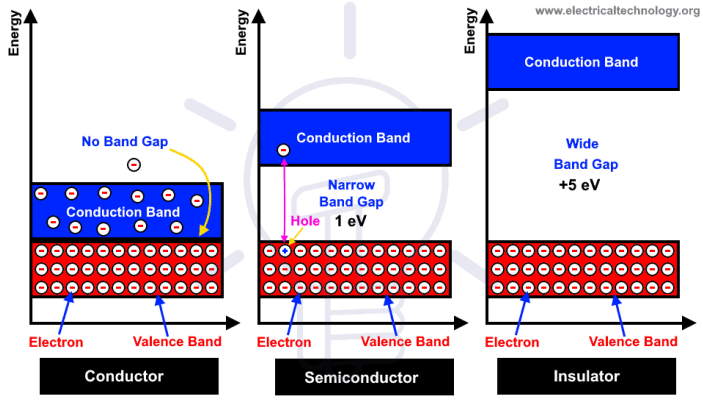

Figure 1.6 Energy diagrams of the conductor, semiconductor, and insulator. [10]

Materials are divided into conductors, semiconductors, and insulators according to their conductivity. Their energy diagrams illustrated the working mechanisms as shown in Figure 1.6. The superior electrical conductivity of metals originates from their partially occupied valence electron bands, allowing delocalized electrons to move freely. The band gap of insulators is large, and overcoming this energy barrier requires significant excitation energy, far exceeding typical thermal energy levels at ambient conditions. Consequently, the absence of mobile charge carriers under normal temperatures makes insulators essentially non-conductive. Semiconductors are located in between insulators and conductors, where the bandgap is relatively small. When the temperature rises or

there is light, a small number of electrons in the valence band are excited to the conduction band, leaving holes in the valence band. These electrons and holes will participate in conduction under an external electric field. Therefore, in semiconductors, both the electrons in the conduction band and the holes in the valence band participate in conduction, which is the biggest difference from metal conductors which free electrons dominate in conduction. The main difference between insulators and semiconductors is that semiconductors have certain conductivities since many electrons could be excited to the conduction band at room temperatures in semiconductors due to the relatively small band gap.

There are unavoidable impurities and traps in the practically used semiconductors, for example, the atom vibration at the equilibrium position in the lattice, the impurities (other chemical elements) introduced during production, the defects arising from the disrupted periodic arrangement of atoms, including point defects (vacancies and interstitial atoms), line defects (dislocations), and surface defects (stacking faults, grain boundaries in polycrystalline materials). Small amounts of impurities and defects can have a decisive influence on the physicochemical properties of semiconductor materials. The presence of impurities and defects will destroy atomic periodic arrangement and may introduce energy states (i.e., energy levels) in the bandgap. Impurities exist in semiconductors in two ways depending on the size of impurity atoms, interstitial and substitutional impurities. In some cases, there is artificial doping with heteroatoms to obtain semiconductors with specific properties, for example, the n-type and p-type semiconductors.

One typical n-type semiconductor can be formed by doping phosphorus (group V elements) in silicon (group IV elements). The phosphorus atoms exist as substitutional impurities in silicon as they have a similar atomic size and similar valence electron shell structures to silicon atoms, where phosphorus atoms replace partial silicon atoms. Phosphorus atoms have 5 valence electrons, and 4 of them form covalent bonds with 4 silicon atoms nearby, leaving one valence electron and a positively charged immobile center phosphorus ion (P^+). This electron moves around the phosphorus ion but with a weak binding force, which easily breaks the binding force and moves free in the lattice

with small external applied energy. The process is called impurity ionization. The schematic diagram by an energy level is shown in Figure 1.7. The number of conductive electrons in the conduction band increases after impurity ionization, enhancing the conductivity of the semiconductor. Thus, the conduction of n-type semiconductors is dependent on conduction band electrons.

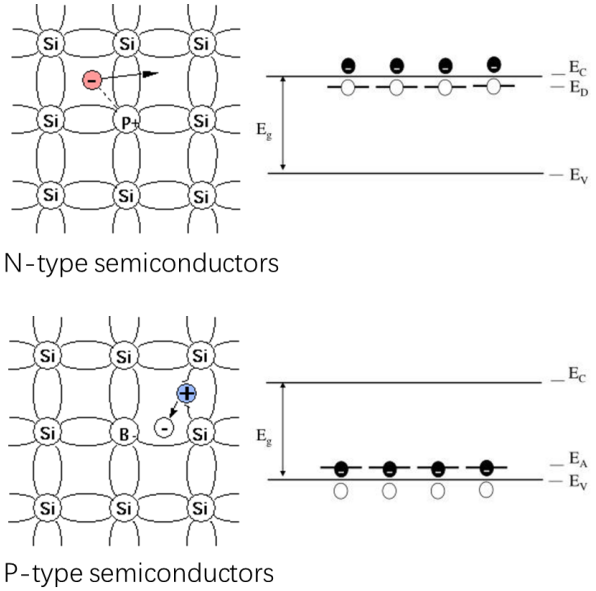

Figure 1.7 The illustration of the n-type and p-type semiconductors and the energy band diagram. [11,12]

The creation of p-type semiconductors involves introducing group III elements (e.g., boron) into crystalline silicon. With only three valence electrons, each boron dopant forms covalent bonds with four adjacent silicon atoms by accepting an electron from the silicon lattice, thereby generating mobile positive charge carriers (holes) within the crystal structure. This process establishes negatively charged boron ions (B^-) that electrostatically interact with neighboring holes. The weak binding energy between these entities enables hole mobility at ambient temperatures, effectively ionizing the dopant sites. Consequently, the increased hole concentration in the valence band elevates the material's electrical conductivity. Semiconductors predominantly conducting through such hole transport are classified as p-type. Thermal energy from lattice vibrations facilitates the ionization of III/V dopants in silicon and germanium at ambient conditions, liberating mobile charge carriers.

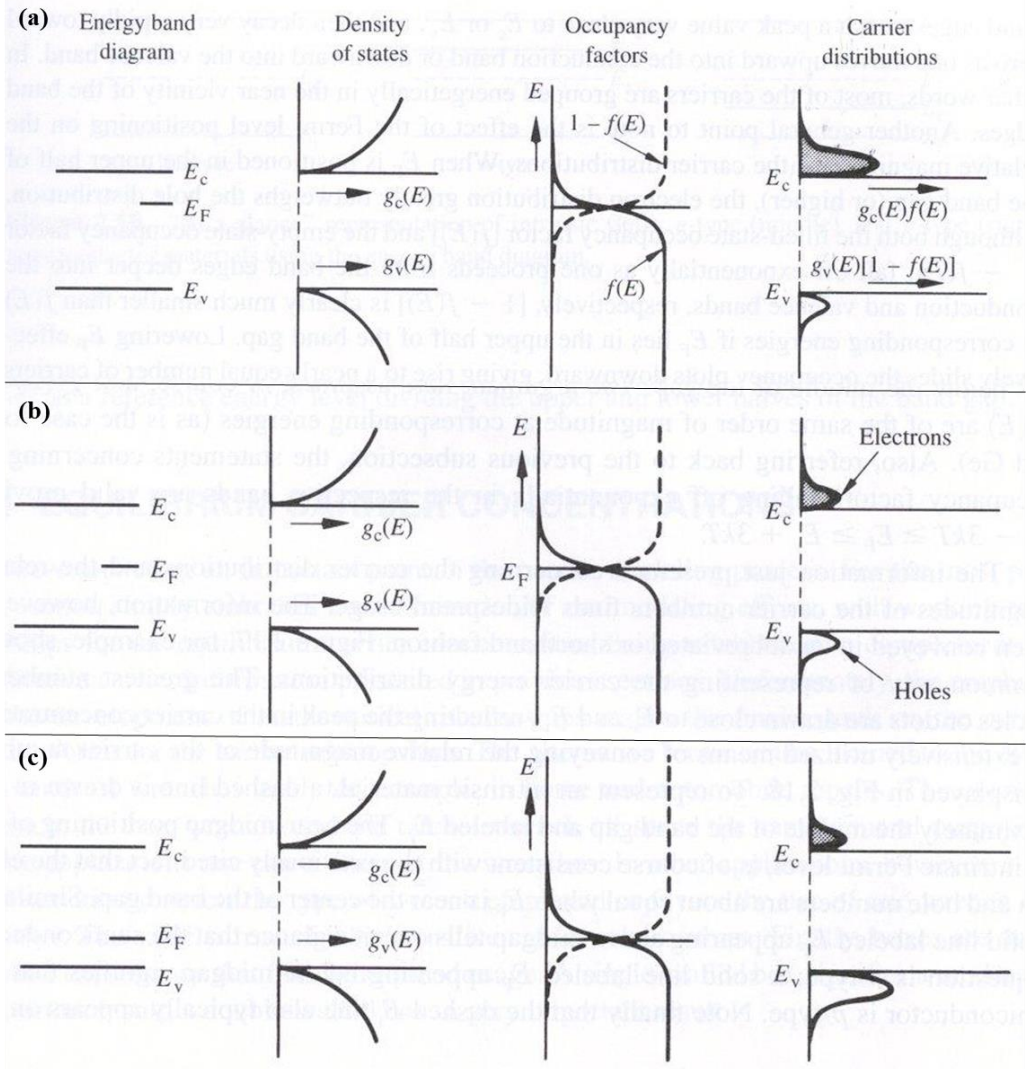

Figure 1.8 The energy band diagram, density of states, occupancy probability, and carrier distribution in (a) n-type semiconductors, (b) intrinsic semiconductors, and (c) p-type semiconductors.

The energy gap of a semiconductor can be considered continuous, as there are many energy levels in the conduction band and the valence band, and their energy gap is small. The density of states (DoS) g (E) is applied to describe the amount of quantum states per unit energy interval around energy E. Therefore, the distribution of the quantum states along with the energy can be calculated by the following equation. As shown in Figure 1.8, The higher the electron energy, the larger the density of states.

$$g_c(E) = \frac{V}{2\pi^2}\frac{(2m_n^*)^{\frac{3}{2}}}{\hbar^3}(E - E_c)^{\frac{1}{2}} \qquad 1\text{-}10$$

$$g_v(E) = \frac{V}{2\pi^2}\frac{\left(2m_p^*\right)^{\frac{3}{2}}}{\hbar^3}(E_v - E)^{\frac{1}{2}} \quad 1\text{-}11$$

There are a large number of the electrons in a semiconductor. For a certain electron, its energy is various, while the total energy and electron distribution follows a certain law for a semiconductor in thermal equilibrium. Fermi-Dirac distribution defined the probability of an electron to take a quantum state with an energy of E

$$f(E) = \frac{1}{1 + \exp\left(\frac{E - E_F}{k_0 T}\right)} \quad 1\text{-}12$$

The probability of a hole to take a quantum state is described by

$$1 - f(E) = \frac{1}{1 + \exp\left(\frac{E_F - E}{k_0 T}\right)} \quad 1\text{-}13$$

From Figure 1.8, it can be considered that electrons tend to take the quantum states below E_F, and holes tend to take the quantum states above E_F.

The carrier distribution can thus be obtained. The electron in the conduction band can be calculated by $f(E)g_c(E)$, and the hole in the valence band is $[1\text{-}f(E)]g_v(E)$. It can be seen from Figure 1.8 that multiple electrons in the conduction band are enriched at the conduction band minimum (CBM), and holes are enriched at the valence band maximum (VBM).

1.2.3 PN junction

A PN junction would form at the contacting area by connecting one p-type and one n-type semiconductor. Commonly used processes for forming PN junctions include alloying and diffusion methods. As mentioned above, there are many ionized electrons in the n-type semiconductor and many holes in the p-type semiconductor, leading to the charge carrier diffusion driven by the carrier concentration gradient (holes move from p to n region and electrons in a reverse direction). Therefore, a negative charge region appears in the p region and a positive charge region appears in the n region, forming the built-in electric field directing from the n to the p region. The charge carriers therefore could drift under the built-in field. The diffusion and drift of the carriers are

in opposite directions, eventually reaching a dynamic equilibrium with a net current of 0 (without applied voltage). The energy level of the PN junction is depicted in Figure 1.9, where E_{Fn} moves down with the n-region energy level, while E_{Fp} moves up with the p-region energy level until the Fermi energy level is equal. The potential energy difference (barrier height) between the n and p region is qV_D. V_D is related to the doping concentration, temperature, and band gap width:

$$V_D = \frac{k_0 T}{q}(ln\frac{N_D N_A}{n_i^2}) \qquad 1\text{-}14$$

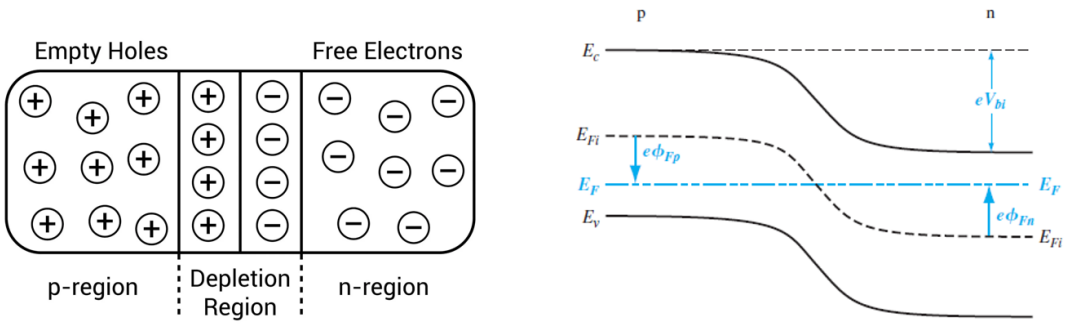

Figure 1.9 The illustration of a PN junction and its energy level diagram. [13,14]

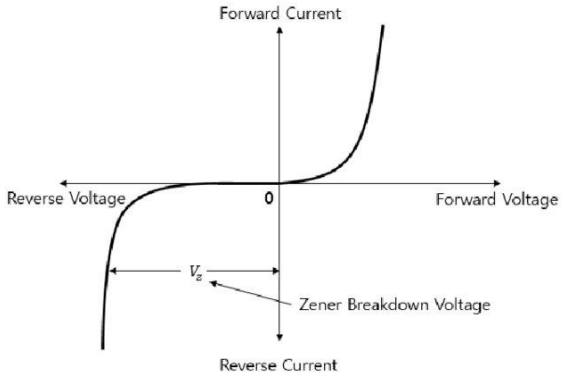

Figure 1.10 The *J-V* curve of an ideal PN junction. [15]

An electric field in the opposite direction with the built-in electric field would be generated if applying a forward bias on an ideal PN junction. The electric field weakens the built-in electric field strength in the depletion region and thus reduces the potential difference V_D, facilitating electron diffusion from the n region to the p region and holes in the opposite orientation. Electrons are non-equilibrium minority carriers for the p

region that is full of holes, and charge recombination occurs once electrons reach the p region. When the applied bias is determined, the electron diffusion flow through a certain cross-section remains constant, and holes, and vice versa. Under reverse bias conditions, the externally applied electric field aligns with and reinforces the intrinsic built-in field. This synergistic interaction augments the total field intensity, elevating the potential barrier from V_D to V_D+V. Consequently, the majority carrier drift currents intensify—electrons migrate from the *p*-region to the *n*-region, while holes exhibit counter-directional motion. Simultaneously, reverse biasing drastically suppresses minority carrier populations. The resultant carrier density gradient becomes negligible, effectively minimizing diffusion currents across the depletion region. When the reverse voltage is large, the minority carriers at the boundary can be considered to be zero. At this time, the concentration gradient no longer changes with voltage. Therefore, under reverse bias, the current in the PN junction is small and tends to remain unchanged. This indicates the unidirectional conductivity of a PN junction (rectification effect). The current-voltage equation (Shockley equation) and the corresponding *J-V* curve in **Figure 1.10** of an ideal PN junction can explain this phenomenon more significantly.

$$J = J_s\left[\exp\left(\frac{qV}{k_0T}\right) - 1\right] \qquad 1\text{-}15$$

Where k_0 denotes the Boltzmann constant, q the element charge, T the absolute temperature, V the external bias, J the current density, and J_s the reversed saturated current density. Apart from the unidirectional conductivity, temperature determines current density. The factors causing deviation from the idea equation include: 1) surface effect; 2) generation and recombination in the depletion region; 3) large injection conditions; and 4) series resistance effect.

1.2.4 Working mechanism of photovoltaic cells

When a PN junction is irradiated with light of appropriate wavelength, an electromotive force (photovoltaic voltage) is generated inside the semiconductor; if the PN junction is short-circuited, a current (photocurrent) will appear. This effect caused by the built-

in field is called the photovoltaic effect, which was first reported by French scientist Edmond Becquerel in 1839.[16]

The photogenerated carriers would be affected by the built-in field under light irradiation, where electrons move from the p side to the n side and holes move in the opposite direction, generating a photogenerated current I_L directing from the n to the p side. Simultaneously, the movement of charge carriers decreases the potential difference across the PN junction, forming a photogenerated electromotive force at the two sides of the PN junction, equivalent to applying a forward bias. The potential difference decreased to qV_D-qV and a forward current I_F is generated directing from the p to the n side. If connecting the PN junction with an external circuit, there is a current I flowing through the circuit under continuous light irradiation. The PN junction here is a power source, called photocell (photovoltaic cell, PV cell, solar cell). According to the rectification equation,

$$I_F = I_S\left[\exp\left(\frac{qV}{k_0T}\right) - 1\right] \quad 1\text{-}16$$

Where V is the photogenerated voltage and I_S is the reverse saturation current. The current flows through the load of the external circuit can be calculated by the following equation

$$I = I_L - I_F = I_L - I_S\left[\exp\left(\frac{qV}{k_0T}\right) - 1\right] \quad 1\text{-}17$$

The photogenerated voltage is

$$V = \frac{k_0T}{q}\ln\left(\frac{I_L - I}{I_S} + 1\right) \quad 1\text{-}18$$

When the PN junction is open-circuited (R = ∞), I = 0, the voltage across the PN junction is open-circuit voltage V_{OC}.

$$V_{OC} = \frac{k_0T}{q}\ln\left(\frac{I_L}{I_0} + 1\right) \quad 1\text{-}19$$

When the PN junction is short-circuited (V = 0), I_F = 0, the current is the short-circuit current (I_{SC}).

$$I_{SC} = I_L \quad 1\text{-}20$$

V_{OC} and I_{SC} can be obtained from the intercept of the *J-V* curve for a solar cell. The *J-V* curve for the load is a straight line and the slope is determined by its resistance. The intersection of two *J-V* curves is the working point. There exists a maximum power point where the solar cell generates a maximum output power, corresponding to a maximum power voltage (V_{max}) and a maximum power current (I_{max}).

The fill factor is applied to evaluate the output feature of a solar cell

$$FF = \frac{P_{\max}}{V_{\mathrm{OC}} \cdot I_{SC}} = \frac{V_{\max} \cdot I_{\max}}{V_{\mathrm{OC}} \cdot I_{SC}} \quad 1\text{-}21$$

PCE is applied to evaluate the overall performance of a solar cell and could be calculated by

$$PCE = \frac{P_{\max}}{P_{\mathrm{in}}} = \frac{V_{\mathrm{OC}} \cdot I_{SC} \cdot FF}{P_{\mathrm{in}}} \times 100\% \quad 1\text{-}22$$

where P_{in} refers to the power of the incident light (100mW·cm^{-2} for the AM1.5G spectrum).

External quantum efficiency (EQE) is defined as the ratio of the carriers collected to the incident photons for a solar cell.

$$EQE(\lambda) = \frac{I_{SC}(\lambda)}{qAQ(\lambda)} \quad 1\text{-}23$$

Where Q (λ) is the incident photon density spectrum and A is the effective area. EQE is smaller than 1 due to the existence of light reflection, the short diffusion length of the carrier, excess minority recombination, etc.

In a practical solar cell, there are resistances including the resistance from the semiconductor materials and the metal electrodes and the contacting resistance between different layers, which is equivalent to a series resistance (R_S). In addition, there are defects causing charge carrier recombination and leading to the leakage current inside the cell, equivalent to a shunt resistance (R_{Sh}) (Figure 1.11). Under this circumstance, the output current to an external circuit is

$$I = I_L - I_S\left[\exp\left(\frac{qV}{k_0T}\right) - 1\right] - \frac{V + IR_s}{R_{Sh}} \quad 1\text{-}24$$

When it is the open-circuit condition, $I = 0$, then

$$I_L = I_S\left[\exp\left(\frac{qV}{k_0T}\right) - 1\right] + \frac{V_{OC}}{R_{Sh}} \quad 1\text{-}25$$

$$V_{OC} = \frac{k_0 T}{q} \ln\left(\frac{I_L - \frac{V_{OC}}{R_{Sh}}}{I_0} + 1\right) \qquad 1\text{-}26$$

It is noted that R_S does not affect V_{OC} and V_{OC} decreases if R_{Sh} is smaller. However, both R_S and R_{Sh} reduce the FF and the current output to the external circuit. The influence of R_s on FF is more significant when the cell is exposed to a strong light, while the influence of R_{Sh} is severe at a dim light[17].

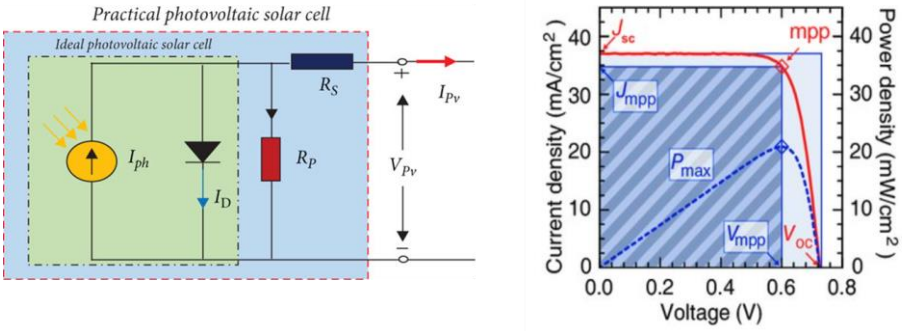

Figure 1.11 The equivalent circuit and the *J-V* curve of a solar cell. [18,19]

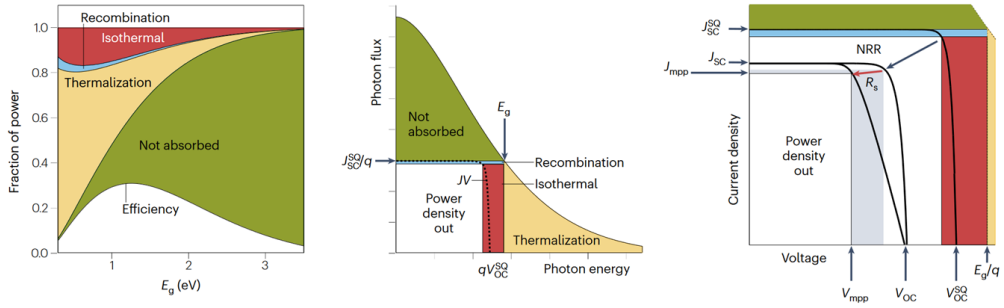

Figure 1.12 The schematic diagram of the energy loss in the SQ module relevant to the bandgap.[24]

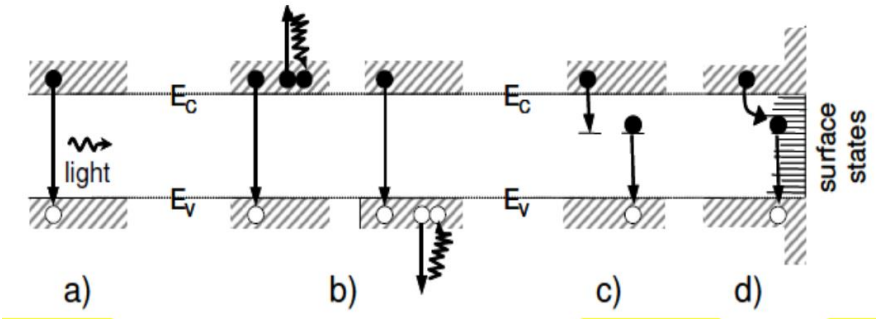

Figure 1.13 The recombination process in solar cells. (a) Radiative recombination, (b) Auger recombination, (c) indirect (Trap-assisted/SHR) recombination, and (d) surface recombination.[26]

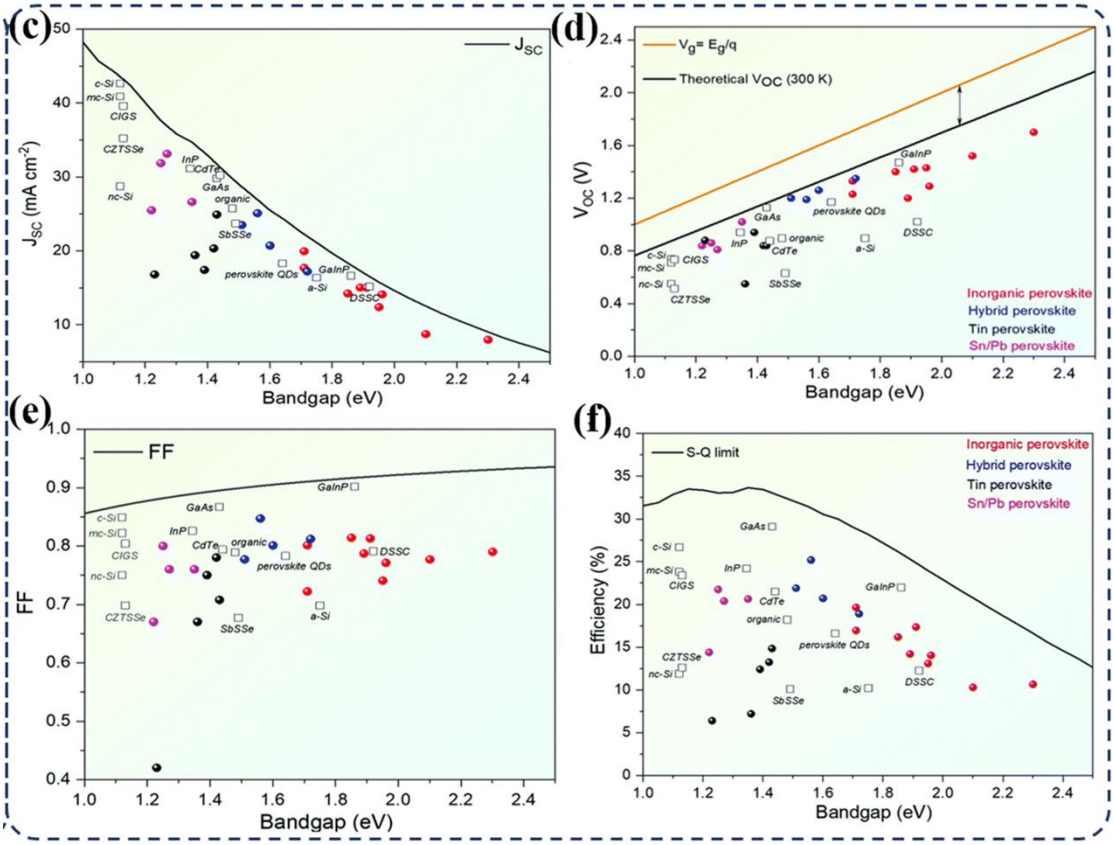

Figure 1.14 The J_{SC}, V_{OC}, FF, and PCE versus the bandgap of several types of solar cells under SQ limit.[22]

To estimate the upper limit efficiency of the PN-junction solar cells, W. Shockley and H. J. Queisser raised the "SQ limit" in 1961.[20,21] Several assumptions were made for an ideal solar cell: 1) the cell absorbs photons with energy larger than or equal to the bandgap of the solar cell ($E \geq E_g$); 2) one photon generates one exciton (electron-hole pair); 3) ideal charge collection efficiency; 4) The residual energy (E-E_g) was discarded and the temperature of the electron-hole pairs equal the temperature of the cell and the ambient; 5) there is only radiative recombination; and 6) there is no contacting resistance between layers and the interlayers selectively pass electrons/holes. Therefore, there exist four types of energy loss: 1) the energy loss from the not-absorbed photons; 2) the loss from excessive kinetic energy (Thermalization); 3) loss of radiative recombination; and 4) loss from isothermal dissipation (Figure 1.12). However, in a practical solar cell, there is non-radiative recombination loss, including trap-assisted

(SRH) recombination (the recombination through defects or impurities), Auger recombination (the transfer of energy or momentum to a third particle), and surface recombination (the defects and impurities on the surface) (Figure 1.13). Therefore, theoretically, the SQ limit gives the upper limit of a solar cell with a certain bandgap (Figure 1.14).[22–24] However, the SQ limit is based on the PN junction-based single-junction solar cell, and tandem solar cells and non-PN junction-based solar cells can surpass the SQ limit. Additionally, due to the variation between the practical cells with the assumptions, there are some reports close to or surpassing the SQ limit.[25]

1.2.5 Evolution of photovoltaic technology

In 1839, Edmond Becquerel first discovered the photovoltaic effect in the experiment of the effect of light on electrolytic cells.[27] In 1883, C. Fritts produced the first solid-state photovoltaic cell by coating selenium on a gold foil.[28] In 1954, three scientists, Calvin Fuller, Daryl Chapin, and Gerald Pearson, demonstrated the first practical solar cell in Bell Labs.[29] Since then, the exploration of solar cells has never been suspended.

The first generation of solar cells is the silicon-based solar cells, including monocrystalline silicon, polycrystalline silicon, and single-crystal GaAs solar cells. The monocrystalline silicon solar cells currently achieved an efficiency of 27.6%, which are made of highly pure single-crystal silicon rods, and therefore, have the highest production cost. The polycrystalline solar cells greatly reduce the production cost and achieve a PCE of 23.3% according to the certification of NREL (Figure 1.15). The silicon-based solar cells is the most mature PV technology and take 95% of the global market.[30] In 2024, China's new photovoltaic installed capacity reached 277.57GW, and the cumulative installed capacity exceeded 880GW.[31] GaAs (III-V group semiconductor) solar cells have currently achieved the highest efficiency of 27.8% (30.8% for the concentrator solar cells) among single-junction solar cells. Compared with silicon, GaAs is brittle, but it has better temperature resistance properties and a larger bandgap to match well with the spatial solar spectrum. Therefore, it is widely

used in space, for example, artificial satellites, space stations, space probes, and landing probes.

The second generation is the thin-film solar cells, including the amorphous silicon, GaAs, CdTe, and CIGS thin-film solar cells. This type of solar cell has a low production cost and is portable, light, and flexible. Currently, the GaAs thin-film solar cells have achieved a PCE of 29.1%, surpassing the silicon-based solar cells. Amorphous silicon solar cells are p-i-n junction-based and have many defects, whose long-range disorder destroys the momentum conservation selection rule of the electron transition, and thus, they could be taken as a direct bandgap material and have a high absorption coefficient for photons. CdTe thin film solar cells have the merits of low toxicity and a short period of recycling compared with silicon-based solar cells. However, tellurium is a rare material, which significantly increases the production cost. The advantage of CIGS is that its bandgap is tunable by changing the amount of indium and gallium, which is attractive for the tandem solar cells. However, CIGS thin-film solar cells conventionally apply a CdS buffer layer, which is toxic. Therefore, the development of CdS-free buffer layers is of great importance.

The third-generation solar cells contain Dye-Sensitized (DSSCs), perovskite (PSCs), organic/polymer (OSCs), and quantum dot (QD) solar cells, which are still in the laboratory stage. The light harvesting in DSSCs depends on dye molecules. Then the excited electrons transferred to the conduction band of TiO_2, followed by electron transport through the nanoparticle network to the substrate. There are dye regeneration and electrolyte regeneration. Perovskite solar cells' light-harvesting layer is organic-inorganic hybrid perovskite materials (metal-halide, ABX_3, where A is organic cation or inorganic ion, B is metal cation, and X is halogen anion), which have high absorption coefficients and high charge carrier mobility. The excitons in PSCs are Wannier excitons (weak binding energy, nearly free electrons and holes), which transport to the external circuit via the electron/hole transporting layer (ETL and HTL) and require a cascade energy level between the active layer, transporting layers, and electrodes. The emergence of PSCs was in 2009 by Prof. Tsutomu Miyasaka, and till now, PSCs have achieved a PCE of 27.0% in the single junction devices and 34.6% in perovskite /Si

tandem cells, showing their great commercialization potential. However, the problems of humidity sensitivity and the toxicity of lead need to be addressed at this stage. Quantum dot solar cells' light-harvesting materials are semiconductor nanocrystals (quantum dots), which contain a limited number of atoms. At the nanoscale, quantum dots have the quantum confinement effect, whose bandgap is tunable by changing the size of the quantum dots, and one photon may excite multiple electron-hole pairs. Due to the features of multi-excitons and independence from PN junction, it is possible to surpass the SQ limit and achieve a higher theoretical efficiency. However, it is currently limited by poor stability and efficiency. Organic solar cells are based on organic materials, which possess the attractive merits of low cost, solution processability, light and flexible, colorful and semitransparent, and environmentally friendly, showing their potential in wearable/portable electronics, building-integrated photovoltaics, agricultural photovoltaics, and aesthetic design, which will be introduced detailly in Section 1.3.

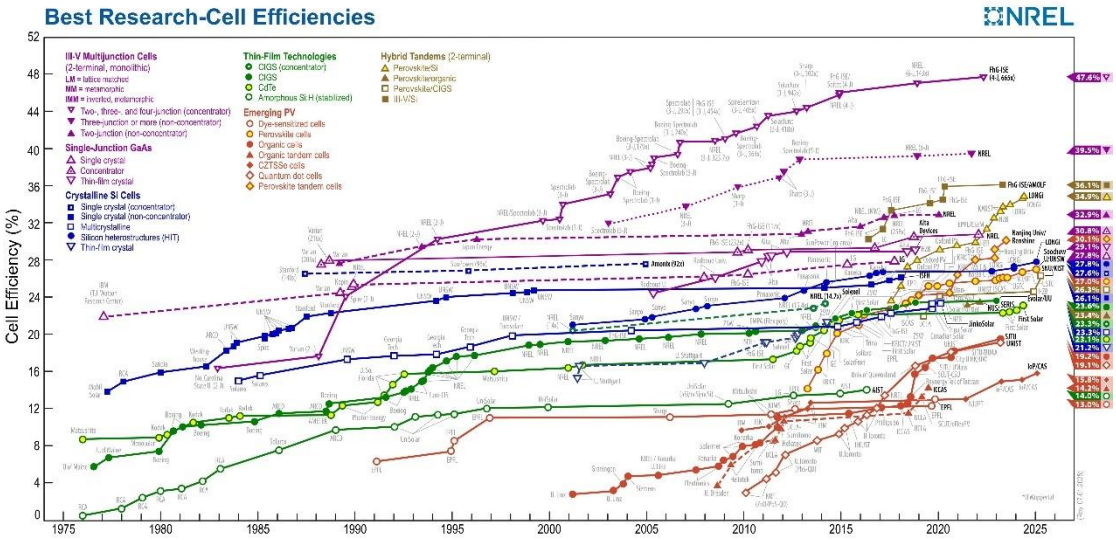

Figure 1.15 The photovoltaic cell efficiencies from NREL.[32]

1.3 Organic photovoltaics

The high production costs and complicated production processes of silicon-based solar cells and the heavy metal-containing/environment pollution problem of CdTe, GaAs, CIS, CIGS, and perovskite solar cells limited their application in certain situations,

which makes OSCs gradually develop and become a current laboratory's dynamic research area due to the merits of flexibility, transparency, low pollution, and roll-to-roll processability. Due to the research on material design and device optimization, organic solar cells have developed rapidly to surpass 20% in single-junction solar cells. Organic photovoltaics is based on organic semiconductors, which possess the basic properties of semiconductors that we introduced above. However, several differences still exist between the organic and inorganic semiconductors. This section first gives a brief introduction to organic semiconductors, and then introduces the basic working mechanism of OSCs, finally followed by the evolution of the OSC device structures.

1.3.1 Fundamental organic semiconductors

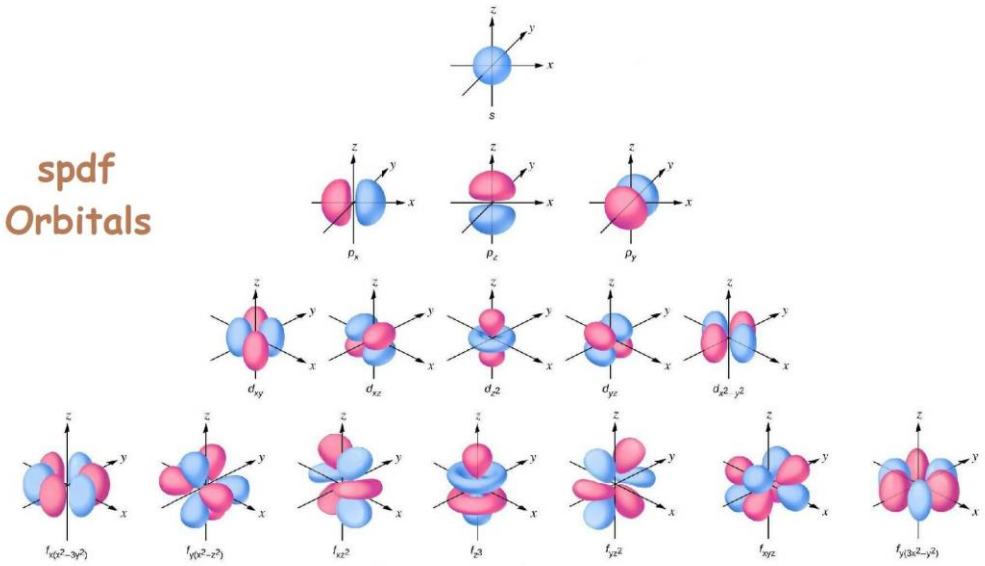

Figure 1.16 The demonstration of the s, p, d, f atomic orbitals.[34]

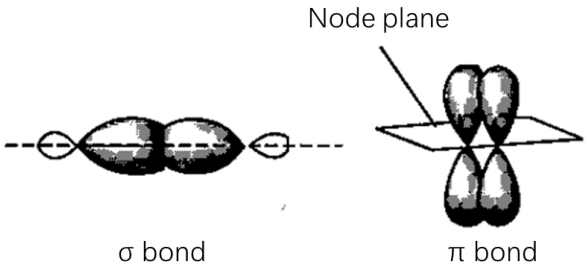

Figure 1.17 The schematic diagram of the formation of the σ bond and the π bond.[33]

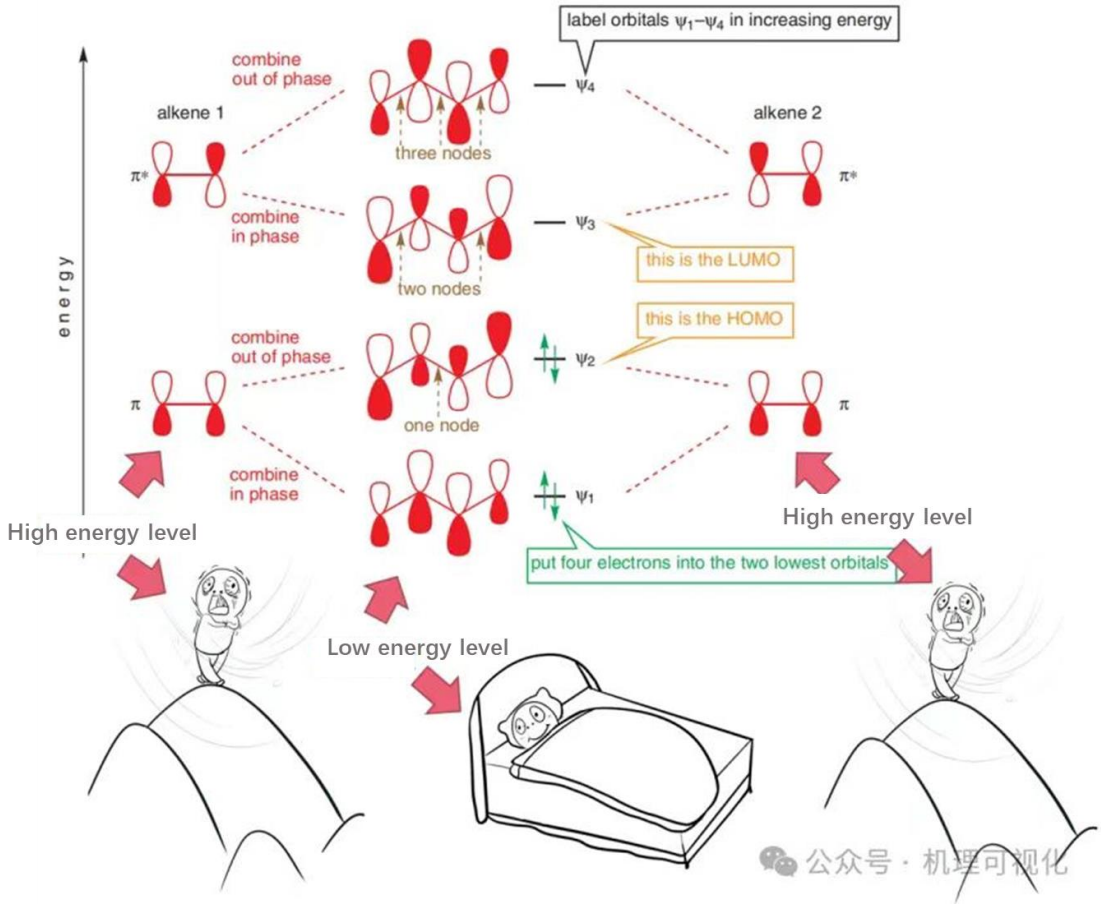

Figure 1.18 The formation of molecular orbitals by linear combination of atomic orbitals.

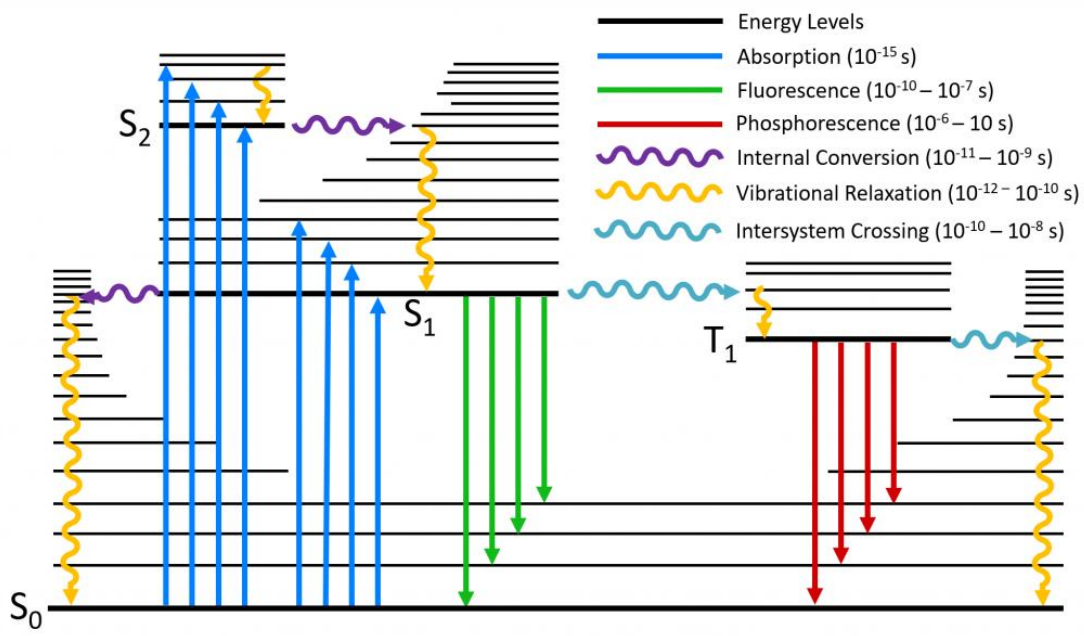

Figure 1.19 A typical Jablonski Diagram. [35]

First, organic materials are carbon-based including small amounts of H, O, N, S, P, and halogen elements. Second, different from inorganic semiconductor materials that are composed of atoms and covalent bonds to be highly crystalized, organic semiconductor molecules are highly conjugated via sp^2 hybridized carbon atoms to form π bonds. Third, the intermolecular interaction in organic semiconductor materials is dominated by van der Waals forces, along with dipole-dipole force and hydrogen bonding, which are weak interactions compared with the covalent bonds in inorganic materials, leading to the amorphous phases in organic semiconductors, making them partially crystalized. In addition, in inorganic semiconductors, the excitons were Wannier excitons with weak binding energy, while the excitons in organic semiconductors are Frenkel excitons or charge transfer excitons with strong binding energy between electrons and holes. The excitons in organic semiconductors are localized with short diffusion lengths. Furthermore, the excitons and carriers in organic semiconductors were usually localized, leading to small charge mobility in organic semiconductors ($10^{-5} \sim 10^{-3}$ $cm^2/(V \cdot s)$) compared with inorganic semiconductors ($10^2 \sim 10^4$ $cm^2/(V \cdot s)$). However, the different structure gives organic semiconductors unique features of easy modification, flexibility, and lightweight, enabling printable large-area modules and flexible electronics.

According to the Schrodinger wave equation, the wave function/electronic orbitals of an atom could be solved. Electron movement trace can be denoted by the electron cloud, and the orbital energy level represents the electronic energy. Electrons have wave properties and obey the uncertainty principle. The electron clouds refer to the probability of an electron appearing around the nucleus, also called electronic/atomic orbitals. There are four types of atomic orbitals (AOs): s, p, d, and f, with different shapes (Figure 1.16). Organic materials are based on the carbon element, which has 6 electrons ($1s^2 2s^2 2p^2$). The formation of the covalent bond between two atoms is by sharing electrons, and can be analyzed by the hybrid orbital theory. Covalent bonds include the σ bond and the π bond (Figure 1.17), where two atoms form a σ bond through head-to-head and form a π bond through shoulder-to-shoulder. π electrons have a stronger delocalization ability and result in intramolecular charge transfer (ICT) effect,

which is important for organic semiconductors required effective charge dissociation and charge transport efficiency. Organic semiconductors with a large π conjugated backbone possess unique optoelectronic properties because of the mobile π electrons. The molecular orbitals (MOs) are developed by the linear combination of atomic orbitals (LCAO) (Figure 1.18), which obey the rules of similar energy, maximum orbital overlap, and symmetry matching. The number of the formed MOs must be the same as the original AOs, and there are bonding orbitals with an energy lower than the previous AOs and anti-bonding orbitals with an energy larger than the previous AOs. Electrons preferentially occupy low-energy MOs following the Pauli exclusion principle. In molecular orbital theory, the highest occupied molecular orbital (HOMO) and lowest unoccupied molecular orbital (LUMO) define the frontier electronic states governing charge transport. For inorganic semiconductors, conductive behavior arises from electron transitions between the valence band (VB) and conduction band (CB). Organic semiconductors exhibit analogous mechanisms, where the HOMO and LUMO serve as the energy level counterparts to the VB and CB in crystalline materials, respectively. These frontier orbitals critically determine the fundamental optoelectronic properties of organic systems through their energy alignment and spatial distribution characteristics.[33] The migration, diffusion, and capture of electrons/holes at LUMO/HOMO energy levels produce the conductive properties of the material.

The electron transition process in organic semiconductors includes intramolecular and intermolecular electron transitions. The intramolecular electron transition can be described by the Jablonski Diagram shown in Figure 1.19. Usually, most of the molecules were in the ground state. Light absorption occurs when electrons transit to higher energy levels and light emission is the reverse process along with the production of fluorescence (spin-allowed) and phosphorescence (spin-forbidden). Electron transitions are spin-allowed only when the electronic states have the same multiplicity unless there is spin-orbital coupling. It is noticed that there are many vibration energy levels originating from the electron vibration at their equilibrium position. The electron transition between these energy levels is called internal conversion which does not emit photons. The electron transition between electronic states with different multiplicity

under spin-orbital coupling is called inter-system crossing, which is also a non-radiative decay process.

The excitons (electron-hole pairs) form when electronic transitions occur from the ground state to higher energy levels under photoexcitation and electroexcitation. Due to the small bandgap and low dielectric constant of organic semiconductors, only Frenkel excitons and charge transfer excitons within organic semiconductors with large Coulomb force. Exciton transport is the energy transport between molecules within the lifetime of excitons (before exciton annihilation). The most important processes of exciton transport in organic molecules include Förster energy transfer and Dexter energy transfer. If the hole/electron concentration is high, the Coulomb repulsion between electrons and holes is large, which tends to reduce the Coulomb attraction and may lead to the dissociation of excitons. In addition, if there exists a built-in electric field inside the solid, it may also induce the exciton separation, thereby generating free charge carriers (Onsager effect). There are two carrier transport modes: band transport and leap transport. Band transport occurs when the interaction between the charge and the lattice phonons is small and the width of the energy band is large enough. The leap transport is highly localized. electrons or holes jump between discrete energy levels and scatter at every point. In amorphous organic solids, the transport of carriers is mainly in a leap mode. Furthermore, in organic solids, the lattice is irregular, and there are many states that help capture carriers, namely traps, such as impurities and lattice defects. Traps limit the movement of carriers and, at the same time, make the movement of carriers more complicated.

1.3.2 Working mechanism of OPV

Due to the large binding force of Frenkel excitons, unlike inorganic photovoltaic devices that produce nearly free electron-hole pairs (Wannier excitons) after absorbing light, organic photovoltaic devices produce mobile excited states (bound electron-hole pairs). Furthermore, the energy required for exciton dissociation is large due to the strong Coulomb force and small dielectric constant of organic materials. These characteristics determine that the working mechanism of OSCs is different from that of

inorganic PN junction photovoltaic devices. The basic OPV working mechanism is shown in Figure 1.20, including exciton formation/diffusion/separation, and charge transport/collection. Generally, the light-harvesting, exciton generation, and charge separation efficiency are determined by material properties, while exciton diffusion and charge transport, to a large extent, depend on the film morphology quality (phase separation size), and charge collection is related to the organic-electrode interface.[36] Thus, the material optoelectronic properties, active layer morphologies, and device overall structures decide the performance of an OSC.

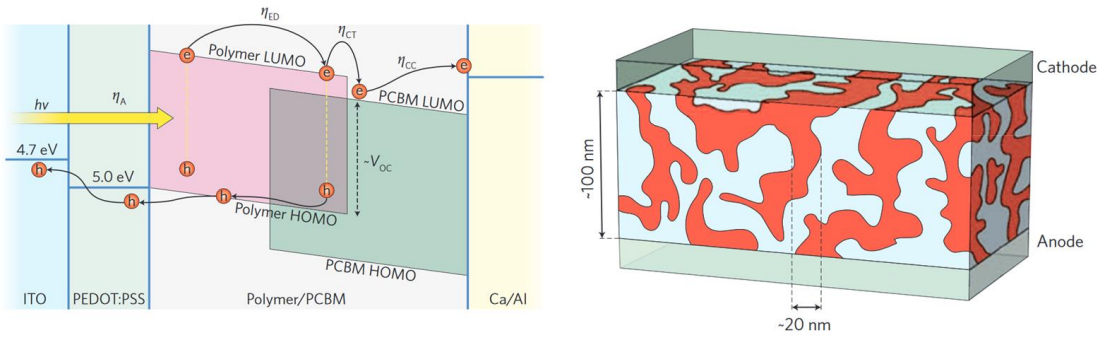

Figure 1.20 Working mechanism and morphology diagram of organic solar cells.[36]

(1) **Exciton formation** When light is irradiated on the donor/acceptor material in the active layer, the electron in the HOMO energy level absorbs a photon and is excited to the LUMO energy level, and left a hole in the original HOMO energy level. The electron and the hole are attracted by positive and negative charges to form an electron-hole pair, that is, a Frenkel exciton. Because of the low dielectric constant of organic semiconductors and the large Coulomb binding force between electrons and holes, it required a large driving force for excitons to separate into free charges in this process.

(2) **Exciton diffusion** Excitons transport along the material to the donor-acceptor interface through Forster energy transfer and Dexter energy transfer. Suppose the distance between the position where the exciton formed and the D/A interface exceeds the exciton diffusion length (the displacement of the exciton motion before exciton annihilation, an empirical value of 10 nm). In that case, the exciton is easy to recombine during diffusion, that is, an invalid charge, causing energy loss.

(3) **Exciton separation** The exciton dissociates and separates into free charges with the help of a built-in electric field driven by the energy level difference between heterogeneous molecules at the D/A interface. The charge transfer state would form during the charge separation, and the exciton dissociation could occur when the exciton's energy is greater than that of the charge transfer state.

(4) **Charge transport and collection** Charges are transferred to their respective electrodes under the built-in electric field derived from the work function difference between the two electrodes. Electrons move along the acceptor material to the cathode (lower work function), and holes transport along the donor material to the anode (higher work function). Another driving force for the charge transport is charge carrier concentration. The carrier concentration is high at the D/A interface and they tend to diffuse to the position with a low carrier concentration, getting close to the electrodes to be collected. The free charges directed movement produced electric current to the external circuit. The charge carrier with a certain possibility to recombine at the D/A interfaces and at the traps/defects in materials, which limited the carrier mobilities.

1.3.3 Device structure of organic photovoltaic

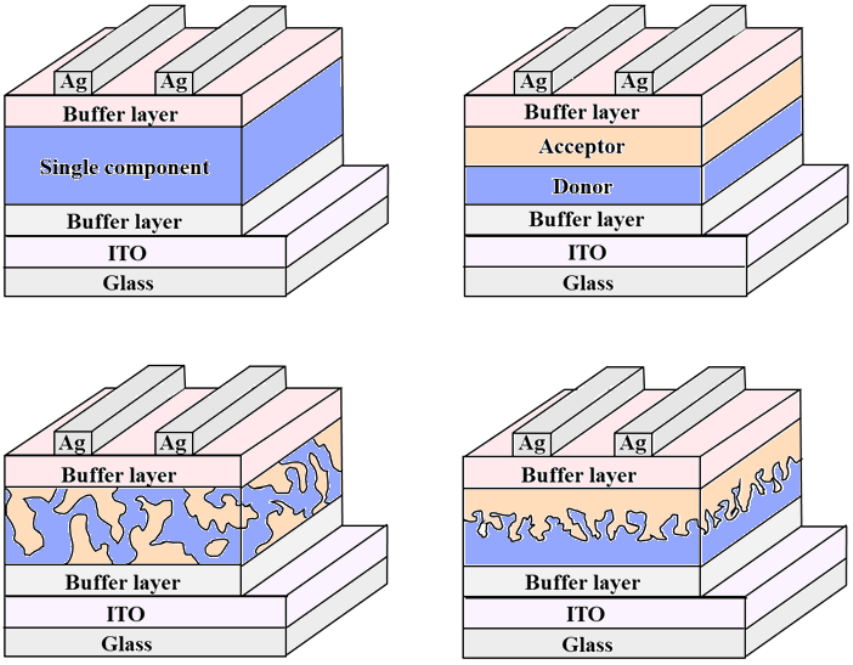

Figure 1.21 Solar cell structures of the Schottky-type, the double-layer heterojunction, the bulk heterojunction, and the quasi-bilayer solar cell.

Figure 1.21 shows four basic solar cell structures including the Schottky-type single-layer structure, the double-layer D/A heterojunction structure, the bulk heterojunction (BHJ) structure, and the p-i-n-type quasi-bilayer structure.

In Schottky-type solar cells, a single organic semiconductor material layer is sandwiched between two electrodes. The main driving force for exciton dissociation is the built-in field caused by the work function difference between the two electrodes. However, it is usually too small to separate excitons in organic materials, so the exciton dissociation efficiency is extremely low, resulting in a low short-circuit current in Schottky solar cells. The performance characterization of D-A double-cable materials usually employs this structure.

Double-layer heterojunction cell includes two heterogeneous organic semiconductors, one donor layer and one acceptor layer. The formed donor-acceptor interface largely improved exciton separation efficiency due to the difference in energy level between the two materials. The dissociated electrons transport along the acceptor and holes transport along the donor, improving charge dissociation efficiency and reducing the possibility of charge recombination.

In 1995, A. Heeger et al. proposed the BHJ device structure with a D/A interpenetrating network structure by blending donor and acceptor together, where the active layer is full of D/A interfaces, greatly improving the exciton diffusion and separation efficiency. However, the charge transport in BHJ is not comparable to that in the double-layer cells. Although the blending of donors and acceptors hinders the transfer of charges to a certain extent, resulting in low carrier mobility, this type of solar cell is widely used in the performance characterization of photovoltaic materials due to its advantages of high power conversion efficiency. Thus, the morphology control in BHJ devices is of great significance. If the domain size is too small, the domain purity is low, and charge transport is poor, with a great probability for charges to recombine. Conversely, the excessive domain size results in non-efficient charge separation due to the limited D/A interfaces. Therefore, the domain sizes must be optimized to simultaneously satisfy highly-efficient charge separation and transport.

The quasi-bilayer structure is proposed combining the merits of double layer heterojunction and BHJ. The quasi-bilayer here refers to the p-i-n structure with a much preferable vertical phase separation where relatively pure donor and acceptor phases accumulate at the bottom and the top of the active layer, respectively, while partial BHJ structure is distributed at the middle. Such a p-i-n structure provided sufficient D/A interfaces for highly efficient charge separation and relatively pure p and n regions for highly efficient charge transport. The relatively separated and pure phases have been proven to resist morphological deterioration to achieve better stability. Therefore, most of the recent researches are based on this structure as it simultaneously possesses superior device performance and enhanced device stability.

1.3.4 Application of organic photovoltaic

Organic solar cells with the merits of being flexible, semitransparent, roll-to-roll producible, and environmentally friendly, showing great potential in application in organic solar panels, building-integrated photovoltaics (BIPV), solar-powered vehicles, and wearable devices, etc. This section introduces several research directions of OSCs regarding commercial applications.

The SQ limit determines the constrained performance (<33%) of single-junction solar cells. People transfer their sight to the tandem solar cells with the promising advantages of broadened absorption ranges, suppressed energy loss, and higher device efficiency beyond the SQ limit. The tandem solar cell includes connections in series and parallel, and according to the active layer materials, includes organic/organic, organic/perovskite, organic/silicon solar cells, etc. Hou et al. applied PBDB-TF: GS-ISO as the bottom subcell, PBDB-TF: BTP-eC9 as the top subcell, and the electron beam evaporated TiOx and PEDOT: PSS as the interconnecting layer (ICL) (Figure 1.22a-b), achieving a PCE of 20.2%.[37] Li et al. reported the acidic magnesium-doped SnO_2 quantum dots interface layer, and based on that, they constructed a highly efficient all-inorganic perovskite/organic tandem solar cell by employing a wide bandgap $CsPBI_2Br$ as the top subcell and a narrow bandgap PM6: BTP-eC9 as the bottom

subcell (Figure 1.22c), achieving a high efficiency of 25.9% in the monolithic n-i-p all-inorganic perovskite/organic tandem solar cells.[38]

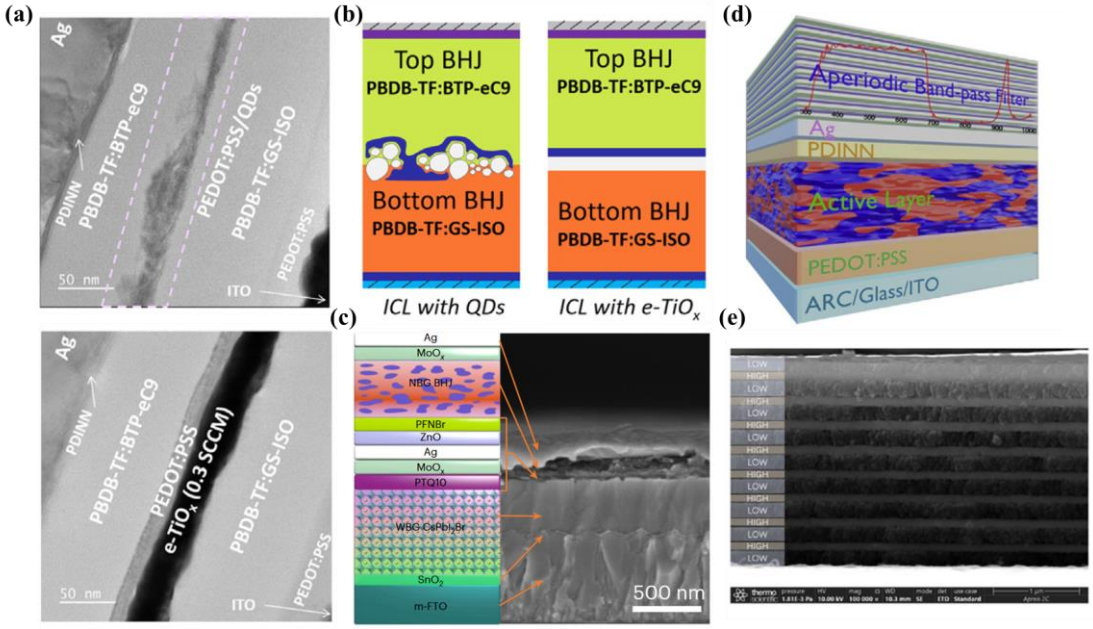

Figure 1.22 (a) Cross-sectional SEM image and (b) schematic diagram of tandem OSCs.[37] (c) Cross-sectional SEM image of the perovskite/organic tandem cell.[38] (d) Device structure of the ARC and ABPF-based transparent solar cell. (e) Cross-sectional SEM image of the ABPF.[39]

Semitransparent solar cells require careful optical design of the transparent rear electrodes and the distributed Bragg reflector (DBR) layer. Li and Yu et al. designed an aperiodic band-pass filter (ABPF) of $[LiF/ TeO2]^8$/LiF and an antireflecting coating (ARC) of $(LiF/TeO2)^4$ (Figure 1.22d-e), which enabled high transparency in the visible and total reflection in the NIR region. They further constructed the transparent OSC applying the integrated ARC-ABPF electrode and a ternary system of PM6: BTP-eC9: L8-BO, achieving a light utilization efficiency (LUE) of 5.35% with a PCE of 11.44%, an average visible transmittance (AVT) of 46.79%, and a color-rendering index (CRI) of 85.39.[39] Li C.Z. et al also designed a novel DBR of MoO_3/LiF/MoO_3, achieving a high AVT of 32.07%, a high color fidelity with the CRI of 90%, a high infrared radiation rejection (IRR) of 0.90, and a transparent OSC module of 11.28%.[40]

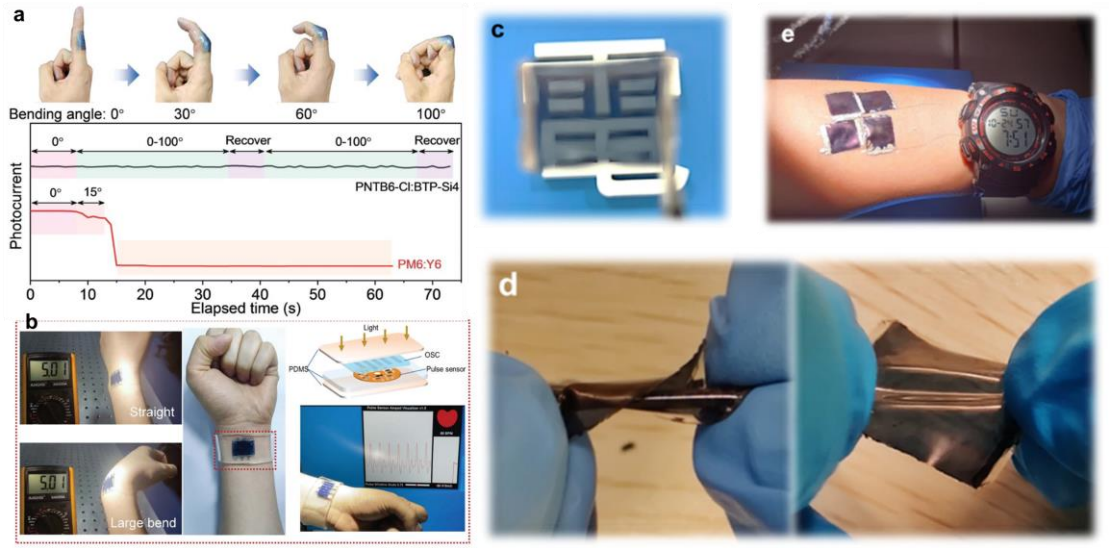

Figure 1.23 The monitor of (a) the photocurrent and (b) human heart rate under different bending angles.[41] Photographs of the intrinsically stretchable OSCs to demonstrate their (c) semitransparent property, (d) twisted and stretchable ability, and (e) ability to power a watch.[42]

The wearable devices are attractive in integrating with photovoltaics, encouraging people to explore the flexible features of OSCs. The flexibility of active layer materials is proven to be a determining factor in stretchable device performance. Shao et al. designed the organosilane-functionalized SMA BTP-Si4 with a low degree of crystallinity and fabricated a stretchable OSC by blending with PNTB6-Cl. The s-OSCs showed excellent ultimate strain of 95.5% and maintained a PCE of 14.6% (82% of the initial efficiency) when the tensional strain is at 80%, largely surpassing its flexible counterparts (Figure 1.23a-b).[41] From the perspective of device engineering, the key point of the innovation of flexible OSCs is the designation of stretchable transparent electrodes (STEs). Li et al. designed an abrasive paper-patterned PDMS flexible substrate and fabricated a stretchable ITO-free OSC, which displayed good condition-insensitive property, gave high PCE under outdoor strong light, indoor dim light, and any light direction condition.[17] They further reported an intrinsically stretchable solution-processed AAA STE (Al-doped zinc oxide (AZO) at silver nanowire (AgNWs)). They further fabricated the all-solution processed OSCs by employing

TPU@AgNWs as front STE and AAA as back STE, achieving a state-of-the-art PCE of 10.9%, which maintained 76.5% of PCE after 500 stretch-release with 10% tensile strains (Figure 1.23c-e).[42]

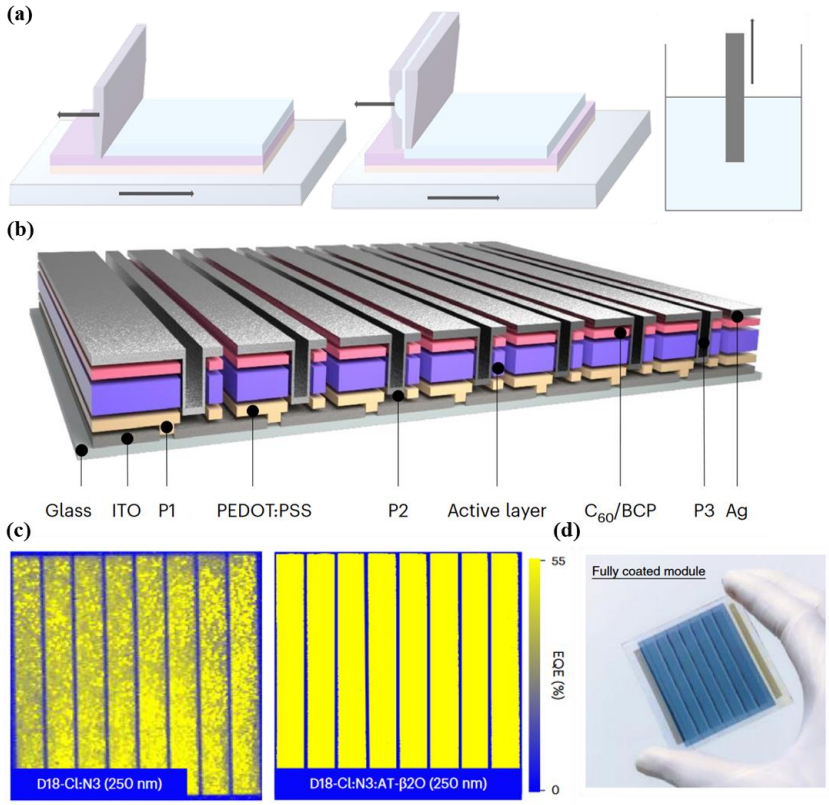

Figure 1.24 (a) Schematic diagram of (a) the doctor-blade coating, slot-die coating, and dip coating and (b) a large-area OSC module. (c) The light-beam-induced current (LBIC) mapping of the AT-β2O-based solar module.[43] (d) A picture of the EDOT: F HTL-based solar module.[44]

The large-area production is the prerequisite condition for OSC commercialization. Meniscus-guided coating (MGC) is the commonly used fabrication method for large-area fabrication, including doctor-blade coating, slot-die coating, and dip coating (Figure 1.24a), and the morphology control in large-area fabrication is of primary significance towards high-performance organic solar modules. Li Y.W. et al synthesized a crystallization regulator AT-β2O and changed the crystallization sequence during film formation to improve the film morphology and achieve desirable phase separation in the active layer, which enabled uniform and smooth pinhole-free film (Figure 1.24c)

and achieved a PCE of 18.36% on a 15.03 cm^2 module.[43] Zhou et al. designed an alcohol-dispersed HTL PEDOT: F and applied it in the fully-printed OSCs, which achieved a PCE of 15.26% and displayed outstanding light stability with a T_{83} of 1330h. They further fabricated the all-printed organic solar module, achieving a PCE of 13.07% with an area of 12.2 cm^2 (Figure 1.24d).[44]

1.4 Research motivation and objectives

1.4.1 Research motivation

It is of great significance to develop OSCs as they possess multiple practical and attractive merits. However, there is still a long path to their industrial and commercial applications. The challenges include: 1) the hard-to-control film aggregation kinetics and morphology in upscaling manufacturing; 2) the lagged device efficiency during the transition from halogenated solvent to environmentally friendly nonhalogenated solvent; 3) large nonradiative recombination loss originating from the amorphous morphology; and 4) inferior device operational stability regarding long-term applicable OSCs. Current studies mainly focus on efficiencies instead of the underlying film formation mechanism and typically ignore the correlation between molecular design and device properties. This work provides a bridge to understand the relationship between molecular structure, crystallization process, and device performance, possessing valuable guidance for further research on molecular design and material selection rules, helping to construct highly efficient and stable OSCs towards industrialization.

1.4.2 Research objectives

This thesis mainly focused on highly efficient and stable organic solar cells with the exploration of morphology manipulation and energy loss suppression. The objectives are listed as follows:

1. To address the over-aggregation issue in blade coating processing and to achieve high-performance and long-term stable OSCs under open-air coating conditions.

2. To achieve highly effective and long-operational halogen-free solvent-processed OSCs and further unveil the trade-off relationship between miscibility and crystallinity of active layer components.
3. To explore the material and device degradation pathway and provide possible solutions to alleviate the deterioration towards long-term used high-performance OSCs.
4. To figure out the underlying correlation between the precursor solution, crystallization kinetics, and final film microstructures, along with their impact on the charge carrier dynamics and device photovoltaic properties.
5. To suppress the radiative and nonradiative recombination loss in OSCs by regulating material crystallinity and molecular packing to reduce Urbach energy and reorganization energy.

1.4.3 Thesis outline

Chapter 1 briefly introduced the background of OSCs. Basic knowledge of solar energy, including photons, solar spectrum, and air mass, was first summarized. The second part introduced photovoltaics, containing the fundamentals of semiconductors, PN junctions, and the working mechanism and basic parameters for photovoltaic technology. Finally, organic photovoltaics were introduced from the aspects of organic semiconductors, working mechanisms, and the evolution of device structures.

Chapter 2 gave the literature review of recent research on photoactive layer materials and photoactive layer manipulation. The common design rules for active layer materials were introduced and then mainly focused on the evolution of polymer donors and small molecular acceptors. The second part is regarding the photoactive layer manipulation by a ternary strategy, where the effect of a third component on morphology regulation, energy loss suppression, and stability improvement was reviewed.

Chapter 3 proposed an ink solubility tuning strategy by a multi-component approach to address the challenges in controlling the film aggregation kinetics and

morphology in doctor blade coating. Incorporating a twisted third component (BTP-4Cl) can induce rapid crystallization behavior and promote fine phase separation size between the donor polymer (PM6) and the acceptor (BTP-eC9) to effectively alleviate the excessive aggregation in blade coating. Simultaneously, this work gave insights into the correlation between solubility tuning, crystallization kinetics, and device performance from the perspective of molecular structure and intermolecular interactions, enabling the realization of highly efficient and stable open-air-coated, eco-friendly OSCs (19.67%).

Chapter 4 demonstrated two highly crystalline 2D acceptors, ATIC-C11 and ATIC-BO, with acenaphthene-expanded quinoxaline central cores. The difference in side chains induces their distinctive molecular packing mode and unique crystal structure, in which ATIC-C11 displays a 3D structure with an elliptical framework, and ATIC-BO gives a rectangular framework. ATIC-C11's suitable crystallinity and compatibility positively regulate the crystalline kinetics during film formation, thus forming a much more ordered molecular packing and favorable domain size in blends. However, ATIC-BO's strong self-aggregation and immiscibility induce large aggregates and severely impede charge transfer (CT) and dissociation. As a result, ATIC-C11-based ternary devices achieve a high efficiency of 19.28% with potential in scalability and stability.

Chapter 5 synthesized and applied two highly crystalline 2D extended materials, PhIC-BO and AnIC-BO, in the quasi-planar heterojunction (Q-PHJ) OSCs to improve device efficiency and stability. Phenanthrene-extended PhIC-BO showed a 3D network crystal structure with an elliptical framework, and anthracene-extended AnIC-BO gave a linear packing to form the quasi-3D network crystal structure. Further investigation showed that the participation of the highly crystalline acceptors effectively suppressed the material chemical oxidation reaction and morphological degradation. Eventually, the PhIC-BO, as a good energy donor in the ternary system, exhibited largely improved device operational stability and a PCE of 19.44% thanks to the optimal charge carrier behaviors.

Chapter 6 first gave a summary of the thesis and followed by the prospects for further research on highly efficient and stable OSCs towards commercial and industrial applications.

Chapter 2 Literature Review

The photoactive layer is important in OSCs as it is the photo-harvesting and photoelectric conversion layer. The properties of active layer materials and the active layer film morphology dominate the charge carrier behavior and the device's overall performance, which motivates researchers to explore material design and morphological optimization. This chapter first introduces the evolution of photoactive layer materials regarding polymer donors and small molecular acceptors, followed by the introduction of photoactive layer manipulation by a ternary strategy, including the effects on morphology regulation, energy loss suppression, and stability improvement.

2.1 Photoactive layer materials

Photoactive layer materials are one of the most significant components in OSCs since their optimal physicochemical, optoelectronic, and photovoltaic properties are the key for OSCs to show off their superb performance. Most of the current OSCs are D/A blend-based, and the basic requirements are that the donor has a strong capability to donate electrons, the acceptor has a strong capability to accept electrons, and their energy levels must be matched. Generally, material design should consider several basic aspects, including solution processability, light-harvesting capability, energy level alignment, and efficient molecular packing. The planar π-conjugated backbone with alkyl side chains is the basic structure for OSC materials. The π-conjugated backbone ensures compact and ordered molecular packing for efficient charge transport. Extending the molecular conjugated backbone could redshift the absorption range. The alkyl side chain modification is a useful strategy to regulate material solubility and molecular stacking. The introduction of halogen atoms could effectively downshift the energy levels. Additionally, enhancing the intra- and inter-molecular interactions by employing heteroatoms (S, N, O, Se, F, Cl, etc.) and utilizing strong electron-donating and electron-withdrawing groups to promote the intramolecular charge transfer (ICT) effect are the commonly used methods to regulate molecular energy level (Figure 1.25),

molecular planarity, and π electron conjugation, towards high-performance photoactive layer materials.

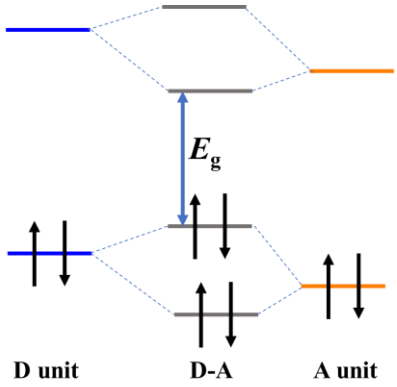

Figure 1.25 The Orbital hybridization of D and A units in a D-A type molecule.

From the perspective of structures, OSC materials include polymers, oligomers, and small molecules. Due to the optimal flexibility and good thermodynamic stability of polymers, all polymer solar cells (APSCs) were employed to achieve highly stable OSCs with excellent robustness. However, APSCs face the problem of complicated synthesis, hard-to-control molecular weight, and poor phase separation due to the improper miscibility between polymers.[45–48] All small molecular solar cells (ASMSCs) are an important branch of OSCs. Small molecules possess specific chemical structures and strong crystallinity, where the batch difference is small and tend to form ordered molecular packing, while ASMSCs face challenges in morphological instability and poor mechanical properties, as small molecules are highly brittle.[48–52] Oligomers are equipped with features of polymers and small molecules, which have a defined chemical structure, high glass transition temperature, and high viscosity, enabling it the key research direction. However, they have the issues of relatively poor mechanical properties and complex synthesis, limiting their further application.[53–58] Additionally, there are a few studies reported the single-component OSCs and the combination of small molecular donors and polymeric acceptors, while the lagging device performance impeded their further prosperity.[59–61] Currently, the most commonly used active layer is composed of polymer donors and small molecular acceptors, which has pushed the power conversion efficiencies to surpass 20%.[1–5] Thus, this section mainly summarizes the research progress of polymer donors and small molecular acceptors.

2.1.1 Development of polymer donors

In the early research, polymer donors were mainly poly(phenylene-vinylenes) (PPV) and polythiophene (PT) derivatives. Wudl et al. in 1992 discovered the photoinduced ultrafast electron transfer from the excited MEH-PPV to buckminsterfullerene C60[62] The next year, they further reported the MEH-PPV: C_{60} double-layer D/A heterojunction device with a PCE of 0.04%[63]. Heeger et al. in 1995 reported the bulk heterojunction solar cell, which employed MEH-PPV (D) and C_{60} and its derivatives (A)[64]. In 2001, Hummelen et al employed MDMO: PPV/$PC_{61}BM$ and improved the PCE to 2.5%[65]. Brabec et al. in 2002 used P3HT and $PC_{61}BM$ to improve the PCE of OSCs to 2.8%[66]. In 2005, Yang and Li et al. investigated the effect of thermal annealing on the film quality based on the P3HT: $PC_{61}BM$ and enabled the efficiency to 4.4%[67]. However, the optical band gap of PPV and PT derivatives is large and their structure is not conducive to modification and regulation of energy levels, limiting the further development of OSCs. The alternative D-A unit copolymers were employed as they have various substituted sites for structure modification to regulate the absorption profile and energy level. Additionally, D-A alternative polymers possess the mutually changed aromatic structure and quinone structure, promoting the planarity and conjugation degree of the polymer chain, conducive to π electron delocalization and smaller band gap. Current PDs usually employ side chains and π bridges to regulate the solubility, planarity, molecular packing, carrier transport performance, etc. Here, we listed several commonly used polymer donors.

BDT unit In 1983, the Benzo[1,2-b:4,5-b']dithiophene (BDT) structure was first reported[68]. In 1992, the concept of D-A alternative copolymerization was raised[69]. In 2008, Yang et al. first used the BDT structure as an electron-donating unit to copolymerize with several commonly used electron-withdrawing units, including thiophene, thieno[3,4-*b*]pyrazine (TPZ), and benzo[*c*][1,2,5]thiadiazole (BT), to construct a series of polymer donors [70]. The next year, they employed 2,4-dioctylthiophene on the BDT unit (BDT-T) and developed PBDTTBT[71]. In 2011, Hou et al. used 2-ethylhexylthiophene as the conjugated side chain on BDT and found that

this structure has a more effective conjugated area, ensuring good π electron delocalization and molecular stacking[72]. The BDT unit was the most used electron-donating moiety in constructing high-performance polymer donors.

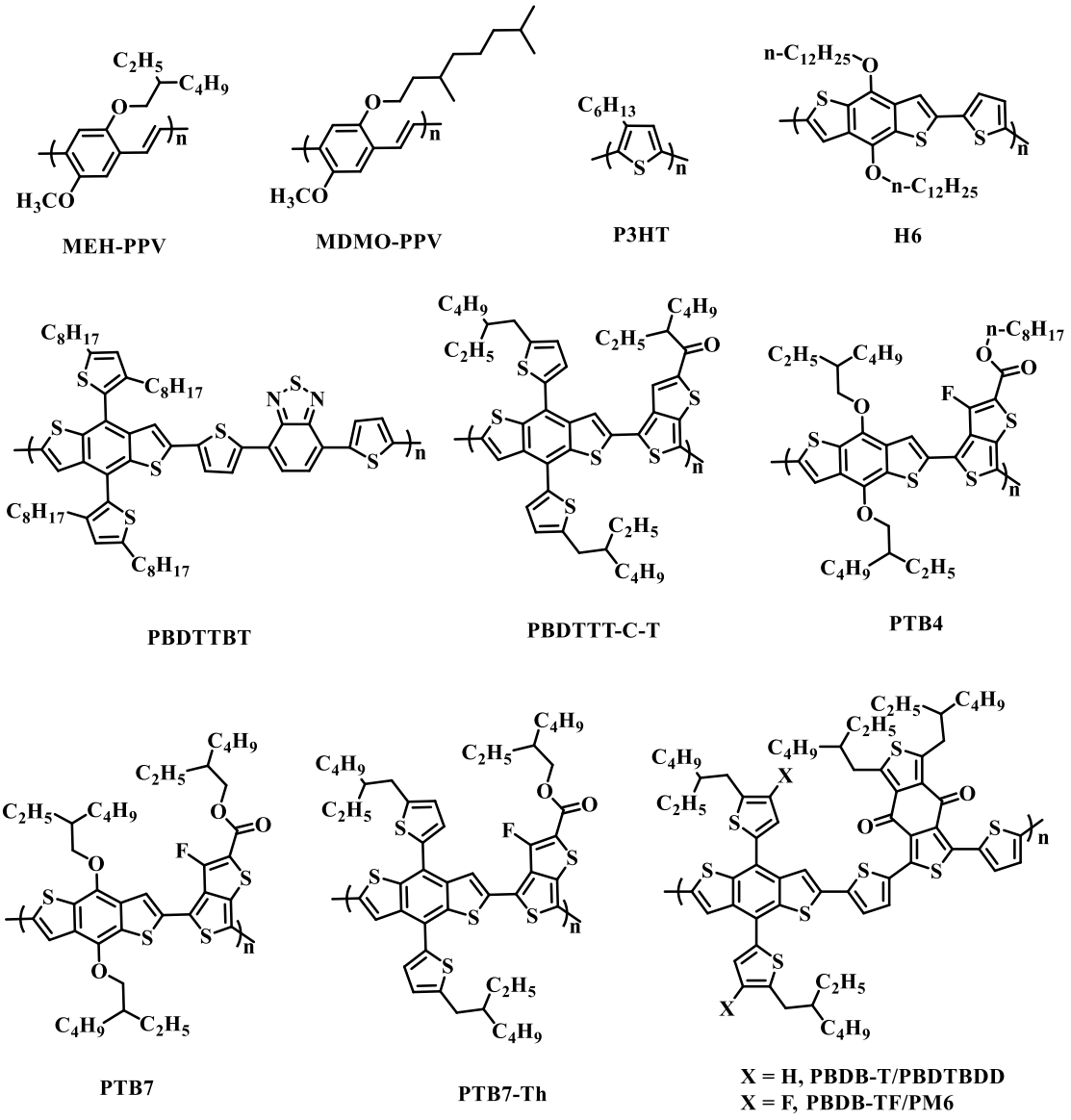

Figure 2. 1 Chemical structure of the representative donor materials.

TT unit PTB series refers to the polymer donors that employed BDT as the electron-donating unit and thieno[3,4-*b*]thiophene (TT) as the electron-accepting moiety. In 2009, Yu et al. synthesized an array of PDs by copolymerization between BDT and TT derivatives, among which PTB4 using fluorine- and ester-substituted TT as the electron-withdrawing unit reached a PCE of 6% after blending with $PC_{61}BM$[73]. The next year, they further developed PTB7 and achieved a PCE of 7.4% by blending

with $PC_{71}BM$[74]. In 2011, Hou et al further synthesized PBDTTT-C-T using the 2-ethylhexyl substituted BDT-T unit and a TT derivative, achieving a PCE of 7.59%[72]. Later in 2013, Chen et al. developed PTB7-Th using BDT-T and fluorinated/ester-substituted TT. The device, by blending with $PC_{71}BM$, achieved a higher efficiency of 9.35%[75].

BDD unit In 2012, Hou et al. synthesized PBDTBDD (hereinafter referred to as PBDB-T) by employing the 2-ethylhexyl substituted BDT-T unit and BDD unit, producing a device with an efficiency of 6.67% by blending with $PC_{61}BM$.[28] With the awareness of the merits of the halogenation strategy, including lowering HOMO energy level, improving V_{OC}, and optimizing film morphology. In 2015, they synthesized PBDB-TF (PM6) by introducing fluorine atoms onto the thiophene side chain of PBDB-T, and the device with $P_{C71}BM$ had an efficiency of 9.2%[77]. PM6 is the star molecule and still one of the most commonly used donors currently due to its generality and outstanding photovoltaic properties. In 2017, they further developed PBDB-T-SF and IT-4F by the alkyl thiolation strategy and the fluorination strategy on PBDB-T and ITIC, respectively. The resultant device displayed a PCE of 13%, achieving the highest efficiencies at that time[78].

BT unit Janssen et al. in 2001 synthesized the first benzothiadiazole (BT)-based polymer donor for OSCs[79]. In 2010, Yang et al. reported the first conjugated side chain substituted BDT unit (BDT-T) and synthesized PBDTTBT by using BT as the electron-accepting unit[71]. Later on, You et al.[80] and He et al.[81] employed the fluorination and chlorination strategy on the BT unit and synthesized PBnDT-DTffBT and PBDTHD-ClBTDD, obtaining a PCE of 7.2% and 9.11%, respectively. The fused ring electron-accepting units based on the BT unit were also explored. In 2011, Cao et al. fused two BT units and synthesized the so-called NT unit. The corresponding polymer donor PBDT-DTNT obtained a PCE of 6% with $PC_{71}BM$[82]. Ding et al. in 2020 developed the DTBT unit that was synthesized by fusing two thiophenes with the BT unit. The resultant polymer donor D18 showed a deeper HOMO and strong aggregation due to the extended conjugated plane. A surprising PCE of 18.22% was obtained by blending with Y6 thanks to the complementary absorption, matching energy levels, and

preferable fiber network morphology[83]. They further synthesized D18-Cl by fluorinating D18 and achieved a PCE of 18.13% by blending with N3[84]. Many currently reported high-performance OSCs employed D18 series donors, pushing the PCE over 20%[1,2,5].

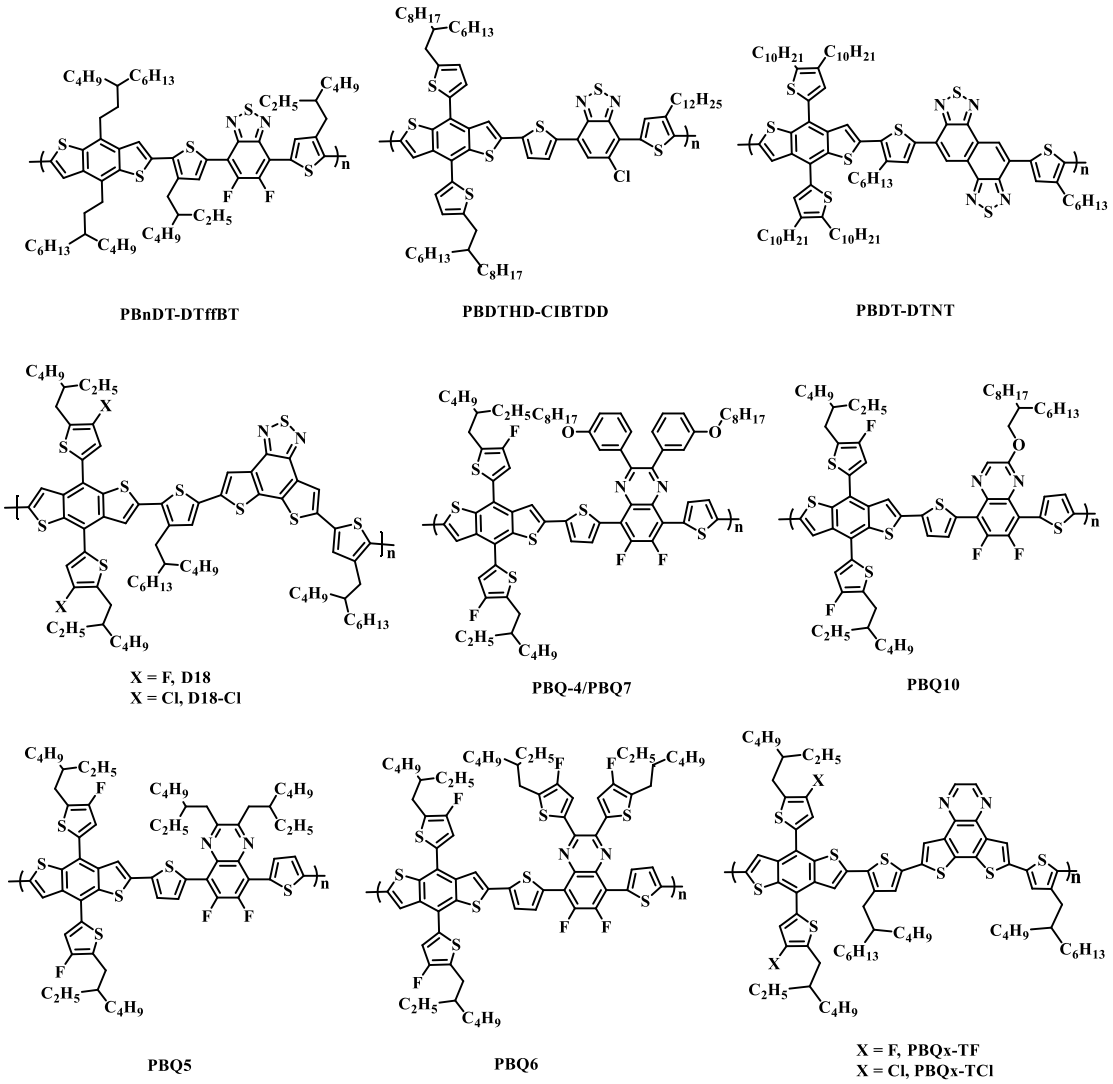

Figure 2. 2 Chemical structure of the representative donor materials.

Qx unit In 2015, Hou et al. applied BDT-T as the donor unit, 2,3-diphenyl-5,8-di(thiophen-2-yl)quinoxaline as the acceptor unit, and thiophene as the π-bridges to synthesize a series of polymer donor PBQ1-4, among which PBQ4 with two conjugated dialkoxyphenyl groups achieved the highest PCE of 8.55% with $PC_{71}BM$[85]. In 2020, Li et al. synthesized PBQ10 by copolymerizing BDT-T and monoalkoxy-substituted bifluoroquinoxaline. Compared to PBQ7 (also called PBQ4), PBQ10 showed a

downshifted HOMO due to the relatively weaker electron-donating ability of monoalkoxy group, blueshifted absorption resulted from its less conjugated structure, tighter π–π stacking in the vertical direction of the substrate because of the relatively smaller spatial conformation of the monoalkoxy substituent, resulting in a PCE of 16.34% by PBQ10: Y6 devices[86]. In 2021, they further reported PBQ5 and PBQ6 by changing the side chains on difluoroquinoxaline. PBQ6 with conjugated side chains showed redshifted absorption, stronger intermolecular interaction, faster charge transfer (CT) process, and more suitable nanoscale phase separation than PBQ5 with alkyl side chains. The PBQ6: Y6 devices showed a higher PCE of 17.62% (certified value of 17.2%) than PBQ5 devices with a PCE of 15.55%[87]. In 2021, Hou et al. applied BDT-T and dithieno[3,2-f:2'',3''-h]quinoxaline as the alternative moieties, and successively reported PBQx-TCl[88] and PBQx-TF[89]. The PBQx-TF: BTP-eC9-2Cl achieved a higher PCE of 17.7%, and an outstanding PCE of 19.0% (certified value of 18.7%) was obtained by adding a 3rd component, F-BTA3.

2.1.2 Development of small molecular acceptors

Small molecular acceptor (SMA) materials go through three stages: the fullerene acceptor, the A-D-A type acceptor, and the A-DA'D-A type acceptor. The fullerene acceptor dominates the OSCs' efficiency evolution to some extent. Early research was mainly based on fullerene derivatives, such as $PC_{61}BM$ and $PC_{71}BM$. Wudl. et al. in 1992 discovered the ultrafast charge transfer between MEH-PPV and C_{60}[62]. In 1995, the report of the BHJ structure was based on [6,6] PCBM and [5,6] PCBM[64]. In 2003, Janssen et al. reported $PC_{71}BM$, which displayed a higher EQE response than $PC_{61}BM$, resulting in a PCE of 3.0%[90]. In 2010, Li et al. synthesized the indene-C60 bisadduct (ICBA), resulting in a higher V_{OC} than conventional PCBM materials[91]. However, fullerene derivatives have problems such as difficult synthesis and purification, weak absorption, and difficult structural and energy level modification, limiting the device efficiencies of organic photovoltaics.

The imide derivatives are also widely used as acceptor materials at that time, such as perylene diimide (PDI) and naphthalene diimide (NDI). Zhao et al. in 2013

developed a new NFA SF-PDI2 with spirobifluorene as the bridge, obtaining a device efficiency of 2.3% by taking P3HT as the donor[92]. In 2015, Heeger et al. introduced Se atoms into PDI to synthesize SdiPDI-Se and achieved a device efficiency of 8.42% with the donor of PDBT-T1[93]. However, this type of molecule has extremely strong planarity and is prone to excessive aggregation.

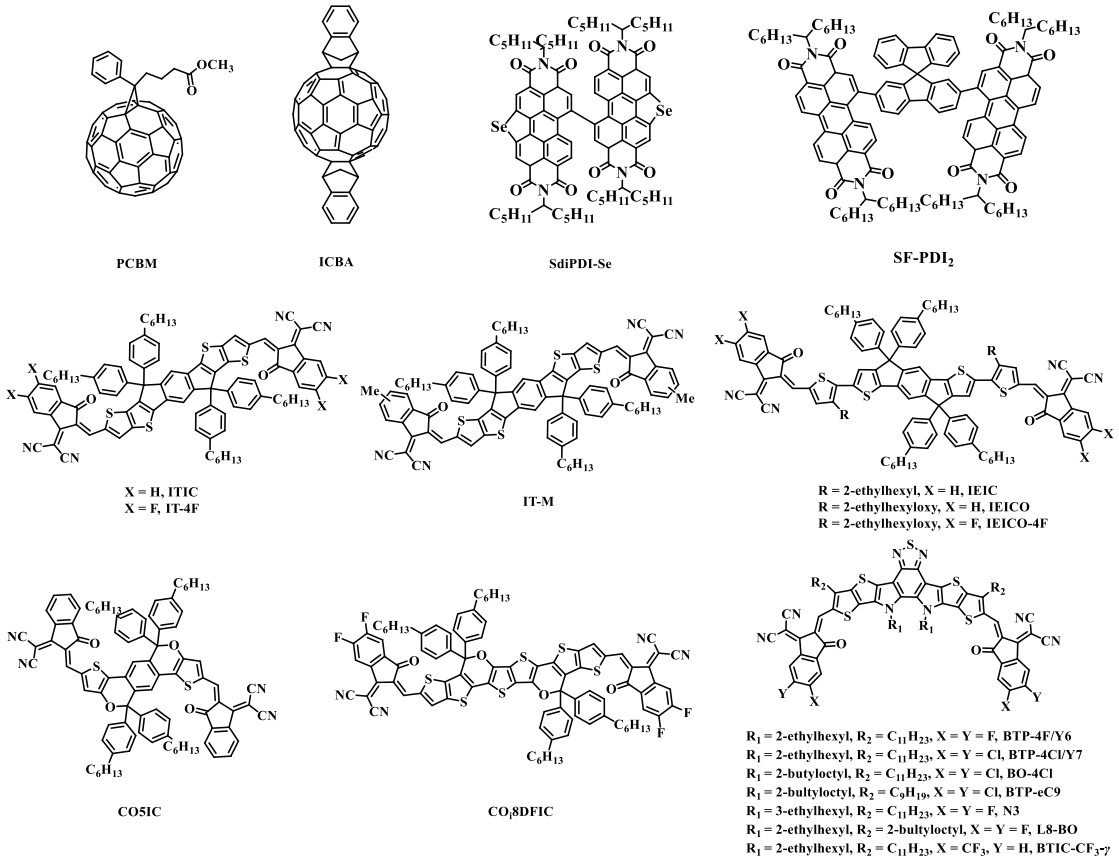

Figure 2. 3 Chemical structure of the representative acceptor materials.

ITIC series Zhan et al. in 2015 first reported an A-D-A type non-fullerene SMA ITIC, taking indacenodithieno[3,2-b]thiophene (IT) as the central electron-donating core, 2-(3-oxo-2,3-dihydroinden-1-ylidene)malononitrile (INCN) as the electron-withdrawing end group, and 4-hexylphenyl group as the conjugated side chain, providing the basic structural framework for non-fullerene small molecular acceptors[94]. In 2016, Hou et al. utilized the methyl group on INCN and reported IT-M. IT-M achieved a remarkable PCE of 12.05% with PBDB-T[95]. Later, they further synthesized IT-4F by using the fluorinated INCN as the endcap group and achieved a PCE of 13.1%

by blending with PBDB-T-SF and a PCE of over 12% in the thick film devices (100-200 nm)[78].

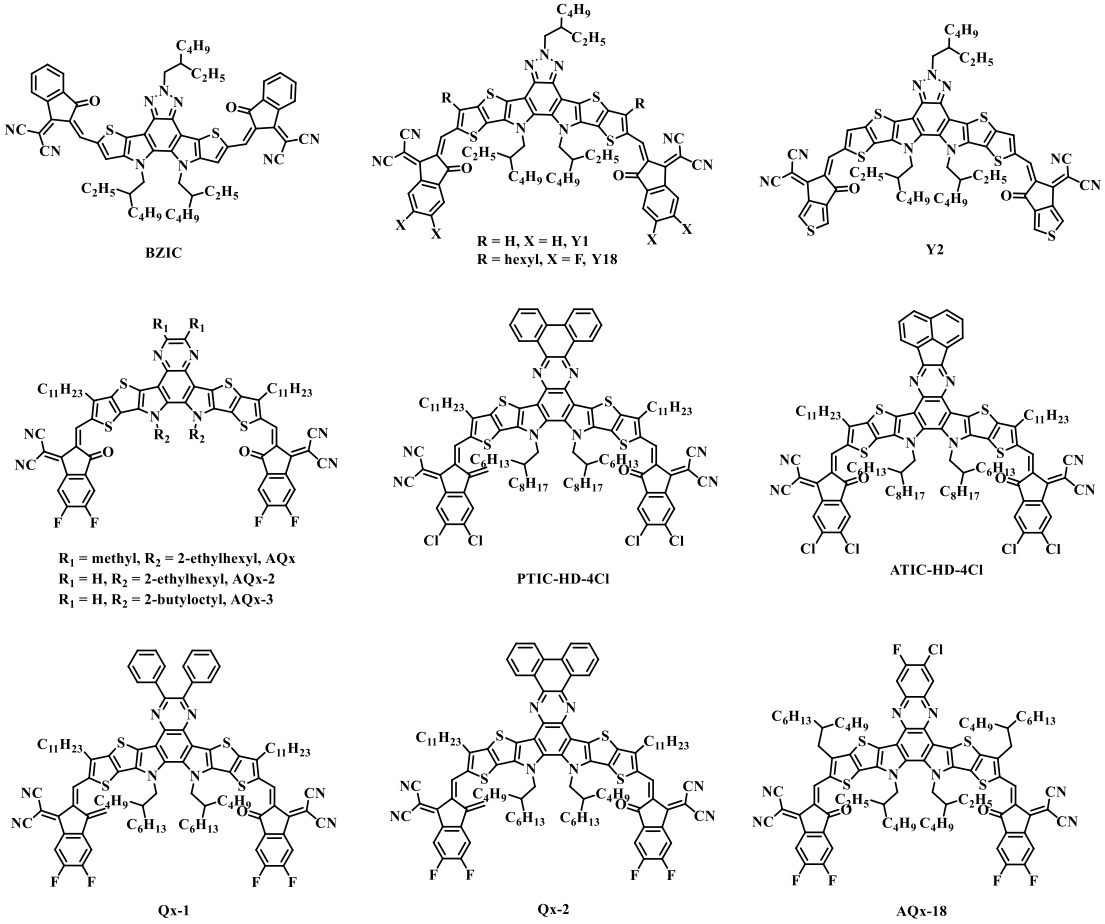

Figure 2. 4 Chemical structure of the representative acceptor materials.

IEICO series In 2015, Zhan et al. developed the IEIC acceptor with a five-ring fused IDT core and two alkyl substituted thiophene π bridges between the core and the end groups. The resultant devices showed a PCE of 6.31% by blending with PTB7-Th[96]. In 2016, Hou et al. changed the alkyl group on the thiophene π bridge to a strong electron-donating alkoxy group and synthesized IEICO, achieving a PCE of 8.4% in the single junction cell and 10.7% in the tandem cell[97]. They further applied fluorination strategy on IEICO and synthesized IEICO-4F, achieving a PCE of 10.9% in the ternary devices[98].

CO*i*8DFIC series In 2017, Ding et al. introduced a carbon-oxygen bridge with a larger electron-donating ability to replace the carbon bridge on the core of a five-fused

ring to obtain the molecule CO5IC, achieving a PCE of 7.49% by blending with PBDB-T[99]. Later on, they further extended the conjugated backbone to an eight-fused ring and employed the fluorinated INCN end groups to synthesize CO*i*8DFIC, achieving a high J_{SC} of 26.12 mAcm^2 and a PCE of 12.16% by taking PTB7-Th as the donor material[100].

Benzothiadiazole (BT) unit Zou et al. in 2019 synthesized the star molecule Y6 with an A-DA'D-A structure, which employed benzothiadiazole as the central electron-deficient core and was connected by the nitrogen atoms with two thieno[3,2-*b*]thiophene donor segments, end-capped by two fluorinated INCN groups. A remarkable PCE of 15.7% is achieved by the PM6: Y6 devices, breaking through the efficiency bottleneck of organic photovoltaics[101]. Later, Hou et al. synthesized BTP-4Cl by replacing the fluorine atoms on Y6 with chlorine atoms. BTP-4Cl displayed a higher crystallinity than Y6 (also refers to BTP-4F), a lower LUMO/HOMO but a higher V_{OC}, resulting a suppressed non-radiative energy loss and a higher PCE of 16.5%[102]. They further changed the 2-ethylhexyl chain on the nitrogen atom to a 2-butyloctyl chain and synthesized BO-4Cl, achieving a PCE of 17.0% due to the improved solubility and better miscibility with the donor[103]. In 2020, they reported BTP-eC9 by shortening the *n*-undecyl chain at the thiophene ring to a *n*-nonyl chain. The PM6: BTP-eC9 devices achieved a PCE of 17.8% thanks to the balanced solubility and crystallinity of the molecule[104]. Yan et al. changed the 2nd-position branched alkyl chain (2-ethylhexyl) on Y6 to the 3rd-position branched alkyl chain and synthesized N3, resulting in a better solubility and a higher PCE of 15.98% than Y6-based devices. In 2020, He et al. synthesized the trifluoromethyl-substituted Y-series acceptor BTIC-CF3-γ and reported its single crystal structure. In Y-series acceptors, synergistic H-aggregation formed by central core stacking and J-aggregation formed by end group packing, along with multiple intermolecular interactions, facilitated the formation of a 3D network single crystal structure, while there is only J-aggregation detected in ITIC series, leading to a linear packing structure. The 3D network single crystal structure produced a denser molecular packing, providing more possible channels for electron transport[105]. In 2021, Sun et al. reported L8-BO by changing the linear *n*-undecyl

group on thiophene to a branched 2-butyloctyl group, achieving an outstanding FF of 81.5% and a PCE of 18.32%[106].

Benzotriazole unit In 2017, Zou et al. reported a new D−π−A−π−D central core dithieno[3,2-b]pyrrolobenzotriazole (BZTP) and synthesized its corresponding SMA called BZIC. The resultant HFQx-T: BZIC devices displayed a PCE of 6.3%[107]. In 2019, Yang et al. still took benzotriazole as the central electron-deficient core and synthesized Y1 and Y2. Both of the molecules achieved a PCE of around 13.4% by incorporation with PBDB-T[108]. In 2020, Li et al. synthesized Y18 with different substituted groups of Y1 and realized a PCE of 16.52% by incorporating PM6[109].

Quinoxaline (Qx) unit Zhu et al. in 2019 developed a quinoxaline-based electron acceptor AQx by taking two methyl group-substituted quinoxaline as the electron-deficient core. The PBDB-TF: AQx-based devices displayed a PCE of 13.31% and a low energy loss of 0.45 eV[110]. Later, they further synthesized AQx-2 and AQx-3 by removing the methyl groups and changing the alkyl side chains. The PBDB-TF: AQx-2 and PBDB-TF: AQx-3 devices possess a PCE of 16.64% and 16.67%, respectively, and a PCE of 18.01% was obtained by PBDB TF: Y6: AQx-3 ternary devices[111,112]. In 2022, He et al. reported the phenanthrene- and acenaphthene-fused Qx unit and synthesized two SMAs named PTIC-HD-4Cl and ATIC-HD-4Cl and their corresponding polymer acceptors named PPTIC-HD-4Cl and PATIC-HD-4Cl. It was found that acenaphthene-based structures exhibited excessive aggregation in SMAs, while phenanthrene-based structures exhibited strong aggregation behavior in polymer systems, indicating that the molecular arrangement in the small molecules and the polymers is different. The same year, Wei et al. reported Qx-1 with the aromatic substitutions on the Qx unit and Qx-2 with the phenanthrene-fused Qx unit. It was found that the reorganization energy was suppressed by suppressing the C-C molecular vibration stretching, leading to a small E_{loss} of 0.508 eV for PM6: Qx-1 and 0.482 eV for Qx-2, for which the corresponding PCE is 17.9% and 18.2%, respectively. In 2023, Zhu et al. further developed AQx-18 by using the phenyl fused Qx as the central core, achieving a PCE of 18.2% in the resultant D18: AQx-18 devices thanks to the enhanced crystallinity and the fibril-like nanostructure.

2.2 Photoactive layer manipulation

There exist multiple trade-off situations in OSCs, for example, the balance between charge dissociation and charge transport, where the over aggregated phase domain is unable to maintain sufficient D/A interfaces for charge separation and the over mixed phase cannot afford a pure domain for efficient charge transport pathway. Both situations are detrimental to OSCs. Therefore, the photoactive layer manipulation plays a significant role in improving OSC device performance. There are many photoactive layer manipulation strategies, including additive strategy, posttreatment like thermal annealing and solvent evaporation annealing, and ternary/multicomponent strategies by introducing extra photovoltaic components. Since 2010, when Hoth et al. first incorporated PCPDTBT into the blend of P3HT/$PC_{61}BM$ and extended its absorption spectra, people have kept research on ternary blends and discovered many merits of ternary strategy, such as complementary absorption, energy level tuning, facilitating energy/charge transfer, morphology regulation, suppression of energy loss, and improvement of stability. Here, we introduce the recent research about the impact of a third component on the morphology regulation, energy loss suppression, and operational stability improvement.

2.2.1 Morphology regulation

A third component could influence the film morphology by tuning the crystallinity, phase separation, molecular orientation and molecular packing, and domain purity. The underlying reason could be that a guest component could induce the molecular reorganization by the intermolecular interaction between the host components. Generally, for a weak crystalline/amorphous system, a highly crystalline third component is introduced to increase the crystallinity of a system, facilitating the more ordered and compact molecular packing towards a higher charge transport property and suppression of non-radiative recombination loss. For a highly crystalline/excessive aggregation system, a weak crystalline material is usually utilized to fine tune the phase separation size to achieve a balanced charge dissociation and transport efficiency.

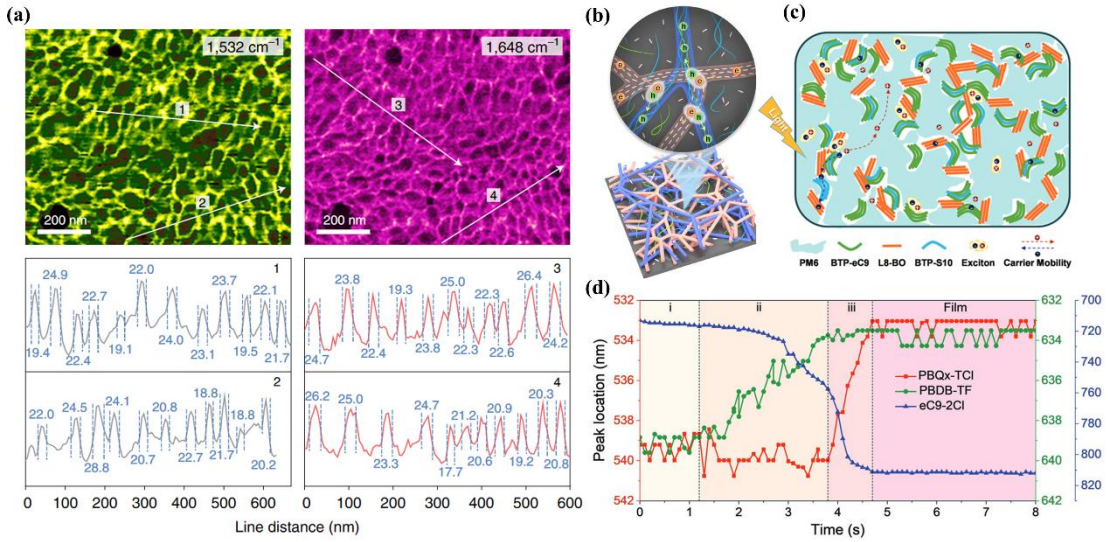

Figure 2. 5 (a) PiFM images of PM6 and L8-BO and the fibril width in the PM6: D18: L8-BO ternary blend. (b) Illustration of the double-fibril network and the charge transfer process.[113] (c) Schematic of carrier dynamics in the multiphase morphology with synergistic alloy-like phase and parallel-like phase.[114] (d) Crystallization kinetics of PBQx-TCl, PBDB-TF, and eC9-2Cl in the ternary film extracted from in-situ UV-vis absorption.[115]

In 2022, Liu et al. investigated a highly efficient ternary component of PM6: D18: L8-BO. It was found that the highly crystalline polymer D18 would crystallize first to provide nucleation sites and facilitate the crystallization process of PM6 to form a high-quality fibril network and improve the crystallinity of the blends. A higher PCE of 19.6% than its binary counterparts was achieved due to the formation of an optimal morphology with increased fibril diameter and distribution[116]. The same year, Chen et al. developed a quaternary system of PM6: L8-BO: BTP-eC9: BTP-S10. It was found that BTP-eC9 and BTP-S10 tend to undergo an alloy-like model, and BTP-S10 and L8-BO tend to undergo a parallel-like model, facilitating the formation of a multiphase morphology, achieving a high PCE of 19.35%[114]. The next year, Hou et al. further advanced this strategy using PBQx-TCl: PBDB-TF: eC9-2Cl, achieving 19.51% PCE through regulating the donor and acceptor crystallization kinetics. Compared to binary systems with suboptimal fibril sizes (PBQx-TCl:eC9-2Cl: ~35 nm; PBDB-TF:eC9-2Cl:

~20 nm), the ternary blend attained ideal 25 nm phase domains - sufficiently large for efficient charge transport yet compact enough for rapid exciton splitting.[115] In 2024, Wang et al. synthesized a new NFA L8-ThCl and employed it as a third component to fabricate the pseudo-bulk heterojunction (p-BHJ) devices. It was found that L8-ThCl interacts with the donor PM6 by the dipole-dipole interaction to induce closer π-π packing and regulate the L8-BO packing structure to be 1D nanofibrils, resulting in the refined fibrillization of the donor and the acceptor, leading to a PCE of 19.4%. The efficiency was further improved to 20.1% by changing the donor to D18[117]. Ge et al. synthesized a highly ordered Qx-based acceptor SMA and achieved a champion PCE of 20.22% by taking SMA as a third component in PM6: BTP-eC9 system. It was found that the addition of 10% SMA delayed the precipitation of PM6, leading to the stronger and more ordered π-π interaction of the acceptor without the interference of PM6. Simultaneously, compared with the binary devices where excitons generated at ~35 nm, in the ternary devices multiple excitons generated at ~45 nm. Given that the exciton generation at the center region is more conducive to charge collection, the ternary devices showed an optimal vertical morphology[4]. In 2025, regarding the excessive aggregation issue in blade-coated (BC) blends, Li et al. utilized BTP-4Cl to regulate the precursor solution solubility and phase transition kinetics of PM6: BTP-eC9. It was found that the relatively twisted molecular backbone of BTP-4Cl would promote a looser and more dispersed molecular distribution in the solution and a reduced intermolecular π-π distance in the solid blend. As a result, a favorable nanoscale phase separation was achieved in the blade-coated binary film, realizing stable and high-performance eco-OSCs via open-air coating with a PCE of 19.67%[118].

2.2.2 Energy loss suppression

Energy loss is significant in determining the V_{OC} of a solar cell. There are three items to evaluate the energy loss in OSCs.

$$E_{loss} = E_g - qV_{OC} \quad (1\text{-}27)$$

$$= (E_g - qV_{OC}^{SQ}) + (qV_{OC}^{SQ} - qV_{OC}^{rad}) + (qV_{OC}^{rad} - qV_{OC}) \quad (1\text{-}28)$$

$$= (E_g - qV_{OC}^{SQ}) + q\Delta V_{OC}^{rad} + q\Delta V_{OC}^{non-rad} \quad 1\text{-}29$$

$$= \Delta E_1 + \Delta E_2 + \Delta E_3 \quad 1\text{-}30$$

Where ΔE_1 refers to the radiative recombination above the bandgap. ΔE2 was the radiative recombination below the bandgap. ΔE3 comes from the non-radiative recombination and was calculated by $\Delta E_3 = -kT \ln EQE_{EL}$, where k is the Boltzmann constant, and T denotes the absolute temperature. The rise of ΔE_3 was the defect-assisted recombination and the electron-phonon coupling from molecular vibration and energy dissipated by thermal emission. OSCs suffered from a high energy loss that limited the improvement of efficiency compared with inorganic and perovskite counterparts. For inorganic solar cells, there is no charge transfer state, and thus no ΔE_2 item, while for a typical OSC, that is ~30-60 meV. More importantly, the non-radiative recombination loss for an OSC is of ~200-300 meV, greatly larger than that in inorganic and perovskite. The suppression of energy loss is an effective way towards high-performance OSCs, and a third component is conducive to suppressing the energy loss of the host system by tuning energy levels, regulation of morphologies, enhancing crystallinity, suppressing energetic disorder, and improving photoluminescence quantum yields (PLQY), etc[119].

In 2021, Hou et al. incorporated BTA3 with a high LUMO into the blend of PBQx-TCl: BTP-eC9, generating a PCE of 18.0% with an improved V_{OC} from 0.82 eV to 0.84 eV[88]. They further employed the component of PBQx-TF: eC9-2Cl: F-BTA3 to construct a highly efficient OSC with a PCE of 19.0%. The ternary devices displayed a higher EQE_{EL} of 2.09×10^{-4} and a lower ΔE_3 of 0.219 V than PBQx-TF: eC9-2Cl binary cells with an EQE_{EL} of 1.45×10^{-4} and a ΔE_3 of 0.229 eV[89]. Huang et al. also employed F-BTA3 to restrain the CT state disorder and the rate of back charge transfer of D18: N3-BO. It was found that incorporating F-BTA3 induced a more ordered molecular packing and a weaker electronic coupling between the spin-triplet charge transfer state and triplet excitation state. As back charge transfer and Triplet exciton formation are greatly related to non-radiative recombination loss, the F-BTA3-based ternary devices displayed much suppressed ΔE_{nr} of 0.183 eV and an impressive PCE of 20.25%[120]. He et al. compared two quinoxaline (Qx)-based SMAs ATIC-C11 and ATIC-BO, and

investigated their properties in collaboration with the other active layer components. Due to their high crystallinity property, the ATIC-C11 and ATIC-BO-based devices showed improved PCE of 19.28% and 18.52% with the suppressed energy loss of 0.524 eV and 0.526 eV, respectively (0.557 eV for the control devices). More importantly, they displayed extremely small ΔE_2 of 0.033 eV and 0.30 eV[122]. Zhu et al. incorporated the tethered phenyl group substituted NFA Z8 into D18: L8-BO blends, obtaining a high PCE of 20.2%. It was found that the incorporation of Z8 effectively alleviated the energetic disorder of band tail states and suppressed charge recombination by reducing trap density. Additionally, an additional exciton dissociation pathway of local excited state-delocalized single exciton state-charge separated state, reducing CT-mediated recombination loss. Therefore, the ternary devices featured high PLQY, delocalized exciton, and faster charge separation, leading to the small ΔE_2 of 0.05 eV and ΔE_3 of 0.19 eV[1]. The same year, Li et al also investigated the material aggregation behavior by introducing B6Cl into PM6: L8-BO blends. Usually, the aggregation-induced luminance quenching would sacrifice the photoluminescence in a strong crystallinity system. However, it was found that the ternary blend film has synergistic ordered and compact π-π stacking and longer photoluminescence lifetime, facilitating a suppressed radiative and non-radiative recombination loss decreasing from 0.05 eV to 0.03 eV and from 0.24 eV to 0.22 eV, respectively. They further ascribed the suppressed ΔE_3 to the limited vibration of C-C and C-H bonds[123]. Recently, Sun et al. reported several asymmetrical SMAs and investigated their crystallinity and PLQYs. Among them, PM6:L8-BO-C_4 achieved the highest PCE of 19.78% due to the fine-tuned crystallinity and PLQY. They further improved the efficiency to 20.42% by incorporating L8-BO-C_4-Br due to the improved V_{OC} of 0.894 V (0.878 V for the binary devices), stronger crystallinity, and suppressed trap-assisted recombination[124]. In 2025, Zhu et al. incorporated BTP-eC9 into the D18: AQx-2F blend, achieving a simultaneously reduced bandgap, widening absorption window, and suppressed energy loss from 0.533 eV to 0.510 eV. AQx-2F is a quinoxaline (Qx)-based SMA that is known for small ΔE_3. The D18: AQx-2F-based devices achieved a low ΔE_3 of 0.194 eV, and the introduction of BTP-eC9 further suppressed the ΔE_3 to 0.180 eV[121].

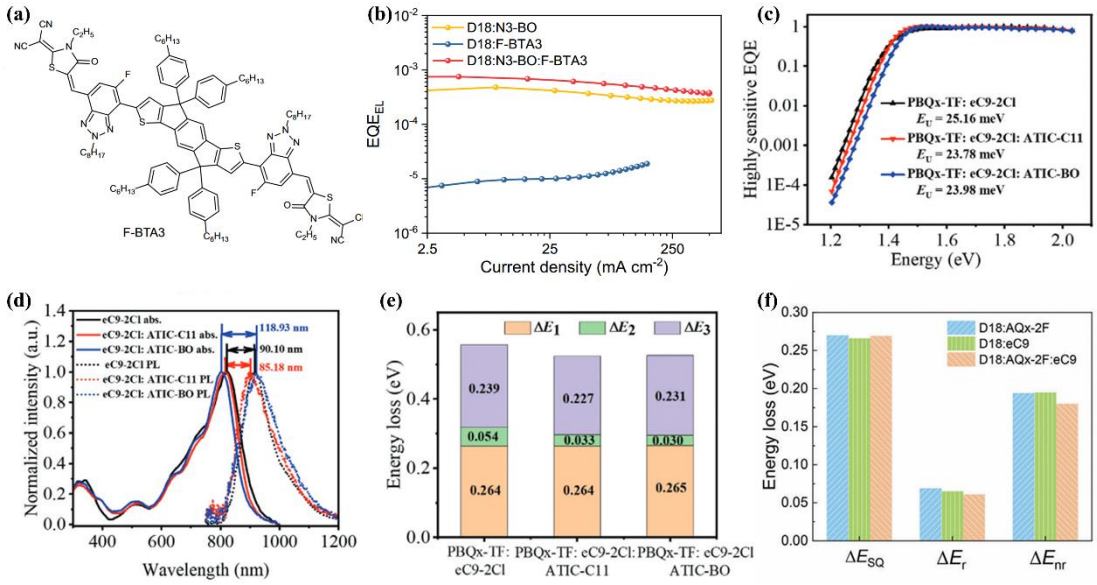

Figure 2. 6 (a) Chemical structure of F-BTA3. (b) EQE_{EL} curves of D18: N3-BO, D18: F-BTA3 and D18: N3BO: F-BTA3 based devices.[120] (c) FTPS-EQEs and Urbach energy of PBQx-TF: eC9-2Cl, and ATIC-C11-/ATIC-BO-based ternary devices. (d) The reorganization energy of eC9-2Cl, eC9-2Cl: ATIC-C11, eC9-2Cl: ATIC-BO extracted from UV–vis absorption (abs.) and photoluminescence (PL) spectra. (e) and (f) The histograms of ΔE_1, ΔE_2, and ΔE_3 for corresponding devices.[121,122]

2.2.3 Operational stability improvement

Device stability is an important indicator of commercialized organic solar cells. The factors influencing devices' operational stability include photo-oxidation of the active layer materials, morphology change, and interlayer/electrode degradation. The external light, temperature, moisture, and oxygen would accelerate the corrosion and deterioration process of devices[125,126]. Li et al. ascribed the degradation of the polymer donor PM6 to the superoxide radical ($\cdot O_2^-$) arising from the UV illumination of O2 and the extraction of the electron in the conduction band, which would oxidize the thiophene in BDT to sulfoxide or sulfone, further destroying the D/A alternative structure and π-π molecular stacking of PM6 (Figure 2. 7a). The degradation of the acceptor was the appearance of hydroxyl radicals (HO·) coming from the valence band hole extraction of H_2O and hydroxyl ion, which leads to vinylidene oxidation to break the core and the

terminal group.[127] Baran et al. also investigated the degradation process of the polymer donor and they ascribed the polymer donor photodegradation to the hydrogen abstraction and homolytic scission, which forms several radicals of Macro-R˙, H˙, Marco˙, and R˙ and multiple by-products due to the recombination of these radicals (Figure 2. 7b).[128] Perepichka et al. investigated the degradation pathway of non-fullerene acceptors and found that the electrocyclic reaction between the thiophene ring on the core and the dicyanomethylene on the terminal group was responsible for the acceptor deterioration (Figure 2. 7c).[129] Additionally, the unstable active layer morphology under light/thermal stress is responsible for device physical degradation. Molecular migration causes over- or de-mixing between D/A phases, which lowers domain purity or forms large segregates, leading to an inferior phase separation in aging films.[130,131] Multiple studies on material synthesis, device structure optimization, interlayer modification, multi-component strategies, and encapsulation methods have been reported, trying to address the material and morphological instability issue.[44,132–142] The incorporation of a guest component has been proven to be useful in suppressing the device degradation by locking in morphology, balancing crystallinity and miscibility, and suppressing radical oxidation[143]. This section summarizes the recent research progress in stability *via* a ternary strategy.

In 2023, Yan et al. synthesized a SMA named BTP-BO-3FO with the fluorine- and methoxy-substituted terminal groups and incorporated it into the blend of PM6: BTP-eC9. The system showed different molecular packing ordering by using different solvents of chloroform and o-xylene. Finally, a higher PCE of 19.24% was achieved in the o-XY-processed T-OSCs with better long-term photo- and thermal-stable potential[144]. The same year, Ge et al. developed regioisomeric derivatives QX-α and QX-γ through differential thiophene ring positioning on the quinoxaline (Qx) core, further investigating their effect on the blend of D18: N3. Qx-α with the S···N non-covalent interactions displayed a larger dipole moment, a higher surface energy, and a more organized molecular packing, achieving a higher efficiency of 19.33%. Additionally, the Qx-based acceptor incorporated devices simultaneously improved the

thermal-, photo-, and storage-stability greatly compared with the non-doped binary devices[145].

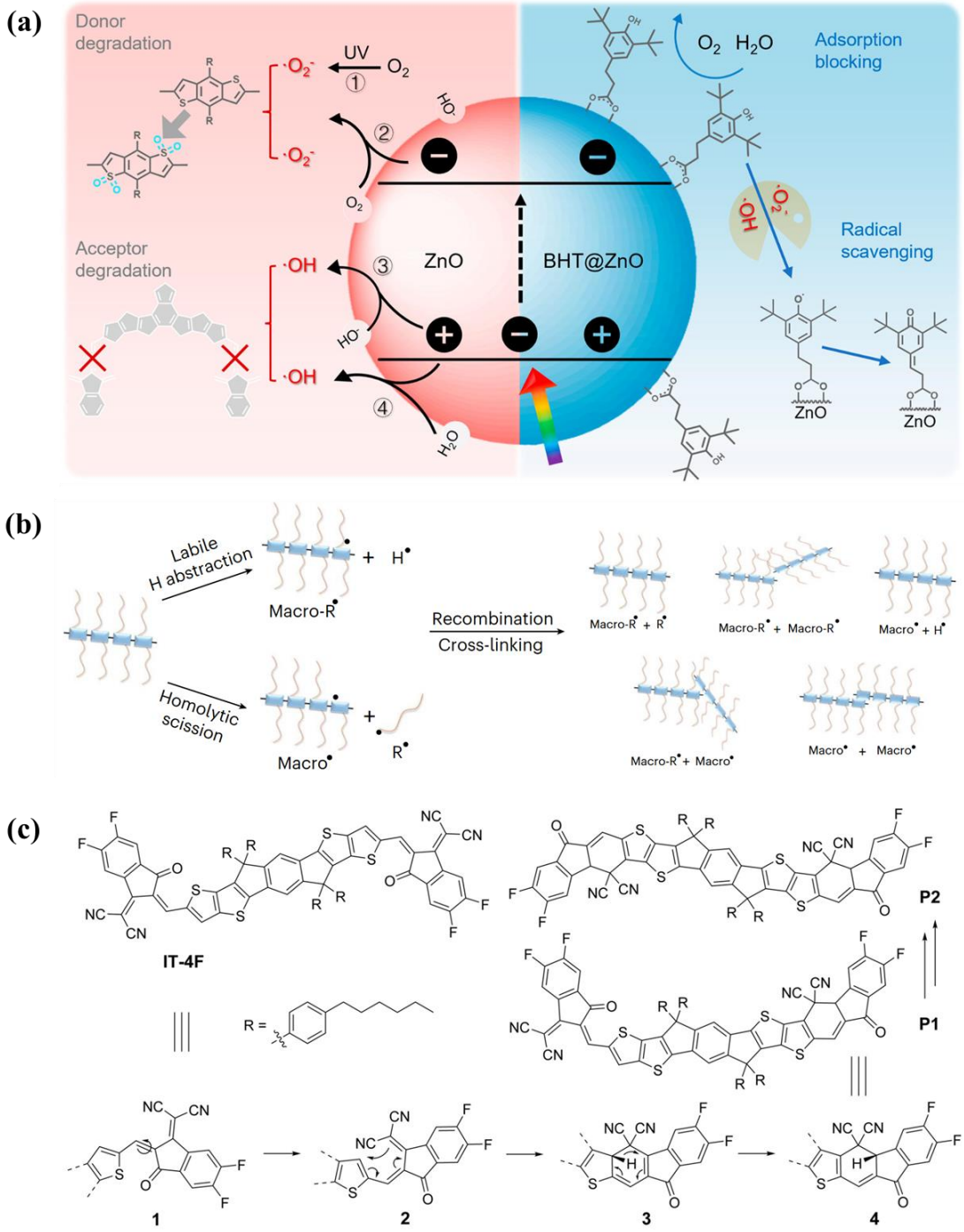

Figure 2. 7 (a) Illustration of the photodegradation pathway of the polymer donor and the non-fullerene SMA.[127] (b) The hydrogen abstraction and homolytic scission process and the by-products via radical recombination.[128] (c) The cyclic reaction in SMAs with a terminal isocyanate group.[129]

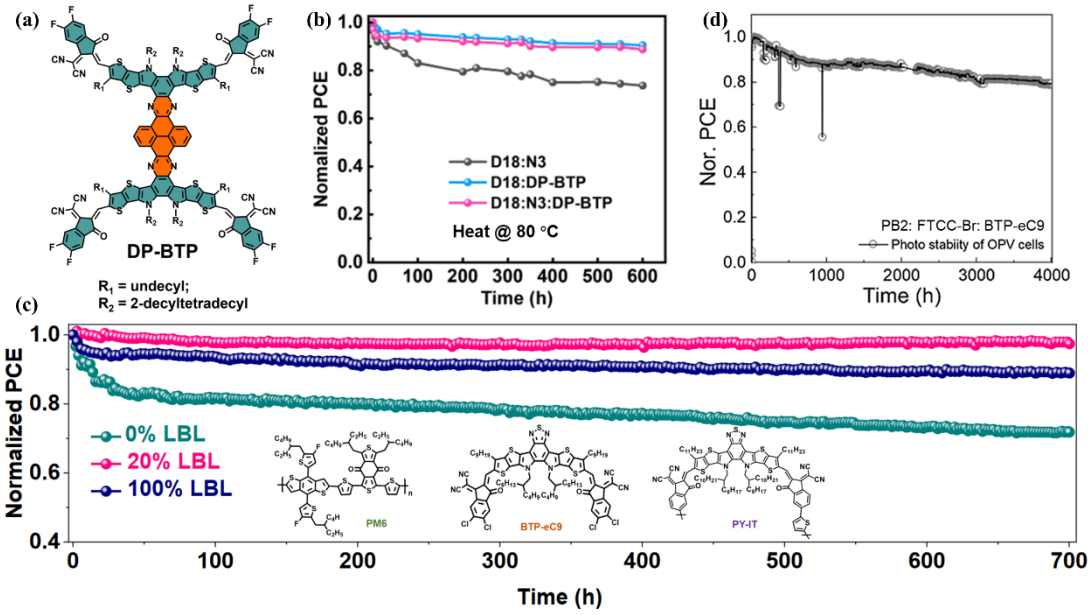

Figure 2. 8 (a) Chemical structure of DP-BTP. (b) The thermal stability of corresponding devices under continuous heating at 80℃.[146] (c) MPP tracking of encapsulated PM6: BTP-eC9: PY-IT LBL OSCs with different ratios.[147] (d) Photostability of the encapsulated PB2:FTCC-Br:BTP-eC9 devices measured in air under the illumination of 100 mWcm^{-2} at ~50 °C.[148]

In 2024, Li W. W. et al. designed and synthesized a pyrene-fused dimer acceptor named DP-BTP and incorporated it into D18: N3 blends. The large conjugated backbone of DP-BTP enabled enhanced electron mobility, reduced non-radiative recombination loss, and elevated V_{OC}, achieving a much-improved PCE of 19.07% than binary counterparts (17.6%). Additionally, it was found that the ternary devices maintained 86.9% and 88.7% under continuous illumination at 1 sun and heating at 80 ℃, respectively, while the binary devices degraded fast and only maintained 64.8% and 73.7% of the initial efficiencies. They further explored the underlying mechanism of the enhanced photo and thermal stability. It was found that two acceptors tended to form the alloy-like acceptor domain and DP-BTP has a higher glass transition temperature of 126 ℃ than N3 (88 ℃), leading to a mediated T_g of 119 ℃ for the N3: DP-BTP blend. According to the molecular interaction-diffusion framework theory, a higher T_g required a larger activation energy for diffusion, which decreased the diffusion

coefficients, impeding the migration of N3 molecules, thus leading to a better device operational stability[146]. Li G. et al. incorporated PY-IT into the LBL blend of PM6: BTP-eC9. It was found that the 20%-doped device showed T_{96} after continuous illumination for 700 h, much higher than its binary counterparts. They ascribed the enhanced stability to the stronger crystallinity caused by the third component[149]. They further reported a highly efficient T-OSC with the component of PM6: BTP-C9: o-BTP-eC9 by blending two isomeric acceptors. Thanks to the suppressed recombination loss and the fine-tuned phase separation morphology, a state-of-the-art PCE of 19.9% is realized with good operational stability, for which the T_{80} lifetime is 724 h[150]. Peng et al. employed a terpolymer strategy by incorporating dithienophthalimide (DPI) into the PM6 backbone to improve the solubility through the dipole moment effect. Additionally, a second donor PBTz-F was introduced to construct a ternary OSC. Finally, the THF-processed devices gave a PCE of 19.45%, representing the highest efficiency for halogen-free solvent-processed OSCs. The ternary devices also gave a significantly prolonged T_{80} lifetime of 450h than binary devices of ~300h[151]. Hou et al. incorporated FTCC-Br into the PB2: BTP-eC9 blend, and found that FTCC-Br effectively abbreviated the time for molecular aggregation to form smaller phase separation and higher degree of crystallinity. More importantly, the ternary devices displayed a surprisingly good photostability with a T_{80} of 4000h[148]. In 2025, Li et al. incorporated AT-β2O into the blend of D18-Cl: N3 to regulate the crystallization sequence of active layer component to form a preferable vertical phase separation, achieving an outstanding PCE of 20.82% and enhanced operational stability of retaining 83% after aging for 1200h under continuous illumination[43]. Zhang et al. utilized an SMD BTR-SCl to regulate the assembly behavior of the polymer donor D18. BTR-SCl's strong crystallinity accelerated the polymer donor's aggregation and extended the aggregation time, facilitating the formation of optimal vertical distribution and much organized molecular packing. The highest PCE of 20% is first achieved for SMD-based ternary devices with the simultaneously enhanced photostability and thermal stability[152].

Chapter 3 Kinetics Manipulation Enabled by Solubility Control Toward 19% Organic Solar Cells via Compatible Air Coating

3.1 Introduction

The distinctive features of organic solar cells (OSCs), including solution processible, polychromatic, semitransparent, and roll-to-roll producible[36,153,154], enable it one of the most dynamic research areas. Benefiting from the rapid evolution of organic electronic devices and materials[155–160], the power conversion efficiencies (PCEs) of OSCs have already reached 20% [37,161–163]. However, the state-of-the-art PCEs were all achieved by conventional spin-coating (SC) techniques on small-area substrates, which is not applicable to industrial production. On one hand, the solution wastage in the spin coating is inevitable[164]. On the other hand, when the substrate size is sufficiently large, the film thickness is nonuniform from the center to the edge because of the non-Newtonian effects coupled with the different radial centrifugal force distribution[165–167]. Therefore, large-area manufacturing techniques have to be developed to facilitate the commercialization of OSCs. The meniscus-guided coating (MGC) methods, including dip coating, slot-die coating, and doctor-blade coating, are good candidates for realizing high-throughput and upscaling fabrication on industrial scales. Different from the outward centrifugal and inward viscous force-controlled spin-coating methods, MGC techniques are governed by the one-directional shear force applied by the coating head and the capillary force induced by the solution's concentration and viscosity near the contact line[168–170]. The different dominant forces in spin-coating and MGC methods enabled different film formation mechanisms and thus different OSC film morphologies[171,172].

To be specific, it has been validated that the solvent evaporation and the film drying time of MGC are greatly prolonged compared to that of spin-coating, with a

great possibility to form oversized aggregates in the active layer[173–175]. The excessive aggregate size usually derives inferior film morphology with pronouncedly enlarged surface roughness and reduced donor/acceptor (D/A) interface area, sacrificing the charge separation, thus leading to poor fill factor (FF) and photocurrent. Therefore, the reasons for the efficiency gap from spin coating to blade coating (BC) could be summarized: 1) The long film-drying time causes the excessive phase separation domain size in blade coating[174,176–179]; 2)The relatively poor solubility of highly efficient OSC materials in nonhalogenated green solvents exacerbate the agglomeration problem in blade-coating based on the Flory–Huggins model,[180–183] as large-scale production required green solvent processing due to the toxic consideration.

Several attempts were made to mitigate the excessive aggregation issues by improving the solubility when transferring from spin coating to blade coating,[40,44,169,177,178,184–193] for example, the side chain modification strategy, which was widely used in improving the solubility of photovoltaic materials.[103,177,187] Additionally, it was reported that copolymerization strategies are also helpful in improving the solubility of OSC materials.[185,186]Although these molecular modification strategies of Y-series acceptors could help to improve the solubility, in the meantime, they also introduce uncertainties that may disrupt molecular packing and lead to undesired energy level alignment, limiting successful attempts in achieving high-efficiency devices processed from high boiling point nonhalogenated solvents. Moreover, current studies in blade coating could typically ignore the correlation between solubility and material crystallization kinetics resulting from coating methods. Therefore, the evolution from solubility and film formation kinetics to final phase separation should be established to provide a clear understanding of morphology manipulation in blade-coating processes.

Here, we develop a feasible and effective multicomponent strategy to simultaneously improve the solubility and crystallization behavior enabling high-performance blade-coated devices. BTP-4Cl was selected as the third component with a twisted molecular backbone to promote the dispersion of mixed acceptors in the

halogenated chlorobenzene (CB) and non-halogenated solvent o-xylene (o-XY). Upon blade coating, the more dispersed acceptors gain greater freedom to self-assemble in the solution state, promoting the formation of fast and fine crystallites in the film. This, in turn, leads to a well-controlled scale of donor-acceptor phase separation. Benefiting from the favorable phase separation nanostructure, we successfully demonstrate an excellent PCE of 19.67% via an open-air coating, which ranks among the top efficiencies in blade-coated devices. We further demonstrate that our approach applies to single green-solvent processed devices. This work not only provides valuable insights into the correlation between solubility tuning, crystallization kinetics, and device performance from the perspective of molecular structure and intermolecular interactions, providing an effective method for controlling phase separation in blade-coated OSCs but also enables the realization of highly efficient and stable open-air-coated, eco-friendly OSCs, achieving state-of-the-art efficiencies of 19.76% for spin-coated and 19.67% for blade-coated devices.

3.2 Experimental section

3.2.1 Materials

All chemicals were utilized without further purification. The photovoltaic materials PM6, BTP-eC9, and BTP-4Cl were commercially sourced from Solarmer Materials Inc.

3.2.2 Instruments

Optical absorption properties were analyzed using an Agilent Cary 4000 UV-Vis-NIR spectrophotometer. For external quantum efficiency (EQE) measurements, a QE-R3-011 integrated spectral response analyzer (Enli Tech) equipped with monochromatic light modulation (10 nm bandwidth) and a calibrated Si reference cell was employed. Prior to testing, the incident light intensity across all wavelengths was adjusted via a reference single-crystalline silicon photovoltaic cell to ensure calibration. Additionally, photoluminescence (PL) spectral analysis was performed on an Edinburgh Instruments FLS 920 spectrometer. GI-XRD measurements were carried out with a Xeuss 2.0 SAXS/WAXS laboratory beamline using a Cu X-ray source (8.05 keV, 1.54 Å) and

Pilatus3R 300 K detector. Atomic force microscopy (AFM) was performed in tapping mode using a multimode 8 atomic force microscope.

3.2.3 Device fabrication

Spin-coated devices The OPV structure of ITO glass/PEDOT: PSS/active layer/PFN-Br/Ag was adopted. A glass substrate with a pre-patterned ITO was ultrasonicated subsequently in detergent, deionized water (DI water), acetone, and isopropanol (IPA) every 20 min. The substrates were first blown dried by high-pressure air, and then treated with UV-ozone (UVO) for 20 min. Next, PEDOT: PSS (Bayer Dayton 4083) was spin-coated at 3000 rpm for 30 s and then baked in a petri dish at 150 °C for 15 min. Then these substrates were sent to an argon-filled glove box. A blend film of donor: acceptor was prepared by spin-coating its mixed solution in chlorobenzene (D: A = 1:1.2, donor concentration: 10.5 mg mL^{-1}, 0.5% DIO) or o-xylene (D: A = 1:1.2, donor concentration: 10.5 mg mL^{-1}) at 3000 rpm for 60 s, then thermal annealing at 85 °C 5 min. A thin layer of PFN-Br (3000 rpm, 30s) and an Ag cathode (90 nm) was subsequently deposited. The effective device area was determined to be 4.0 mm^2.

Blade-coated 0.04 cm^2 and 1 cm^2 devices The spin-coated (SC) and blade-coated (BC) devices have different active layer processing methods. For BC devices, the ITO substrate was heated to and stabilized at 60 °C. A precision-engineered nitrogen stream delivery system was aligned parallel to the substrate plane, maintaining a 20° gas impingement angle for controlled solvent extraction. The as-deposited active layer underwent instantaneous solidification through this laminar gas quenching process, with flow velocity stabilized at 40 m/s (calibrated using Testo 416 flowmeter). Optimal device fabrication employed blade-coating techniques under the following parameters: Coating suspension: 10.5 mg/mL in CB (0.5% DIO additive) or o-xylene; Doctor blade velocity: 33 mm/s; Coater-substrate clearance: 100 μm. Subsequently, the films were treated with thermal annealing at 85 °C for 5 min. Except for the active layer, the fabrication conditions were the same as the spin-coated devices. For 1 cm^2 devices, the silver paste was applied before characterization.

3.2.4 Characterization

Photovoltaic measurement Current density-voltage (J-V) characteristics were evaluated using a Keithley 2400 source-measure unit within a nitrogen-glovebox-integrated testing setup. A Class AAA solar simulator (Enli Tech SS-F5-3A) provided AM 1.5G spectral irradiation at 100 mW/cm², pre-calibrated using a 20 × 20 mm² monocrystalline silicon reference cell with KG5 optical filtering. Forward voltage sweeps (-1.5 - +1.5 V) were executed with 20 mV resolution and 1 ms sampling intervals. Power conversion efficiencies (PCEs) were statistically derived from 20 identically processed devices.

Hole and electron mobility characterization Hole and electron mobilities were extracted via space-charge-limited current (SCLC) modeling using unipolar architectures: hole mobility of ITO/PEDOT:PSS/Active Layer/Au and electron mobility of ITO/ZnO/Active Layer/Ag. Dark current-voltage responses were fitted to the Mott-Gurney equation:

$$J = \frac{9}{8}\varepsilon_0\,\varepsilon_r\,\mu_h\frac{V^2}{d^3} \qquad 1\text{-}31$$

Where J denotes current density, d represents the active layer thickness, μ_0 corresponds to hole (or electron) mobility, ε_r is the relative dielectric constant of the transport medium, and ε_0 is the vacuum permittivity (8.85×10^{-12} F m^{-1}), The internal voltage V is defined as $V = V_{app} - V_{bi}$, with V_{app} as applied bias and V_{bi} as built-in potential from electrode work function offsets.

Contact angle measurement The donor-acceptor interfacial energy ($\gamma_{D/A}$) and Flory-Huggins interaction parameter ($\chi_{D/A}$) were evaluated by the following equations:

$$\gamma_{D/A} = \gamma_D + \gamma_A - \frac{4\gamma_D^d\gamma_A^d}{\gamma_D^d + \gamma_A^d} - \frac{4\gamma_D^p\gamma_A^p}{\gamma_D^p + \gamma_A^p} \qquad 1\text{-}32$$

$$\chi_{D/A} = K(\sqrt{\gamma_D} - \sqrt{\gamma_A})^2 \qquad 1\text{-}33$$

Where γ is the surface energy of the corresponding material; γ^d, γ^p are the dispersive and polar components of γ, respectively; K is a constant.

3.3 Result & Discussion

3.3.1 Molecular structure and chemical properties

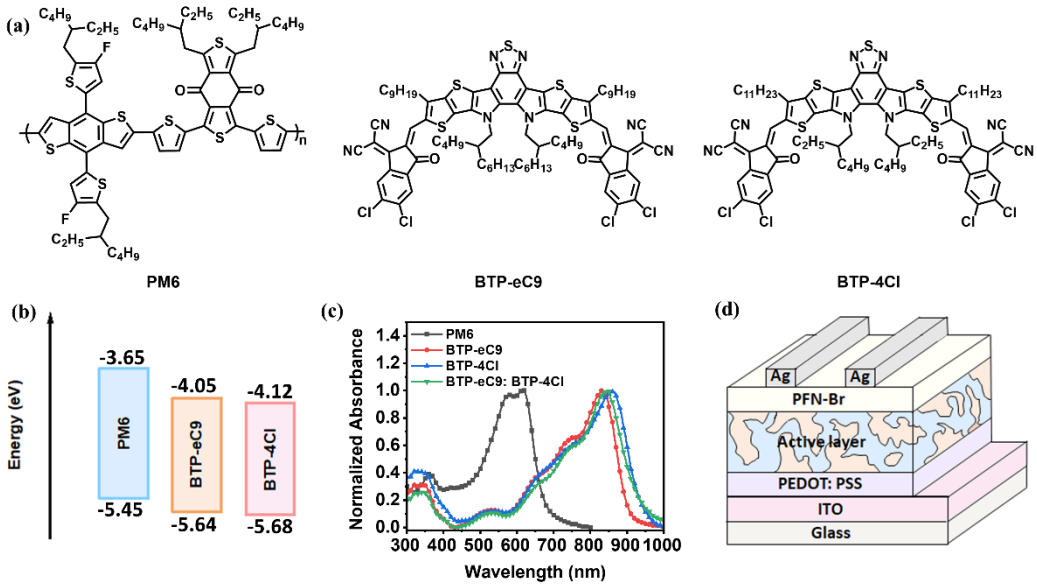

Figure 3.1 (a) The chemical structures, (b) energy levels, and (c) normalized absorption spectra of corresponding substances. (d) Schematic diagram of OSC device structure.

To investigate the different features of SC/BC binary/ternary films, the ternary system of PM6: BTP-eC9: BTP-4Cl was employed. The chemical structures of the three materials were drawn in Figure 3.1a. Two acceptors are structure-like with the same molecular backbone, which are expected to have good compatibility to undergo the alloy-like model. The energy level diagram is provided in Figure 3.1b. The LUMO and HOMO of PM6, BTPeC9, and BTP-4Cl are -3.65/-5.45, -4.05/-5.64, and -4.12/-5.68 eV, respectively. The cascade energy levels guaranteed efficient charge transfer and transport in devices. Figure 3.1c displays the normalized ultraviolet-visible (UV-vis) absorption profile of the PM6, BTP-eC9, BTP-4Cl neat films, and BTP-eC9: BTP-4Cl blend film. PM6 showed strong absorption from 450 to 700 nm, which was complementary to the absorption of acceptors. The absorption onset of BTP-eC9, BTP-4Cl, and blend acceptor are 907.27, 943.82, and 941.43 nm, respectively, corresponding to their optical bandgaps (E_g^{opt}) of 1.37, 1.31, and 1.32 eV. The absorption coefficient

of blend film was calculated by $\alpha = 2.303\ (A/t)$ to evaluate their capacity to harvest photons at certain wavelengths (Figure 3.2), where A is absorbance and t is film thickness.[194] We found that the absorption coefficient was enhanced among the whole spectra, which was expected to contribute to higher photocurrent in ternary devices.

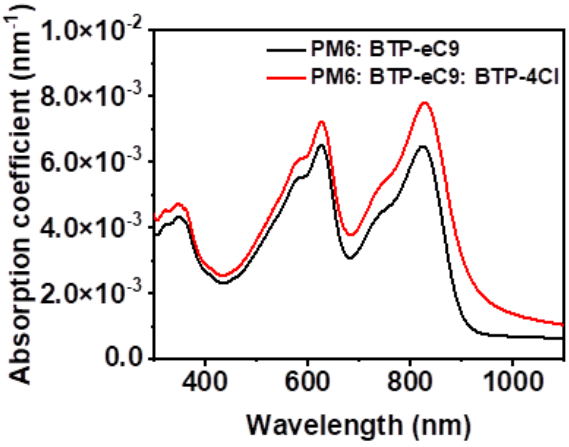

Figure 3.2 Absorption coefficient of the binary and BTP-4Cl-based ternary film.

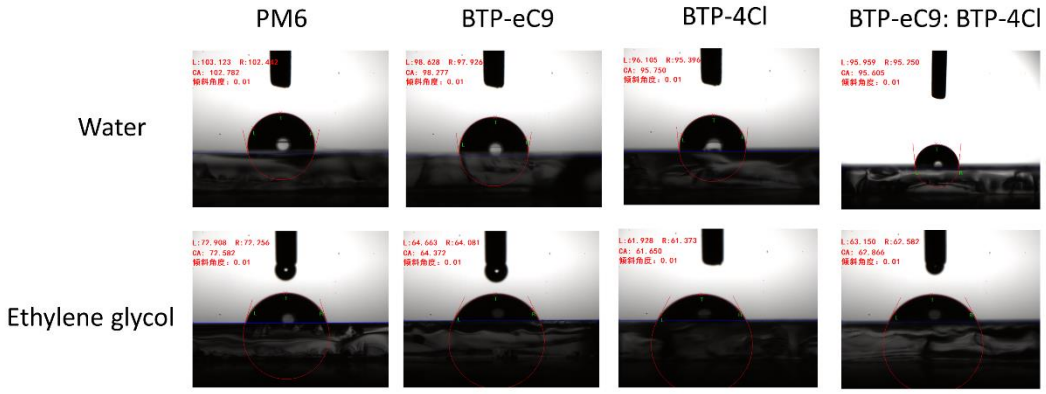

Figure 3.3 The contact angle measurement of the neat and mixed acceptor film.

The contact angle (CA) measurement was performed to determine the phase separation and miscibility between active layer components (Figure 3.3). The two-solvent method (water and ethylene glycol (EG)) was applied to determine the surface tension. The water contact angles (WCA) were measured to be 102.782°, 98.277°, 95.750°, and 95.605° for PM6, BTP-eC9, BTP-4Cl, and BTP-eC9: BTP-4Cl (0.96: 0.24), and the corresponding EG contact angles (EgCA) were measured to be 72.582°,

64.372°, 61.650°, and 62.866°. Accordingly, the surface energies were dedtermined to be 30.133 mN m^{-1}, 36.873 mN m^{-1}, 37.297 mN m^{-1}, and 35.104 mN m^{-1}, respectively. The more approaching surface energy indicated the better compatibility between the donor and the mixed acceptor. The D-A interfacial energy ($\gamma_{D/A}$) and Flory-Huggins parameter ($\chi_{D/A}$) were evaluated and the results were listed in Table 3.1. The smaller the $\gamma_{D/A}$ and $\chi_{D/A}$ value, the better the miscibility of two materials[1]. The calculated $\gamma_{PM6/BTP-eC9}$, $\gamma_{PM6/BTP-4Cl}$, and $\gamma_{PM6/BTP-eC9:\ BTP-4Cl}$ are 0.680 mN m^{-1}, 0.815 mN m^{-1}, and 0.566 mN m^{-1}, respectively. Furthermore, $\chi_{PM6/BTP-eC9:\ BTP-4Cl}$ was calculated to be 0.190, which was far less than $\chi_{PM6/BTP-eC9}$ and $\chi_{PM6/BTP-4Cl}$ with the value of 0.340 and 0.382, respectively, suggesting the BTP-eC9: BTP-4Cl blend acceptor was more miscible with PM6 compared to the neat acceptor. The wetting coefficient (ω) was determined by the equation: $\omega_{A2} = (\gamma_{A1/A2} - \gamma_{D/A2}) / \gamma_{D/A1}$ to confirm the position of the third component. For $\omega_{A2} < 1$, A_2 is in the host acceptor (A_1)'s domain; for $-1 < \omega_{A2} < 1$, A_2 is at the interface of D and A_1; for $\omega_{A2} > -1$, A_2 is in the donor's domain.[184,195] The $\omega_{BTP-4Cl}$ was calculated to be -1.07, which indicated good compatibility between two acceptors and BTP-4Cl could easily diffuse into BTPeC9 phases.

Table 3.1 The summary of WCA, EgCA, surface energy, $\gamma_{donor-acceptor}$, $\chi_{donor-acceptor}$, and ω of materials.

Materials	WCA [°]	EgCA [°]	γ^d [mN m^{-1}]	γ^p [mN m^{-1}]	γ [mN m^{-1}]	$\gamma_{donor-acceptor}$ [mN m^{-1}]	$\chi_{donor-acceptor}$ [mN m^{-1}]	ω
PM6	102.782	72.582	29.981	0.152	30.133	--	--	
BTP-eC9	98.277	64.372	36.712	0.161	36.873	0.680	0.340	
BTP-4Cl	95.750	61.650	36.920	0.377	37.297	0.815	0.382	
BTP-eC9: BTP-4Cl	95.605	62.866	34.531	0.573	35.104	0.566	0.190	
								-1.072

3.3.2 Device performance and charge carrier dynamics

To investigate the different device performances of the SC/BC binary/ternary OPV films, the corresponding OSC devices were fabricated with the structure of ITO/ PEDOT: PSS/active layer/PFN-Br/Ag, as shown in Figure 3.1d. The total D/A ratio was

1:1.2, and the optimized content of BTP-4Cl was 20% (Table 3.2). The detailed experimental processes were provided in the experimental section. The SC-processed binary devices showed a moderate PCE of 17.92% with a V_{OC} of 0.848 V, a FF of 78.94%, and a J_{SC} of 26.77 mA cm^{-2} (Figure 3.4b; Table 3.3). After BTP-4Cl was incorporated, the SC ternary devices gave a maintained V_{OC} of 0.846 V and the largely improved FF and J_{SC} with the value of 80.20% and 27.81 mA cm^{-2}, separately, resulting in an enhanced PCE of 18.87%, indicating the introduction of BTP-4Cl facilitated the morphology optimization and photocurrent improvement. The BC binary devices, however, demonstrated simultaneously declined FF (77.30%) and J_{SC} (25.90 mA cm^{-2}), leading to a lower PCE of 16.98%, It is noteworthy that the efficiency gap was effectively mitigated in BC ternary devices, which preserved a remarkable PCE of 18.62%, with a V_{OC} of 0.846 V, a FF of 79.59%, and a J_{SC} of 27.63 mA cm^{-2}, which was comparable with SC-processed ternary devices. Figure 3.4c depicts the EQE curves for the corresponding devices. The calculated J_{SC} of binary devices was measured to be 26.02 and 25.36 mA cm^{-2} for SC- and BC-processing, separately. For the ternary devices, both SC- and BC-processed devices displayed high photo-responses of above 80% from 500 nm to 850 nm, corresponding to the integrated J_{SC} of 27.01 and 26.86 mA cm^{-2}, respectively, coincident with the J_{SC}s from *J-V* curves with all the deviations < 3%. The result indicated that the introduction of BTP-4Cl was favorable for devices' photon utilization efficiency.

Table 3.2 Photovoltaic parameters of the spin-coated devices with different BTP-4Cl ratios.

Ratio of BTP-4Cl	**V_{oc} (V)**	**PCE (%)**	**FF (%)**	**J_{sc} (mA cm^{-2})**
0	0.845	17.01	77.90	25.85
10%	0.846	17.59	78.34	26.54
20%	0.846	17.73	78.14	26.83
40%	0.845	17.39	78.01	26.37
100%	0.861	16.42	74.71	25.52

Table 3.3 Summary of photovoltaic parameters of the spin-coated (SC) and blade-coated (BC) binary and optimized ternary OSC devices.

Active Layer	V_{OC} (V)	J_{SC} (mA cm^{-2})	FF (%)	PCE (%)	J_{SC}^{cal} (mA cm^{-2})
SC binary	0.848 (0.847 ± 0.004)	26.77 (26.68 ± 0.09)	78.94 (78.84 ± 0.09)	17.92 (17.72 ± 0.09)	26.02
BC binary	0.848 (0.847 ± 0.004)	25.90 (25.65 ± 0.13)	77.30 (77.11 ± 0.16)	16.98 (16.55 ± 0.10)	25.36
SC ternary	0.846 (0.846 ± 0.003)	27.81 (27.67 ± 0.14)	80.20 (79.88 ± 0.18)	18.87 (18.71 ± 0.10)	27.01
BC ternary	0.846 (0.845 ± 0.003)	27.63 (27.59 ± 0.11)	79.59 (79.44 ± 0.08)	18.62 (18.47 ± 0.09)	26.86

The V_{OC} and J_{SC} versus light intensity (P_{light}) were conducted to estimate the charge recombination in SC and BC devices. For the trap-assisted recombination, the relationship of $V_{OC} \propto (nkT/q)\ln P_{light}$ was applied, where n is the ideality factor, T is Kelvin temperature, q is the elementary charge, and k is the Boltzmann constant. The closer the n value to 1, the more suppressed the monomolecular recombination. Four devices gave the n value of 1.07, 1.12, 1.03, and 1.09 for SC-binary, BC-binary, SC-ternary, and BC-ternary, respectively. Relationship between J_{SC} and P_{light} followed the relationship of $J_{SC} \propto P_{light}^{\alpha}$, where the closer the α value to 1, the more suppressed bimolecular recombination process. From Figure 3.5, all devices showed weak bimolecular recombination with the α value of 0.994, 0.992, 0.994, and 0.994 for SC-binary, BC-binary, SC-ternary, and BC-ternary devices, separately. The relatively large n value and small α value for BC-binary devices implied the relatively severe trap-assisted and bimolecular recombination in BC-binary film.

The charge separation and collection of the four OSCs were evaluated by analyzing photocurrent density (J_{ph}) versus effective voltage (V_{eff}) plot (Figure 3.6). The charge dissociation (η_{diss}) and charge collection (η_{coll}) efficiency can be obtained by J_{ph}/J_{sat} under the short-circuit condition and maximum power point, respectively. The calculated η_{diss}s are 95.88%, 93.42%, 98.43%, and 97.09% for SC binary, BC binary, SC ternary, and BC ternary devices, respectively, and the corresponding η_{coll} values

were estimated to be 87.78%, 85.26%, 89.54%, and 89.33%. The much lower charge dissociation and charge collection efficiency in BC-binary devices were ascribed to the oversized pure domain sizes in the active layer, leading to the limited D/A interfaces, and thus much lower FF and J_{SC}. In ternary devices, the BC-processed OSCs gave comparable charge dissociation and charge collection efficiency with SC devices, indicating the over-aggregation problem was effectively alleviated.

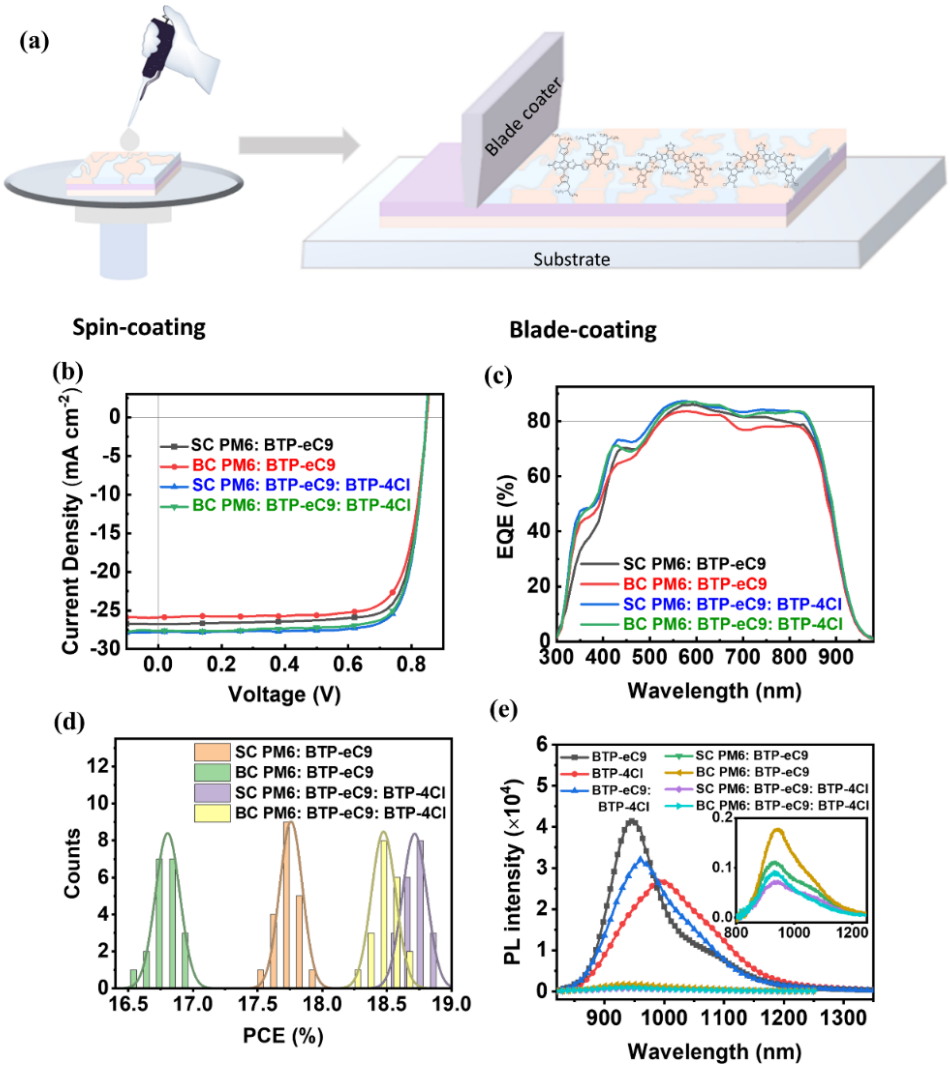

Figure 3.4 (a) Illustrated diagram of spin-coating and doctor-blade coating deposition methods. (b) *J*-*V*, (c) EQE, and (d) histograms of the optimized SC/BC binary/ternary OSCs. (e) PL emission of neat acceptors, the mixed acceptor, and SC/BC binary/ternary blend films.

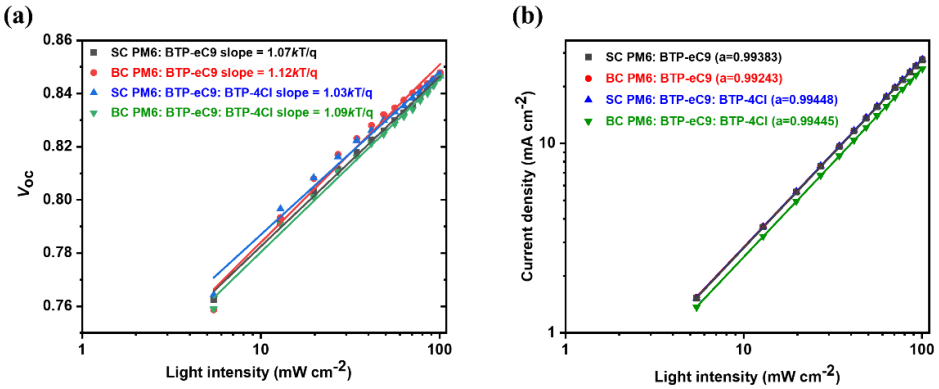

Figure 3.5 (a) V_{oc} and (b) J_{sc} versus P_{light} for optimized SC/BC binary and ternary devices.

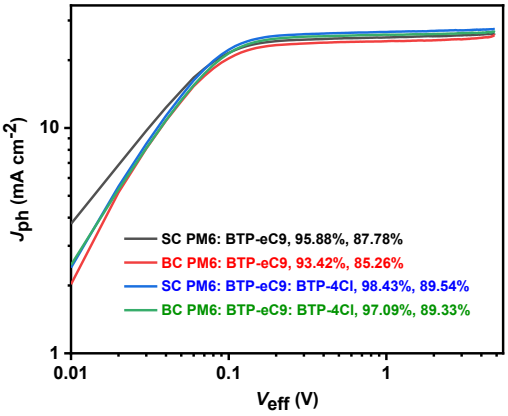

Figure 3.6 J_{ph} versus V_{eff} for SC binary, BC binary, SC ternary, and BC ternary OSC devices.

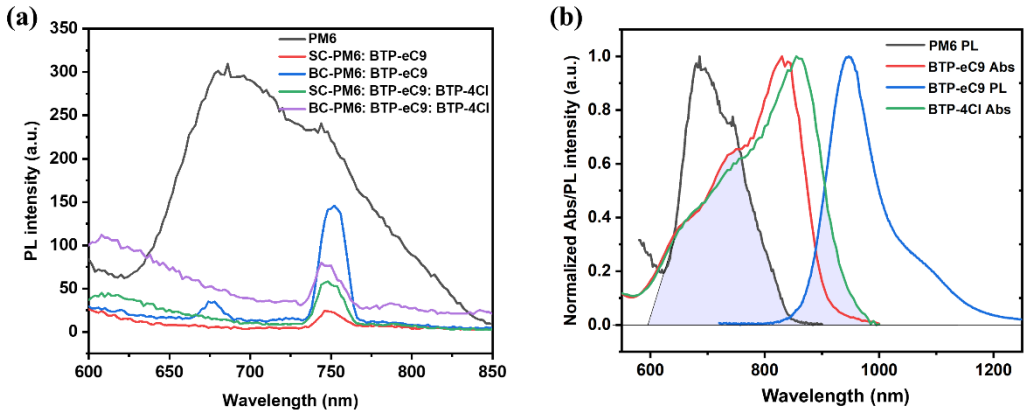

Figure 3.7 (a) PL emission of PM6 neat film and SC/BC binary/ternary blend films. (b) Normalized absorption and PL spectra of corresponding films.

The steady-state photoluminescence (PL) was performed to understand the charge transfer mechanism. The excitation wavelength was determined to be 510 nm for the donor and 640 nm for the acceptors. PM6 neat film exhibited a distinct maximal emission peak at ~680 nm, whose emissive profile overlapped well with two acceptors' absorption spectra, guaranteeing the ultrafast Förster resonance energy transfer process between D/A. Four blend films displayed significant PL quenching compared with neat PM6 film, while BC binary film retained residual PM6 emission peak, indicating a less efficient charge transfer process (Figure 3.7a). The PL spectra of neat acceptors and blend films are depicted in Figure 3.4e. BTP-eC9 neat film showed a distinctive maximal emission peak at 947 nm, and BTP-4Cl presented a relatively weaker emission at 991 nm. The mixed acceptor gave a moderate emission peak at 960 nm, indicating the energy transfer from BTP-eC9 to BTP-4Cl (Figure 3.7b). For blend films, the PL quenching efficiency was calculated to be 95.51%, 93.59%, 96.85%, and 96.64% for SC-binary, BC-binary, SC-ternary, and BC-ternary, respectively. The significantly declined PL quenching efficiency in BC binary blends was ascribed to the limited D/A interfaces resulting from excessive aggregation. It was apparent that the introduction of the third component facilitated the charge transfer efficiency, especially in blade-coated blends.

The SCLC method examined the charge transport (Figure 3.8; Table 3.4). The device structure of ITO/PEDOT: PSS/active layer/Au was used to determine hole mobility, and ITO/ZnO/active layer/Ag was employed to determine electron mobility. The hole mobilities (μ_h) of SC-binary, BC-binary, SC-ternary, and BC-ternary are calculated to be 1.07×10^{-4}, 9.93×10^{-5}, 1.51×10^{-4}, 1.33×10^{-4} $cm^2V^{-1}s^{-1}$, and the corresponding electron mobilities (μ_e) are 1.33×10^{-4}, 1.39×10^{-4}, 1.66×10^{-4}, and 1.75×10^{-4} $cm^2V^{-1}s^{-1}$, respectively. SC devices showed much more balanced charge carrier mobility than BC devices with the μ_e/μ_h ratio of 1.24 and 1.10 for SC binary and SC ternary devices, while 1.40 and 1.32 for BC binary and BC ternary devices. The BC-processed devices were found to have relatively higher electron mobility, probably resulted from the high crystallinity of the acceptor in BC films.

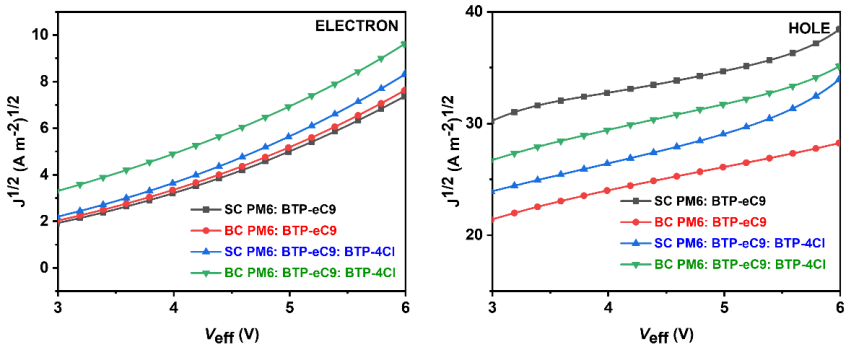

Figure 3.8 Plots obtained from the a) electron and b) hole devices based on the optimal SC binary, BC binary, SC ternary, and BC ternary devices.

Table 3.4 Hole and electron mobility of corresponding SC/BC binary/ternary devices.

Active Layer	μ_h ($cm^2V^{-1}s^{-1}$)	μ_e ($cm^2V^{-1}s^{-1}$)	μ_e/μ_h
SC PM6: BTP-eC9	1.07×10^{-4}	1.33×10^{-4}	1.24
BC PM6: BTP-eC9	9.93×10^{-5}	1.39×10^{-4}	1.40
SC PM6: BTP-eC9: BTP-4Cl	1.51×10^{-4}	1.66×10^{-4}	1.10
BC PM6: BTP-eC9: BTP-4Cl	1.33×10^{-4}	1.75×10^{-4}	1.32

3.3.3 Morphological studies

Prior to morphology analysis, we first detected the solubilities of two acceptors and the mixed acceptor in high boiling point solvent chlorobenzene to gain an initial insight into the molecular interaction between the guest and host components. The UV-vis absorption spectra of standard solutions and the diluted saturated solution are depicted in Figure 3.9. The maximum absorption peak was selected as the characteristic peak to fit the corresponding standard curves (Figure 3.10). According to the fitting equation, the solubility of the neat acceptor and the mixed acceptor in CB could be calculated, which were 37.75, 37.11, and 44.47 mg mL−1 for BTP-eC9, BTP-4Cl, and BTP-eC9: BTP-4Cl, respectively (Table 3. 5). To elucidate the underlying mechanism behind the

increased solubility, the intermolecular interactions between BTP-eC9 and BTP-4Cl molecules were analyzed based on single crystal calculations (Figure 3.11). Only one packing mode was detected in BTP-eC9 with the π–π distance of 3.38 Å, while distinct two packing modes were found in the mixed acceptor with a distance of 3.38 and 3.40 Å, respectively. The larger intermolecular distance indicates the more dispersed and loose molecular distribution in the mixed acceptor, which is expected to facilitate the diffusion of solvent molecules into the cavity between acceptor molecules and thus improve the solubility. Combining the larger dihedral angle of BTP-4Cl (2.70° and 4.22°) than BTP-eC9 (2.62° and 2.72°),[196] it was expected that the twisted molecular backbone would induce large steric hindrance during molecular assembly, inducing large intermolecular distance in the mixed acceptor. The dispersed molecules and improved solubility in the mixed acceptor are expected to suppress molecular aggregation to prevent oversized aggregates in blade-coated blends.[180]

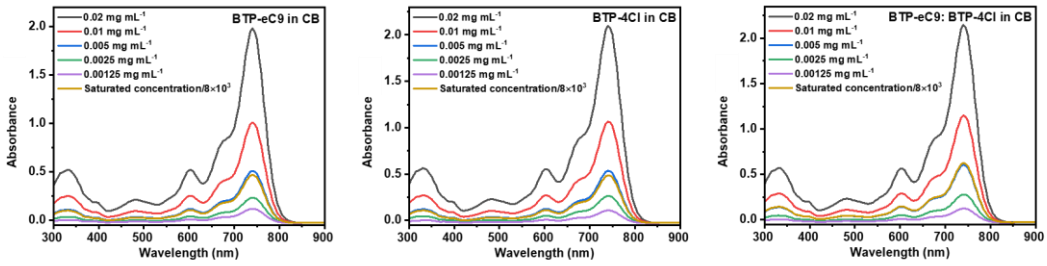

Figure 3.9 UV-vis absorption spectra of standard solution and diluted saturated solution of (a) BTP-eC9, (b) BTP-4Cl, and (c) BTP-eC9: BTP-4Cl in chlorobenzene.

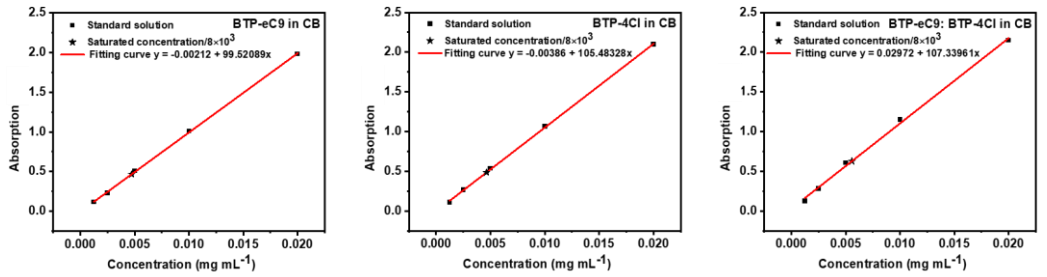

Figure 3.10 The absorbance versus concentration standard curves of (a) BTP-eC9, (b) BTP-4Cl, and (c) BTP-eC9: BTP-4Cl obtained from the maximum absorption peak.

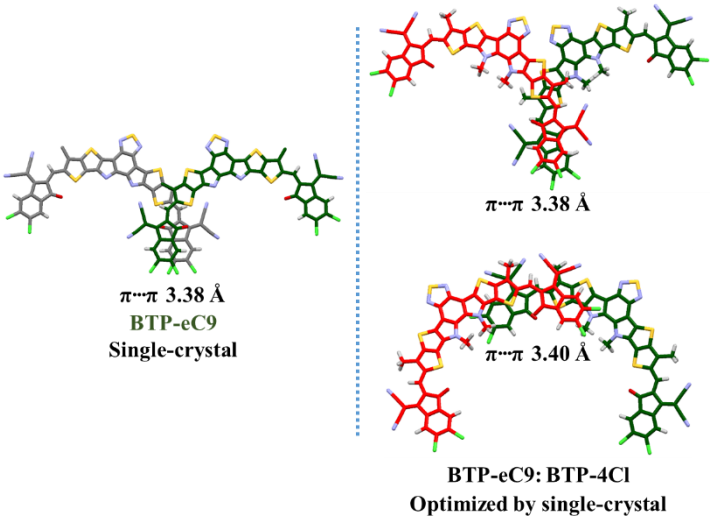

Figure 3.11 The calculated intermolecular distance in the pure BTP-eC9 and in BTP-eC9: BTP-4Cl mixture.

Table 3. 5 The solubility of BTP-eC9, BTP-4Cl, and BTP-eC9: BTP-4Cl in chlorobenzene.

	X in CB (mg mL^{-1})	Solubility (mg mL^{-1})
BTP-eC9	0.00471851	37.75
BTP-4Cl	0.004639	37.11
BTP-eC9: BTP-4Cl	0.00555825	44.47

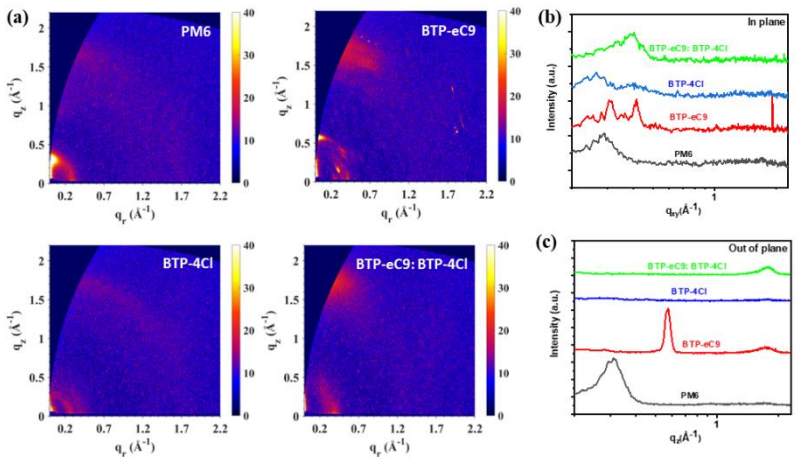

Figure 3. 12 (a) 2D GIWAXS patterns and 1D line profiles in the (b) IP and (c) OOP directions of PM6, BTP-eC9, BTP-4Cl, and BTP-eC9: BTP-4Cl film.

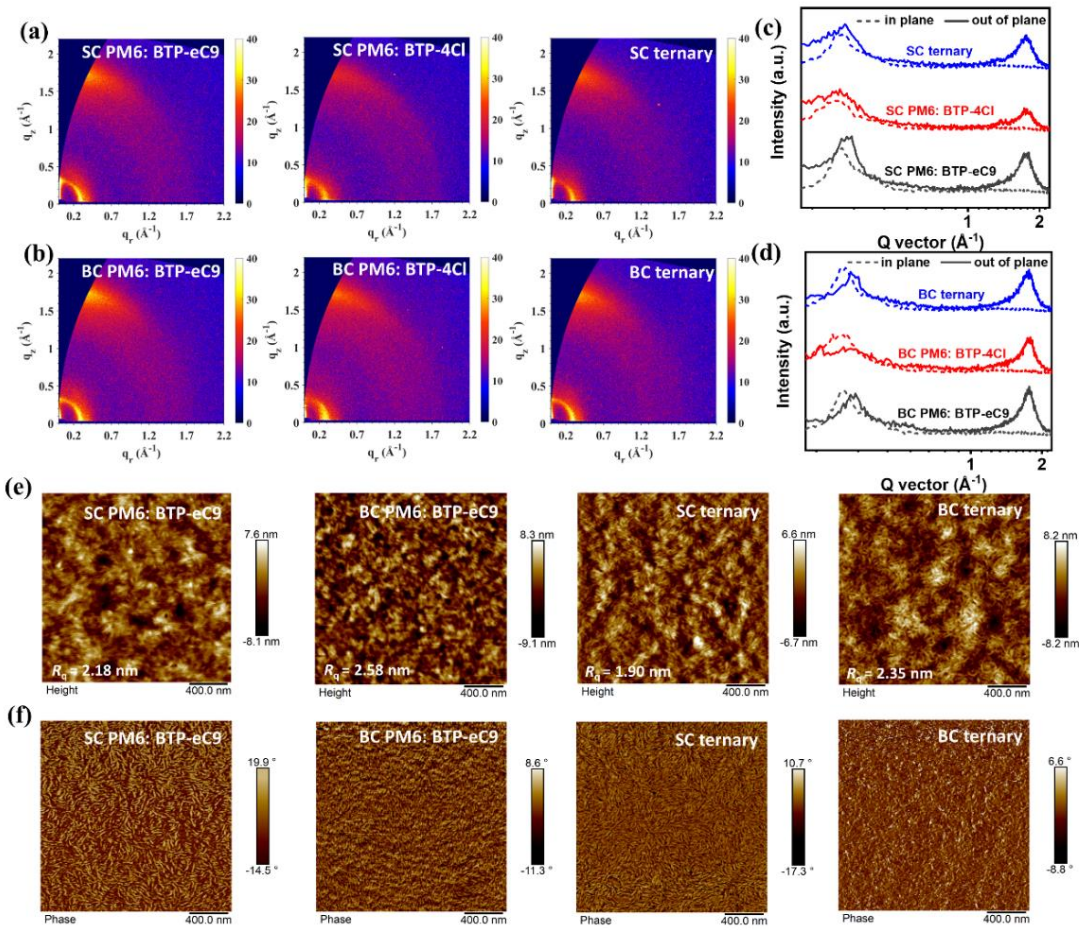

Figure 3.13 2D GIWAXS patterns of (a) spin-coated and (b) blade-coated binary and ternary blends. 1D linecut profiles of (c) spin-coated and (d) blade-coated blend films. AFM (e) height and (f) phase images of SC/BC binary/ternary blends.

Table 3. 6 Summarized *d*-spacing and CCL of the lamellar staking (100) peak along IP direction of neat films.

	q_{xy} (Å^{-1})	*d*-spacing (Å)	FWHM (Å^{-1})	Coherence length (Å)
PM6	0.29	21.67	0.106	53.35
BTP-eC9	0.32	19.63	0.085	66.53
BTP-4Cl	0.26	24.17	0.136	41.58
BTP-eC9: BTP-4Cl	0.35	17.95	0.251	22.53

Table 3. 7 Summarized *d*-spacing and CCL of the *π*-*π* staking (010) peak along OOP direction of neat films.

	q_z (Å^{-1})	*d*-spacing (Å)	FWHM (Å^{-1})	Coherence length (Å)
PM6	1.73	3.63	0.55	10.28
BTP-eC9	1.75	3.59	0.36	15.71
BTP-4Cl	1.77	3.55	0.45	12.57
BTP-eC9: BTP-4Cl	1.78	3.53	0.25	22.62

Table 3. 8 Summarized *d*-spacing and CCL of the lamellar staking (100) peak along IP direction of blend films processed from spin-coating and blade coating.

	q_{xy} (Å^{-1})	*d*-spacing (Å)	FWHM (Å^{-1})	Coherence length (Å)
SC PM6: BTP-eC9	0.29	21.67	0.058	97.50
SCPM6: BTP-4Cl	0.28	22.44	0.099	57.12
SC ternary	0.29	21.67	0.064	88.36
BC PM6: BTP-eC9	0.29	21.67	0.060	94.25
BCPM6: BTP-4Cl	0.28	22.44	0.100	56.55
BC ternary	0.29	21.67	0.062	91.21

Table 3. 9 Summarized *d*-spacing and CCL of the *π*-*π* staking (010) peak along OOP direction of blend films processed from spin-coating and blade coating.

	q_z (Å^{-1})	*d*-spacing (Å)	FWHM (Å^{-1})	Coherence length (Å)
SC PM6: BTP-eC9	1.74	3.61	0.25	22.62
SCPM6: BTP-4Cl	1.74	3.61	0.24	23.56
SC ternary	1.74	3.61	0.21	26.93
BC PM6: BTP-eC9	1.74	3.61	0.24	23.56
BCPM6: BTP-4Cl	1.75	3.59	0.22	25.70
BC ternary	1.74	3.61	0.20	28.27

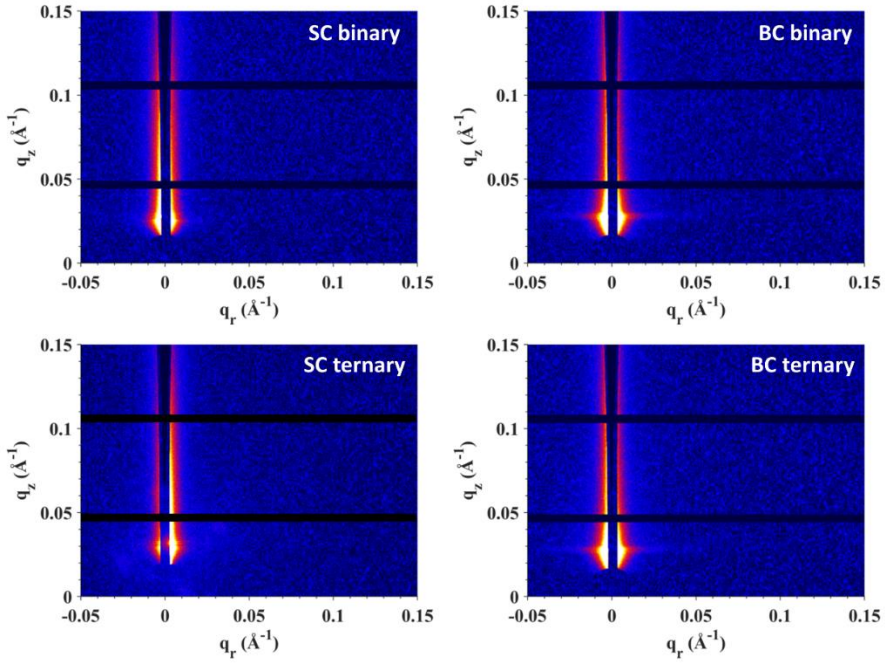

Figure 3. 14 2D GISAXS patterns of SC-binary, BC-binary, SC-ternary, and BC-ternary films.

The molecular orientation and crystallinity properties were evaluated by Grazing incidence wide-angle X-ray scattering (GIWXAS) experiment (Figure 3. 12; Figure 3.13a-d). The extracted parameters were summarized in Table 3. 6-

Table 3. 9 for the neat and blend films. PM6 demonstrated strong lamellar diffraction peaks at both out-of-plane (OOP) and in-plane (IP) directions. Different from BTP-4Cl neat film, where no apparent molecular orientation was detected, BTP-eC9 neat film exhibited preferential face-on orientation with the IP (100) peak at q_{xy} = 0.32 Å^{-1} (*d*-spacing = 19.63 Å and CCL = 66.53 Å) and OOP (010) peak at q_z = 1.75 Å^{-1} (CCL = 15.71 Å). The mixed acceptor film showed highly ordered face-on orientation with the IP lamellar peak at q_{xy} = 0.35 Å^{-1} (*d*-spacing = 17.95 Å and CCL = 22.53 Å) and OOP π-π peak at q_z = 1.78 Å^{-1} (CCL = 22.62 Å). The reduced CCL values in the IP direction but increased CCL in the OOP direction indicate a reduced alky chain stacking in BTP-eC9 along the side chain andimprovedlong-rangeπ–π stacking directions, which is more favorable for charge transport. Additionally, the characteristic peak of BTP-eC9 at q_z = 0.58 Å^{-1} disappeared when blended with BTP-4Cl, indicating the good

compatibility between two acceptors[122] and the modulation of BTP-4Cl on the organization of BTP-eC9 molecules, coincident well with the result from contact angle measurement. All blend films displayed distinct face-on orientation with representative IP (100) lamellar packing peaks and OOP (010) π-π diffraction peaks. The lamellar peaks all appeared at ~q_{xy} = 0.29 Å^{-1} with a *d*-spacing of 21.67 Å, while the reduced CCL in ternary films indicated the reduced alkyl chain stacking via the tuning of a third component. For the OOP (010) peaks, the blade-coated binary blend gave a shorter *d*-spacing and a larger CCL value than the spin-coated blend, indicating the higher crystallinity (severer aggregation) in blade-coated films, which was effectively optimized by the participation of a third component, where the *d*-spacing retained and the increment of CCLs alleviated.

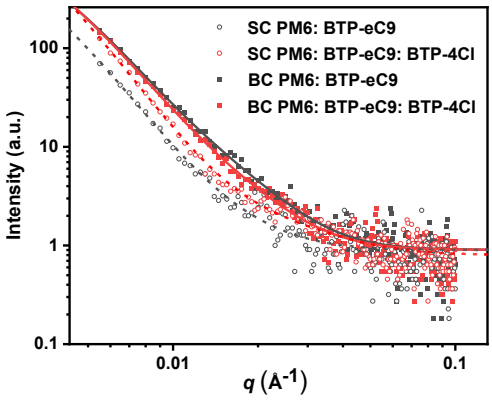

Figure 3. 15 GISAXS line profiles and fitting curves for SC/BC binary/ternary blend films in IP direction.

Table 3. 10 Summarized $2R_g$ and X_{DAB} value extracted from GISAXS fitting curves.

	$2R_g$ (nm)	**X_{DAB} (nm)**
SC Binary	22.4	37.9
SC Ternary	12.3	46.5
BC Binary	26.4	29.7
BC Ternary	25.0	31.5

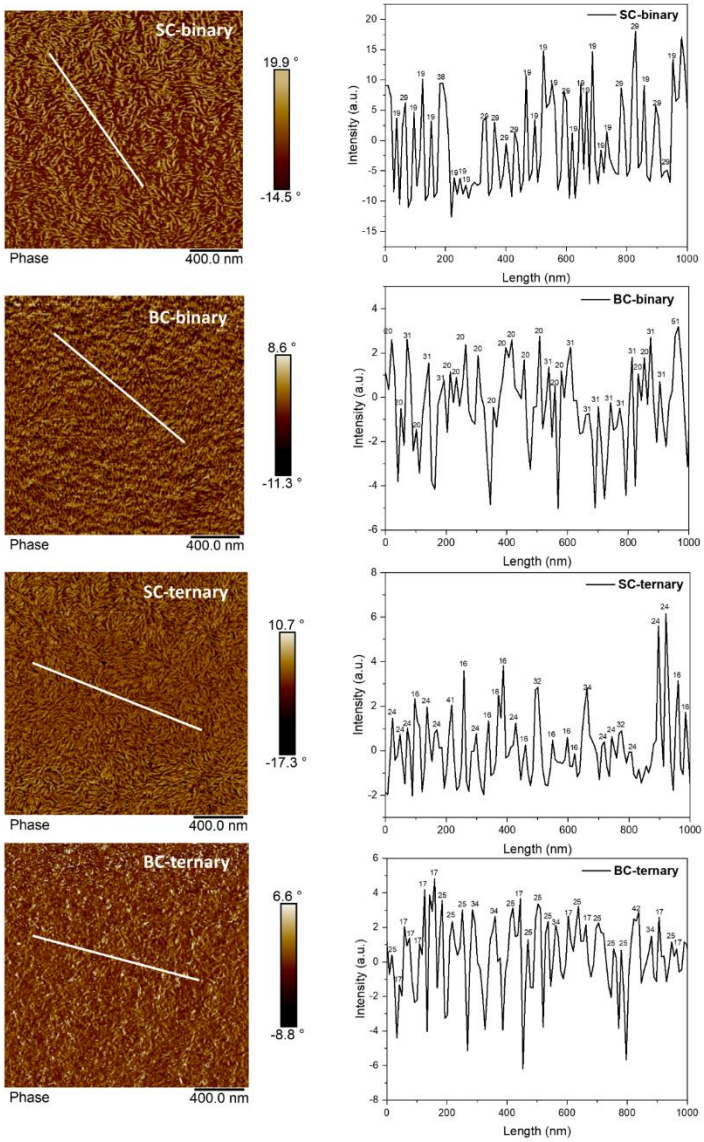

Figure 3. 16 The AFM phase images of the blend films. The line profiles are used to determine the fibril diameters.

The inhibited excessive aggregation was further confirmed by Grazing-incidence small-angle X-ray scattering (GISAXS) measurement (Figure 3. 14 & Figure 3. 15; Table 3. 10), where X_{DAB} represents the average correlation length of the amorphous domain and $2R_g$ represents the average length scale of pure domains, which was extracted from the Debye-Anderson-Brumberger and fractal-like network model in the fitting equation, respectively. It was noticed that the pure domain size magnified and the mixed phases contracted from SC-film to BC-film, indicating the relatively severe

aggregation in blade-coated blends. However, the pure domain size was alleviated in the BC ternary film with $2R_g$ of 25.0 nm and X_{DAB} of 31.5 nm, suggesting the effective suppression of severe aggregation by the regulation of the third component. Additionally, the enlarged intermixing phase ensured a more efficient charge transfer efficiency in ternary blends. According to the previous result, the suppression of the excessive aggregation could be ascribed to the twisted molecular backbone of the third component.[197–199] The weakened molecular interactions between BTP-4Cl and BTP-eC9 molecules could help improve solubility and suppress phase separation in blade-coated films, enabling the formation of an optimal phase-separated length scale. This, in turn, balances charge transport and charge separation processes, leading to improved FF and J_{SC} in the optimized ternary devices.

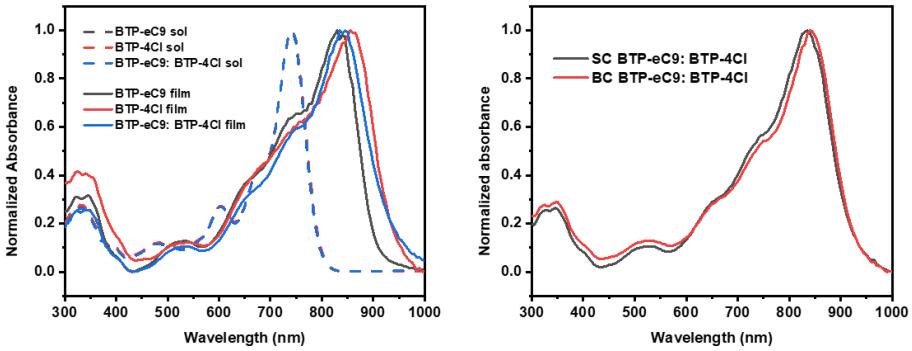

Figure 3. 17 (a) Normalized absorption of BTP-eC9, BTP-4Cl, and BTP-eC9: BTP-4Cl in chlorobenzene and in the film (~740 nm in chlorobenzene; 830 nm for BTP-eC9 film, 855 nm for BTP-4Cl film, and 835 nm for BTP-eC9: BTP-4Cl film). (b) Normalized absorption of BTP-eC9: BTP-4Cl neat film processed from spin-coating and blade-coating.

The surface morphology was detected by tapping-mode atomic force spectroscopy (AFM) (Figure 3.13e-f). The root-mean-square roughness (R_q) of the SC/BC binary/ternary blends was 2.18, 2.58, 1.90, and 2.35 nm, respectively. The BC films afforded a larger R_q, while the third component effectively inhibited excessive

aggregation and optimized film morphology. The nano fibrillar interpenetrating network originating from PM6 crystallization was distinctly recognized in AFM phase images, while the granular aggregates arose in BC blends, which was ascribed to the strong crystallization of Y-series acceptors. There are two dominant fibril sizes in the active layer according to their phase images (Figure 3. 16). The SC and BC binary film showed a fibril size of 19/29 nm and 20/31 nm, respectively. The ternary blend exhibited a reduced fibril size of 16/24 nm and 17/25 nm for SC and BC film, respectively. The fibril structure with a small size of ~20 nm and an oversized domain of ~30 nm is not favorable for efficient charge separation and charge transport. The suitable phase separation size of ~25 nm could afford the simultaneously facilitated charge transfer and charge mobility.[116,163].

Keeping the optimized crystallinity in mind, we go ahead to investigate the effects of BTP-4Cl on BTP-eC9 in the phase transition state. It was noted that these acceptors' maximal absorption peak redshifted greatly from solution to solid film, indicating the compact molecular aggregation in films. Compared to spin-coated film, the blade-coated film exhibited a more bathochromic absorption (Figure 3. 17), suggesting that the molecular aggregation is more profound in blade-coating processing. In-situ UV–vis absorption measurement was performed to comprehend the phase transition process from solutions to solid films. The 2D contour map and the absorption profiles are depicted in Figure 3. 18-Figure 3. 19. The peak position and intensity versus time were plotted by selecting their 0-0 absorption peak as the characteristic peak. The displacement of the peak position and intensity reflected four stages during film formation, including 1) solvent evaporation, 2) preaggregation, 3) crystal growth, and 4) dried films.[154,189,200] It was noticed that the film formation mechanism was different in SC and BC films. In the solvent evaporation stage, obvious solvent evaporation was observed in spin-coating, which, however, was vague (hard to distinguish from the preaggregation stage) in blade-coating due to lower shear force and Reynold number.[168–170] In the preaggregation stage, the time duration was much longer and the preaggregation rate was much slower in blade-coating, explaining the severe

aggregation in BC blends. In the crystal growth stage, apparent peak redshift along with an abrupt change of peak intensity was observed in both the spin- and blade-coating process due to the ordered and compact molecular aggregation from solution to solid film.

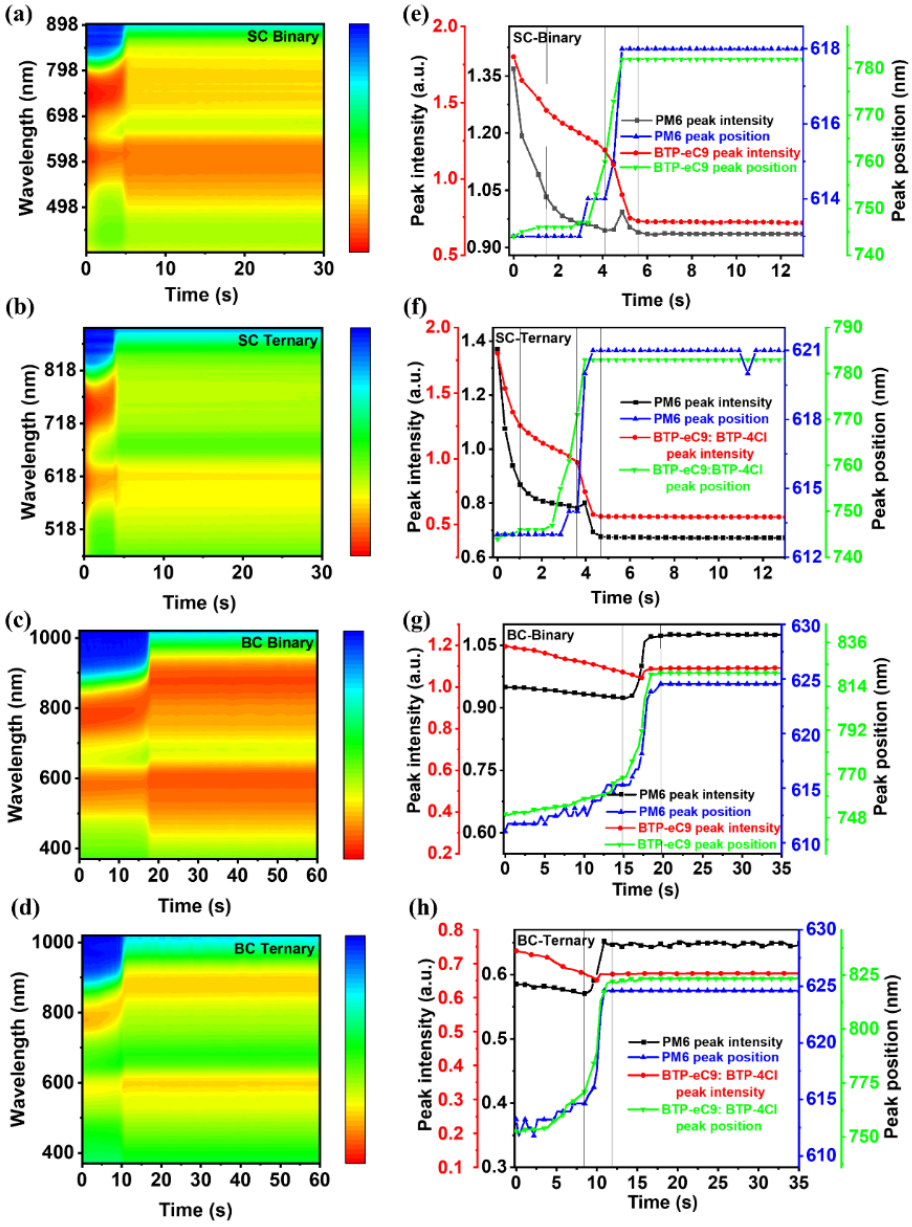

Figure 3. 18 In-situ UV-vis absorption measurement. The contour map of (a) SC binary film, (b) SC ternary film, (c) BC binary film, and (d) BC ternary film. The donor and acceptor peak position and peak intensity versus time for (e) SC binary film, (f) SC ternary film, (g) BC binary film, and (h) BC ternary film.

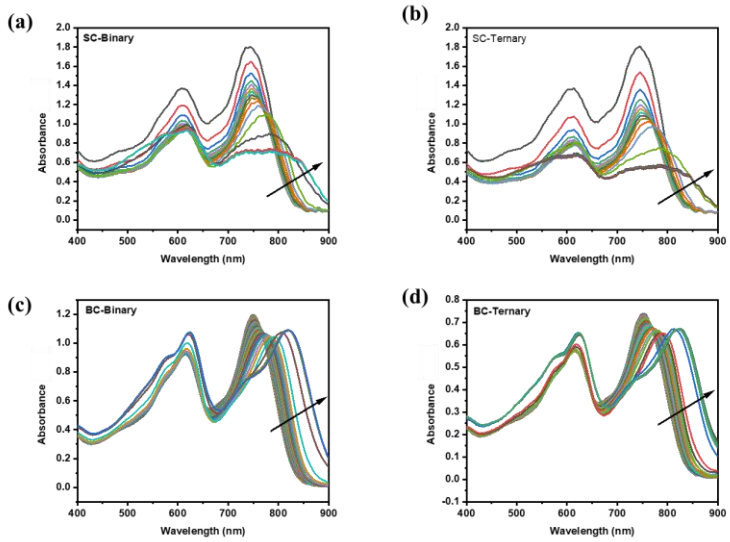

Figure 3. 19 In-situ UV-vis absorption profiles of (a) SC binary, (b) SC ternary, (c) BC binary, and (d) BC ternary blends.

The role of the third component in regulating molecular aggregation behavior during phase transition was investigated. It was found that the solvent evaporation time was abbreviated and the solvent evaporation rate was accelerated in ternary blends (Figure 3. 20), indicating that the third component could facilitate the solvent removal and promote film solidifying. In the preaggregation stage, given the relatively poor solubility of BTP-4Cl and the solvent removal function, the BTP-4Cl was considered to first reach the solubility limit and crystallize.[201] The crystalized BTP-4Cl provides the nuclei seeding sites enabling the advanced onset of crystalline than in the binary system. Additionally, the more dispersed molecular distribution in the solution enabled more dispersed seeding sites during phase transition, leading to a much-shortened preaggregation time and finer crystal grains. In the crystal growth stage, ternary blends underwent earlier and faster crystal growth, which was ascribed to the larger amount and more dispersed pre-aggregates, enabling a faster crystal growth rate and finer phase domain. Furthermore, the dispersed and loose molecular distribution along with the enhanced solubility ensured sufficient time for order and favorable molecular reassembly during film formation. Thus, finer and higher-quality crystallites were expected in the blade-coated ternary blends.

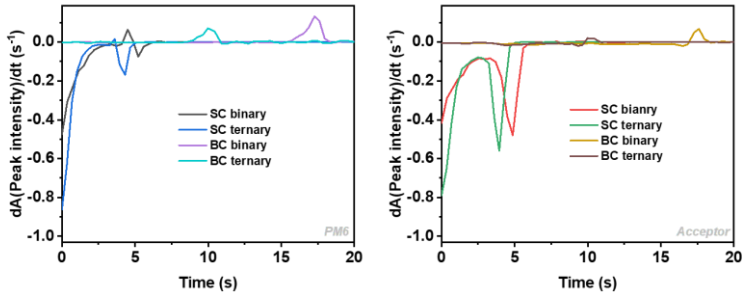

Figure 3. 20 The derivative of peak intensity of the donor (left) and the acceptor (right) to time.

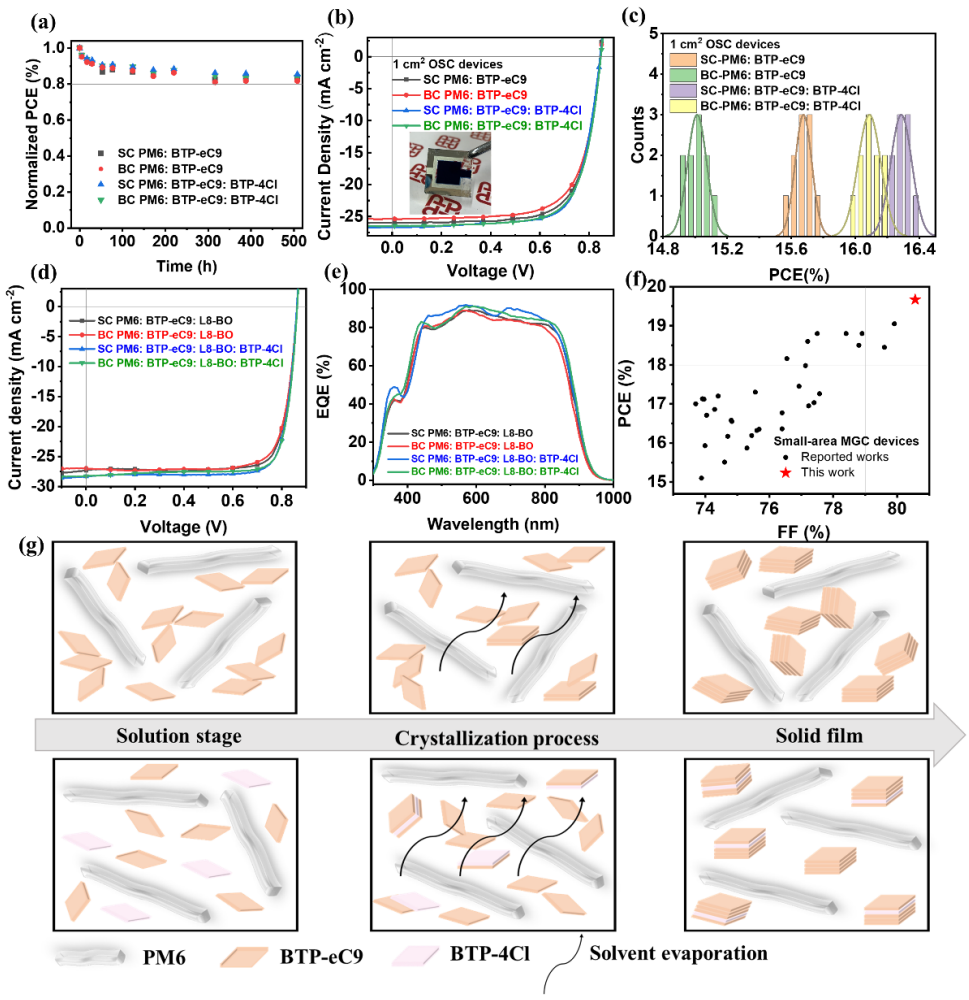

Figure 3. 21 (a) Light stability of SC/BC binary/ternary OSCs. (b) *J-V* curves and (c) histograms of the 1 cm^2 SC/BC binary/ternary OSCs. (d) *J-V* and (e) EQE curves of the optimized ternary/quaternary OSCs. (f) Summary of the representative MGC OSCs with area smaller than 0.1 cm^2. (g) Schematic crystallization process in the binary and ternary film.

Based on ex situ and in situ morphological results, we propose a visualized crystallization landscape that illustrates how BTP4Cl enables the self-assembly of BTP-eC9 when processed from high-boiling-point solvents during blade coating (Figure 3. 21g). In the solution state (preaggregation stage), the twisted molecular backbone of BTP-4Cl promotes a more dispersed and loose molecular distribution within the ternary solution, improving solubility and preventing excessive preaggregation. During the crystallization process, BTP-4Cl aids in promoting solvent removal, shortening crystallization time, accelerating crystallization, and facilitating the formation of fine and high-quality crystallites in the blade-coated blends. As a result, we achieved an ordered microstructure with well-defined donor and acceptor domains, leading to optimized crystallinity with a preferred face-on orientation.

3.3.4 Stability and Generality Test

Light stability was measured to evaluate the capability of four blends to resist light-induced degradation (Figure 3. 21a). All blends showed a burn-in loss in the first 100 h and were then kept stable with the T_{80} > 500 h under continuous illumination in a glovebox under nitrogen. After the third component was added, the photostability was improved in both SC and BC devices, which could be ascribed to the locking-in morphology effect of the third component.[143] It was found that the light stability of SC devices was superior to that of BC devices, where SC devices tended to have a faster J_{SC} decay and BC devices tended to have a quicker V_{OC} and FF degradation (Figure 3. 22). One possible explanation is that during the formation of BC film, the slow film formation and air atmosphere would induce more traps in blends, which is a potential crisis for BC films' stability. For SC films, however, the D/A intermixing phases are larger than that in BC films, with a greater possibility of de-mixing between donor and acceptor, leading to deteriorated J_{SC}s. Thus, we would infer that SC devices have a severer morphological degradation and BC devices have a severer defect-induced loss[126,202]. However, further research was needed to figure out their photodegradation mechanism.

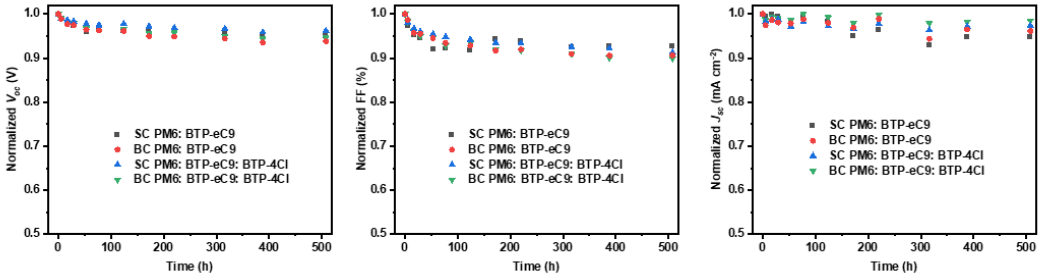

Figure 3. 22 The normalized V_{oc}, FF, J_{sc} versus light-soaking time of SC binary, BC binary, SC ternary, and BC ternary devices under continuous illumination in a glovebox under nitrogen.

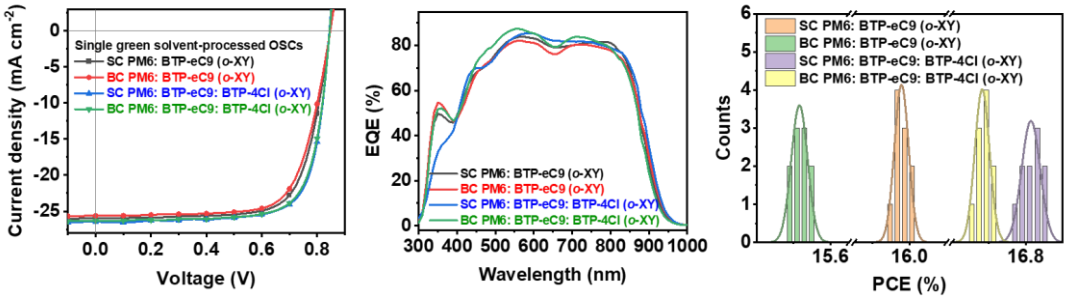

Figure 3. 23 *J*-*V* curves, EQE curves, and histogram of the optimized single-component green solvent (*o*-XY)-processed SC/BC binary/ternary OSC devices.

Table 3. 11 Photovoltaic parameters of the single-component halogen-free solvent (*o*-XY)-processed SC/BC binary/ternary OSC devices.

Active Layer	V_{OC} **(V)**	J_{SC} **(mA cm^{-2})**	**FF (%)**	**PCE (%)**	J_{SC}^{cal} **(mA cm^{-2})**
SC binary	0.847 (0.847 ± 0.002)	25.98 (25.94 ± 0.06)	72.79 (72.76 ± 0.03)	16.01 (15.98 ± 0.04)	25.32
BC binary	0.847 (0.847 ± 0.001)	25.63 (25.64 ± 0.07)	71.63 (71.56 ± 0.04)	15.55 (15.52 ± 0.05)	24.95
SC ternary	0.844 (0.844 ± 0.001)	26.42 (26.45 ± 0.04)	75.54 (75.50 ± 0.07)	16.85 (16.81 ± 0.06)	25.73
BC ternary	0.845 (0.845 ± 0.001)	26.33 (26.34 ± 0.01)	75.11 (75.03 ± 0.07)	16.71 (16.68 ± 0.04)	25.64

Table 3. 12 Photovoltaic parameters of 1 cm^2 SC/BC binary/ternary OSC devices.

Active Layer	V_{OC} (V)	FF (%)	J_{SC} (mA cm^{-2})	PCE (%)
SC binary	0.844 (0.842 ± 0.003)	71.81 (71.76 ± 0.03)	25.98 (25.87 ± 0.05)	15.75 (15.68 ± 0.05)
BC binary	0.845 (0.844 ± 0.02)	70.64 (70.55 ± 0.04)	25.34 (25.27 ± 0.03)	15.12 (15.02 ± 0.06)
SC ternary	0.845 (0.844 ± 0.01)	72.83 (72.76 ± 0.04)	26.65 (26.54 ± 0.06)	16.40 (16.29 ± 0.07)
BC ternary	0.847 (0.845 ± 0.02)	72.30 (72.23 ± 0.05)	26.44 (26.35 ± 0.07)	16.19 (16.08 ± 0.07)

Table 3. 13 Photovoltaic parameters of the SC binary/ternary devices.

PM6: eC9-2Cl: BTP-4Cl	V_{OC} (V)	FF (%)	J_{SC} (mA cm^{-2})	PCE (%)
0%	0.877	75.28	25.88	17.07
10%	0.873	75.66	26.07	17.23
20%	0.869	76.25	26.62	17.64
40%	0.854	76.60	26.58	17.40

Table 3. 14 Photovoltaic parameters of the SC ternary/quaternary devices.

PM6: BTP-eC9: L8-BO: BTP-4Cl	V_{OC} (V)	FF (%)	J_{SC} (mA cm^{-2})	PCE (%)
1: 0.6: 0.6: 0	0.857	80.22	27.10	18.63
1: 0.55: 0.55: 0.1	0.857	80.39	27.57	18.99
1: 0.5: 0.5: 0.2	0.855	79.25	27.44	18.59
1: 0.4: 0.4: 0.4	0.852	79.30	27.17	18.36

Table 3. 15 Photovoltaic parameters of the optimized SC/BC binary/ternary OSC devices.

Active Layer	V_{OC} (V)	FF (%)	J_{SC} (mA cm^{-2})	PCE (%)
SC PM6: eC9-2Cl	0.876	76.03	25.94	17.28
BC PM6: eC9-2Cl	0.879	74.30	25.24	16.48
SC PM6: eC9-2Cl: BTP-4Cl	0.872	77.72	26.76	18.14
BC PM6: eC9-2Cl: BTP-4Cl	0.873	77.01	26.38	17.74

Table 3. 16 Photovoltaic parameters of the SC/BC ternary/quaternary OSC devices.

Active Layer	V_{OC} (V)	FF (%)	J_{SC} (mA cm^{-2})	PCE (%)	J_{SC}^{cal} (mA cm^{-2})
SC PM6: BTP-eC9: L8-BO	0.862 (0.861 ± 0.004)	80.46 (80.10 ± 0.45)	27.34 (27.45 ± 0.18)	18.96 (18.93 ± 0.05)	26.61
BC PM6: BTP-eC9: L8-BO	0.862 (0.865 ± 0.003)	79.59 (79.42 ± 0.47)	26.98 (26.90 ± 0.20)	18.51 (18.48 ± 0.06)	26.17
SC PM6: BTP-eC9: L8-BO: BTP-4Cl	0.862 (0.860 ± 0.003)	80.89 (80.67 ± 0.49)	28.34 (28.31 ± 0.20)	19.76 (19.68 ± 0.05)	27.64
BC PM6: BTP-eC9: L8-BO: BTP-4Cl	0.863 (0.861 ± 0.002)	80.56 (80.48 ± 0.50)	28.29 (28.26 ± 0.23)	19.67 (19.56 ± 0.06)	27.51

The suppression of excessive aggregation in blade coating *via* the ternary strategy was further confirmed by the green solvent-processed OSCs and upscaling devices (1cm^2). When changing the processing solvent from chlorobenzene (0.5% DIO) to single component green solvent o-xylene (Figure 3. 23), the SC PM6: BTP-eC9 devices displayed a moderate PCE of 16.01%, while that of BC binary devices was 15.55% resulting from the decreased FF and J_{SC}. However, such a downward trend was effectively suppressed by introducing BTP-4Cl. SC ternary and BC ternary devices showed comparable PCE of 16.85% and 16.71% (Table 3. 11). When magnifying the device area to 1 cm^2 (Figure 3. 21b), SC binary devices gave a PCE of 15.75% (FF = 71.81%, and J_{SC} = 25.98 mA cm^{-2}.) and BC binary devices showed a lagged PCE of

15.12%, resulting from the inferior FF (70.64%) and J_{SC} (25.34 mA cm^{-2}). However, in ternary devices, the SC and BC devices manifested comparable photovoltaic parameters with a PCE of 16.40% and 16.19%, respectively (Table 3. 12).

This morphology-tuning strategy was demonstrated on other photoactive layer components, the ternary component of PM6: eC9-2Cl: BTP-4Cl and the quaternary component of PM6: BTP-eC9: L8-BO: BTP-4Cl. The optimized ratio of BTP-4Cl is shown in

Table 3. 13 and

Table 3. 14, respectively. The device efficiency increased with the optimized ratio of BTP-4Cl thanks to the enhanced FFs and J_{SC}s. Compared with PM6: eC9-2Cl binary devices, BTP-4Cl-based ternary devices showed good tolerance by different processing methods (Table 3. 15), consistent with previous results. This trend was maintained in the quaternary devices, where BTP-4Cl alleviated the efficiency gap from spin-coating to blade-coating. The SC-PM6: BTP-eC9: L8-BO gave a PCE of 18.96%, while the BC processed devices dropped to 18.51% due to the lower FF and J_{SC}. However, the quaternary devices maintained well in both SC and BC devices. The SC quaternary devices exhibited an optimal FF of 80.89% and PCE of 19.76%. Comparably, the BC-processed devices gave a PCE of 19.67% with an outstanding FF of 80.56% (Figure 3. 21d and

Table 3. 16), which was the highest efficiency among blade-coating processed small-area (<0.1cm^2) devices (Figure 3. 21f and Table 3. 17). The greatly improved device performance is ascribed to the incorporation of L8-BO facilitating the formation of hierarchical morphology with both parallel and alloy-like structures, which is believed to enhance charge transport and charge separation, ultimately contributing to improved device performance.[184,203]

Table 3. 17 Photovoltaic parameters of the representative MGC OSCs with area smaller than 0.1 cm^2.

Active Layer	Area (cm^2)	Processing method	V_{OC} (V)	FF (%)	J_{SC} (mA cm^{-2})	PCE (%)	References
PM6: BTP-eC9: L8-BO: BTP-4Cl (10%)	0.04	Blade-coating	0.863	80.56	28.29	19.67	This work

PM6: L8-BO: YHD-SeNF (1:1:0.2)	0.042	Blade-coating	0.874	78.9	27.3	18.8	[204]
PM6: L8-BO: YHD-SeNF (1:0.8:0.4)	0.042	Blade-coating	0.866	77.5	28.0	18.8	[204]
PM6: L8-BO: YDT-SeNF (1:1:0.2)	0.042	Blade-coating	0.871	78.8	26.9	18.5	[204]
PM6/L8-BO	0.04	Slot-die	0.867	77.23	25.37	16.95	[205]
PM6:L8-BO	0.04	Slot-die	0.865	75.61	24.97	16.32	[205]
PM6/T8	0.05	Blade-coating	0.864	77.13	26.98	17.98	[206]
PM6:T8	0.05	Blade-coating	0.866	76.93	26.2	17.45	[206]
PM6/T8	0.05	Slot-die	0.866	74.29	26.21	16.86	[206]
PM6:T8	0.05	Slot-die	0.860	72.09	25.89	16.05	[206]
PM6/BTP-eC9	0.04	Blade-coating	0.836	76.4	26.26	16.77	[154]
PM6:BTP-eC9	0.04	Blade-coating	0.835	75.3	25.24	15.87	[154]
PM6/BTP-eC9: 5vol% PM6	0.04	Blade-coating	0.836	77.57	26.61	17.26	[207]
PM6/BTP-eC9	0.04	Blade-coating	0.830	75.45	25.85	16.19	[207]
PM6:BTP-eC9	0.036	Blade-coating	0.839	77.4	26.20	17.03	[149]
PM6:BTP-eC9:PY-IT (20%)	0.036	Blade-coating	0.857	79.6	27.08	18.45	[149]
PM6:L8-*i*-EH	0.04	Blade-coating	0.885	75.56	25.86	17.30	[208]
PM6:L8-*i*-EB	0.04	Blade-coating	0.869	74.04	25.97	16.71	[208]
PM6:L8-*i*-BO	0.04	Blade-coating	0.881	76.40	24.31	16.36	[208]
PM6:BTP-eC9	0.048	Blade-coating	0.856	74.83	25.82	16.55	[209]

PM6:BTP-eC9	0.04	Blade-coating	0.84	74.81	26.37	16.58	[210]
PM1:L8-BO:BTP-F3Cl (THF)	0.05	Blade-coating	0.876	78.4	27.4	18.8	[164]
PM1:L8-BO:BTP-F3Cl (CF)	0.05	Blade-coating	0.882	77.2	27.3	18.6	[164]
PM6:BTP-BO-4Cl	0.06	Blade-coating	0.85	73.96	27.23	17.12	[211]
PM6:Y6	0.04	Blade-coating	0.837	70.47	26.34	15.63	[170]
PM6:Y6-2Cl	0.04	Blade-coating	0.859	74.70	25.2	16.17	[212]
PM6:BTP-eC9	0.04	Blade-coating	0.865	76.55	27.43	18.16	[213]
PT2:Y6	0.04	Slot-die	0.82	69.1	27.3	15.5	[214]
PM6/Y6	0.04	Blade-coating	0.834	75.68	25.90	16.35	[215]
PM6/Y6-C2	0.04	Blade-coating	0.834	73.99	25.82	15.93	[215]
PM6:Y6	0.08	Blade-coating	0.834	74.6	24.9	15.51	[216]
D18:BTR-Cl:Y6 (1:0:1.6)	0.04	Slot-die	0.849	73.7	27.2	17.0	[217]
D18:BTR-Cl:Y6 (1:0.2:1.6)	0.04	Slot-die	0.858	74.4	26.9	17.2	[217]
D18:Y6	0.04	Slot-die	0.844	73.91	27.37	17.13	[172]
PBDB-T/PYT	0.05	Blade-coating	0.890	73.88	22.95	15.10	[218]

3.4 Conclusion

To summarize, we developed a solubility-tuning strategy via multi-component to manipulate crystallization kinetics and aggregate sizes to achieve well-behaved phase separation in blade-coated blends. By incorporating BTP-4Cl, both ex-situ and in-situ investigations illustrated that the twisted molecular backbone of BTP-4Cl facilitates a dispersed and loose molecular distribution in the ternary solution. This leads to the

formation of dispersed nuclei seeding sites and pre-aggregates, thereby advancing the crystallization process and achieving fine nanoscale phase domains. As a result, the blade-coated small-area OSCs achieved an outstanding PCE of 19.67% (19.76% for SC devices), which is the top-ranking efficiency among reported blade-coated OSCs. Overall, this work gave a new insight into the material selection criteria from the point of solubility control, and established the correlation between solubility, crystallization kinetics, and solid film microstructure, providing valuable guidance for achieving stable and high-performance eco-OSCs via open-air coating.

Chapter 4 Balanced Miscibility and Crystallinity by 2D Acceptors Enabled Halogen-Free Solvent-Processed Organic Solar Cells to Achieve 19.28% Efficiency

4.1 Introduction

OSCs have made great strides in recent years as NFAs have sprung up, especially with the emergence of Y-series acceptors. The modification of chemical structure on active layer materials, including core engineering[155,219,220], alkyl chain tuning[156,221,222], terminal group modification[223,224], asymmetric strategy[225,226], heteroatomic substitution[227,228], and polymerization/oligomerization[54,229,230], together with device engineering, including device structure optimization[149,154,231,232], additive strategy[233,234], interface engineering[44,235,236], and ternary/tandem strategy[37,115,200,237], pushed PCE of OPVs to 20%, demonstrating the huge business prospects of OPVs.

The material properties and morphology controls determined the overall performance of OPVs. On one hand, material development dominated the evolution of OSCs. The prosperity of fullerene derivatives, ADA-type acceptors, Y-series acceptors represented the different stages of OPVs. The un-tunable chemical structure and large energy offset required for charge separation in fullerene-based OSCs limited their further development[238]. While the elongated exciton lifetime in non-fullerene acceptors (NFAs)-based OPVs enabled negligible energy offset between D/A and thus low charge transfer (CT) state[239]. The electronic coupling between CT states and local excited (LE) states thus facilitated the suppression of radiative and non-radiative recombination[240,241]. The V_{OC} value therefore has a leap from fullerene derivatives to NFAs. Compared with ADA-type acceptors, the Y-series acceptors displayed distinctive 3D interpenetrating network crystal structure providing multiple pathways for electron hopping benefited from synergistic H- and J-aggregation together with various

heteroatomic interactions[158,196,242,243]. The distinctive packing ways in Y-series acceptors facilitated their redshifted absorption, optimized morphology, enhanced photocurrent, accompanied with largely suppressed non-radiative recombination loss from the strong electronic coupling between molecules[244], enabling great improvement in fill factor (FF) and photocurrent. Thus, as the performance of OSCs was closely related to material properties, it is of paramount significance to develop new active layer materials with satisfactory physicochemical and photovoltaic properties.

On the other hand, crystallinity and miscibility played a critical role in morphology control. In 2018, the influence of acceptor crystallinity on active layer morphology was deeply investigated, and it was found that the stronger crystalline acceptor IDIC afforded a much higher PCE than its counterpart ITIC due to their distinctive morphology and phase separation difference.[245]. In 2020, 4TIC with a high degree of crystallinity was added to the ZnPTBO:6TIC blend. The enhanced crystallinity optimized charge extraction and recombination by facilitating exciton propagation to D/A interfaces.[246]. The next year, it was reported that a highly crystalline acceptor FCC-Cl with a high absorption coefficient achieved a high EQE of 85% and a high FF of 80%.[247] Recently, the oligomers with high crystallinity were proven to provide nucleation sites for host components to crystalline growth to control the crystallization kinetics during film formation.[55] Additionally, OSCs suffered from lagged open-circuit voltage (V_{OC}), compared to its counterparts, inorganic and hybrid solar cells, originating from large non-radiative recombination loss (ΔE_{nr}) and additional radiative recombination from sub-gap absorption. Given that Urbach energy and energetic disorder played an important role in determining energy loss[248,249], the strong crystallinity of materials has been proven to be conducive to inducing more ordered and compact molecular packing[250,251], thus reducing Urbach energy and energetic disorder raised from the amorphous morphology[252,253]. It was also found that triplet exciton formation was a significant charge recombination loss pathway, and materials with high crystallinity possessed much shorter triplet lifetime than amorphous ones[254,255].

Furthermore, close crystalline packing and strong intermolecular interaction were considered as a factor to induce face-on molecular packing, pure domain purity, efficient charge extraction[256,257], and conducive to stabilized morphology resisting degradation[255].

Extremely strong crystallinity, however, was suspected to self-aggregation, and excessive aggregation was detrimental to OPV performance if there was rough morphology and insufficient D/A interfaces for charge dissociation[199,258]. Different from inorganic and hybrid solar cells, where low exciton binding energy enabled fast and voluminous free carrier generation, the carrier generation mechanism in OPV required sufficient D/A interfaces for charge separation. According to the surface energy, D/A molecules at interfaces were affected by the interaction applied by internal bulk molecules and external hetero-molecules. If the adhesive force from bulk molecules was larger than that applied by external hetero-molecules, the two substances exhibited a repulsive trend to repeal each other, and in the active layer, showed a repulsive tendency between D/A pair and prone to the formation of oversized phase separation. Especially in green solvents for industrialization, where poor solubility of materials would exacerbate excessive aggregation problem[180,259]. The oversized aggregates would cause rough morphologies, non-efficient charge transfer and separation, and severe charge recombination, etc. [260] A dilemma here is that over miscible D/A pair would also be disastrous, as amorphous film damaged the domain purity required by carrier migration[261], and the energetic disorder brought by amorphous film would be severe. Thus, the competitive and restrictive relationship between crystallinity and miscibility is required to be considered carefully to achieve a perfect OPV film morphology when it comes to material design and device fabrication.

Previous work has demonstrated that the 2D expanded central core effectively regulates the molecular aggregation in both polymeric and small molecular acceptors, with acenaphthene expansion showing high crystallinity in small molecular acceptors (SMAs).[258]. Given the limited studies on the crystallinity of 2D materials and their role in regulating morphology as a third component, we designed and synthesized two 2D-

expanded acceptors, ATIC-C11 and ATIC-BO, to thoroughly investigate their physicochemical and photovoltaic properties. The acenaphthene-extended quinoxaline rings in these acceptors promoted high crystallinity, leading to reduced energetic disorder and suppressed recombination loss due to the ordered and compact molecular packing. Their distinct chemical structure induced different intermolecular interactions resulting in unique single crystal structures. Their difference in self-aggregation and compatibility with other active layer components further determined their specific roles in blend films. As a result, the PBQx-TF: ATICC11-based OSCs achieved a PCE of 17.60 % with an impressive V_{OC} of 0.931 V and a FF of 77.27% using the nonhalogenated solvent toluene. By incorporating a guest acceptor, eC9-2Cl, the PBQx-TF: ATIC-C11: eC9-2Cl-based OSCs elevated the PCE up to 19.28% with the V_{OC} of 0.901V. Adjusting the ratio of two acceptors, all the devices showed consistently high FF and PCEs, indicating good compatibility between the two acceptors. The ternary system based on ATIC-BO also delivered a satisfactory PCE of 18.52% with a V_{OC} of 0.916V. To the best of our knowledge, ATIC-C11 ternary devices achieved state-of-the-art performance among nonhalogenated solvent-processed OSCs with high VOC. The charge carrier dynamics, film formation mechanism, and solid film morphology were systematically studied to elucidate the performance of the two ATIC acceptors in collaboration with PBQx-TF and eC9-2Cl. This work provides valuable insight into the relationship between "structure–morphology–property" and offers guidance for material design and selection toward highly efficient and stable halogen-free solvent-processed OSCs.

4.2 Experimental section

4.2.1 Synthesis of ATIC-C11 and ATIC-BO

All reagents and solvents did not conduct further purification and were used directly as received from the merchant.

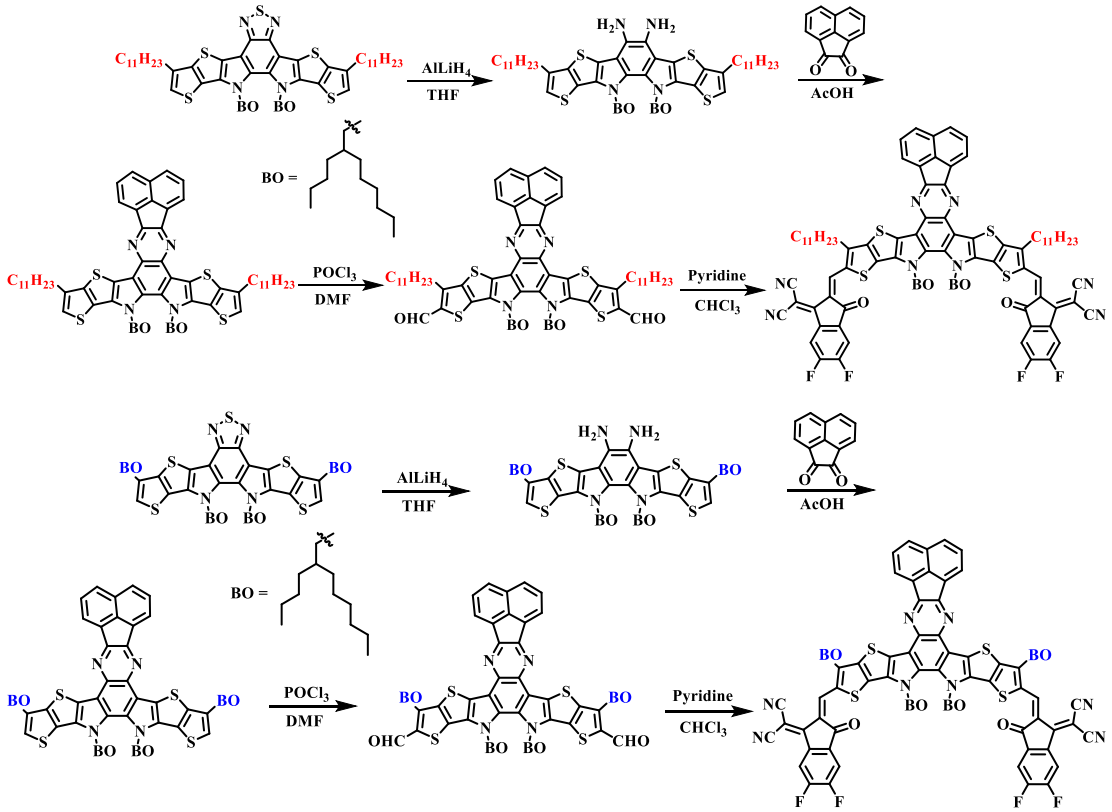

Scheme S1. The synthetic routes of ATIC-C11 and ATIC-BO.

Compound 2: In a 100 mL round-bottom flask, Compound 1 (1.0 g) was dissolved in anhydrous THF (50 mL) under nitrogen atmosphere. To this homogeneous solution maintained at 0°C using an ice-water bath, a 2.5 M aluminum lithium hydride solution (10 mL) was introduced via dropwise addition over 15 minutes. The reaction vessel was subsequently immersed in a preheated oil bath at 80°C and stirred vigorously (800 rpm) under reflux conditions for 12 hours. Following gradual cooling to 25°C, the crude mixture was subjected to liquid-liquid extraction with dichloromethane (3 × 30 mL). The combined organic extracts underwent sequential washing cycles with saturated sodium chloride solution (20 mL) and dehydration through an anhydrous magnesium sulfate bed, producing a crude product suitable for downstream synthetic applications without further purification.

Compound 3: Compound 2 (500 mg) was combined with 20 mL EtOH and 20 mL AcOH in a 100 mL flask, followed by the addition of 1 g phenanthraquinone. The resultant mixture underwent reflux condensation at 100°C for 18 h. Post-reaction

extraction with CH_2Cl_2 afforded the organic layer, which was purified through flash chromatography (gradient elution: CH_2Cl_2/petroleum ether) to yield 450 mg product (78.4% yield).

Compound 4: A chilled solution of $POCl_3$ (1 mL) in DMF (5 mL) was preconditioned at 0°C for 1 h to generate the Vilsmeier reagent. This activated mixture was gradually introduced to a CH_2Cl_2 solution (20 mL) containing Compound 3 (450 mg), maintaining the temperature at 0°C. Subsequent thermal activation at 40°C for 10 h preceded standard workup procedures involving CH_2Cl_2 extraction and chromatographic purification, ultimately delivering 370 mg product (78.9% yield).

Compound ATIC-C11: Compound 4 (100 mg) and 2-(5,6-dichloro-3-oxo-2,3-dihydro-1H-inden-1-ylidene) malononitrile (INCN) (100 mg) were dissolved in $CHCl_3$/pyridine (20 mL/0.5 mL) under an argon atmosphere. After 24 h reflux condensation, the cooled reaction mixture underwent $CHCl_3$ extraction followed by sequential chromatographic purification ($CHCl_3$ mobile phase) and cyclic preparative HPLC, yielding 70 mg target compound (51.8% yield).

Compound 6: In a 100 mL round-bottom flask, Compound 5 (1.0 g) was dissolved in anhydrous THF (50 mL) under nitrogen atmosphere. To this homogeneous solution maintained at 0°C using an ice-water bath, a 2.5 M aluminum lithium hydride solution (10 mL) was introduced via dropwise addition over 15 minutes. The reaction vessel was subsequently immersed in a preheated oil bath at 80°C and stirred vigorously (800 rpm) under reflux conditions for 12 hours. Following gradual cooling to 25°C, the crude mixture was subjected to liquid-liquid extraction with dichloromethane (3 × 30 mL). The combined organic extracts underwent sequential washing cycles with saturated sodium chloride solution (20 mL) and dehydration through an anhydrous magnesium sulfate bed, producing a crude product suitable for downstream synthetic applications without further purification.

Compound 7: Compound 6 (500 mg) was combined with 20 mL EtOH and 20 mL AcOH in a 100 mL flask, followed by the addition of 1 g phenanthraquinone. The resultant mixture underwent reflux condensation at 100°C for 18 h. Post-reaction

extraction with CH_2Cl_2 afforded the organic layer, which was purified through flash chromatography (gradient elution: CH_2Cl_2/petroleum ether) to yield 450 mg product (78.4% yield).

Compound 8: A chilled solution of $POCl_3$ (1 mL) in DMF (5 mL) was preconditioned at 0°C for 1 h to generate the Vilsmeier reagent. This activated mixture was gradually introduced to a CH_2Cl_2 solution (20 mL) containing Compound 7 (450 mg), maintaining the temperature at 0°C. Subsequent thermal activation at 40°C for 10 h preceded standard workup procedures involving CH_2Cl_2 extraction and chromatographic purification, ultimately delivering 370 mg product (78.9% yield).

Compound ATIC-BO: Compound 8 (100 mg) and 2-(5,6-dichloro-3-oxo-2,3-dihydro-1H-inden-1-ylidene)malononitrile (INCN) (100 mg) were dissolved in $CHCl_3$/pyridine (20 mL/0.5 mL) under an argon atmosphere. After 24 h reflux condensation, the cooled reaction mixture underwent $CHCl_3$ extraction followed by sequential chromatographic purification ($CHCl_3$ mobile phase) and cyclic preparative HPLC, yielding 70 mg target compound (51.8% yield).

4.2.2 Device Fabrication

For **spin-coated devices**, organic photovoltaic (OPV) devices were fabricated following a standard structure: ITO/PEDOT: PSS/Active Layer/PDINN/Ag. The glass/ITO substrates underwent sequential cleaning steps: sonication in detergent, deionized water (DI water), acetone, and isopropanol (IPA) (20 minutes per solvent), followed by ultraviolet ozone (UVO) treatment for 20 minutes. A thin layer of PEDOT: PSS was then deposited via spin-coating at 3000 rpm (30 s) onto the pre-treated substrates. The HTL was baked at 150 °C for 15 minutes and then transferred to a nitrogen-filled glovebox. Finally, the photoactive layer was formed by spin-coating an 11 mg/mL toluene-based solution onto the HTL (D: A = 1: 1.2, 5mg/mL TCB, with different weight ratio of eC9-2Cl (0%, 20%, 40%, 60%, 80%, 100% in the acceptor mixture) at 3000 rpm for 60 s, followed by thermal annealing (TA) at 100 ℃ for 5 min. For **blade-coated devices**, PBQx-TF, ATIC-C11, and eC9-2Cl were dissolved at a total

concentration of 11 mg/mL with the optimized ratio of 1: 0.6: 0.6 at 100 °C stirring for 1h. When coating the active layer, the temperature of the bottom plate of doctor-blade equipment is controlled at 60 ℃. A laminar nitrogen knife was positioned adjacent to the substrate surface, with its gas flow oriented at a 20° angle relative to the substrate. The freshly deposited wet active layer underwent rapid solidification via nitrogen-assisted gas quenching, employing a constant flow velocity of 40 m/s (verified via Testo 416 flowmeter calibration) to accelerate solvent evaporation and crystallize the film. An optimal blade coating speed of 33 mm/s was identified for the active layer deposition. Following this, thermal annealing at 100 °C for 5 minutes was applied to the films. For all fabricated devices, a cathode buffer layer consisting of ~5 nm-thick PDINN was solution-processed by spin-coating a methanol-based PDINN solution (1.5 mg/mL). Device completion involved thermal evaporation of a 90 nm-thick silver electrode, defining an active area of 4 mm^2. *J-V* characterization was conducted under simulated AM 1.5G illumination (100 mW cm^{-2}) using an Enlitech SS-F5-3A solar simulator, with light intensity calibrated against an SRC-2020 certified silicon reference cell. Spectral response measurements for external quantum efficiency (EQE) were acquired through an Enlitech RE-R specialized spectral-response analysis system.

4.2.3 Characterization and measurement

^{1}H NMR spectra were conducted on a Bruker AV-400 instrument (400 MHz) using deuterated chloroform ($CDCl_3$) as the solvent, with tetramethylsilane (TMS) employed as the internal reference.

Preparative high-performance liquid chromatography A JAI LC-9104 recycling prep-HPLC system was utilized, operating with chloroform as the mobile phase.

Crystal growth: diffraction quality crystals were grown by solvent diffusion method. Acceptors (5 mg) was dissolved in CH_2Br_2 or $CHCl_3$ or toluene (5 mL) in the 15 mL sample bottle, then 10 mL of ethanol or methanol or ether was added it slowly. The bottle was then sealed tightly, and left undisturbed for 10 days[3].

Crystallography: The single crystal X-ray diffraction (SCXRD) data were collected at 100K or 150K on a Bruker D8 VENTURE diffractometer using Cu Kα radiation (λ = 1.54178 Å) or Ga Kα radiation (λ = 1.34139 Å). Lorentz/polarization corrections were applied during data reduction and the structures were solved by the direct method (SHELXT). Refinements were performed by using full-matrix least squares (SHELXL-2014) on F^2 in the Olex2 program.[4] Severe disorder problems were encountered during all the refinements, and considerable amounts of constrains and restrains such as DFIX, SADI, SIMU, AFXI and DANG were used when necessary. Anisotropic thermal parameters were applied to most of the non-hydrogen atoms. Hydrogen atoms were added geometrically and refined using a riding model where possible. The severe disorder of the long and bulky alkyl chains hindered us to collect diffraction data with a satisfactory resolution.

Ultraviolet photoelectron spectroscopy (UPS) was applied to determine energy levels of materials. The HOMO energy level was determined by the cut-off line and the fermi energy level, and the LUMO energy level was determined according to the optical bandgap from UV-vis absorption.

FTPS-EQE was acquired using an integrated PECT600 system (Enlitech), incorporating lock-in amplification for photocurrent signal modulation. Electroluminescence quantum efficiency (EQEEL) assessments employed an ELCT3010 instrument (Enlitech) to apply controlled voltage/current biases across the devices. E_{loss} values were calculated according to previously established protocols.[233]. The energy loss was described by three parts, $\Delta E = \Delta E_1 + \Delta E_2 + \Delta E_3$, where ΔE_1 referred to the radiative recombination above the bandgap. The theoretical limits (Shockley-Queisser (SQ) limit) as a function of bandgap was applied for any type of single junction solar cells. ΔE_2 was the radiative recombination below the bandgap. As the room temperature blackbody radiation is strong at low-energy region, any sub-gap absorption would cause large radiative loss[21]. ΔE_3 comes from the non-radiative recombination and was calculated by $\Delta E_3 = -kT \ln EQE_{EL}$. The arise of ΔE_3 was the electron-phonon coupling from molecular vibration, and energy dissipated by thermal

emission. Urbach energy was calculated by $1/k_{slope}$, where k_{slope} was obtained by fitting the band tail of FTPS-EQE.

Transient absorption spectroscopy (TAS) was measured with an amplified Ti:sapphire femtosecond laser (800 nm wavelength, 50 fs, 1 kHz repetition; Coherent Libra) and a Helios pump/probe setup (Ultrafast Systems).

Transient photocurrent (TPC) and transient photovoltage (TPV) were performed with a Paios 4.0 measurement instrument (FLUXiM AG, Switzerland). The carrier lifetime (τ) and sweeping out times (t_s) were obtained by fitting TPC/TPV curves with a mono-exponential decay function.

Space-charge limited current (SCLC) Hole and electron mobilities in pristine and blend films were evaluated via SCLC methodology. Hole mobility employed the structure of ITO/PEDOT: PSS/Active Layer/Au, and electron mobility adopted the structure of ITO/ZnO/Active Layer/Ag, maintaining active layer thicknesses consistent with photovoltaic devices. Dark current-voltage characteristics were fitted to the Mott-Gurney law (Equation 1-31), where $V = V_{app} - V_{bi}$ accounts for electrode work function differences. Mobility values were extracted from the linear regime of $J^{1/2} \sim V$ plots.

Contact angle measurements were determined via sessile drop measurements using deionized water and ethylene glycol. Surface tension components were derived through the two-solvent (H_2O/EG) Owens-Wendt approximation method. The donor-acceptor interfacial energy ($\gamma_{D/A}$) and Flory-Huggins interaction parameter ($\chi_{D/A}$) were evaluated by Equations 1-32 and 1-33, respectively. γ is the surface energy of the corresponding material; γ^d, γ^p are the dispersive and polar components of γ, respectively; K is a constant. The wetting coefficient (ω) was calculated by the equation: $\omega_{A_2} = (\gamma_{A_1/A_2} - \gamma_{D/A_2})/\gamma_{D/A_1}$ to confirm the position of the third component in the ternary blend. For $\omega_{A_2} < -1$, the third component is in the host acceptor (A_1)'s domain; for $-1 < \omega_{A_2} < 1$, the third acceptor is at the interface of donor and the host acceptor (D and A_1); for $\omega_{A_2} > -1$, the third component is in the host donor (D)'s domain.

In-situ UV–vis spectra Real-time UV-vis spectral data were recorded on an F20 spectrometer (Filmetrics, Inc.) equipped with a halogen light source (1.5 mm spot

diameter). To isolate the absorption/reflection contributions from the active layer, measurements were referenced against an ITO/PEDOT: PSS-coated glass substrate. Spin-coating parameters matched those employed in device fabrication to ensure process consistency.

Atomic force microscopy (AFM) was probed via Bruker Dimension EDGE in amplitude-modulated tapping mode.

Transmission electron microscopy (TEM) was resolved through transmission electron microscopy using a Hitachi H-7650 instrument operated at 100 kV accelerating potential.

4.3 Result & Discussion

4.3.1 Material Synthesis and Single Crystal Structure

The synthetic route and chemical structure of ATIC-C11 and ATIC-BO are provided in Figure 4. 1**a**. The synthesis of acenaphtho[1,2-b]dipyrrolo[3,2-f:2',3'-h]quinoxaline central core was first to reduce benzothiadiazole, and then a cyclization reaction between two amino groups and acenaphthoquinone, followed with the Knoevenagel reaction to get the final product. A detailed description was provided in the experimental section. The energy levels of these materials were determined by ultraviolet photoelectron spectroscopy (UPS) and Ultraviolet-Visible (UV-vis) Spectroscopy (Figure 4. 2-Figure 4. 5). ATIC-BO afforded deeper ionization energy (IE) and hyperchromic absorption. The reorganization energy was estimated by stokes shifts (Figure 4. 6). ATIC acceptors afforded smaller stokes shifts compared with benzothiadiazole-based acceptors, which was expected to give a smaller recombination loss. Therefore, a higher VOC was expected in the ATIC acceptors-based devices.

The single crystal structure of the two molecules was obtained to get a deep insight into their molecular packing patterns in the solid state. Surprisingly, ATIC-C11 with a straight alkyl chain (*n*-$C_{11}H_{23}$) gave a relatively twisted molecular backbone with a dihedral angle of 3.09°, while ATIC-BO with a bulky and branch side chain (butyl octane) showed a highly planar configuration with the dihedral angle of 0.51° (Figure

4. 1b). The synergistic H- and J-aggregation were detected in both acceptors from their molecular packing patterns (Figure 4. 1c). In ATIC-C11, two packing modes were detected, core to terminal group (CT) and terminal group to terminal group (TT), with the π-π distance of 3.36 and 3.38 Å, respectively, which was closer than the common benzothiadiazole-based acceptors.[196] In ATIC-BO, three packing modes were found, CT-1 and TT aggregates, along with CT-2 packing where a tilt angle existed between two molecules. It should be noted that ATIC-BO's planar conformation and shorter π-π distance implied its higher crystallinity. As a result, the difference in structures and their distinct packing modes enabled their unique 3D network crystal structure (Figure 4. 1d). ATIC-C11 formed an elliptical framework with the size of 14.4 Å (L_x) and 18.7 Å (L_y), while ATIC-BO displayed a rectangular framework of 12.3 Å (Lx) and 20.0 Å (Ly). The periodic molecular distance was found in single crystal, 20.11 Å for ATIC-C11 and 20.77/15.43 Å for ATIC-BO, in accordance with the lamellar stacking in thin-film GIWAXS, 18.48 Å for ATIC-C11 and 21.67/15.71 Å for ATIC-BO (Figure 4. 1f), indicating that the crystal structure partially preserved in thin-film state. In OOP direction, ATIC-C11 and ATIC-BO gave the characteristic peak at q_z = 0.42 $Å^{-1}$ and 0.55 $Å^{-1}$, respectively. The (010) peak was extracted, where ATIC-C11 gave a π-π stacking peak at 1.76 $Å^{-1}$ with the CCLs of 17.14 Å, and ATIC-BO presented a π-π peak at 1.85 $Å^{-1}$ with the CCLs of 29.76 Å. Compared with the benzothiadiazole-based eC9-2Cl neat film, the much shorter *d*-spacing and larger CCL value of ATIC acceptors indicated the higher crystallinity of the acenaphthene extended 2D acceptors. To further demonstrate the crystalline property of ATIC acceptors, the thin-film X-ray diffraction (XRD) measurement was conducted and shown in Figure 4. 7, where both ATIC-C11 and ATIC-BO exhibited distinctive diffraction peaks, while no obvious peak was found in the benzothiadiazole-based acceptor, indicating the much higher crystallinity of the acenaphthene-extended quinoxaline-based 2D acceptors.

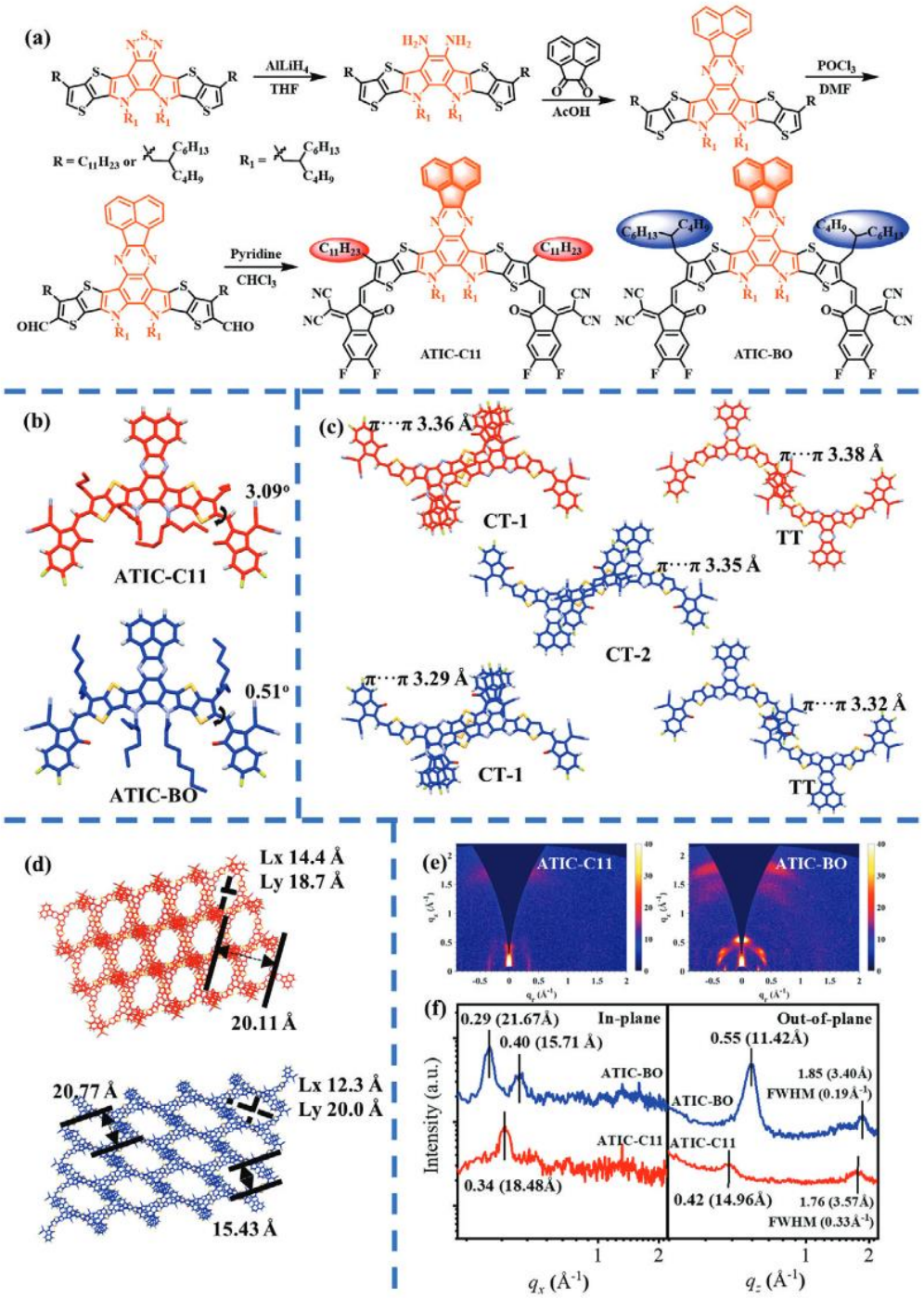

Figure 4. 1 The synthetic routes and molecular packing in single crystal and thin-film. a) The synthetic route of ATIC-C11 and ATIC-BO. b) The dihedral angle of ATIC-C11 and ATIC-BO from the single crystal. c) The single crystal packing arrangement and d) the 3D network structure and periodic distance of ATIC-C11 (red) and ATIC-BO (blue). e) 2D GIWAXS patterns and f) 1D GIWAXS line cut profiles of ATIC-C11 and ATIC-BO neat film.

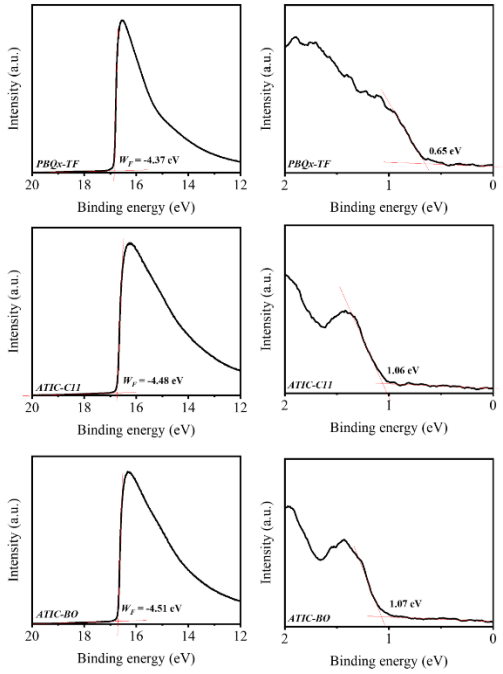

Figure 4. 2 (Left) Photoemission cutoff spectra and (Right) Valence band (VB) structure of PBQx-TF, ATIC-C11, ATIC-BO. a.u., arbitrary units.

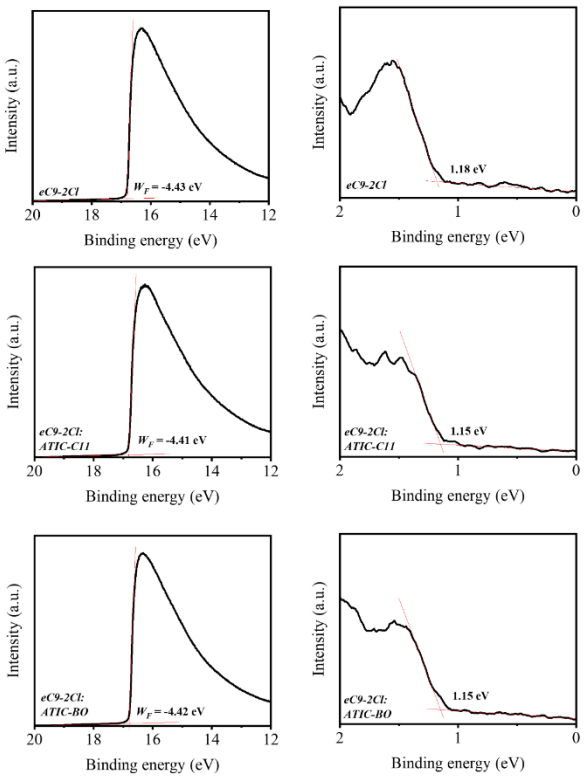

Figure 4. 3 (Left) Photoemission cutoff spectra and (Right) Valence band (VB) structure of eC9-2Cl, eC9-2Cl: ATIC-C11, eC9-2Cl: ATIC-BO. a.u., arbitrary units.

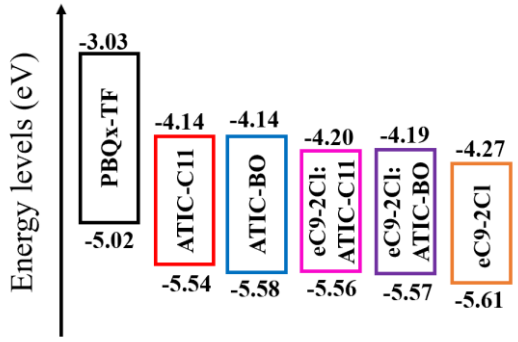

Figure 4. 4 The energy level of PBQx-TF, ATIC-C11, ATIC-BO, eC9-2Cl, eC9-2Cl: ATIC-C11 (1: 1), and eC9-2Cl: ATIC-BO (1: 1).

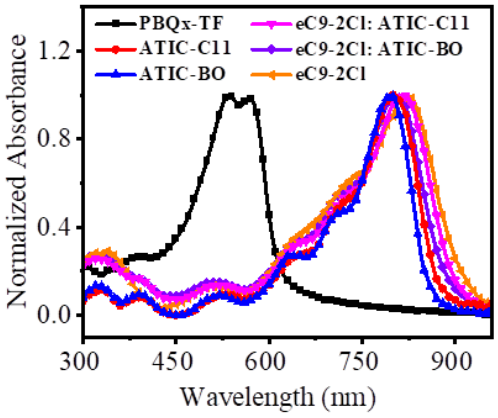

Figure 4. 5 The UV-vis absorption profiles of PBQx-TF, ATIC-C11, ATIC-BO, eC9-2Cl: ATIC-C11 (1: 1), and eC9-2Cl: ATIC-BO (1: 1).

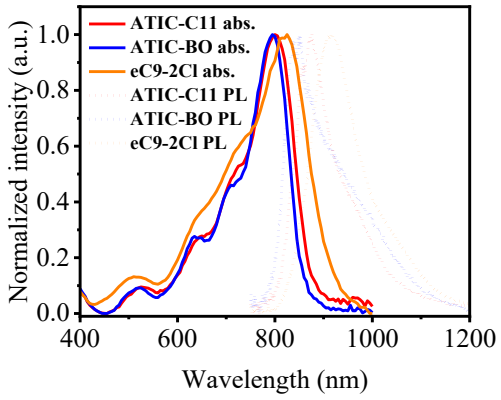

Figure 4. 6 The UV-vis absorption profiles and photoluminescence (PL) (excited at 730 nm) profiles of ATIC-C11, ATIC-BO, eC9-2Cl.

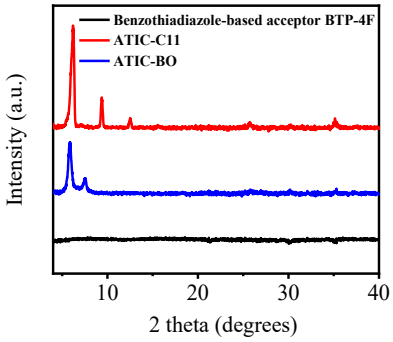

Figure 4. 7 The XRD spectra of benzothiadiazole-based acceptor BTP-4F, ATIC-C11, and ATIC-BO.

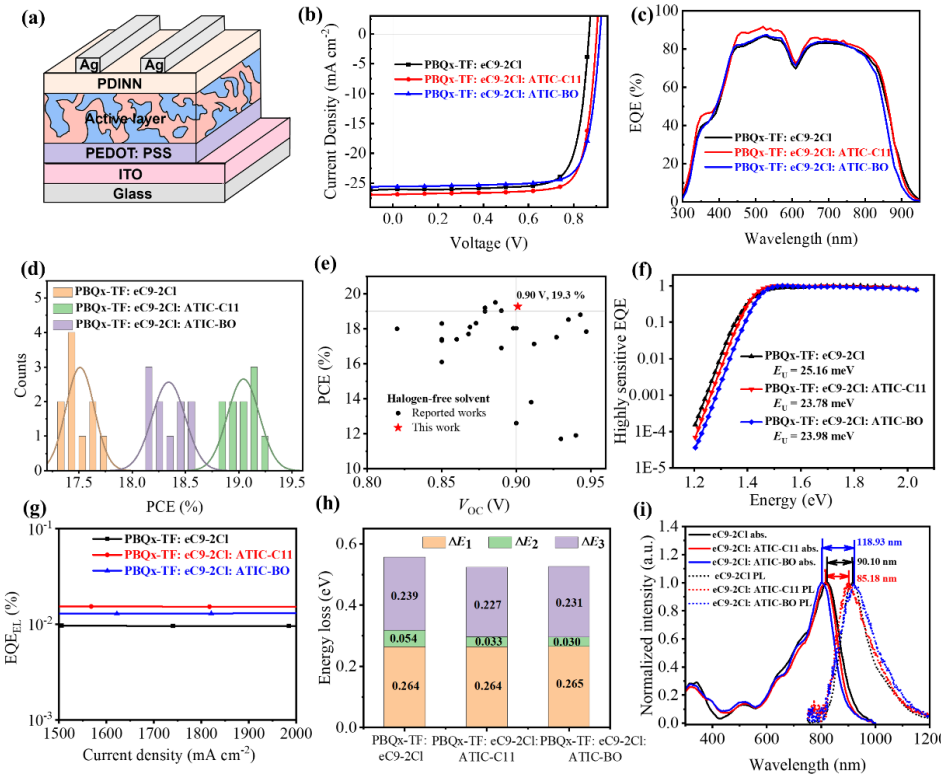

Figure 4. 8 Photovoltaic properties and energy loss analysis. a) Device architecture schematic diagram. b) *J-V*, c) EQE curves, and d) Histogram for PBQx-TF: eC9-2Cl, PBQx-TF: eC9-2Cl: ATIC-C11, and PBQx-TF: eC9-2Cl: ATIC-BO devices. e) Non-halogen solvents processed OSCs extracted from the literature. f) FTPS-EQEs and g) EQE_{EL}s for the corresponding binary and ternary devices. h) The histograms of ΔE_1, ΔE_2 and ΔE_3 for corresponding devices. i) Normalized absorption (abs.) and photoluminescence (PL) emission spectra of eC9-2Cl, eC9-2Cl: ATIC-C11, eC9-2Cl: ATIC-BO in the film (excited at 730 nm).

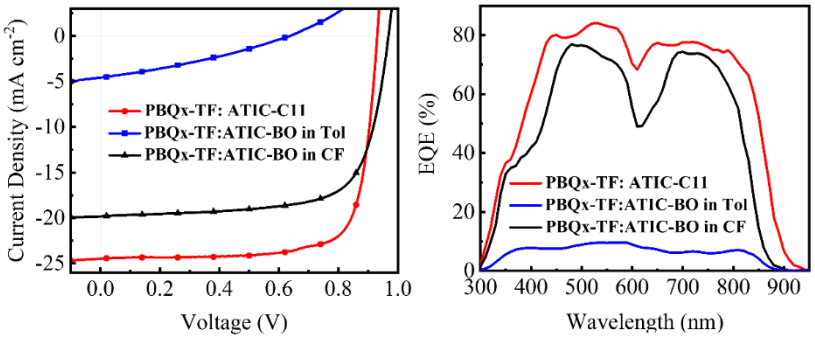

Figure 4. 9 The *J-V* and EQE curves for ATIC-C11 and ATIC-BO binary devices.

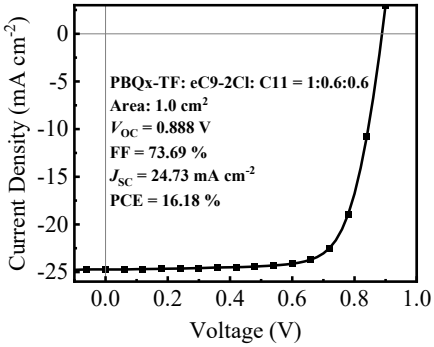

Figure 4. 10 *J-V* curve for optimized PBQx-TF: eC9-2Cl: ATIC-C11-based scale-up devices (1cm^2).

4.3.2 Device Performance and Energy Loss Analysis

The photovoltaic properties of two acceptors were studied by blending with the donor PBQx-TF with a conventional device structure (Figure 4. 8a). Detailed procedure was provided in the supplemental information. ATIC-C11-based devices showed a much higher PCE of 17.60% with a high V_{OC} of 0.931 V, a FF of 77.27%, and a J_{SC} of 24.46 mA cm^{-2}, while due to the poor solubility of ATIC-BO in non-halogenated solvent, the efficiency of ATIC-BO was lagged much behind (0.92%) (Figure 4. 9). By changing the solvent from toluene to chloroform, the efficiency improved to 13.62% with a high V_{OC} of 0.97 V (Table 4. 1). To expand the application of ATIC acceptors and further investigate their collaboration with other acceptors, an assisted acceptor eC9-2Cl was introduced. The acceptor ratio was tuned and all ratios displayed outstanding FFs and PCEs in ATIC-C11-based devices (Table 4. 2), implying a good accordance between

the two acceptors. However, with the ratio of ATIC-BO rising, the solubility problem limited its device performance (

Table 4. 3). Finally, with the optimized ratio of 1: 0.6: 0.6, the ternary devices of PBQx-TF: eC9-2Cl: ATIC-C11 achieved a high PCE of 19.28%, along with a V_{OC} of 0.901 V, a FF of 79.62%, and a J_{SC} of 26.87 mA cm^{-2}. The ternary devices based on ATIC-BO had a greater effect on V_{OC} (0.916 V), affording a satisfactory PCE of 18.52%. It should be noted that the efficiency of ATIC-C11-based OSCs ranks in the top list among green-solvent processed OSCs (Figure 4. 8e and Table 4. 4). The active layer of PBQx-TF: ATIC-C11: eC9-2Cl was applied to fabricate the scale-up devices (1cm^2), and a PCE of 16.18% was obtained (Figure 4. 10). Additionally, their storage stability, light stability, and thermal stability were tested to demonstrate their operation lifetime in various ambient (Figure 4. 11Figure 4. 13). The devices maintained 88% of their initial PCE at 2500 h for storage, and the T_{80} lifetime was 400 h for light soaking, and 350 h in a harsh environment (heat at 70°C), suggesting its industrial application prospects.

Table 4. 1 The photovoltaic parameters of the corresponding binary and ternary devices.

Active Layer	V_{OC} (V)	FF (%)	J_{SC} (mA cm^{-2})	PCE (%)	J_{SC}^{cal} (mA cm^{-2})
PBQx-TF: ATIC-C11	0.931	77.27	24.46	17.60 (17.32 ± 0.17)	23.65
PBQx-TF: ATIC-BO[a]	0.637	31.29	4.59	0.92	/
PBQx-TF: ATIC-BO[b]	0.969	70.91	19.82	13.62 (13.47 ± 0.11)	19.17
PBQx-TF: eC9-2Cl	0.868	78.47	26.02	17.72 (17.51 ± 0.13)	25.06
PBQx-TF: eC9-2Cl: ATIC-C11	0.901	79.62	26.87	19.28 (19.04 ± 0.15)	25.99
PBQx-TF: eC9-2Cl: ATIC-BO	0.916	79.11	25.56	18.52 (18.34 ± 0.16)	24.68

[a)] Processed from toluene.

[b)] Processed from chloroform.

Table 4. 2 The PV parameters of PBQx-TF: eC9-2Cl: ATIC-C11 ternary devices with different acceptor ratios.

PBQx-TF: eC9-2Cl: ATIC-C11	V_{OC} **(V)**	**FF (%)**	J_{SC} **(mA cm^{-2})**	**PCE (%)**
1:1.2:0	0.868	78.47	26.02	17.72
1:1.0:0.2	0.879	78.69	26.44	18.29
1:0.8:0.4	0.885	79.55	26.69	18.79
1:0.6:0.6	0.901	79.62	26.87	19.28
1:0.4:0.8	0.906	79.43	26.10	18.78
1:0.2:1.0	0.914	78.84	25.35	18.27
1:0:1.2	0.932	76.66	24.56	17.55

Table 4. 3 The PV of PBQx-TF: eC9-2Cl: ATIC-BO ternary devices with different acceptor ratios.

PBQx-TF: eC9-2Cl: ATIC-BO	V_{OC} **(V)**	**FF (%)**	J_{SC} **(mA cm^{-2})**	**PCE (%)**
1:1.2:0	0.868	78.47	26.02	17.72
1:1.1:0.1	0.879	78.58	26.06	18.00
1:1.0:0.2	0.887	78.79	25.91	18.11
1:0.8:0.4	0.899	79.18	25.72	18.31
1:0.6:0.6	0.914	78.66	25.85	18.59
1:0.4:0.8	0.918	64.20	23.28	13.72
1:0.2:1.0	0.900	45.64	14.57	5.98
1:0:1.2	0.637	31.29	4.59	0.92

Table 4. 4 Representative halogen-free processed OSC devices from literature.

Active Layer	Solvent	Additive	V_{OC} (V)	FF (%)	J_{SC} (mA cm^{-2})	PCE (%)	References
D18-Cl: L8-BO-X	Tol	DTT	0.89	79.6	26.78	19.04	[262]
D18-Cl:L8-BO	Tol	DTT	0.90	76.3	26.37	18.03	[262]
PBQx-TF: eC9-2Cl: F-BTA3	Tol	DIO	0.879	80.9	26.7	19.0	[161]
PBQx-TF: eC9-2Cl	Tol	DIO	0.868	78.6	25.9	17.7	[161]
PBQx-TF: F-BTA3	Tol	DIO	1.15	75.6	13.2	11.5	[161]
PBQx-TCl: PBDB-TF: eC9-2Cl	Tol	DIO	0.886	81.14	26.83	19.51	[115]
PBQx-TCl: eC9-2Cl	Tol	DIO	0.873	79.94	26.27	18.32	[115]
PBDB-TF: eC9-2Cl	Tol	DIO	0.898	76.29	26.31	18.03	[115]
PBQx-TF: eC9-2Cl	Tol	DCBB	0.879	80.4	27.2	19.2	[234]
PBQx-TF: eC9-2Cl	Tol	DIO	0.869	78.4	26.6	18.1	[234]
PBQx-TF: eC9-2Cl	Tol	/	0.890	73.1	25.9	16.9	[234]
PBDB-T-b-PYT	o-XY	CN	0.90	68.5	20.6	12.6	[263]
TPD-3F:IT-4F	o-XY	DIO	0.91	73.8	20.5	13.8	[264]
PM7:IT-4F	CS2	/	0.93	73.4	17.1	11.7	[265]
PM6:BO-4Cl:Y6-1O	o-XY	/	0.85	80.0	26.8	18.3	[266]
PTzBI-dF:CH1007:PC71BM	o-XY: TMB	/	0.82	77.8	28.2	18.0	[267]
PM6:BTP-BO-4Cl	Tol	BV	0.85	77.7	26.10	17.33	[268]
PM6:Y6:BTO:PC71BM	PX	CN	0.85	75.8	27.1	17.4	[180]
PM6:A-2ThCl:A-4Cl:PC71BM	Tol	DIO	0.86	77.0	26.3	17.4	[269]
PM6:YSe-C6	o-XY	/	0.85	73.0	25.9	16.1	[270]
PM6: PTer-N25	o-XY	2-MN	0.94	65.1	19.5	11.9	[271]
PBQx-TCl: PY-IT	Tol	CN	0.947	77.9	24.18	17.84	[46]
PBQx-TCl:PY-IT:PY-IV (1:1:0.2)	Tol	CN	0.943	79	25.25	18.81	[46]

PBQx-TCl:PY-IT:PY-IV (1:0.8:0.4)	Tol	CN	0.935	78.4	25.28	18.53	[46]
PBQx-TCl:PY-IT:PY-IV (1:0.4:0.8)	Tol	CN	0.927	77.6	24.35	17.52	[46]
PBQx-TCl: PY-IV	Tol	CN	0.912	77.1	24.36	17.13	[46]
PBQx-TF: ATIC-C11	Tol	TCB	0.931	77.27	24.46	17.60	This work
PBQx-TF: eC9-2Cl: ATIC-C11	Tol	TCB	0.901	79.62	26.87	19.28	This work
PBQx-TF: eC9-2Cl: ATIC-BO	Tol	TCB	0.916	79.11	25.56	18.52	This work

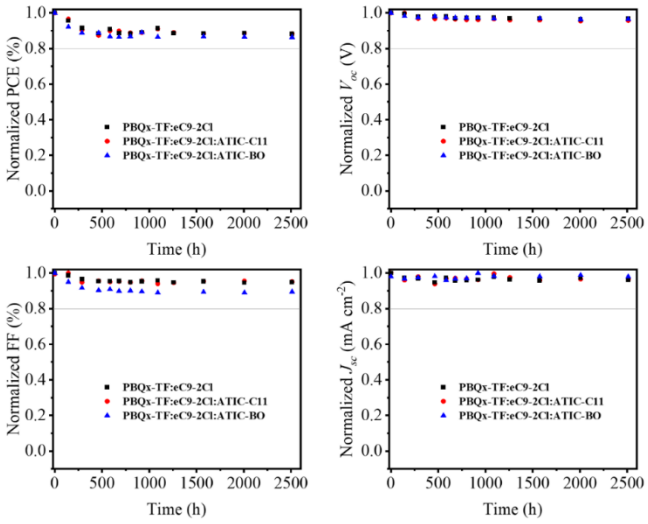

Figure 4. 11 The storage stability of corresponding devices.

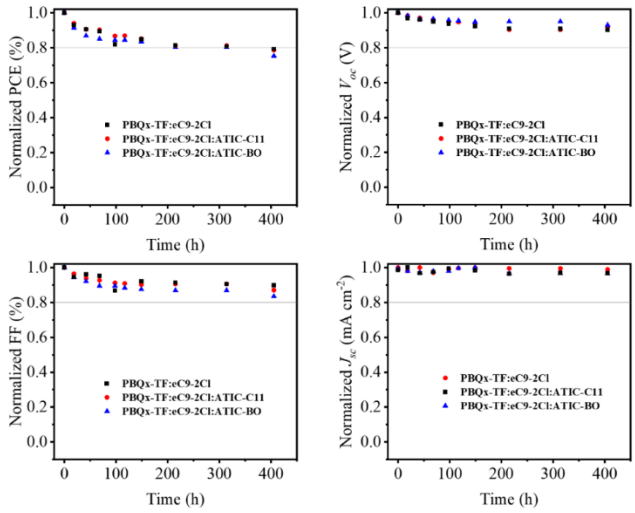

Figure 4. 12 The light-soaking stability of corresponding devices.

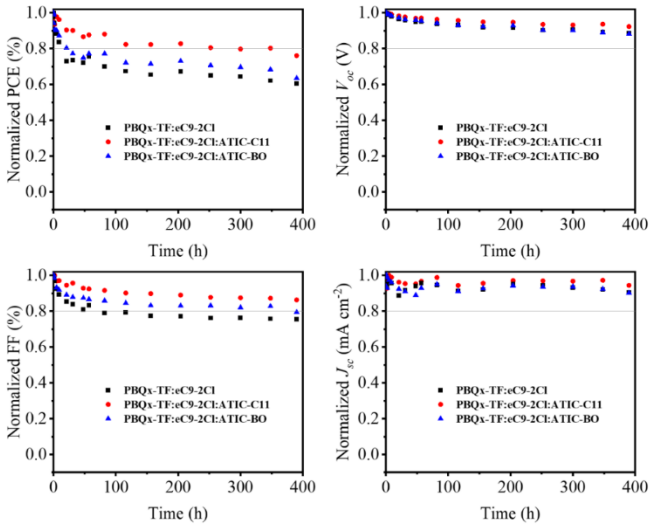

Figure 4. 13 The thermal stability of corresponding devices.

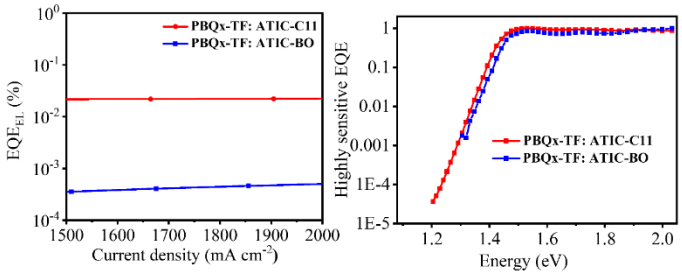

Figure 4. 14 Highly sensitive EQEs and EQE_{EL}s for ATIC-C11 and ATIC-BO (Toluene) binary devices.

Table 4. 5 Energy loss parameters of corresponding devices.

Active Layer	band gap (eV)	qV_{OC} (eV)	ΔE (eV)	ΔE_1 (eV)	ΔE_2 (eV)	ΔE_3 (eV)	E_U (meV)	$\Delta\lambda$ (nm)
PBQx-TF: ATIC-C11	1.442	0.932	0.510	0.265	0.027	0.218	23.55	73.51
PBQx-TF: ATIC-BO[a]	1.494	0.637	0.857	0.269	0.266	0.322	28.60	41.04
PBQx-TF: eC9-2Cl	1.425	0.868	0.557	0.264	0.054	0.239	25.16	90.10
PBQx-TF: eC9-2Cl: ATIC-C11	1.425	0.901	0.524	0.264	0.033	0.227	23.78	85.18
PBQx-TF: eC9-2Cl: ATIC-BO	1.442	0.916	0.526	0.265	0.030	0.231	23.98	118.93

[a)] Processed from toluene.

The energy loss was analyzed by FTPS-EQE and EQE_{EL} to reveal the high V_{OC} obtained by ATIC acceptors. The energy loss was described by three parts, $\Delta E = \Delta E_1 + \Delta E_2 + \Delta E_3$, where ΔE_1 referred to the radiative recombination above the bandgap. The theoretical limit (Shockley-Queisser (SQ) limit) as a function of bandgap was applied for any type of single junction solar cells. ΔE_2 was the radiative recombination below the bandgap. As the room temperature blackbody radiation is strong at the low-energy region, any sub-gap absorption would cause large radiative loss. ΔE_3 comes from the non-radiative recombination and was calculated by $\Delta E_3 = -kT \ln EQE_{EL}$. The rise of ΔE_3 was the electron-phonon coupling from molecular vibration, and energy dissipated by thermal emission. The bandgap of PBQx-TF: ATIC-C11 and PBQx-TF: ATIC-BO devices were 1.442 and 1.494 eV, respectively, corresponding to the ΔE_1 of 0.265 and 0.269 eV. The ΔE_2 and ΔE_3 of ATIC-BO (0.266 eV and 0.322 eV) were much higher than that of ATIC-C11 (0.027 eV and 0.218 eV) ascribed to its insolubility (Figure 4. 14). In ternary devices, the participation of eC9-2Cl reduced the bandgap to 1.425 eV and 1.442 eV for ATIC-C11 and ATIC-BO ternary devices, respectively. The ΔE_2 was determined to be 0.033 eV and 0.030 eV for ATIC-C11 and ATIC-BO-based devices, and the EQE_{EL} was measured to be 1.539×10^{-4} and 1.299×10^{-4}, corresponding to the ΔE_3 value of 0.227 eV and 0.231 eV for PBQx-TF: ATIC-C11: eC9-2Cl and PBQx-TF: ATIC-BO: eC9-2Cl, respectively (Figure 4. 8g). The total energy loss was calculated to be 0.524 eV and 0.526 eV for ATIC-C11 and ATIC-BO ternary devices, respectively, while that for PBQx-TF: eC9-2Cl devices was 0.557 eV (Table 4. 5), indicating that ATIC acceptors were conducive to suppressing recombination loss. By calculating reorganization energy ($\Delta\lambda$) and Urbach energy (E_U), it was found that ATIC acceptors showed a very low energetic disorder. ATIC-BO neat film displayed much smaller $\Delta\lambda$ than ATIC-C11 profiting from its higher crystallinity, while ATIC-BO afforded a much higher energetic disorder in blend films ascribed to its inferior film morphology in lateral analysis. As a comparison, ATIC-C11 effectively reduced $\Delta\lambda$ and E_U in PBQx-TF: eC9-2Cl film, where $\Delta\lambda$ decreased from 90.10 nm to 85.18 nm and E_U declined from 25.16 meV to 23.78 meV.

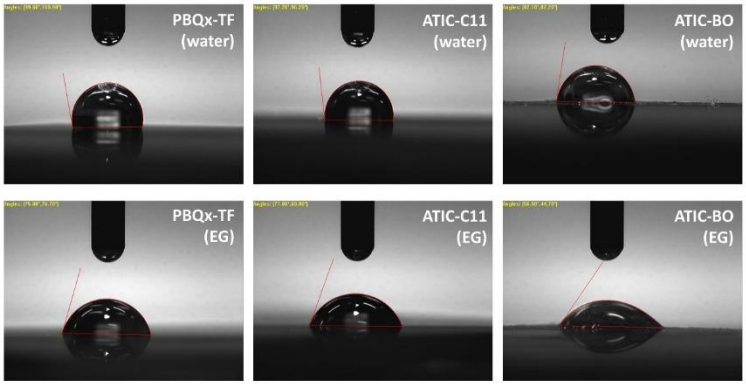

Figure 4. 15 Contact angle measurement of PBQx-TF, ATIC-C11, and ATIC-BO neat film.

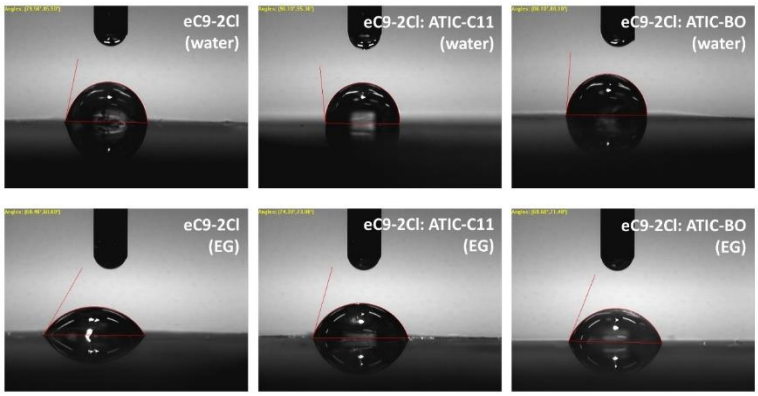

Figure 4. 16 Contact angle measurement of eC9-2Cl, eC9-2Cl: ATIC-C11, and eC9-2Cl: ATIC-BO film.

Table 4. 6 Contact angle parameters and surface energy of materials.

Materials	**WCA** [°]	**EgCA** [°]	γ^d [mN m^{-1}]	γ^p [mN m^{-1}]	γ [mN m^{-1}]
PBQx-TF	100.25	75.85	20.95	1.43	22.38
ATIC-C11	93.50	69.60	20.59	3.31	23.90
ATIC-BO	82.15	50.60	30.41	4.79	35.20
eC9-2Cl	82.50	60.50	17.81	9.02	26.83
eC9-2Cl: ATIC-C11	95.70	73.65	17.96	3.31	21.27
eC9-2Cl: ATIC-BO	87.10	70.50	11.69	9.73	21.42

Table 4. 7 Interfacial tension (γ), χ, and wetting coefficient (*ω*) of materials, Donor: PBQx-TF.

Materials	$\gamma_{D\text{-}A}$ **[mN m^{-1}]**	$\chi_{D\text{-}A}$**/K** [a]	$\gamma_{A1\text{-}A2}$ **[mN m^{-1}]**	$\chi_{A1\text{-}A2}$**/K**	***ω***
ATIC-C11	0.75	0.02	/	/	/
ATIC-BO	3.56	1.45	/	/	/
eC9-2Cl	5.77	0.20	/	/	/
eC9-2Cl: ATIC-C11	0.98	0.01	2.85	0.08	0.04
eC9-2Cl: ATIC-BO	8.80	0.01	4.59	0.57	0.91

[a] K is a constant.

4.3.3 Film Morphology

As stated, ATIC acceptors showed high crystallinity, especially ATIC-BO with a distinct self-aggregation tendency. Another factor determining morphological quality is compatibility between active layer components. The contact angle (CA) measurement was used to investigate the miscibility between active layer components (Figure 4. 15 and Figure 4. 16). The surface energies were determined to be 22.38 mN m^{-1}, 23.90 mN m^{-1}, 35.20 mN m^{-1}, and 26.83 mN m^{-1} for PBQx-TF, ATIC-C11, ATIC-BO, and eC9-2Cl (Table 4. 6), respectively. ATIC-C11 neat film showed comparable surface energy with PBQx-TF film, indicating their good compatibility. $\gamma_{D/A}$ and $\chi_{D/A}$ were to evaluate their miscibility (Table 4. 7). The smaller the γ and χ values, the better the miscibility between components. It was found that with the introduction of ATIC-C11, both γ and χ effectively reduced from eC9-2Cl neat film to eC9-2Cl: ATIC-C11 film (Figure 4. 17a), where γ value reduced from 5.77 mN m^{-1} to 0.98 mN m^{-1} and χ value reduced from 0.20K to 0.01K, indicating that ATIC-C11 was conducive to the improvement of miscibility between PBQx-TF and eC9-2Cl, while in eC9-2Cl: ATIC-BO film, γ enlarged to 8.80 mN m^{-1}. The γ and χ between acceptors were also calculated, and ATIC-C11 presented much smaller $\gamma_{A1/A2}$ and $\chi_{A1/A2}$ values, indicating the better compatibility between ATIC-C11 and eC9-2Cl. *ω* was employed to determine the position of the 3rd component in the system. $\omega_{ATIC\text{-}C11}$ and $\omega_{ATIC\text{-}BO}$ were calculated to be 0.04 and 0.91, respectively, which represented ATIC acceptors tend to be at the

interface of PBQx-TF and eC9-2Cl and underwent the parallel-like model[114], where ATIC series offered an extra charge separation and transport channel, facilitating the exciton separation and carrier transport.

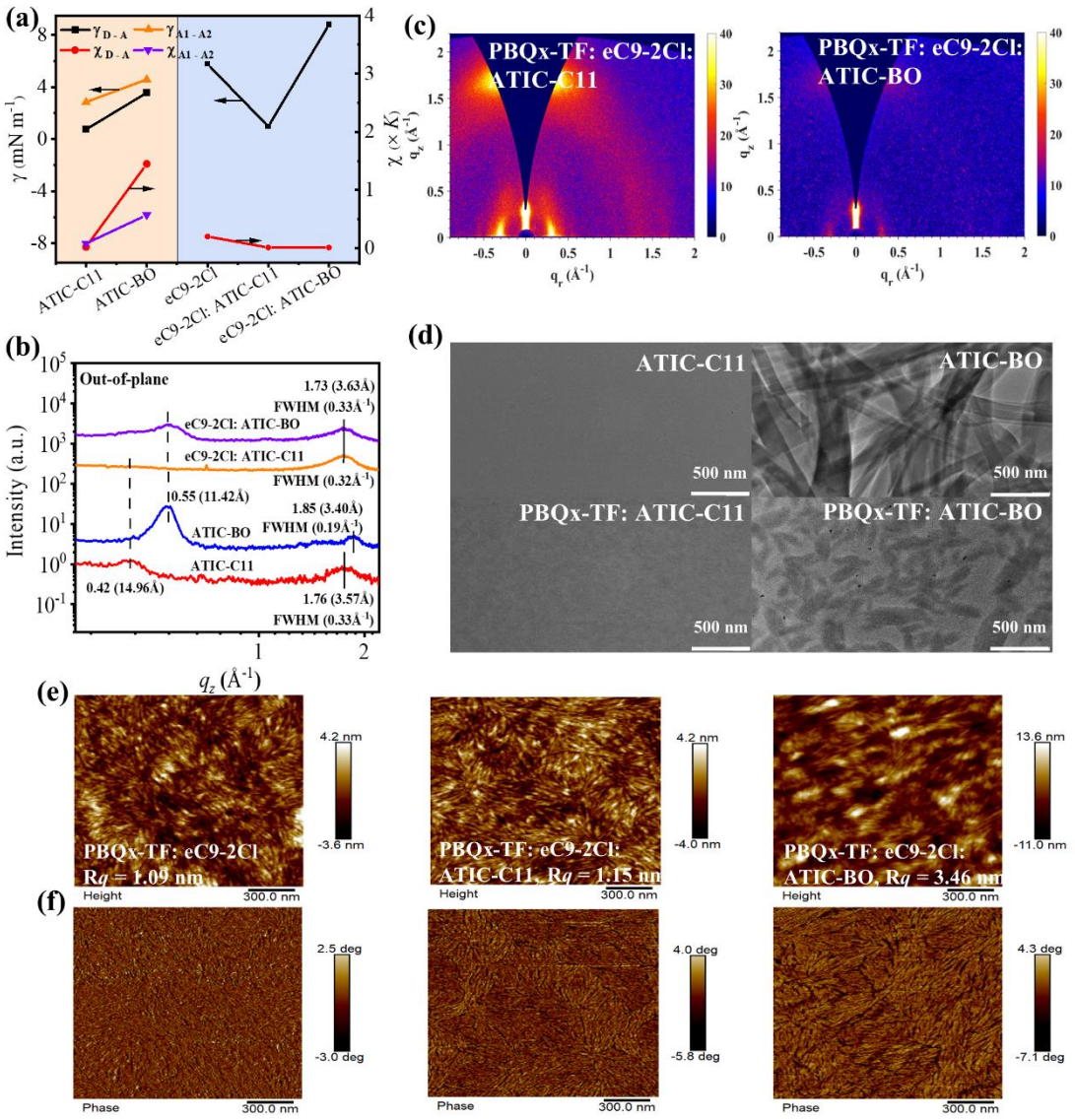

Figure 4. 17 Film morphology study on corresponding binary and ternary systems. a) The interfacial energy (γ) and Flory-Huggins parameter (χ) between D/A and A1/A2. b) The line cut profiles of ATIC-C11, ATIC-BO, eC9-2Cl: ATIC-C11, and eC9-2Cl: ATIC-BO film along OOP direction. c) The 2D GIWAXS patterns for PBQx-TF: eC9-2Cl: ATIC-C11 and PBQx-TF: eC9-2Cl: ATIC-BO blend films. d) TEM images for ATIC-C11, ATIC-BO, PBQx-TF: ATIC-C11, and PBQx-TF: ATIC-BO film. AFM e) height and f) phase images for three blends.

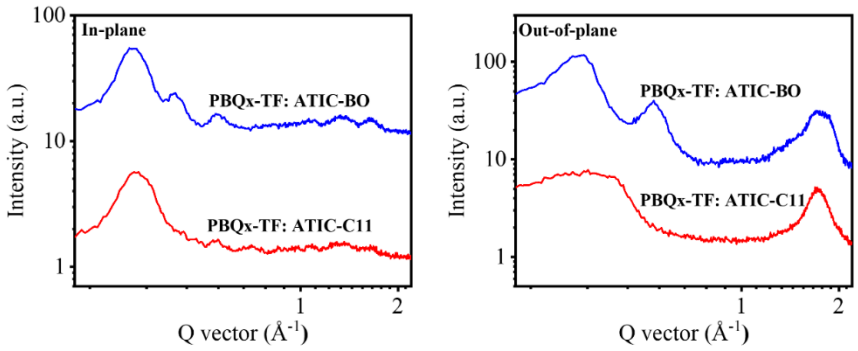

Figure 4. 18 1D GIWAXS Line cut profiles of PBQx-TF: ATIC-C11 and PBQx-TF: ATIC-BO blend film along IP and OOP direction.

Table 4. 8 Summarized *d*-spacing and CCL of the lamellar staking (100) peak along IP direction of PBQx-TF: ATIC-C11, PBQx-TF: ATIC-BO, PBQx-TF: eC9-2Cl, PBQx-TF: eC9-2Cl: ATIC-C11, and PBQx-TF: eC9-2Cl: ATIC-BO blend film.

	q_{xy} (Å^{-1})	*d*-spacing (Å)	FWHM (Å^{-1})	Coherence length (Å)
PBQx-TF: ATIC-C11	0.31	20.27	0.09	62.83
PBQx-TF: ATIC-BO	0.30	20.94	0.08	70.69
PBQx-TF: eC9-2Cl	0.31	20.27	0.09	62.83
PBQx-TF: eC9-2Cl: ATIC-C11	0.31	20.27	0.08	70.69
PBQx-TF: eC9-2Cl: ATIC-BO	0.31	20.27	0.08	70.69

Table 4. 9 Summarized *d*-spacing and CCL of the π-π staking (010) peak along OOP direction of PBQx-TF: ATIC-C11, PBQx-TF: ATIC-BO, PBQx-TF: eC9-2Cl, PBQx-TF: eC9-2Cl: ATIC-C11, and PBQx-TF: eC9-2Cl: ATIC-BO blend film.

	q_{xy} (Å^{-1})	*d*-spacing (Å)	FWHM (Å^{-1})	Coherence length (Å)
PBQx-TF: ATIC-C11	1.72	3.65	0.29	19.50
PBQx-TF: ATIC-BO	1.73	3.63	0.38	14.88
PBQx-TF: eC9-2Cl	1.72	3.65	0.33	17.14
PBQx-TF: eC9-2Cl: ATIC-C11	1.72	3.65	0.29	19.50
PBQx-TF: eC9-2Cl: ATIC-BO	1.71	3.67	0.34	16.63

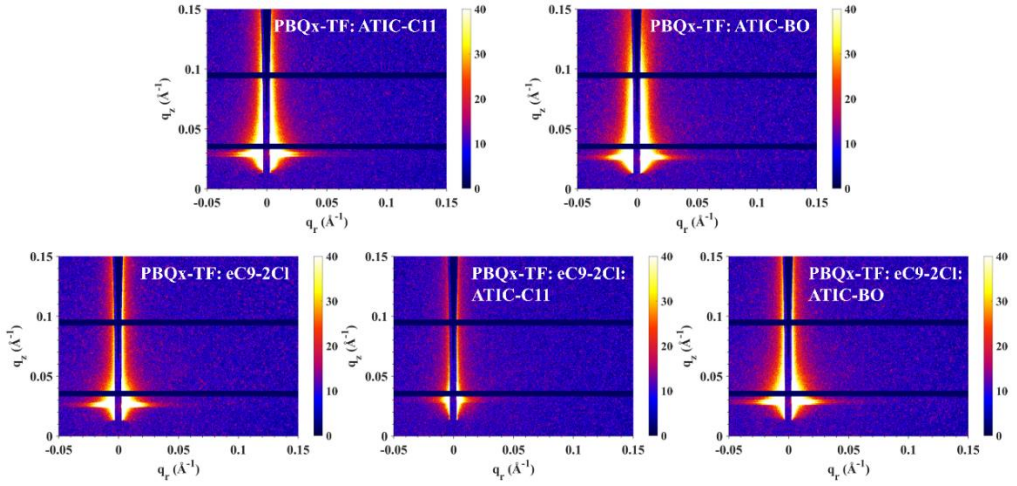

Figure 4. 19 2D GISAXS patterns of corresponding binary and ternary blend film.

Table 4. 10 Summarized $2R_g$ and X_{DAB} value extracted from GISAXS fitting curves.

	$2R_g$ (nm)	**X_{DAB} (nm)**
PBQx-TF: ATIC-C11	33.3	22.8
PBQx-TF: ATIC-BO	53.9	N/A
PBQx-TF: eC9-2Cl	53.9	N/A
PBQx-TF: eC9-2Cl: ATIC-C11	11.4	15.9
PBQx-TF: eC9-2Cl: ATIC-BO	37.7	23.2

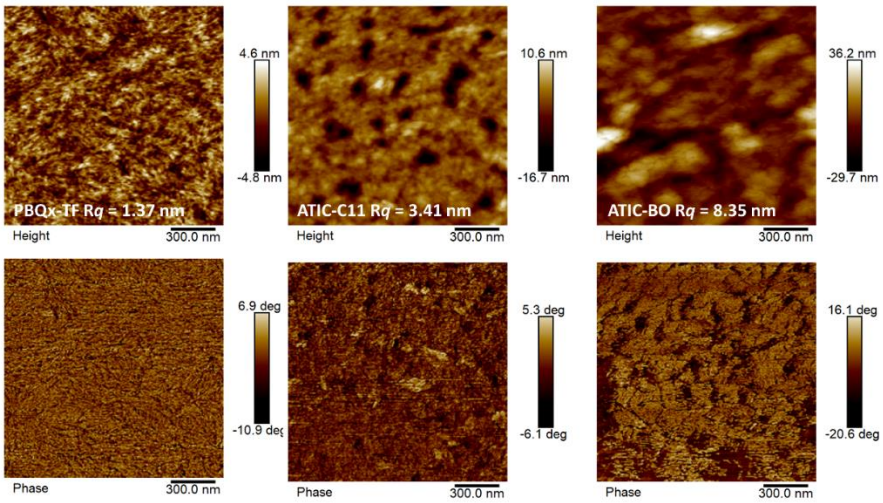

Figure 4. 20 AFM images for PBQx-TF, ATIC-C11, and ATIC-BO neat film.

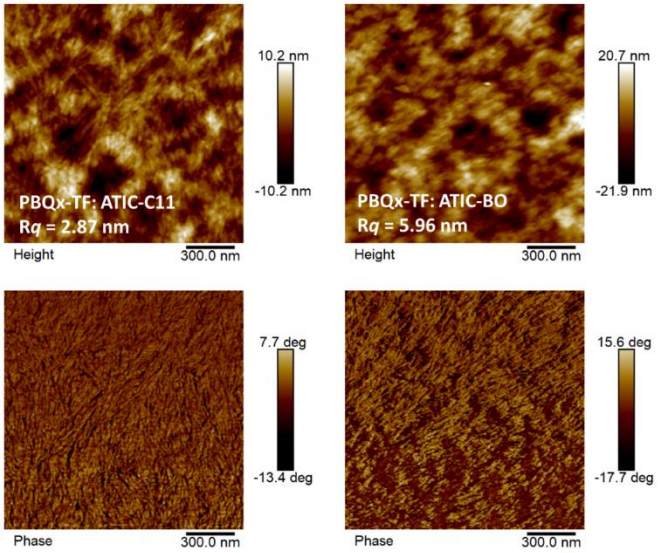

Figure 4. 21 AFM images for PBQx-TF: ATIC-C11 and PBQx-TF: ATIC-BO blend film.

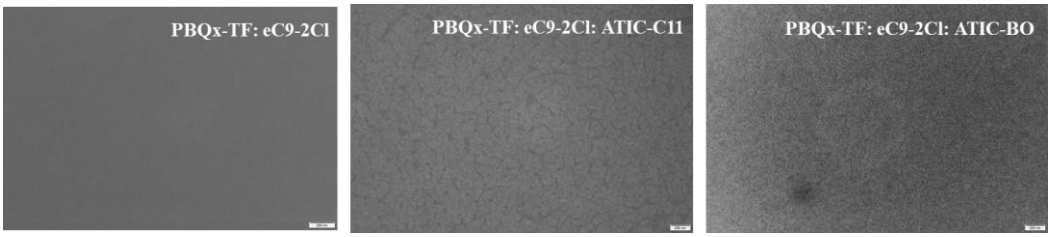

Figure 4. 22 TEM images for PBQx-TF: eC9-2Cl, PBQx-TF: eC9-2Cl: ATIC-C11, and PBQx-TF: eC9-2Cl: ATIC-BO blend film.

GIWAXS measurement was applied to study the molecular packing of solid films. It was noticed that ATIC-BO's characteristic peak (q_z = 0.55 Å^{-1}) was preserved when blended with eC9-2Cl, while ATIC-C11's peak disappeared in eC9-2Cl: ATIC-C11 film. The peak at 0.55 Å^{-1} also appeared in PBQx-TF: ATIC-BO blend film (Figure 4. 18), implying the incompatibility between ATIC-BO and the other active layer components, coincident well with the CA measurement. The incompatible property was responsible for the large agglomerates and relatively random molecular packing in ATIC-BO blend films. In binary blends, PBQx-TF: ATIC-BO possessed larger CCLs for lamellar stacking (70.69 Å) but smaller CCLs for π-π stacking (14.88 Å) than PBQx-TF: ATIC-

C11 film, whose CCLs for lamellar peak is 62.83 Å and for π-π peak is 19.50 Å (Table 4. 8 and

Table 4. 9). In ternary films, ATIC-BO ternary film gave the (010) peak at 1.71 $Å^{-1}$ with a CCL value of 16.63 Å, where the molecular packing was even less order than that in PBQx-TF: eC9-2Cl binary film (CCL = 17.14 Å). On the contrary, ATIC-C11-based film showed much organized and compact molecular packing with the (010) peak at 1.72 $Å^{-1}$ (CCL = 19.50 Å), indicating that the synergistic high crystallinity and suitable compatibility were the prerequisites for tight and organized molecular packing.

GISAXS measurement was applied to analyze the phase separation size of amorphous domain (X_{DAB}) and pure domain ($2R_g$) in blends (Figure 4. 19). It was noted that both PBQx-TF: eC9-2Cl and PBQx-TF: ATIC-BO blends showed a very large pure domain size of 53.9 nm, which was ascribed to the immiscibility between the donor and two acceptors. The possible reason for the relatively high efficiency of PBQx-TF: eC9-2Cl would be the large exciton diffusion length of eC9-2Cl. Conversely, the good compatibility between PBQx-TF and ATIC-C11 achieved the balanced intermixing phase and pure phase size (Table 4. 10), guaranteeing efficient charge transfer and charge transport, resulting in superior film morphology and device performance in both binary and ternary blends.

AFM and TEM were employed to further detect the blends' surface/bulk morphology. PBQx-TF showed a distinctive fibril structure, which was preserved in blend films and was conducive to charge transfer and transport (Figure 4. 20). Two ATIC acceptors showed high crystallinity with the root-mean-square (R_q) value of 3.41nm for ATIC-C11 and 8.35 nm for ATIC-BO neat film, respectively. The large aggregates alleviated in blend films, where PBQx-TF: ATIC-C11 gave a moderate R_q value of 2.87 nm and PBQx-TF: ATIC-BO film kept rough morphology (R_q = 5.96 nm) (Figure 4. 21). In ternary blends, ATIC-C11-based film gave a superior morphology of 1.15 nm with uniform distribution. However, ATIC-BO-based film showed large cracks and aggregates, which was ascribed to its strong self-aggregation and the poor miscibility between ATIC-BO and other two active layer components (Figure 4. 17e

and f). TEM images showed the micro-structure of ATIC acceptors. ATIC-C11 showed nanoscale homogeneous distribution, while ATIC-BO showed crude fiber structure with micron scales (Figure 4. 17d). The excessive phase separation preserved in ATIC-BO binary film, largely inhibiting charge separation and device performance. As a comparison, ATIC-C11 works well with PBQx-TF (Figure 4. 22), indicating moderate and balanced miscibility and crystallinity were of principal importance in determining morphologies.

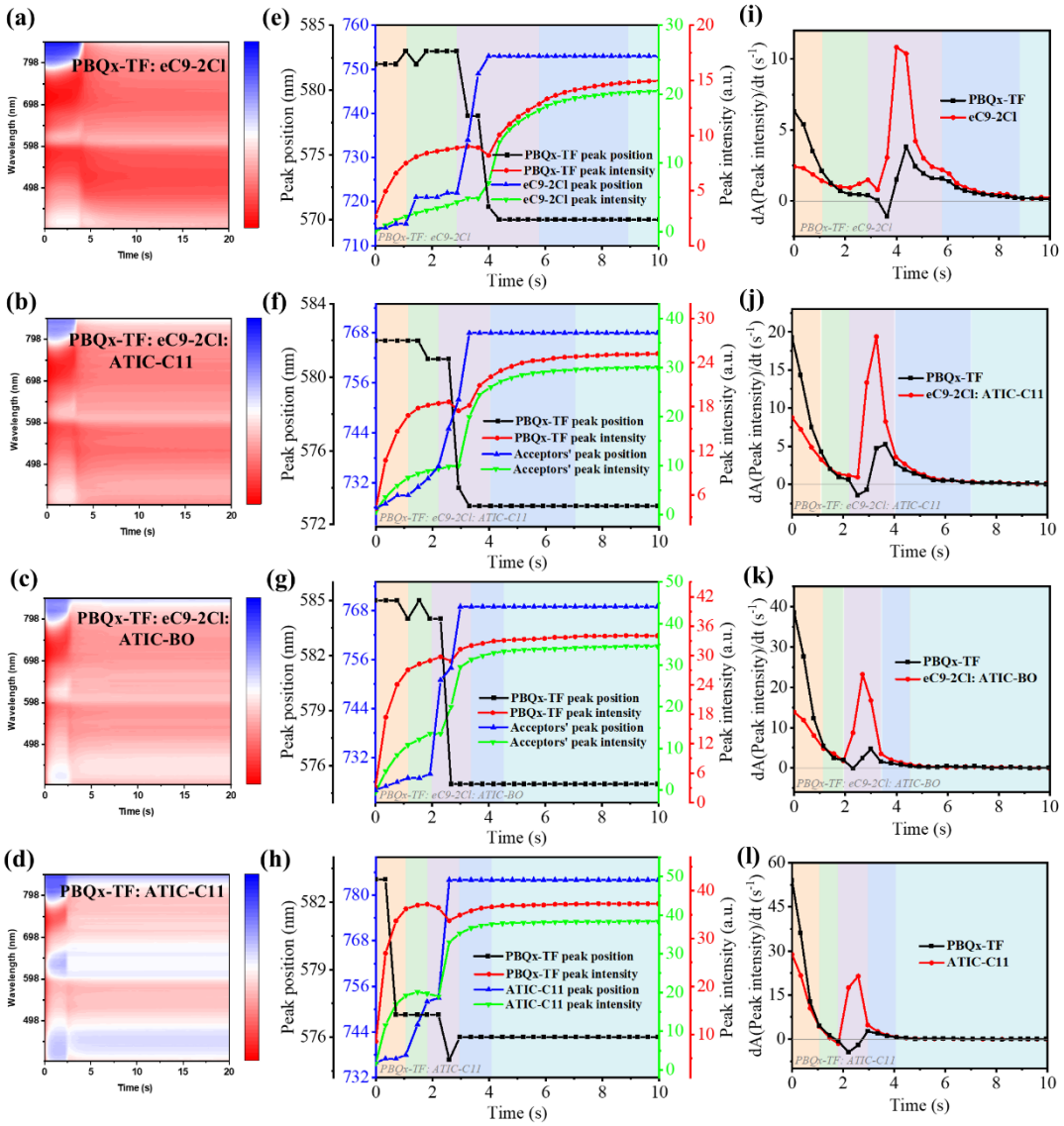

Figure 4. 23 The film formation process from solution to solid film by in-situ UV-vis absorption measurement. a-d) The in-situ 2D contour map, e-h) the characteristic peak position and intensity versus time, and i-l) the derivative of peak intensity with respective of time for a, e, i) PBQx-TF: eC9-2Cl, b, f, j) PBQx-TF: eC9-2Cl: ATIC-

C11, c, g, k) PBQx-TF: eC9-2Cl: ATIC-BO, and d, h, l) PBQx-TF: ATIC-C11 blend films.

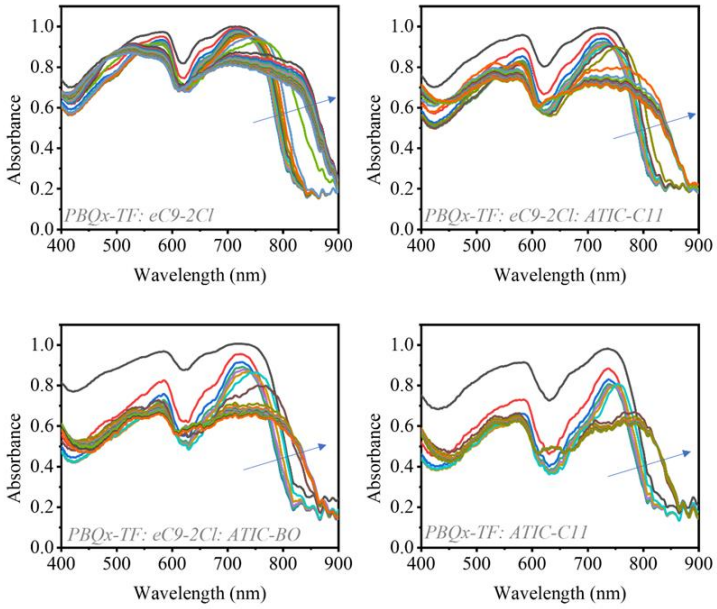

Figure 4. 24 In-situ absorption profiles of PBQx-TF: ATIC-C11, PBQx-TF: eC9-2Cl, PBQx-TF: eC9-2Cl: ATIC-C11, and PBQx-TF: eC9-2Cl: ATIC-BO blend film.

To comprehend the formation mechanism of ATIC acceptors' distinctive morphology, in-situ UV-vis measurement was applied to detect the phase transition process from solution to solid film. From the 2D contour map of corresponding films (Figure 4. 23a-d), it was found that the overall film drying time shortened in the order of PBQx-TF: eC9-2Cl, PBQx-TF: ATIC-C11: eC9-2Cl, PBQx-TF: ATIC-BO: eC9-2Cl, PBQx-TF: ATIC-C11. The insolubility of ATIC-BO changed the concentration of its binary blend solution, whose phase transition process was not presented to avoid misinterpretation. From solution to film, PBQx-TF showed blue-shifted absorption and strong shoulder peak due to the change of molecular packing from J-aggregation to H-aggregation, while acceptors showed red-shifted absorption ascribed to more compact molecular packing (Figure 4. 24). To get a deeper insight into the film formation process, the 0-0 characteristic absorption peak of the donor and acceptors was extracted as a function of time (Figure 4. 23e-h). The variation of peak intensity (absorbance) and peak position (wavelength) reflected various stages during film formation, including

solvent evaporation, nucleation, crystal growth, additive removal, and final solid film. Initially, the peak position kept stable while peak intensity enhanced greatly, which was ascribed to the solvent evaporation. The addition of ATIC acceptors was found to facilitate the solvent evaporation as the solvent evaporation rate greatly enhanced (Figure 4. 23i-l). It was noted that PBQx-TF's nucleation was not observed in PBQx-TF: eC9-2Cl film, however, which appeared in ternary films, shown as slightly blue-shifted peak position, indicating ATIC acceptors could induce the nucleation of PBQx-TF, which was confirmed in PBQx-TF: ATIC-C11 binary film, where PBQx-TF nucleation began at solvent evaporation stage (Figure 4. 23h). Simultaneously, the nucleation of eC9-2Cl became moderate in ternary film. The distinct displacement of peak position and peak intensity represented the crystal growth stage. It was found that the aggregation rate enhanced with the introduction of ATIC acceptors, indicating ATIC acceptors with high crystallinity could provide nuclei seeding sites for host materials and facilitate their crystal growth. The highest crystal growth rate in ATIC-BO ternary film explained its largest aggregates in solid film. In the fourth stage, the peak position stabilized and the peak intensity kept changing, corresponding to the removal of the additive. ATIC acceptors were found to accelerate additive exclusion from obviously shortened post-treatment time. The results demonstrated that ATIC acceptors derived distinctive film morphology by regulating the removal of solvent and additive, and simultaneously controlling PBQx-TF and eC9-2Cl's nucleation and crystal growth.

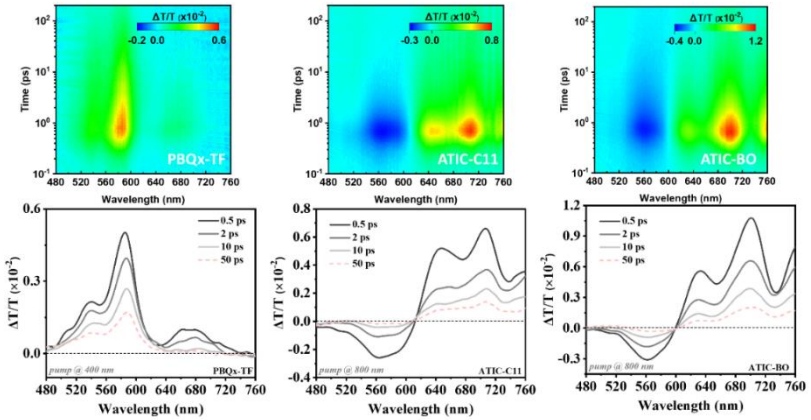

Figure 4. 25 The TA images and the corresponding TA spectra with various decay times of the neat films with 400 or 800 nm excitation wavelength.

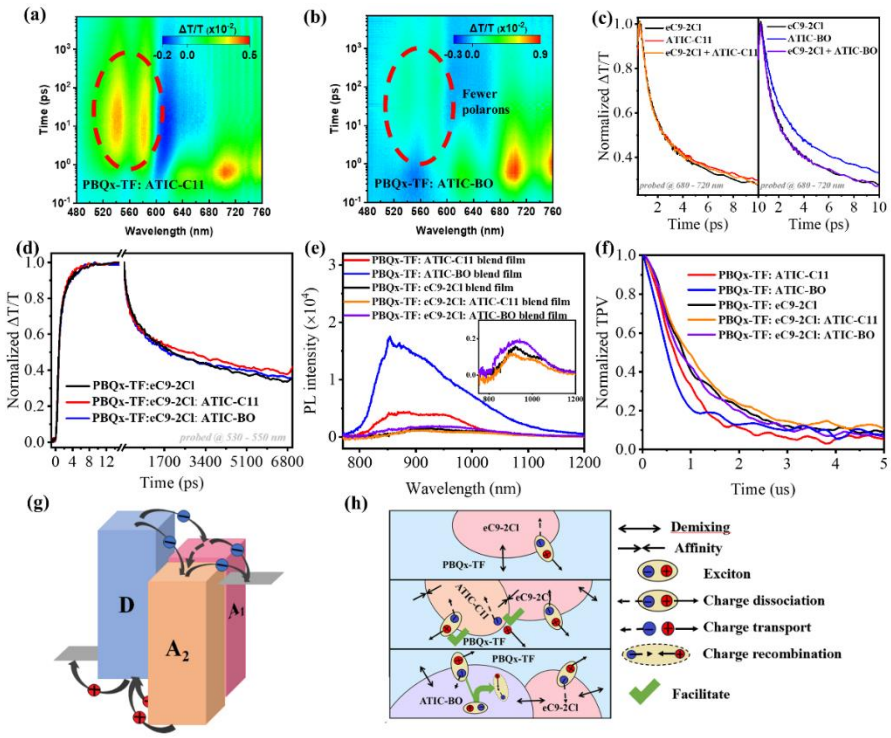

Figure 4. 26 Charge carrier dynamics in corresponding binary and ternary devices. The TA image of a) PBQx-TF: ATIC-C11 and b) PBQx-TF: ATIC-BO blend film. c) The electron-transfer process in eC9-2Cl: ATIC-C11 and eC9-2Cl: ATIC-BO film. d) The hole-transfer process in PBQx-TF: eC9-2Cl, PBQx-TF: eC9-2Cl: ATIC-C11 and PBQx-TF: eC9-2Cl: ATIC-BO film. e) Steady-state PL profiles of corresponding binary and ternary blend film. (The inserted figure was a magnified view with the Y-axis range from -0.1×10^4 to 0.3×10^4) f) Normalized TPV curves for corresponding binary and ternary devices. g) The Parallel-like model in ternary devices. h) The schematic working mechanism of the control and ternary devices.

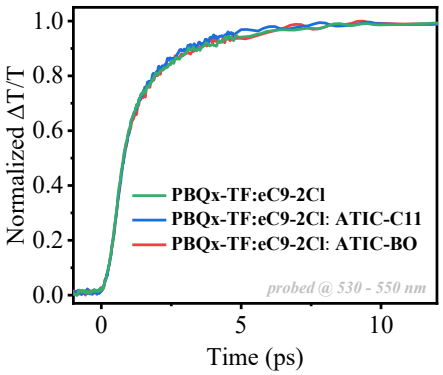

Figure 4. 27 The hole-transfer processes in PBQx-TF: eC9-2Cl, PBQx-TF: eC9-2Cl: ATIC-C11, and PBQx-TF: eC9-2Cl: ATIC-BO blend films.

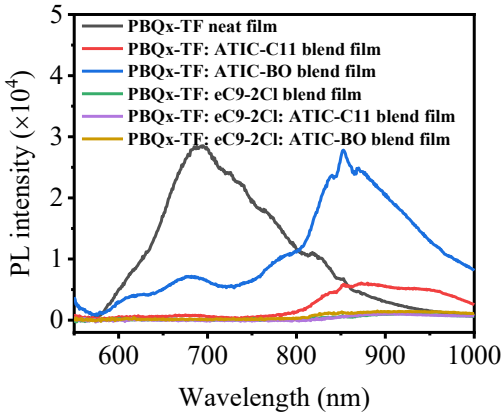

Figure 4. 28 Steady-state PL spectra of corresponding neat, binary, and ternary blend films (Excited at 530 nm).

4.3.4 Charge Carrier Dynamics

The transient absorption (TA) was measured to detect the charge generation and recombination situation. ATIC-C11 and ATIC-BO displayed distinctive ground state bleaching (GSB) signals in the range of 640-720 nm and 680-720 nm (Figure 4. 25), respectively. When blended with PBQx-TF, the donor GSB signal appeared with the relaxation of the ATIC-C11 GSB signal (Figure 4. 26a). As the pump wavelength is at 800 nm, the donor GSB signal was ascribed to the hole transfer from the acceptor to the donor. However, few polarons were detected in PBQx-TF: ATIC-BO blend, indicating less efficient charge transfer between PBQx-TF and ATIC-BO (Figure 4. 26b). When blended with eC9-2Cl, the electron transfer between acceptors was studied by the decay profiles of their representative GSB peaks. The exciton lifetime did not change significantly, while the middle location of the eC9-2Cl: ATIC-C11 decay profile indicated a little charge transfer between ATIC-C11 and eC9-2Cl. The long exciton lifetime of ATIC-BO, however, contributed nothing in eC9-2Cl: ATIC-BO film, which preserved the decay profile of the neat eC9-2Cl film, indicating less (or none) charge transfer at eC9-2Cl/ ATIC-BO interfaces (Figure 4. 26c). The hole transfer and charge recombination process in ternary devices were studied by probing the GSB signal of PBQx-TF. The hole transfer rate was found to be relatively faster in ATIC-C11 ternary film (Figure 4. 27), and the ternary films have comparable recombination rate with eC9-

2Cl binary film in 1ns, while ATIC acceptors were able to suppress the recombination beyond 1 ns, especially ATIC-C11 (Figure 4. 26d). The charge transfer was also studied by photoluminescence (PL) measurement. The excitation wavelength was determined to be 530 nm for the donor and 730 nm for the acceptors. In PBQx-TF: ATIC-BO binary film, non-efficient charge transfer was detected (Figure 4. 26e and Figure 4. 28). The PL quenching efficiency was calculated according to acceptors emission peak to be 93.72%, 95.57%, and 91.44% for PBQx-TF: eC9-2Cl, PBQx-TF: ATIC-C11: eC9-2Cl, and PBQx-TF: ATIC-BO: eC9-2Cl, respectively. The participation of ATIC-C11 facilitated the charge transfer in ternary film, while ATIC-BO, on the contrary, impeded the charge transfer.

The relationship of $V_{OC} \propto (nkT/q)\ln P_{light}$ was applied to evaluate the trap-assisted recombination, and $J_{SC} \propto P_{light}^{\alpha}$ was used to describe bimolecular recombination. Compared with ATIC-C11, ATIC-BO binary devices showed more suppressed trap-assisted recombination but severed bimolecular recombination (Figure 4. 29). Both trap-assisted and bimolecular recombination were suppressed in ternary devices with the addition of ATIC acceptors, especially ATIC-C11. The charge dissociation and extraction efficiency were calculated by plotting J_{ph} versus V_{eff}. ATIC-BO showed inferior charge separation and extraction efficiency than ATIC-C11 due to its oversized aggregates (Figure 4. 30). In ATIC-C11 ternary blend, both charge separation and charge collection efficiency enhanced, while the charge dissociation efficiency in ATIC-BO ternary film declined due to the decreased D/A interfaces originating from ATIC-BO's large aggregates. To further understand the charge collection in devices, the TPV and TPC were applied to determine the carrier lifetime (τ) and sweeping out times (t_s) (Figure 4. 26fFigure 4. 31). ATIC-C11 binary devices have a longer carrier lifetime and faster charge extraction rate than ATIC-BO devices, explaining the much higher FF and J_{SC}. In ternary systems, t_ss were almost the same, while ATIC acceptors improved the carrier lifetime, especially in ATIC-C11 ternary devices (Table 4. 11), benefited from the reduced trap densities and suppressed charge recombination, well explained its higher photocurrent. The charge transport was evaluated by the SCLC method (Figure

4. 32Figure 4. 34). The electron mobility of ATIC-C11 and ATIC-BO neat film was calculated to be 3.52×10^{-4} and 4.89×10^{-4} $cm^2V^{-1}s^{-1}$, respectively (Table 4. 12), which was much higher than the mobility of eC9-2Cl (2.26×10^{-4} $cm^2V^{-1}s^{-1}$). The higher charge mobility was ascribed to the higher crystallinity of the acenaphthene extended quinoxaline central core. In blend films, however, the ATIC-C11 showed much higher and balanced carrier mobility than ATIC-BO. The inferior charge transport in ATIC-BO-based devices was ascribed to its rough morphology, which induced more traps for charge carriers.

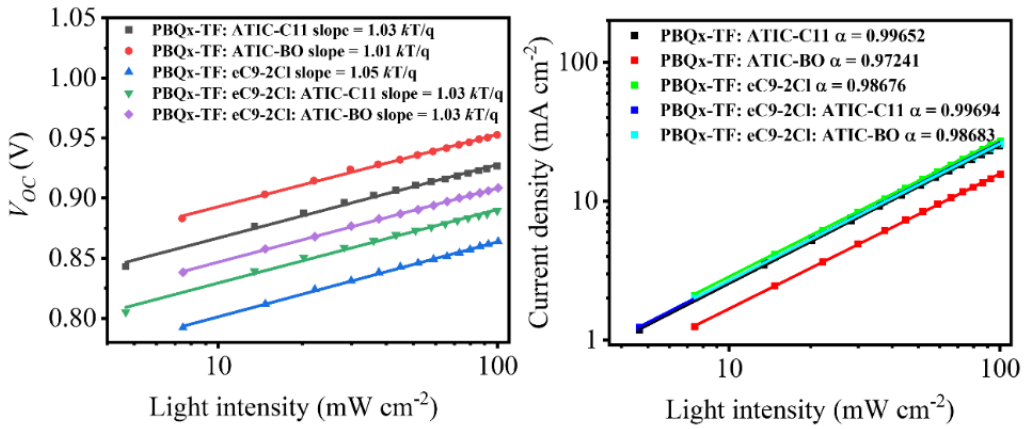

Figure 4. 29 Trap-assisted and bimolecular recombination in corresponding binary and ternary devices.

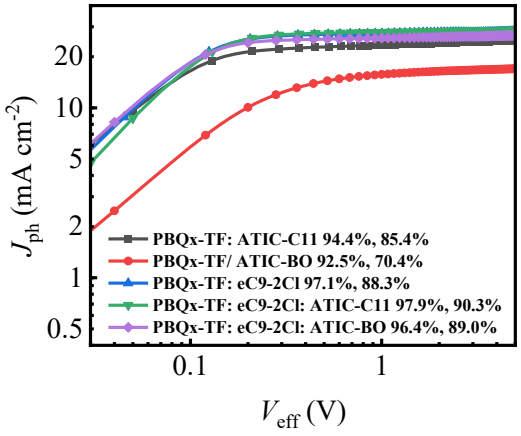

Figure 4. 30 J_{ph}-V_{eff} plot of corresponding binary and ternary devices.

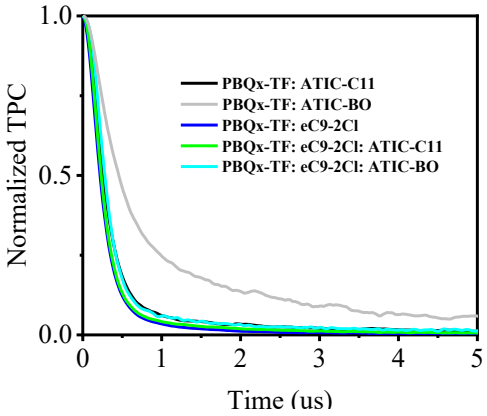

Figure 4. 31 Transient photocurrent (TPC) curves of corresponding binary and ternary devices.

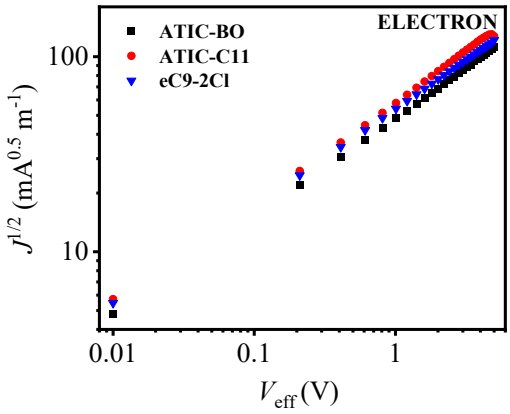

Figure 4. 32 Electron mobility of ATIC-C11, ATIC-BO, and eC9-2Cl neat films.

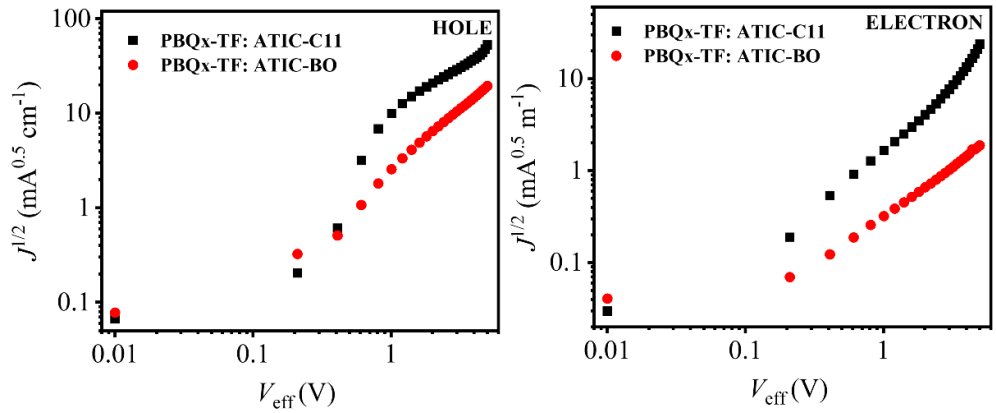

Figure 4. 33 Charge mobility of ATIC-C11 and ATIC-BO binary blend films.

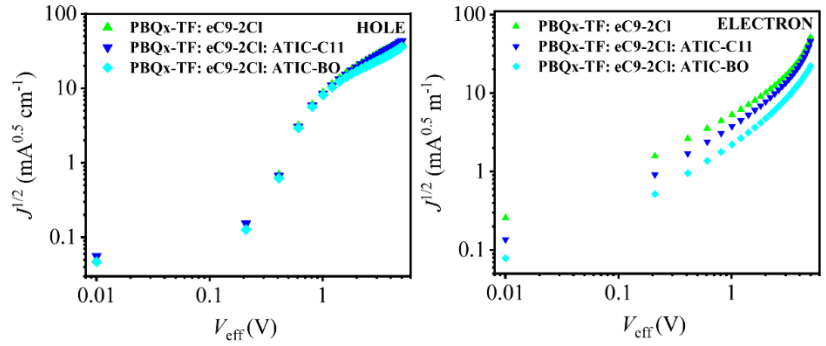

Figure 4. 34 Charge mobility of control, ATIC-C11, and ATIC-BO ternary blend films.

Table 4. 11 The carrier lifetime and sweeping out time from TPV and TPV measurement.

Active Layer	Carrier lifetime τ (us)	Sweeping out time t_s (us)	τ/t_s
PBQx-TF: ATIC-C11	0.73	0.33	2.21
PBQx-TF: ATIC-BO	0.53	0.57	0.93
PBQx-TF: eC9-2Cl	0.93	0.31	3.00
PBQx-TF: eC9-2Cl: ATIC-C11	1.07	0.31	3.45
PBQx-TF: eC9-2Cl: ATIC-BO	0.97	0.30	3.23

Table 4. 12 The charge mobility of corresponding neat, binary blend, and ternary blend films.

Active Layer	Hole mobility μ_h ($cm^2V^{-1}s^{-1}$)	Electron mobility μ_e ($cm^2V^{-1}s^{-1}$)	μ_e/μ_h
ATIC-C11	/	3.52×10^{-4}	/
ATIC-BO	/	4.89×10^{-4}	/
eC9-2Cl	/	2.26×10^{-4}	/
PBQx-TF: ATIC-C11	3.68×10^{-4}	3.54×10^{-4}	0.96
PBQx-TF/ ATIC-BO	4.03×10^{-5}	6.48×10^{-7}	0.02
PBQx-TF: eC9-2Cl	3.75×10^{-4}	4.95×10^{-4}	1.32
PBQx-TF: eC9-2Cl: ATIC-C11	3.61×10^{-4}	3.91×10^{-4}	1.08
PBQx-TF: eC9-2Cl: ATIC-BO	3.43×10^{-4}	1.12×10^{-4}	0.33

4.4 Conclusion

To summarize, two acenaphthene-expanded 2D acceptors were synthesized and systematically studied. The ATIC acceptors demonstrated high crystallinity, particularly ATIC-BO, which, despite its bulky-branched side chain, unexpectedly adopted a more planar conformation. Their distinct chemical structure led to unique molecular packing modes and crystal structures, with ATIC-C11 forming an elliptical framework and ATIC-BO displaying a rectangular one. The ATIC acceptors exhibited low reorganization energy and Urbach energy, which are beneficial for suppressing sub-gap absorption and non-radiative recombination losses. Through detailed investigation into carrier kinetics and morphologies, it was found that the ATIC acceptors underwent the parallel-like model, providing additional pathways for charge separation and transport. However, the strong aggregation and poor compatibility of ATIC-BO led to large aggregates that hindered charge transfer and dissociation, resulting in lower FF and J_{SC}. In contrast, ATIC-C11, with its optimal crystallinity and compatibility, effectively regulated crystalline kinetics to achieve more ordered molecular packing and nanoscale phase separation. This, combined with the reduced energetic disorder, improved charge transfer and dissociation, and enhanced carrier lifetime, allowed ATIC-C11-based ternary devices to achieve a high efficiency of 19.28%, with great potential for scalability and stability. To the best of our knowledge, this is the top-ranking efficiency among non-halogenated solvent-processed OSCs. This work not only presents an outstanding green-solvent processed OPV based on the "structure–performance–property" relationship but also offers new insights into material design and selection criteria for achieving highly efficient and stable OPVs, paving the way for OPV industrialization.

Chapter 5 Highly crystalline 2D acceptors enabling highly efficient and stable quasiplanar heterojunction organic solar cells

5.1 Introduction

Assembled with the promising merits of solution-processable, semitransparent, flexible, and environmentally friendly, OSCs are expected to be industrially producible and practically applicable. Recently, the research on photoactive layer materials and device optimization strategies has pushed OSCs to surpass 20% of power conversion efficiencies (PCEs).[1–5] However, OSCs still face challenges in device long-term operational stability. On one hand, the active layer materials are prone to photo-oxidation degradation, where the polymer donor would be photo-oxidized to singlet oxygen and superoxide anions, and Y-series acceptors are prone to vinylidene oxidation to break the core and the terminal group.[130,132,272,273] On the other hand, the unstable active layer morphology under light/thermal stress is responsible for device physical degradation. Molecular migration causes over- or de-mixing between D/A phases, which lowers domain purity or forms large segregates, leading to an inferior phase separation in aging films.[130,131] However, it was found that the planar and rigid molecular conformation could prevent light-induced material degradation and morphological change.[274–276] Additionally, acceptors with a high degree of crystallinity were proved to possess a high cold crystallization temperature to resist thermal-induced molecular diffusion and aggregation.[140,142,277] Therefore, it is significant to develop highly crystalline materials with good resilience to thermal/light-induced deterioration.

From the perspective of device engineering, the quasiplanar heterojunction (Q-PHJ) processed by orthogonal solvents was proposed to address the inferior stability issue in OSCs.[278–281] The conventional bulk heterojunction (BHJ) active layer is considered thermodynamically metastable as D/A would segregate and evolve into individual excessive aggregation.[282–285] In Q-PHJ, the donor and acceptor are deposited

sequentially, where the reduced D/A intermixing phase and improved D/A phase purity alleviate active layer morphological change and thus pronouncedly improve device stability.[278,280,286] Additionally, the swelling of the solvent and the downward diffusion of the upper layer molecules facilitate the formation of a tiny nanoscale BHJ region at the D/A interface. Such an optimal vertical p-i-n phase distribution largely profits device performance thanks to the synergistically promoted charge separation and charge transport.[147,281,287] Moreover, morphology control is challenging in the BHJ structure when facing the differences between the donor and the acceptor in molecular solubility, molecular weight, and crystallinity/miscibility.[3,201,288] Conversely, Q-PHJ is a desirable candidate for extending material systems as it satisfies independent manipulation of D/A morphology. Furthermore, regarding the problem of the long distance between the exciton formation position and the D/A interface in Q-PHJ devices, the highly crystalline acceptors with compact molecular packing and strong aggregation afford large exciton diffusion coefficients and long exciton diffusion lengths for efficient exciton diffusion.[289] Thus, highly crystalline acceptors are expected to play an important role in achieving long-term operational high-performance Q-PHJ OSCs.

Further literature studies revealed highly crystalline materials' multiple optimistic advantages beyond improving device stability. Primarily, highly crystalline guest materials could fine-tune photoactive layer crystallization kinetics and final film morphological nanostructures.[3,113,290–293] The introduction of the highly crystalline polymer donor D18 in PM6: L8-BO blend was found to manipulate the crystallization of host components, where D18 would precipitate out rapidly and induce a high degree of crystallinity in the ternary blend, achieving an outstanding efficiency of 19.6% *via* forming a high-quality double-fibril network morphology.[113] Additionally, highly crystalline materials are effective in suppressing energy loss.[122–124,289,294,295] The reduced energetic disorder and inhibited triplet exciton formation induced by highly crystalline materials feasibly reduced the radiative and non-radiative recombination and elevated open-circuit voltage (V_{OC}).[296–299] Furthermore, highly crystalline materials are proven to boost charge transport by inducing favorable face-on molecular

orientation and ordered and compact molecular packing.[300–303] In our previous work, the acenaphthene-extended 2D acceptor ATIC-C11 with a high degree of crystallinity was studied and proved to function in regulating crystallization kinetics, forming nanoscale phase separation, suppressing energy loss, and improving device stability[122]. Thus, a highly crystalline guest component was believed to be feasible in improving devices' overall performance.

Here, the "crystallinity-tuning" strategy was employed in the Q-PHJ OSCs, aiming to construct a highly efficient and stable bilayer OSC. Specifically, two highly crystalline acceptors, AnIC-BO and PhIC-BO, featuring different 2D-extended electron-deficient central cores, were synthesized, and their role in collaboration with active layer components was deeply investigated. The phenanthrene-extended PhIC-BO displayed a typical 3D network crystal structure with an elliptical framework, while the anthracene-extended AnIC-BO gave a linear packing to form a quasi-3D network structure. The difference in crystal structure induced distinct crystallization kinetics, molecular packing, and carrier dynamics in the ternary blends. As a result, PhIC-BO-based achieved a high PCE of 19.44% with an outstanding V_{OC} of 0.904 V. Further investigation into device stability found that the highly crystalline guest acceptors functioned in impeding material degradation and morphological change. The PhIC-BO-based devices displayed prominent operational stability with a T_{80} of 388h for thermal stability and 1040h for photostability, and a T_{99} of 3000 h for shelf-storage stability, which enabled it to be one of the state-of-the-art long-term stable bilayer ternary OSCs. This work illustrated the "structure-property" correlation by giving an insight into two highly crystalline acceptors and constructed a long-term stable high-performance OSC, providing valuable guidance for further research on highly efficient and stable OSCs.

5.2 Experimental section

5.2.1 Synthetic routes for PhIC-BO and AnIC-BO

All solvents and reagents were used as received from commercial sources and used without further purification unless otherwise specified.

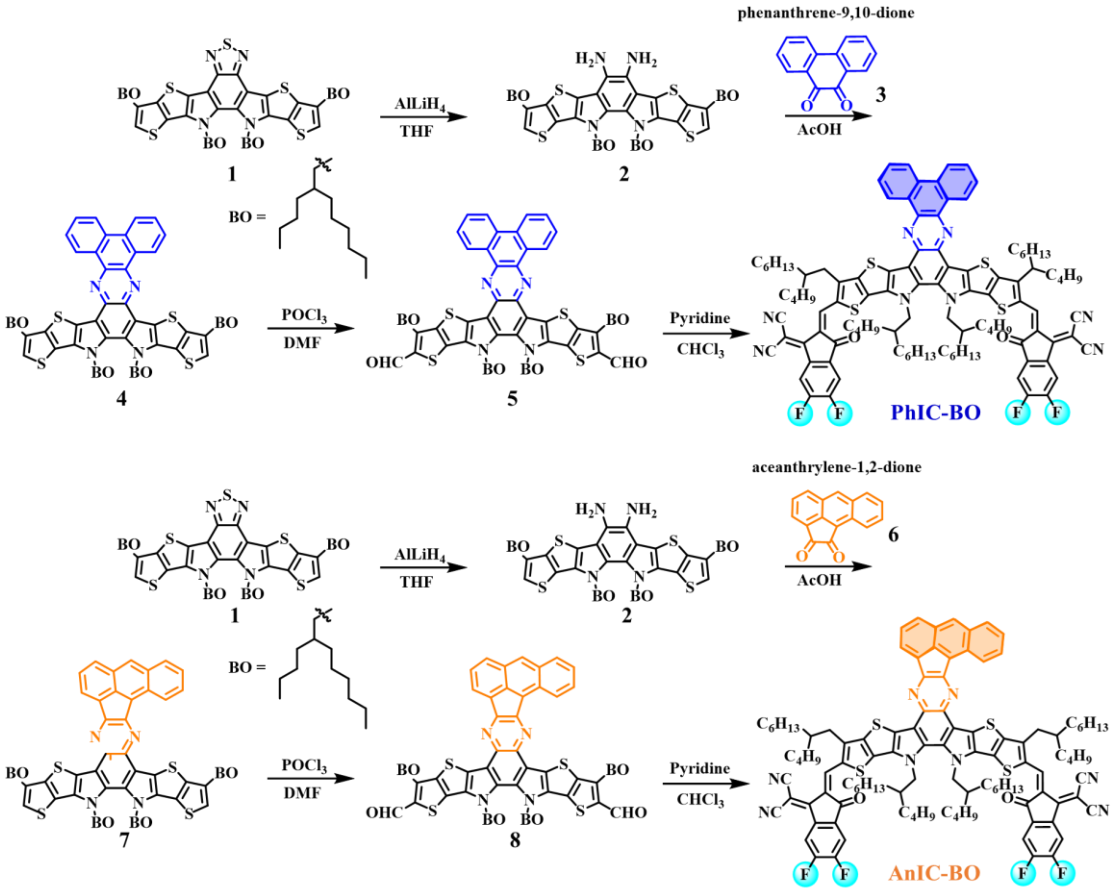

Scheme S2. The synthetic routes of PhIC-BO and AnIC-BO.

Compound 2: A 100 mL round-bottom flask was charged with Compound 1 (1 g) dissolved in 50 mL THF. Under ice-cooling conditions, a 2.5 M solution of $LiAlH_4$ (10 mL) was introduced dropwise at 0°C. Following complete addition, the reaction was maintained at 80°C with vigorous stirring for 12 h. After gradual cooling to ambient temperature, liquid-liquid extraction was performed using CH_2Cl_2. The isolated organic fraction underwent sequential brine washing and $MgSO_4$ drying, providing crude material for direct use in subsequent steps.

Compound 4: To a solution of Compound 2 (200 mg) in a mixed solvent system (EtOH: AcOH = 40 mL: 20 mL) contained in a 250 mL flask, Compound 3 (200 mg) was introduced. Thermal activation at 80°C under continuous agitation proceeded for 18 h. Post-cooling extraction with CH_2Cl_2 yielded an organic phase that was subjected to chromatographic purification (CH_2Cl_2: petroleum ether gradient), affording 160 mg purified product.

Compound 5: A pre-chilled $POCl_3$/DMF mixture (1 mL: 4 mL) activated at 0°C for 60 min was transferred via cannula to a CH_2Cl_2 solution (20 mL) containing Compound 4 (160 mg) under temperature control. After thermal equilibration at 40°C for 10 h, conventional workup involving CH_2Cl_2 extraction and column chromatographic isolation delivered 120 mg target compound.

Compound PhIC-BO: In a reflux apparatus, Compound 5 (120 mg) and INCN (100 mg) were combined in $CHCl_3$/pyridine (30 mL: 0.5 mL) under an inert atmosphere. *Post-24 h condensation*, phase separation with $CHCl_3$ followed by sequential purification (chromatography: $CHCl_3$; preparative HPLC cycling) yielded 130 mg final product.

Compound 7: A suspension of Compound 2 (500 mg) and Compound 6 (500 mg) in EtOH (30 mL) underwent thermal cyclization at 80°C for 18 h. Standard extraction protocols with CH_2Cl_2 preceded flash chromatography (CH_2Cl_2: petroleum ether), generating 350 mg isolated material.

Compound 8: Vilsmeier reagent ($POCl_3$: DMF = 1 mL:5 mL, performed at 0°C) was slowly infused into a CH_2Cl_2 solution of Compound 7 (350 mg). Following 10 h activation at 40°C, chromatographic processing (CH_2Cl_2: petroleum ether) furnished 220 mg of purified intermediate.

Compound AnIC-BO: Condensation of Compound 8 (100 mg) with INCN (100 mg) in $CHCl_3$/ pyridine (20 mL: 0.5 mL) under argon reflux for 24 h yielded crude product, which was refined through $CHCl_3$ chromatography and preparative HPLC cycles to obtain 90 mg pure compound.

5.2.2 Device Fabrication

Organic photovoltaic devices were manufactured with a standard ITO/3-BPIC-F/Active Layer/PDINN/Ag architecture. Prior to fabrication, ITO substrates underwent sequential solvent cleaning (detergent, deionized water, acetone, isopropanol; 20 min per solvent) followed by 20-minute ultraviolet ozone treatment. A 3-BPIC-F hole transport layer (HTL) was solution-cast by spin-coating an ethanol-based 0.5 mg/mL 3-

BPIC-F solution at 3000 rpm for 30 s. The HTL was thermally cured at 100°C (10 min) under nitrogen atmosphere. The donor layer was subsequently deposited from spin-coating a 7 mg/mL D18 chlorobenzene solution, followed by deposition of a acceptor system comprising L8-BO-X: guest acceptor (PhIC-BO/AnIC-BO) dissolved in chloroform (9 mg/mL total concentration, 50 wt% OFN) at ~3400 rpm, yielding an ~120 nm active layer. Following 5-minute thermal annealing at 100°C, a 1.5 mg/mL methanol-processed PDINN solution was deposited to generate a ~5 nm ETL layer. Device completion involved thermal evaporation of a 100 nm-thick silver electrode, defining a 4 mm^2 active area. *J-V* measurements were evaluated under AM 1.5G illumination (100 mW/cm^2) using an Enlitech SS-F5-3A solar simulator, with light intensity calibrated against an SRC-2020 certified reference cell. EQE spectra were acquired through an Enlitech RE-R spectral response measurement system.

5.2.3 Characterizations and Measurements

^{1}H NMR spectra were conducted on a Bruker AV-400 instrument (400 MHz) using deuterated chloroform ($CDCl_3$) as the solvent, with tetramethylsilane (TMS) employed as the internal reference.

Preparative high-performance liquid chromatography A JAI LC-9104 recycling prep-HPLC system was utilized, operating with chloroform as the mobile phase.

Crystal growth: diffraction quality crystals were grown by solvent diffusion method. Acceptors (5 mg) was dissolved in CH_2Br_2 or $CHCl_3$ or toluene (5 mL) in the 15 mL sample bottle, then 10 mL of ethanol or methanol or ether was added it slowly. The bottle was then sealed tightly, and left undisturbed for 10 days[3].

Crystallography: The single crystal X-ray diffraction (SCXRD) data were collected at 100K or 150K on a Bruker D8 VENTURE diffractometer using Cu Kα radiation (λ = 1.54178 Å) or Ga Kα radiation (λ = 1.34139 Å). Lorentz/polarization corrections were applied during data reduction and the structures were solved by the direct method (SHELXT). Severe disorder problems were encountered during all the refinements, and

considerable amounts of constrains and restrains such as DFIX, SADI, SIMU, AFXI and DANG were used when necessary.

Ultraviolet photoelectron spectroscopy (UPS) was applied to determine energy levels of materials. The ionization energy (IE) was determined by $\Phi = h\nu$ (21.2 eV) - (E_0-E_f) and the electronic affinity energy was determined according to the optical bandgap from UV-vis absorption.

FTPS-EQE was acquired using an integrated PECT600 system (Enlitech), incorporating lock-in amplification for photocurrent signal modulation. Electroluminescence quantum efficiency (EQEEL) assessments employed an ELCT3010 instrument (Enlitech) to apply controlled voltage/current biases across the devices. E_{loss} values were calculated according to previously established protocols.[233]. The energy loss was described by three parts, $\Delta E = \Delta E_1 + \Delta E_2 + \Delta E_3$, where ΔE_1 referred to the radiative recombination above the bandgap. The theoretical limits (Shockley-Queisser (SQ) limit) as a function of bandgap was applied for any type of single junction solar cells. ΔE_2 was the radiative recombination below the bandgap. As the room temperature blackbody radiation is strong at low-energy region, any sub-gap absorption would cause large radiative loss[21]. ΔE_3 comes from the non-radiative recombination and was calculated by $\Delta E_3 = -kT \ln EQE_{EL}$. The arise of ΔE_3 was the electron-phonon coupling from molecular vibration, and energy dissipated by thermal emission. Urbach energy was calculated by $1/k_{slope}$, where k_{slope} was obtained by fitting the band tail of FTPS-EQE.

Transient absorption spectroscopy (TAS) was measured with an amplified Ti:sapphire femtosecond laser (800 nm wavelength, 50 fs, 1 kHz repetition; Coherent Libra) and a Helios pump/probe setup (Ultrafast Systems).

Transient photocurrent (TPC) and transient photovoltage (TPV) were performed with a Paios 4.0 measurement instrument (FLUXiM AG, Switzerland). The carrier lifetime (τ) and sweeping out times (t_s) were obtained by fitting TPC/TPV curves with a mono-exponential decay function.

Space-charge limited current (SCLC) Hole and electron mobilities in pristine and blend films were evaluated via SCLC methodology. Hole mobility employed the structure of ITO/PEDOT: PSS/Active Layer/Au, and electron mobility adopted the structure of ITO/ZnO/Active Layer/Ag, maintaining active layer thicknesses consistent with photovoltaic devices. Dark current-voltage characteristics were fitted to the Mott-Gurney law (Equation 1-31). $V = V_{app} - V_{bi}$ accounts for electrode work function differences. Mobility values were extracted from the linear regime of $J^{1/2} \sim V$ plots.

Contact angle measurements were determined via sessile drop measurements using deionized water and ethylene glycol. Surface tension components were derived through the two-solvent (H_2O/EG) Owens-Wendt approximation method. The donor-acceptor interfacial energy ($\gamma_{D/A}$) and Flory-Huggins interaction parameter ($\chi_{D/A}$) were evaluated by Equations 1-32 and 1-33. γ is the surface energy of the corresponding material; γ^d, γ^p are the dispersive and polar components of γ, respectively; K is a constant. The wetting coefficient (ω) was calculated by the equation: $\omega_{A_2} = (\gamma_{A_1/A_2} - \gamma_{D/A_2})/\gamma_{D/A_1}$ to confirm the position of the third component in the ternary blend. For $\omega_{A_2} < -1$, the third component is in the host acceptor (A_1)'s domain; for $-1 < \omega_{A_2} < 1$, the third acceptor is at the interface of donor and the host acceptor (D and A_1); for $\omega_{A_2} > -1$, the third component is in the host donor (D)'s domain.

In-situ UV–vis spectra Real-time UV-vis spectral data were recorded on an F20 spectrometer (Filmetrics, Inc.) equipped with a halogen light source (1.5 mm spot diameter). To isolate the absorption/reflection contributions from the active layer, measurements were referenced against an ITO/PEDOT: PSS-coated glass substrate. Spin-coating parameters matched those employed in device fabrication to ensure process consistency.

Atomic force microscopy (AFM) was probed via Bruker Dimension EDGE in amplitude-modulated tapping mode.

Transmission electron microscopy (TEM) was resolved through transmission electron microscopy using a Hitachi H-7650 instrument operated at 100 kV accelerating potential.

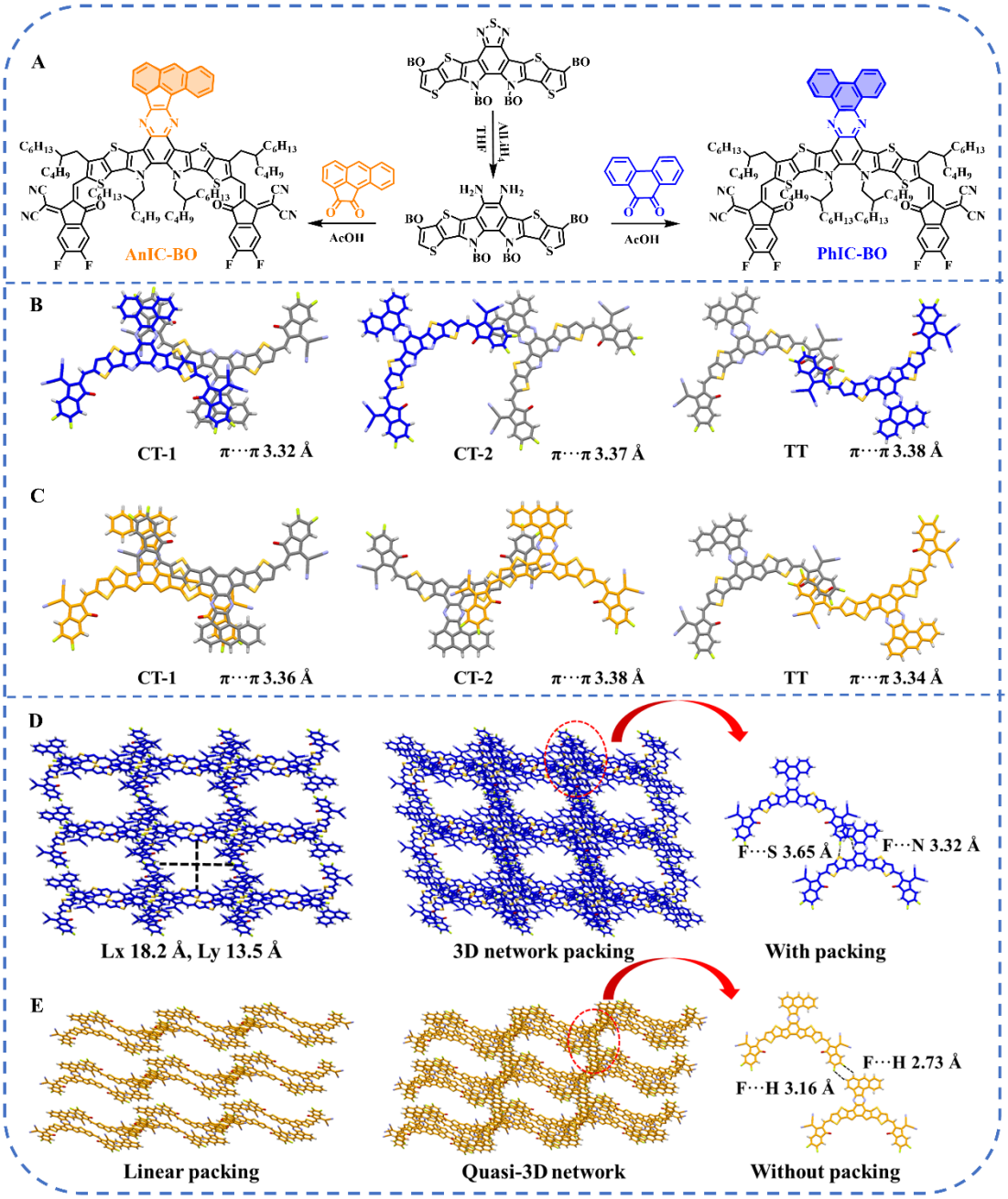

Figure 5. 1 (a) The synthetic routes of PhIC-BO and AnIC-BO. The single crystal packing arrangement of (b) PhIC-BO and (c) AnIC-BO. The 3D network structure and intermolecular heteroatomic interaction of (d) PhIC-BO and (e) AnIC-BO.

5.3 Result & Discussion

5.3.1 Material synthesis and single-crystal structure

The chemical structure and synthetic route of AnIC-BO and PhIC-BO were shown in Figure 5. 1a. Detailed synthetic procedures were provided in the experimental section. The anthracene- and phenanthrene-extended central core was obtained by reducing benzothiadiazole, followed by a cyclization reaction between the amino groups and aceanthrylene-1,2-dione/phenanthrene-9,10-dione. The ionization energy (IE) of the acceptors was determined by ultraviolet photo-electron spectroscopy (UPS) (Figure 5. 2), which was measured to be -5.26 eV, -5.31 eV, and -5.69 eV for PhIC-BO, AnIC-BO, and L8-BO-X, respectively. Their corresponding optical bandgap was estimated by Ultraviolet-Visible (UV-vis) Spectroscopy, which was determined to be 1.49 eV, 1.48 eV, and 1.45 eV, respectively. All the acceptors displayed a complementary absorption profile with the polymer donor D18, and a more balanced D/A absorption intensity was observed in AnIC-BO and PhIC-BO ternary blends (Figure 5. 3).

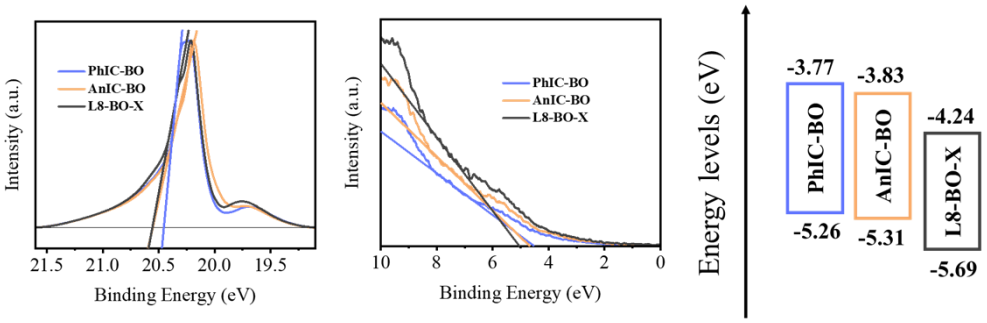

Figure 5. 2 The UPS spectra and the energy level diagram of AnIC-BO, PhIC-BO, and L8-BO-X.

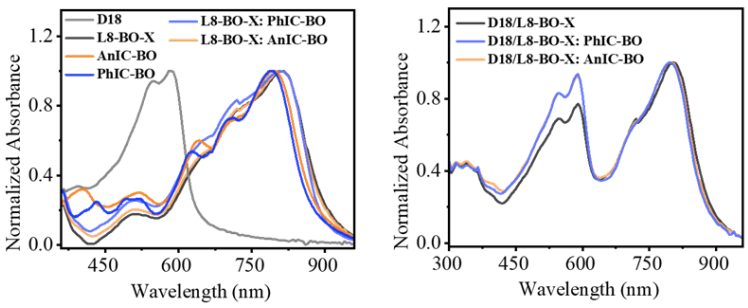

Figure 5. 3 The normalized absorption of the AnIC-BO- and PhIC-BO-based neat and blend films.

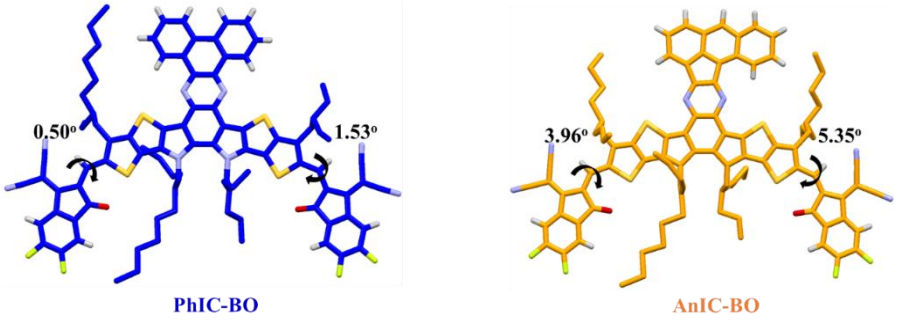

Figure 5. 4 The dihedral angle of PhIC-BO and AnIC-BO from single crystal.

The single crystal of two acceptors was cultivated and analyzed to understand their molecular packing and crystal structure. The phenanthrene-extended PhIC-BO gives a relatively rigid and planar conformation with the dihedral angle between the molecular backbone and end groups of 0.50° and 1.53°, which was 3.96° and 5.35° for AnIC-BO (Figure 5. 4). The molecular packing mode was studied by detecting the interaction between two adjacent molecules (Figure 5. 1b-c). Both acceptors showed three packings, two core-to-terminal group packing modes (CT-1 and CT-2) and one terminal group-to-terminal group packing mode (TT). CT-1 and TT packing modes were similar for the two acceptors but with different packing distances, where PhIC-BO gave a π-π distance of 3.32 Å for CT-1 packing and 3.38 Å for TT packing, while AnIC-BO displayed a π-π distance of 3.36 Å for CT-1 packing and 3.34 Å for TT packing. Their different packing motif was reflected by CT-2 packing, where PhIC-BO showed a small overlap area between the terminal group and phenanthrene central core with the π-π distance of 3.37 Å, whereas the CT-2 packing of AnIC-BO is similar to CT-1 packing but with a tilt angle, exhibiting a large overlapping between two molecules with the π-π distance of 3.38 Å. Additionally, PhIC-BO displayed F···S (3.65 Å) and F···N (3.32 Å) intermolecular heteroatomic interactions (Figure 5. 1d). However, no heteroatomic interaction was detected in AnIC-BO (Figure 5. 1e). As a result, PhIC-BO functioned by synergistic H- and J-aggregation and multiple intermolecular heteroatomic interactions displayed a typical 3D network structure with an elliptical framework of 18.2 Å (Lx) and 13.5 Å (Ly). As a comparison, AnIC-BO gave a linear packing pattern due to the lack of heteroatomic packing, forming a quasi-3D network packing structure.

PhIC-BO's preferred 3D interpenetrating network is expected to afford a more efficient charge transport pathway than the linear-packed AnIC-BO and collaborate well with conventional Y-series acceptors.

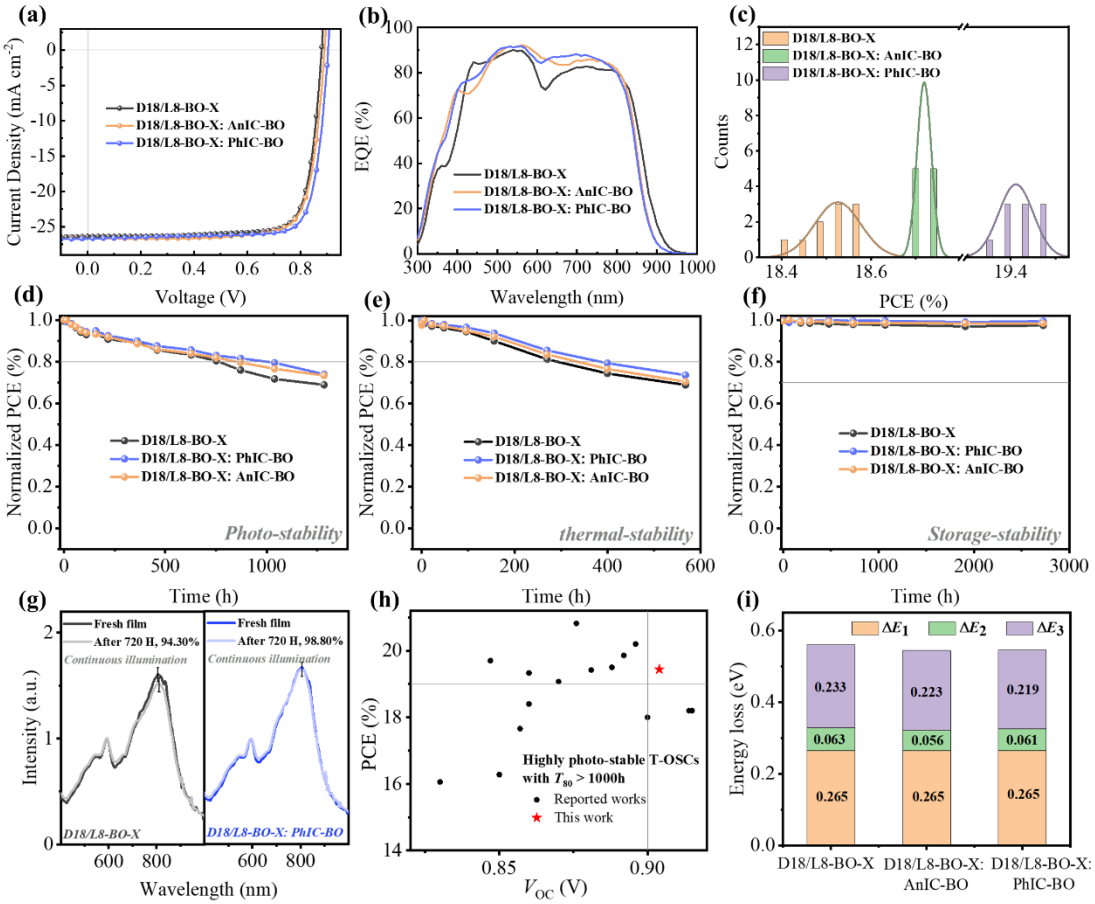

Figure 5. 5 (a) *J-V* curves, (b) EQE curves, (d) histogram, (d) photo-stability, (e) thermal stability, and (f) storage stability for the binary and AnIC-BO- and PhIC-BO-based ternary devices. (g) Absorption decay of the binary and PhIC-BO-based ternary active layer under continuous illumination. (h) Summary of the reported ternary OSCs with T_{80} for photo-stability larger than 1000 h. (i) The histograms of ΔE_1, ΔE_2, and ΔE_3 for corresponding devices.

5.3.2 Device performance, stability, and energy loss analysis

The OSC devices were fabricated to give an insight into the photovoltaic properties of two 2D acceptors in collaboration with other components. The highly crystalline donor D18 was adopted to fabricate the Q-PHJ devices with the structure of ITO/

PEDOT: PSS/donor/acceptor(s)/PDINN/Ag. The detailed device fabrication process was provided in the supporting information. A variety of ratios of the guest acceptors were estimated, and the optimized ratio was determined to be 10% for D18/L8-BO-X: PhIC-BO and 5% for D18/L8-BO-X: AnIC-BO (Table 5. 1-

Table 5. 2). After introducing PhIC-BO and AnIC-BO, an obvious increment in V_{OC} was observed. The pristine D18/L8-BO-X devices showed a PCE of 18.60% with an outstanding FF of 80.19% (Figure 5. 5a and Table 5. 3). For the optimized PhIC-BO ternary devices, the highest PCE of 19.44% was achieved with a V_{OC} of 0.904 V, a FF of 80.61%, and a J_{SC} of 26.70 mA cm^{-2}. For AnIC-BO-based devices, a PCE of 19.01% was achieved in 5%-doped devices, and 18.77% was achieved for 10%-doped devices. It was noted that both PCE and FF declined with the increasing ratio of AnIC-BO, indicating the incompatibility between AnIC-BO and the host component, which was ascribed to its linear-packed crystal structure and inferior charge transport pathway.

Table 5. 1 The PV parameters of D18/ L8-BO-X: PhIC-BO ternary devices with different acceptor ratios.

PhIC-BO content	V_{OC} **(V)**	**FF (%)**	J_{SC} **(mA cm^{-2})**	**PCE (%)**
0%	0.877	80.72	26.16	18.52
5%	0.886	80.30	26.62	18.94
10%	0.898	79.95	26.81	19.25
20%	0.910	79.08	26.11	18.79
40%	0.922	74.17	25.00	17.10

Table 5. 2 The PV parameters of D18/ L8-BO-X: AnIC-BO ternary devices with different acceptor ratios.

AnIC-BO content	V_{OC} **(V)**	**FF (%)**	J_{SC} **(mA cm^{-2})**	**PCE (%)**
0%	0.877	80.72	26.16	18.52
5%	0.883	80.12	26.87	19.01
10%	0.890	79.12	26.66	18.77
20%	0.906	75.52	26.00	17.79
40%	0.919	68.97	25.03	15.86

Table 5. 3 The *J-V* parameters of the binary and AnIC-BO- and PhIC-BO-based ternary devices.

Active Layer	V_{OC} (V)	FF (%)	J_{SC} (mA cm^{-2})	PCE (%)	J_{SC}^{cal} (mA cm^{-2})
D18/L8-BO-X	0.879 (0.880±0.004)	80.19 (79.96±0.77)	26.37 (26.34±0.25)	18.60 (18.53±0.05)	25.37
D18/L8-BO-X: 10% AnIC-BO	0.890 (0.890±0.002)	79.12 (80.13±0.51)	26.66 (26.25±0.18)	18.77 (18.72±0.02)	25.67
D18/L8-BO-X: 10% PhIC-BO	0.904 (0.899±0.003)	80.61 (80.56±0.63)	26.70 (26.80±0.21)	19.44 (19.41±0.04)	25.80

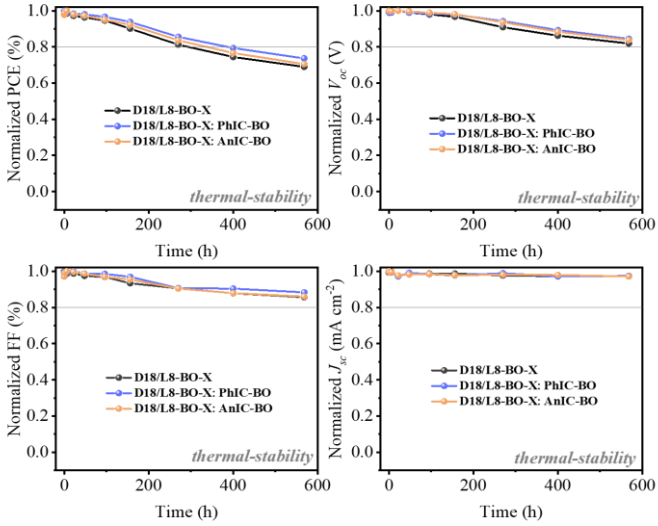

Figure 5. 6 The thermal stability for the binary and AnIC-BO- and PhIC-BO-based ternary devices.

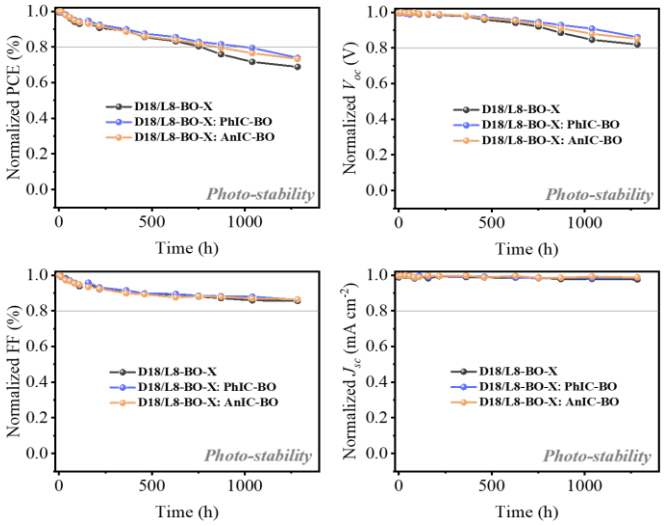

Figure 5. 7 The Photo-stability for the binary and AnIC-BO- and PhIC-BO-based ternary devices.

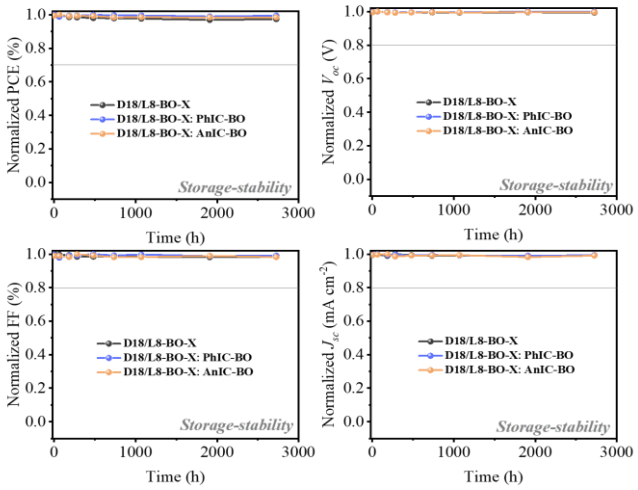

Figure 5. 8 The storage stability for the binary and AnIC-BO- and PhIC-BO-based ternary devices.

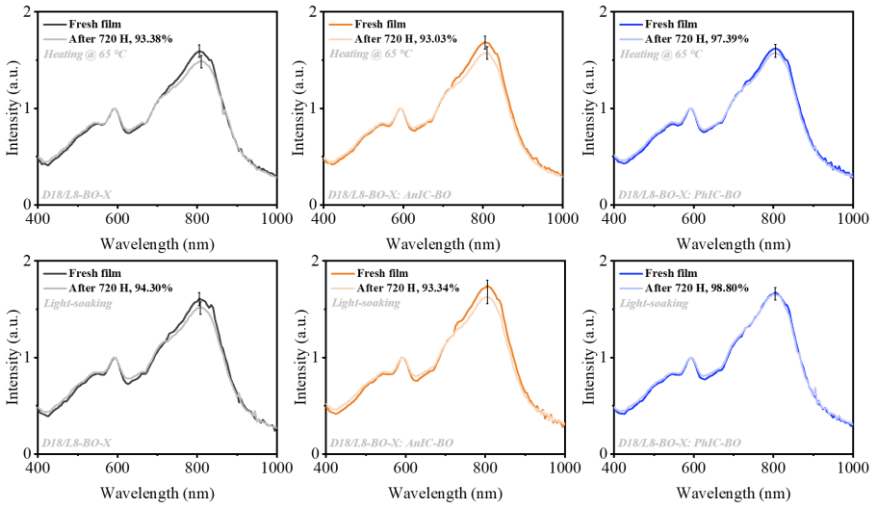

Figure 5. 9 Absorption decay for the binary and AnIC-BO- and PhIC-BO-based ternary active layer under different aging conditions.

The thermal stability, photostability, and storage stability were measured to investigate the effect of the highly crystalline acceptors on device operational stability (Figure 5. 5d-f). Thermal stability was tested under continuous heating at 65℃. The T_{80} (80% of the initial efficiency) for the binary devices is 293 h, and that for the PhIC-BO- and AnIC-BO-based ternary devices is 388 h and 324 h, respectively. The photo-stability was tested under continuous illumination, where the control devices declined to 80% of the initial efficiency after light-soaking for 759 hours. Surprisingly, the T_{80}

for PhIC-BO and AnIC-BO ternary devices improved to 1040 hours and 870 hours, respectively. For storage stability, all devices exhibited outstanding stability without burn-in loss, especially the PhIC-BO-based device, which maintained 99% of its initial PCE after 3000 hours. The variation of V_{OC}, FF, and J_{SC} along with time was extracted to study the device degradation pathway (Figure 5. 6-Figure 5. 8). It was found that the greatly declined V_{OC} and FF were responsible for device deterioration, and the introduction of PhIC-BO and AnIC-BO was feasible in alleviating V_{OC} and FF decay under photo and thermal stress. Material stability was studied by investigating the UV-vis absorption spectra of the fresh and aged films (Figure 5. 5g and Figure 5. 9). In D18/L8-BO-X binary film, the maximum absorption peak of L8-BO-X redshifted and maintained 93.38% and 94.30% of its initial intensity under continuous heating and continuous illumination for 720h, respectively. However, the PhIC-BO-based ternary film showed unchanged absorption peak position and maintained the peak intensity of 97.39% and 98.80% under continuous heating and illumination, respectively. For the AnIC-BO-based film, 93.03% and 93.34% of peak intensity were detected after aging, indicating the poor material stability of AnIC-BO. The result indicates that PhIC-BO with a high crystallinity and a more planar and rigid molecular conformation would afford higher material and morphological stability.

To further investigate the elevated V_{OC} by incorporating AnIC-BO and PhIC-BO, the energy loss analysis was conducted by Fourier-transform photocurrent spectroscopy (FTPS-EQE) and electroluminescence (EQE_{EL}) measurement (Figure 5. 10). The energy loss (ΔE) was described by three parts, $\Delta E = \Delta E_1 + \Delta E_2 + \Delta E_3$, where ΔE_1 referred to the radiative recombination above the bandgap described by the Shockley–Queisser (SQ) limit[304]. ΔE_2 is the radiative recombination below the bandgap. As the blackbody radiation at room temperature is strong in the low-energy region, any sub-gap absorption would cause large radiative loss. ΔE_3 comes from the nonradiative recombination and could be estimated by $\Delta E_3 = -kT \ln EQE_{EL}$. ΔE_3 was ascribed to the defect-assisted recombination, electron-phonon coupling from molecular vibration, and energy dissipated by thermal emission. D18/L8-BO-X binary devices gave a ΔE_2 of

0.066 eV and a ΔE_3 of 0.233 eV. For 10% AnIC-BO-based ternary devices, the ΔE_2 and ΔE_3 were suppressed to 0.058 eV and 0.223 eV, respectively. For PhIC-BO-based devices, the ΔE_2 and ΔE_3 were 0.056 eV and 0.219 eV, respectively. It was also noticed that ΔE_2 and ΔE_3 continuously decreased with the increasing ratio of PhIC-BO and AnIC-BO (Table 5. 4-

Table 5. 5), indicating the effectiveness of the highly crystalline materials in inhibiting radiative and non-radiative recombination loss. The Urbach energy (E_U) was also evaluated to give an insight into the molecular ordering and energetic disorder situation in blends. Compared with the binary devices with an E_U of 26.14 eV, the ternary devices gave a reduced energetic disorder with the E_U of 25.08 eV and 24.98 eV for AnIC-BO and PhIC-BO-based devices, respectively. The reorganization energy was evaluated by the Stokes shift, where L8-BO-X: PhIC-BO exhibited the smallest Stokes shift of 108 nm compared with L8-BO-X neat film (113 nm) and L8-BO-X: AnIC-BO (110 nm) (Figure 5. 11 and

Table 5. 6), implying a suppressed electron and intramolecular vibration in the ternary blends.[305] The reduced Urbach energy and reorganization energy indicated the effectiveness of crystallinity-tuning by highly crystalline guest acceptors in suppressing radiative and nonradiative recombination and elevating V_{OC}.

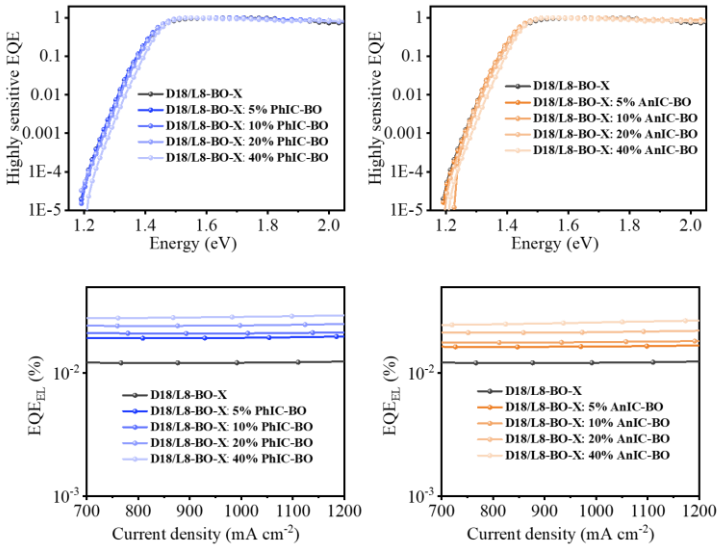

Figure 5. 10 FTPS-EQEs and EQE$_{EL}$s for the corresponding optimized binary and ternary devices.

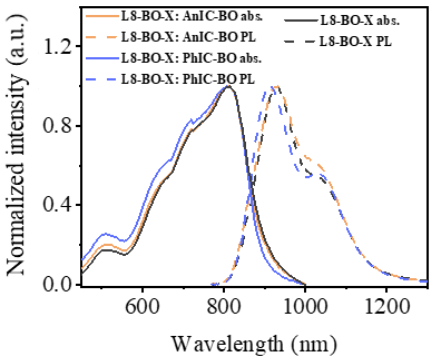

Figure 5. 11 Photoluminescence (PL) spectra of L8-BO-X: AnIC-BO and L8-BO-X: PhIC-BO films with different ratio (Excited at 750 nm).

Table 5. 4 Energy loss parameters of the control and AnIC-BO-based ternary devices

Content of AnIC-BO	band gap (eV)	qV_{OC} (eV)	ΔE (eV)	ΔE_1 (eV)	ΔE_2 (eV)	ΔE_3 (eV)	E_U (meV)
0%	1.441	0.880	0.561	0.265	0.063	0.233	27.08
5%	1.435	0.885	0.550	0.265	0.060	0.225	26.47
10%	1.436	0.892	0.544	0.265	0.056	0.223	26.23
20%	1.441	0.903	0.538	0.265	0.055	0.218	25.96
40%	1.449	0.919	0.530	0.266	0.049	0.215	24.54

Table 5. 5 Energy loss parameters of the control and PhIC-BO-based ternary devices

Content of PhIC-BO	band gap (eV)	qV_{OC} (eV)	ΔE (eV)	ΔE_1 (eV)	ΔE_2 (eV)	ΔE_3 (eV)	E_U (meV)
0%	1.441	0.880	0.561	0.265	0.063	0.233	27.08
5%	1.437	0.889	0.548	0.265	0.062	0.221	27.01
10%	1.438	0.893	0.545	0.265	0.061	0.219	26.24
20%	1.440	0.901	0.539	0.265	0.059	0.215	26.01
40%	1.452	0.922	0.530	0.266	0.053	0.211	24.92

Table 5. 6 The maximum absorption peak, maximum emission peak, and Stokes shift extracted from UV-vis absorption spectra and PL spectra.

Component	$\lambda_{max, abs}$ (nm)	$\lambda_{max, PL}$ (nm)	Stokes shift (nm)
L8-BO-X	815	928	113
L8-BO-X: AnIC-BO	815	925	110
L8-BO-X: PhIC-BO	805	913	108

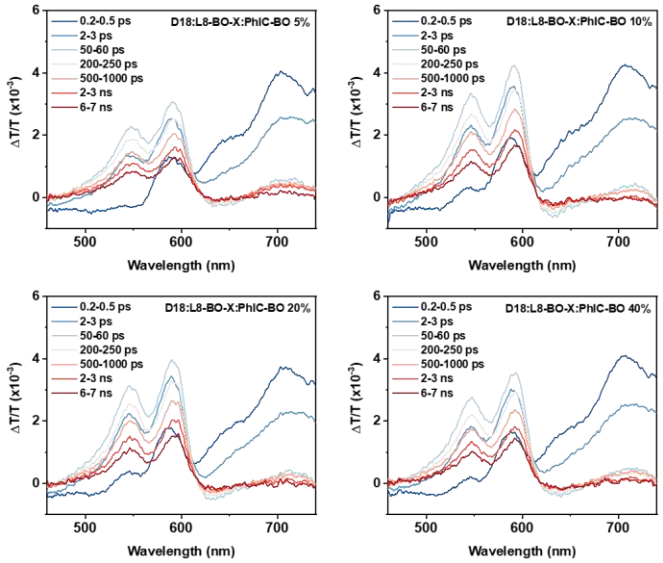

Figure 5. 12 TA spectra with various decay times of D18/L8-BO-X: PhIC-BO films with different ratios.

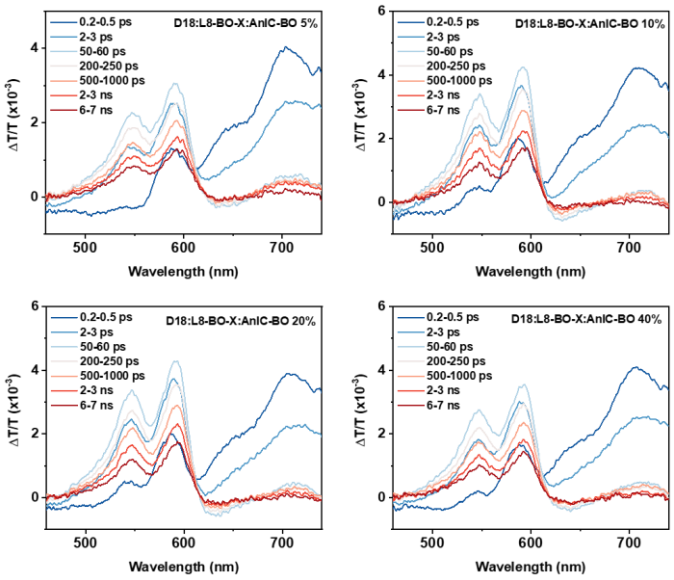

Figure 5. 13 TA spectra with various decay times of D18/L8-BO-X: AnIC-BO films with different ratios.

5.3.3 Charge carrier dynamics

The transient absorption (TA) was measured to study the charge transfer process in the blends. The peaks at 550 nm - 590 nm were ascribed to the ground state bleaching (GSB) signals of D18, and the peak at around 700 nm was the GSB signal of acceptors (Figure

5. 12-Figure 5. 13). It was observed that the donor GSB peak arises with the relaxation of the acceptor peak when selectively exciting acceptors, indicating the efficient hole transfer from the acceptor to the donor[306]. The detailed charge transfer process was studied by tracking the donor GSB signal (Figure 5. 14c-d). For D18/L8-BO-X devices, it takes 113 ps to reach a peak value, while only 21 ps and 22 ps were needed for PhIC-BO and AnIC-BO ternary devices, respectively. Therefore, the two 2D acceptors are highly effective in facilitating charge transfer and charge generation rate. It was also observed that the fastest charge generation rate occurs when the doping ratio is 5% for AnIC-BO and 10% for PhIC-BO (Figure 5. 15), coincident with their device performance.

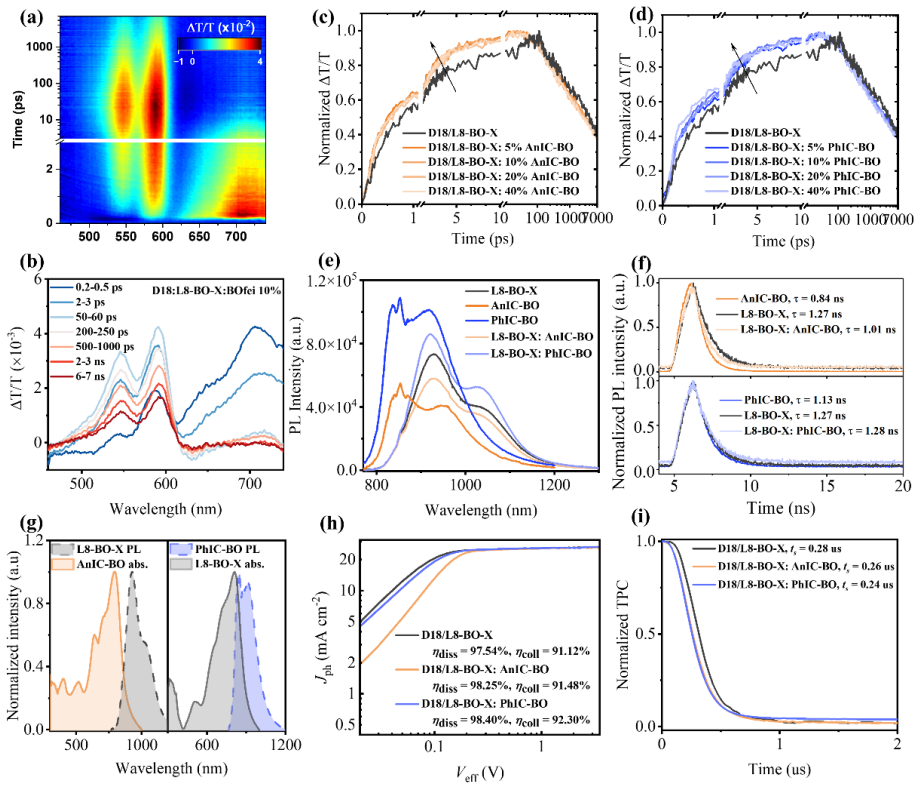

Figure 5. 14 (a) The TA image and (b) TA spectra with various delay times of D18/L8-BO-X: PhIC-BO blend film. The hole-transfer processes in (c) AnIC-BO- and (d) PhIC-BO-based films with different ratios. (e) The PL intensity of the neat and mixed acceptor. (f) The FRET process in AnIC-BO: L8-BO-X and PhIC-BO: L8-BO-X films. (g) Exciton lifetime of the corresponding films. (h) Charge dissociation and collection efficiency, and (i) TPC curves of the corresponding devices.

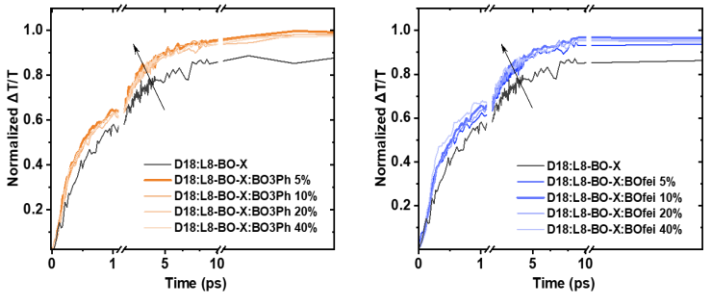

Figure 5. 15 The magnified hole-transfer processes in AnIC-BO- and PhIC-BO-based films with different ratios.

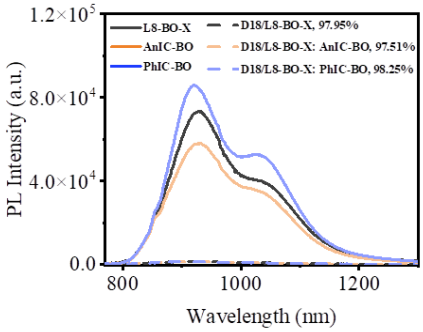

Figure 5. 16 Steady-state PL spectra of the acceptor films and the corresponding D/A blend films with the excitation wavelength of 750 nm.

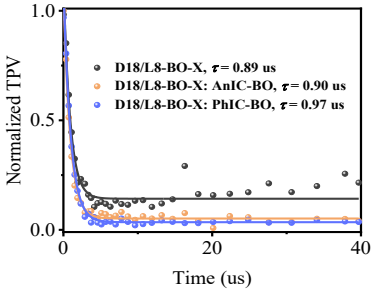

Figure 5. 17 Normalized TPV curves for corresponding binary and ternary devices.

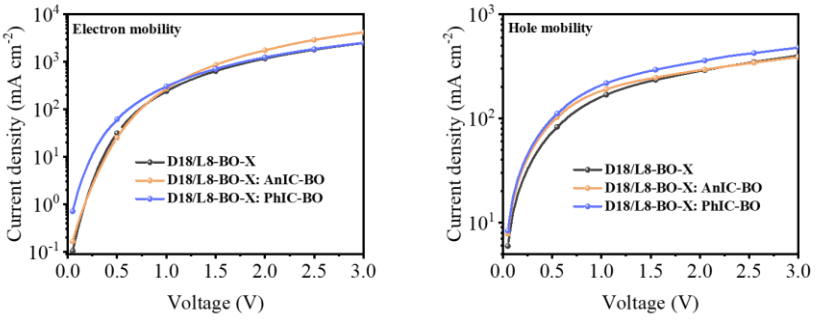

Figure 5. 18 Charge mobility of corresponding binary and ternary devices.

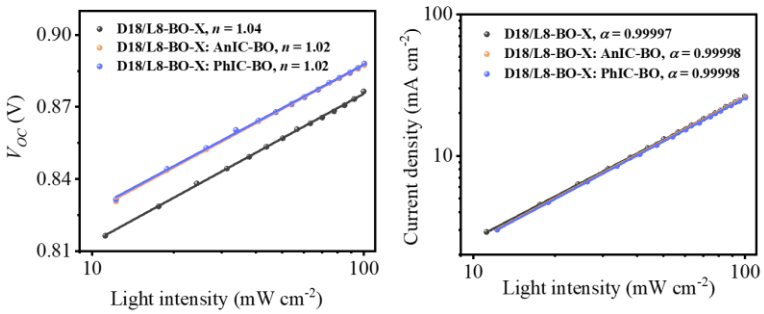

Figure 5. 19 The recombination situation in the corresponding devices.

Table 5. 7 The sweeping out time and carrier lifetime from TPC and TPV measurement.

Active layer	Carrier lifetime τ (us)	Sweeping out time t_s (us)
D18/L8-BO-X	0.89	0.28
D18/L8-BO-X: AnIC-BO	0.90	0.26
D18/L8-BO-X: PhIC-BO	0.97	0.24

Table 5. 8 The charge mobility of the corresponding binary control and AnIC-BO- and PhIC-BO-based ternary blend films.

Active Layer	Electron mobility μ_e ($cm^2V^{-1}s^{-1}$)	Hole mobility μ_h ($cm^2V^{-1}s^{-1}$)	μ_e/μ_h
D18: L8-BO-X	5.88×10^{-4}	5.40×10^{-4}	1.09
D18: L8-BO-X: AnIC-BO	6.66×10^{-4}	6.17×10^{-4}	1.08
D18: L8-BO-X: PhIC-BO	7.42×10^{-4}	7.00×10^{-4}	1.06

The photoluminescence measurement was further applied to study the energy and charge transfer efficiency between active layer components. The excitation wavelength was determined to be 550 nm for the donor and 750 nm for the acceptors. It was noticed that the PhIC-BO neat film displayed a higher PL intensity and the AnIC-BO neat film showed a lower PL intensity compared with the L8-BO-X neat film. The mixed acceptor film gave a moderate PL intensity located between their corresponding neat films (Figure 5. 14e), indicating L8-BO-X an energy donor for AnIC-BO and an energy acceptor for PhIC-BO. The result was further confirmed by the time-resolved photoluminescence (TRPL) (Figure 5. 14f). The exciton lifetime of AnIC-BO: L8-BO-

X is 1.01 ns, located between AnIC-BO (0.84 ns) and L8-BO-X (1.27 ns) neat film, indicating an energy transfer from L8-BO-X to AnIC-BO. The PhIC-BO: L8-BO-X film gave a larger exciton lifetime of 1.28 ns than the L8-BO-X neat film, implying an energy transfer from PhIC-BO to L8-BO-X. According to their absorption and PL spectra (Figure 5. 14g), the overlap between L8-BO-X's PL and AnIC-BO's absorption is small, indicating less efficient Förster resonance energy transfer (FRET) from L8-BO-X to AnIC-BO, while the overlap between PhIC-BO's PL and L8-BO-X's absorption is relatively large, indicating PhIC-BO a good energy donor and L8-BO-X a good energy acceptor and a highly efficient FRET. The PL quenching efficiency was calculated according to the PL intensity of the acceptor films and the corresponding D/A blends (Figure 5. 16). The significant PL quenching in the blends indicates efficient charge transfer between the donor and the acceptors. The calculated PL quenching efficiency in the D18/L8-BO-X binary blend is 97.95%, and that in PhIC-BO and AnIC-BO ternary films is 98.25% and 97.51%, respectively. The more efficient charge transfer and energy transfer efficiency in PhIC-BO-based film explained its highest photocurrent and the best device performance.

The J_{ph}-V_{eff} plot was employed to describe the charge dissociation (η_{diss}) and collection (η_{coll}) efficiency in blends.[118] The D18/L8-BO-X devices showed a η_{diss} and η_{coll} of 97.54% and 91.12%, respectively (Figure 5. 14h). A higher η_{diss} and η_{coll} values were obtained in ternary blends, which were 98.25% and 91.48% for D18/L8-BO-X: AnIC-BO and 98.40% and 92.30% for D18/L8-BO-X: PhIC-BO, respectively. The TPV and TPC were applied to determine the charge carrier lifetime (τ) and sweeping out times (t_s). It was found that two guest acceptors effectively elongated the charge carrier lifetime in blends, where the binary devices gave a carrier lifetime of 0.89 us and which increased to 0.90 us and 0.97 us in AnIC-BO and PhIC-BO ternary devices (Figure 5. 17 and Table 5. 7), respectively. Additionally, the abbreviated charge extraction time was detected in the ternary device, which was 0.28 us in the control device and shortened to 0.26 us and 0.24 us for the AnIC-BO- and PhIC-BO-based device (Figure 5. 14i), respectively. The SCLC method was employed to study the

charge transport property of the binary and ternary devices (Figure 5. 18). All devices gave balanced electron mobility (μ_e) and hole mobility (μ_h) with the μ_e/μ_h ratio of 1.09, 1.08, and 1.06 for D18/L8-BO-X, D18/L8-BO-X: AnIC-BO, and D18/L8-BO-X: PhIC-BO, respectively (

Table 5. 8). However, largely increased charge mobility was observed in the highly crystalline acceptor-doped devices, where PhIC-BO-based ternary devices showed the highest μ_e and μ_h of 7.42 × 10^{-4} $cm^2V^{-1}s^{-1}$ and 7.00 × 10^{-4} $cm^2V^{-1}s^{-1}$, respectively and AnIC-BO-based devices gave a relatively higher mobility of 6.66 × 10^{-4} $cm^2V^{-1}s^{-1}$ and 6.17 × 10^{-4} $cm^2V^{-1}s^{-1}$ than the binary device with the μ_e and μ_h of 5.88 × 10^{-4} $cm^2V^{-1}s^{-1}$ and 5.40 × 10^{-4} $cm^2V^{-1}s^{-1}$, respectively. The light intensity dependence was employed to evaluate device charge recombination (Figure 5. 19). All devices showed limited charge recombination, and the highly crystalline guest acceptors were able to further suppress the trap-assisted and bimolecular recombination.

5.3.4 Vertical phase separation

As shown in Figure 5. 20a, the quasibilayer structure was employed in this work, which has been proven to be effective in achieving high device performance and superior device stability. The cross-section scanning electron microscopy (SEM) was measured to reveal the vertical microstructure of the Q-PHJ active layer (Figure 5. 20b), where D/A phases existed independently with distinguishable interfaces, suggesting relatively pure donor and acceptor domains. The vertical phase separation was further studied by dynamic X-ray photoelectron spectroscopy (DXPS). To better demonstrate and distinguish the donor and acceptor layers, the upper acceptor material was replaced by BTP-eC9 featuring a characteristic element chlorine (Cl), where the other processing conditions were strictly kept the same as the OSCs in this manuscript. With the evolution of etch time, the Cl 2p peak disappeared (Figure 5. 21) and the F 1s peak appeared (Figure 5. 20c) at around 5min, implying a typical D/A bilayer distribution where the acceptor is located at the top of the active layer and the donor is enriched in

the bottom. As a comparison, there is no obvious fluctuation of the Cl 2p peak in the BHJ active layer (Figure 5. 22).

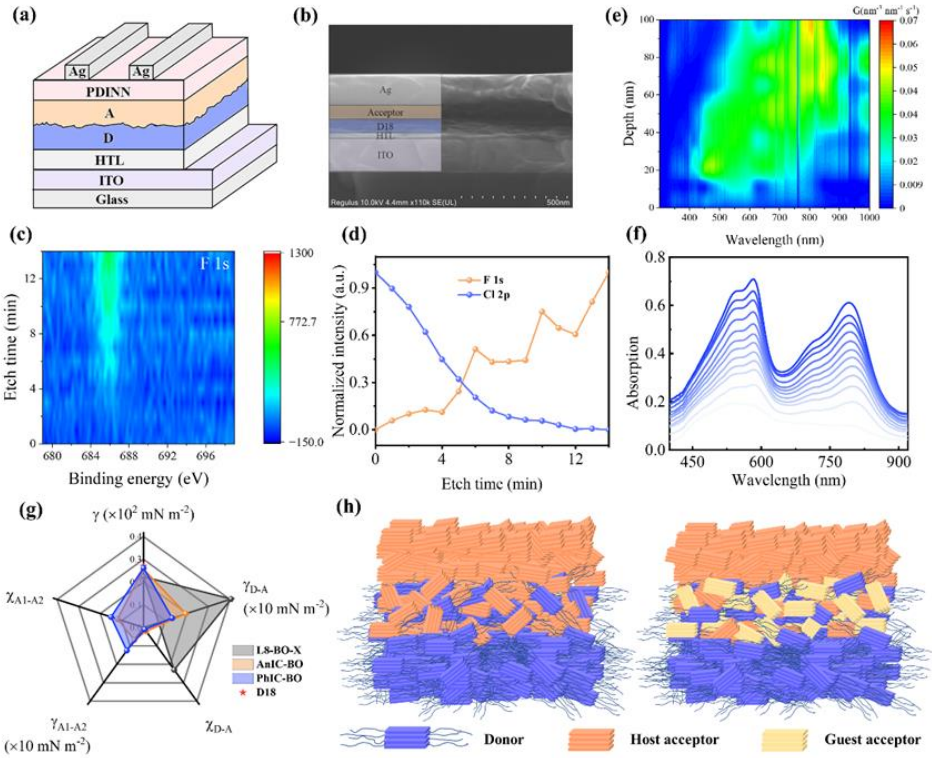

Figure 5. 20 (a) Device structure schematic diagram. (b) Cross-section SEM image of the Q-PHJ device. (c) DXPS spectra of the Q-PHJ device with F 1s signal (D18/BTP-eC9). (d) Normalized intensity of F 1s and Cl 2p content in the active layer of Q-PHJ device (D18/BTP-eC9). (e) Film-depth dependent light absorption spectra for the PhIC-BO ternary film. (f) Exciton generation contours for D18/L8-BO-X: PhIC-BO films. (h) The summary of the surface energy, interfacial energy, and interaction parameters from the contact angle measurement. (i) The Schematic diagram of vertical distribution in the binary and ternary blend.

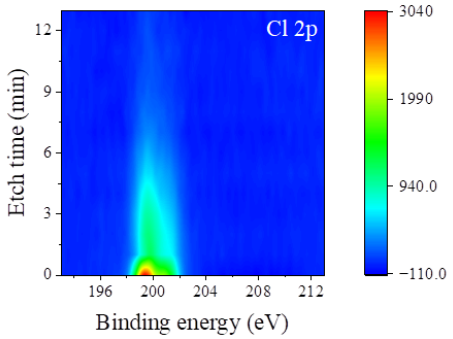

Figure 5. 21 DXPS spectra of the Q-PHJ device with Cl 2p signal (D18/BTP-eC9).

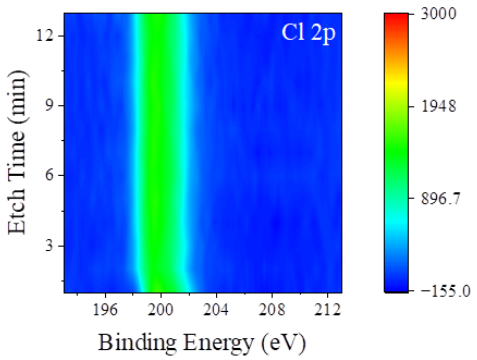

Figure 5. 22 DXPS spectra of the BHJ device with Cl 2p signal (D18: BTP-eC9).

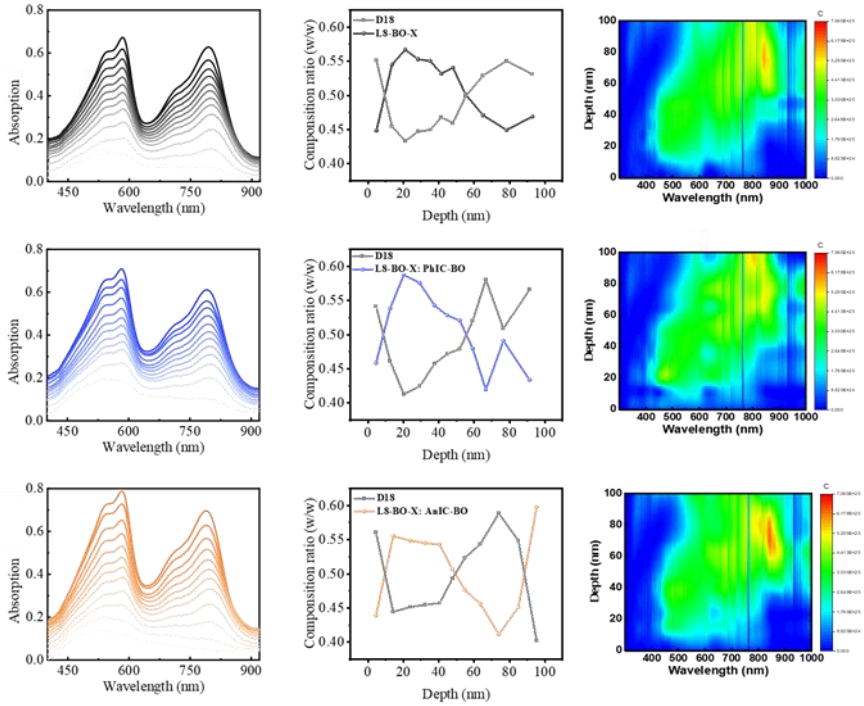

Figure 5. 23 The FLAS spectra, composition ratio, and exciton generation contours for the binary and AnIC-BO- and PhIC-BO-based ternary devices.

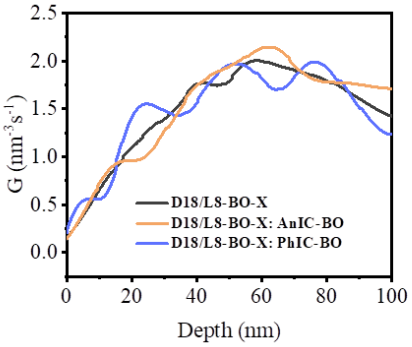

Figure 5. 24 The film depth dependence of simulated exciton generation rate for the binary and AnIC-BO- and PhIC-BO-based ternary devices.

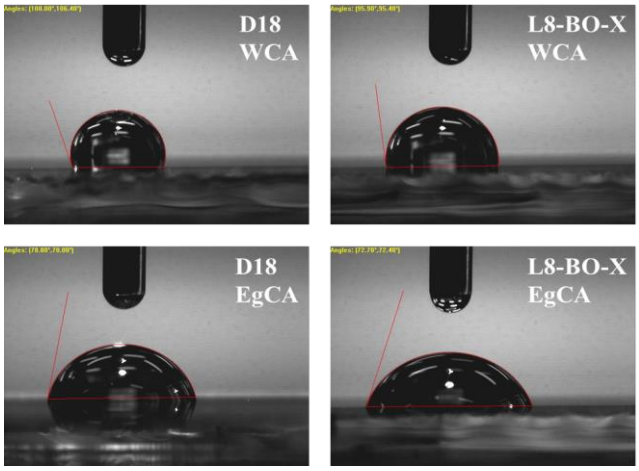

Figure 5. 25 Contact angle measurement of D18 and L8-BO-X neat film.

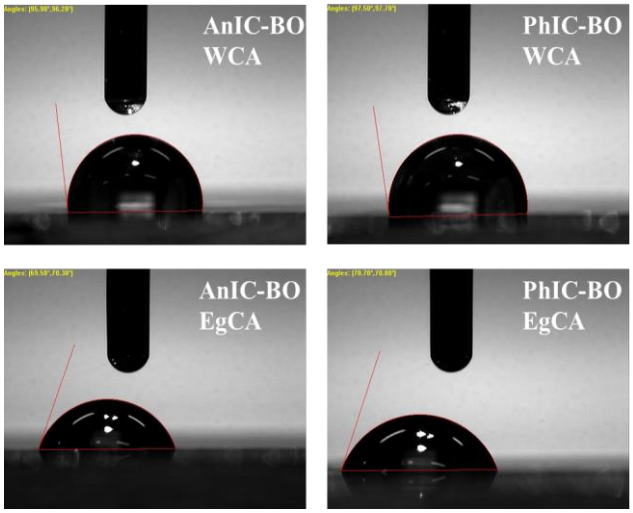

Figure 5. 26 Contact angle measurement of L8-BO-X: AnIC-BO films with different ratios.

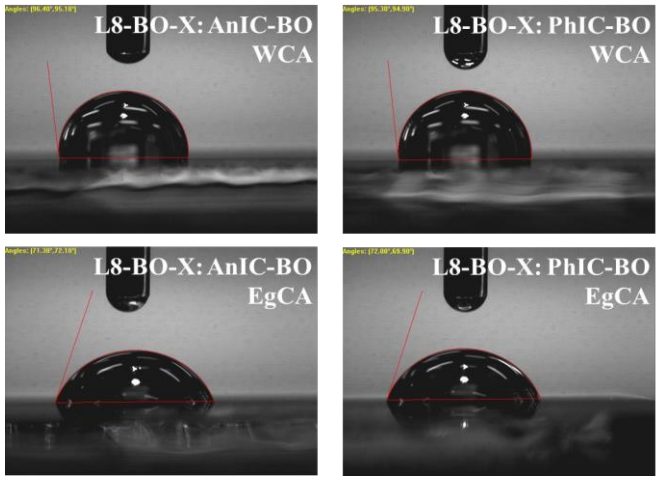

Figure 5. 27 Contact angle measurement of L8-BO-X: PhIC-BO films with different ratios.

Table 5. 9 Contact angle parameters, surface energy, interfacial tension (γ), and Flory-Huggins parameter (χ) of materials.

Material	WCA [°]	EgCA [°]	γ^d [mN m^{-1}]	γ^p [mN m^{-1}]	γ [mN m^{-1}]	γ_{D-A} [mN m^{-1}]	χ_{D-A}/K [a]	ω
D18	107.20	78.40	27.02	0.04	27.05	/	/	/
L8-BO-X	95.65	72.55	19.40	2.94	22.34	4.06	0.23	/
AnIC-BO	95.05	69.9	23.81	1.88	25.69	1.96	0.02	/
PhIC-BO	97.6	70.75	24.83	1.36	26.19	1.33	0.01	/
L8-BO-X: AnIC-BO	95.75	71.70	20.73	2.59	23.32	3.29	0.14	0.33
L8-BO-X: PhIC-BO	95.10	70.95	20.90	2.74	23.64	3.39	0.11	0.51

[a] K is a constant.

Table 5. 10 The interfacial tension (γ) and Flory-Huggins parameter (χ) between acceptors.

Material	γ [mN m^{-1}]	γ_{A1-A2} [mN m^{-1}]	χ_{A1-A2}/K [a]
L8-BO-X	22.34	/	/
AnIC-BO	25.69	0.68	0.12
PhIC-BO	26.19	1.25	0.15

[a] K is a constant.

The film-depth dependent light absorption spectroscopy (FLAS) was employed to detect the effect of two acceptors on vertical phase distribution. The absorption profiles and D/A composition ratio at different depths are shown in Figure 5. 23. A redshifted maximum absorption peak was observed from the top to the bottom of the film, indicating the various crystallinity at different depths and optimized charge transport channels[138]. By analyzing D/A ratios at different depths, it was found that the donor enriches at the bottom of the active layer and the acceptor enriches at the top, coincident with the SEM and DXPS results. By incorporating PhIC-BO and AnIC-BO, a slightly increased donor and acceptor ratio was detected at the bottom and the top of the active layer, respectively, indicating a relatively distinct Q-PHJ structure and improved domain purity in the ternary film, explaining the improved morphological stability. The exciton generation was simulated by combining FLAS with the optical transfer matrix.

It was found that the incorporation of PhIC-BO and AnIC-BO results in a higher exciton generation rate. The maximum exciton generation rate for D18/L8-BO-X occurs at 58 nm, and that for PhIC-BO- and AnIC-BO-based devices is at 52 nm and 62 nm (Figure 5. 24), respectively. Exciton generation at the central region favors highly efficient charge dissociation and extraction,[307] explaining the largest J_{SC} in PhIC-BO-based devices. It was observed that there are two additional G peaks at 25 nm and 76 nm for PhIC-BO-based devices, indicating highly efficient exciton generation at these positions. Given that highly crystalline materials possess a large exciton diffusion coefficient and long exciton diffusion length,[289] it is reasonable that these excitons would facilitate higher photocurrent in the highly crystalline acceptor-based devices.

The distribution of the third component was revealed by the two-solvent method (water and ethylene glycol (EG) contact angle (CA) measurement (Figure 5. 25-Figure 5. 27). The surface energy of D18, AnIC-BO, PhIC-BO, and L8-BO-X is determined to be 27.05 mN m^{-1}, 25.69 mN m^{-1}, 26.19 mN m^{-1}, and 22.34 mN m^{-1}, respectively (Table 5. 9). The miscibility between the guest acceptors and the host components was evaluated. The donor-acceptor interfacial energy ($\gamma_{D\text{-}A}$) and Flory-Huggins interaction parameter ($\chi_{D\text{-}A}$) were calculated to be 1.96 mN m^{-1} and 0.02K for AnIC-BO neat film, 1.33 mN m^{-1} and 0.01K for PhIC-BO neat film, and 4.06 mN m^{-1} and 0.23 for L8-BO-X neat film, respectively, indicating better miscibility between D18 and AnIC-BO/PhIC-BO than that between D18 and L8-BO-X (Figure 5. 20g). The $\gamma_{D\text{-}A}$ and $\chi_{D\text{-}A}$ was 3.29 mN m^{-1} and 0.14K for L8-BO-X: AnIC-BO film and 3.39 mN m^{-1} and 0.11K for L8-BO-X: PhIC-BO film, respectively, indicating that the participation of the two guest acceptors fine-tuned the surface energy of the host component and improved the miscibility between the donor and the acceptor. $\gamma_{A1\text{-}A2}$ and $\chi_{A1\text{-}A2}$ were further calculated to be 0.68 mN m^{-1} and 0.12K between L8-BO-X and AnIC-BO and 1.25 mN m^{-1} and 0.15K between L8-BO-X and PhIC-BO (Table 5. 10), indicating a good miscibility between the two guest components and the host acceptor. Further calculations of the wetting coefficient (ω) found that the guest acceptors tend to be in the middle of the donor and acceptor layer, where the ω was measured to be 0.33 and 0.51 for AnIC-BO

and PhIC-BO, respectively, indicating the guest acceptors are at the interface of the donor and the host acceptor.[122,308,309] Therefore, we could gave a diagram of the vertical composition distribution in the ternary blends (Figure 5. 20h), where the pure donor phase located at the bottom of the active layer and pure acceptor phase enriched at the top of the active layer, accompanied with a tiny BHJ region composed of the donor, the host acceptor and the third component. The third component functioned in the middle BHJ region, facilitating the exciton generation, charge transfer, energy transfer, charge dissociation, etc., explaining the largely increased device performance. Additionally, the two acceptors with high crystallinity and rigid molecular conformation afford higher material stability and limited molecular migration. Their gathering in the middle layer functioned as a protective layer to suppress the molecular migration and the molecular interdiffusion of the upper and lower layers, explaining the improved device stability.

Morphological analysis

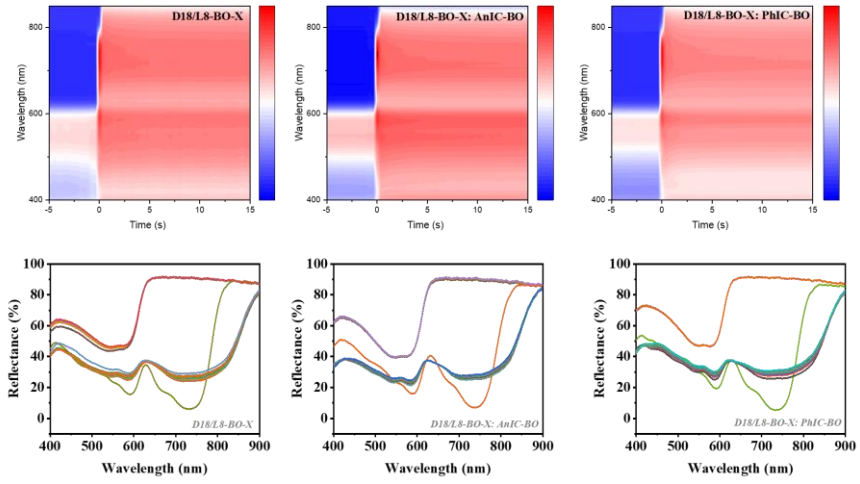

Figure 5. 28 The in situ 2D contour map and absorption profiles for AnIC-BO- and PhIC-BO-based ternary blends.

The in-situ UV-vis measurement was conducted to give an insight into the crystallization kinetics during film formation. The 2D projection contour maps and 1D

absorption profiles are shown in Figure 5. 28-Figure 5. 31. The phase transition process was investigated by tracking the peak intensity of the characteristic peak (737 nm for acceptors). Due to the fast evaporation of chloroform solvent and the existence of the crystallized D18, the film drying time for the upper layer was abbreviated within 0.5s, where the PhIC-BO-based film gave a film drying time of 0.34 s (Figure 5. 32b), slightly shorter than the D18/L8-BO-X binary film (0.35 s). However, the D18/L8-BO-X: AnIC-BO film displayed a delayed film formation time of 0.38 s. It was expected that the high crystallinity and poor solubility of PhIC-BO would make it precipitate out first to provide nucleation sites, facilitate the crystallization of L8-BO-X, and advance the film formation process. However, the incompatible crystal structure of AnIC-BO hindered the crystallization process and delayed the crystallization time. It was also noted that there is a gradual change in the peak intensity before the film is solidified (Figure 5. 32c), which was ascribed to the slow removal of the solid additive. As a comparison, the film without the solid additive showed a sharp and distinct turning point. The slow and gentle additive removal process was expected to induce D/A self-organization and more ordered molecular stacking.[304] The thermal annealing process was also recorded (Figure 5. 32d), where the decreased peak intensity was ascribed to the residual solvent removal.[310] The effect of the self-assembled monolayer hole transporting layer material 3-BPIC-F was also investigated by detecting the phase transition process of D18 with the characteristic peak at 585 (Figure 5. 32e). 3-BPIC-F was found to induce faster and regulated donor crystallization than PEDOT: PSS, which would be one of the reasons for the higher device performance in SAM-based devices.

GIWXAS measurement was conducted to investigate the molecular orientation and molecular packing in films. The 2D GIWAXS patterns and extracted 1D line profiles are shown in Figure 5. 32g and Figure 5. 33-Figure 5. 35. All the acceptors exhibited face-on orientation with distinct π-π stacking peaks. With the participation of two acceptors, it was found that the L8-BO-X: AnIC-BO film gave a larger *d*-spacing (3.58 Å) and smaller crystal coherent length (CCL) value (18.46 Å) than the L8-BO-X neat film (*d*-spacing = 3.55 Å; CCL = 19.52 Å) (Table 5. 11). The decreased crystallinity

was ascribed to the inferior linear-packed crystal structures. Conversely, the L8-BO-X: PhIC-BO film gave a reduced *d*-spacing (3.54 Å) and increased CCL (20.98 Å), indicating an enhanced crystallinity and a much more ordered molecular packing. For the D/A blend films, the guest acceptor-doped blends exhibited enhanced CCL and higher crystallinity (

Table 5. 12), where D18/L8-BO-X binary blend gave a *d*-spacing of 3.58 Å and a CCL of 18.74 Å, D18/L8-BO-X: AnIC-BO gave a *d*-spacing of 3.60 Å and a CCL of 19.12 Å, and D18/L8-BO-X: PhIC-BO gave a *d*-spacing of 3.58 Å and a CCL of 20.15 Å. The highest crystallinity of the PhIC-BO-based blend indicated the most favorable molecular packing and aggregation behavior induced by PhIC-BO.

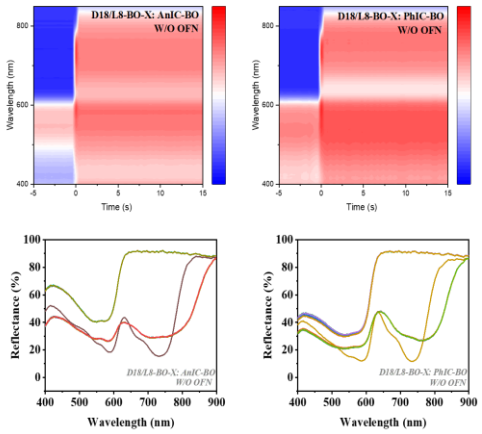

Figure 5. 29 The in situ 2D contour map and absorption profiles of D18/L8-BO-X: AnIC-BO and D18/L8-BO-X: PhIC-BO blend film without solid additive OFN.

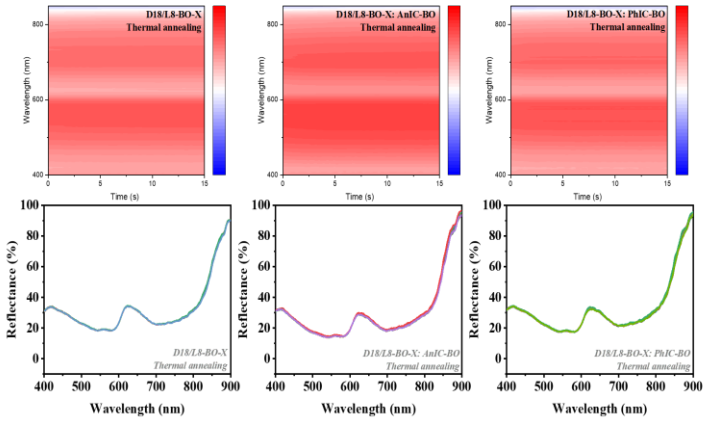

Figure 5. 30 The in situ 2D contour map and absorption profiles of D18/L8-BO-X, D18/L8-BO-X: AnIC-BO and D18/L8-BO-X: PhIC-BO blend film under thermal annealing.

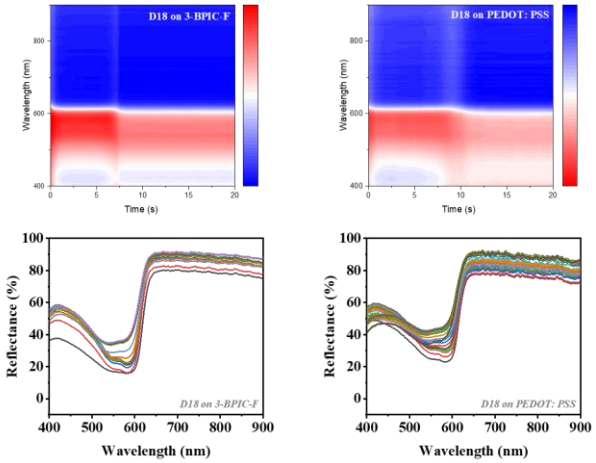

Figure 5. 31 The in situ 2D contour map and absorption profiles of D18 on 3-BPIC-F and PEDOT: PSS.

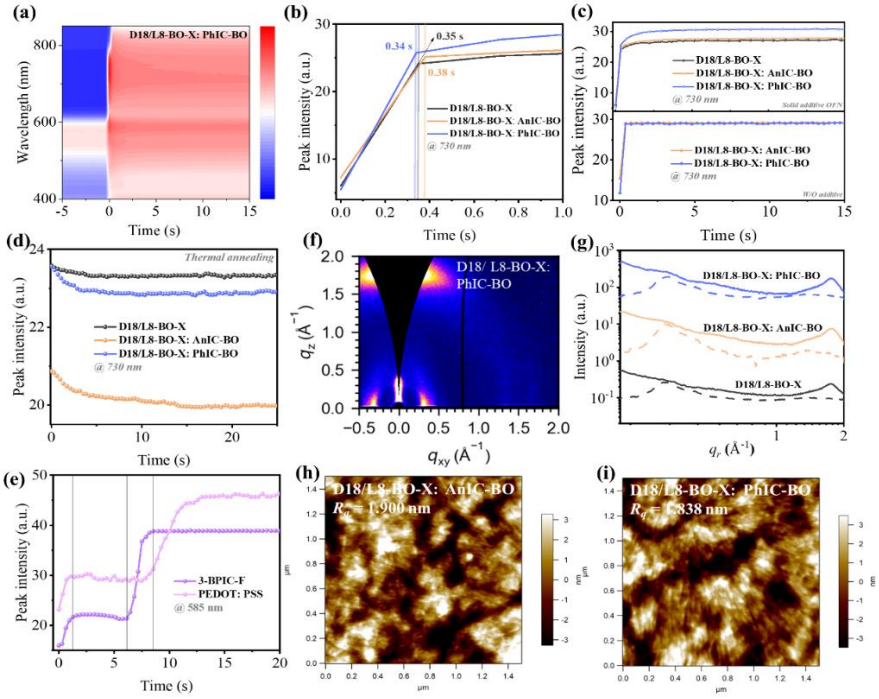

Figure 5. 32 (a) The in-situ 2D contour map of D18/L8-BO-X: PhIC-BO. The characteristic peak intensity versus time of (b) the binary control and AnIC-BO- and PhIC-BO-based ternary film, (c) films with and without solid additive, (d) films under thermal annealing, and (e) films on PEDOT: PSS and 3-BPIC-F. (f) The 2D GIWAXS pattern of D18/L8-BO-X: PhIC-BO. (g) The GIWAXS 1D line profiles of the corresponding binary control and AnIC-BO- and PhIC-BO-based ternary films (solid line: OOP direction; dash line: IP direction). AFM height images of (h) AnIC-BO- and (i) PhIC-BO- based ternary film.

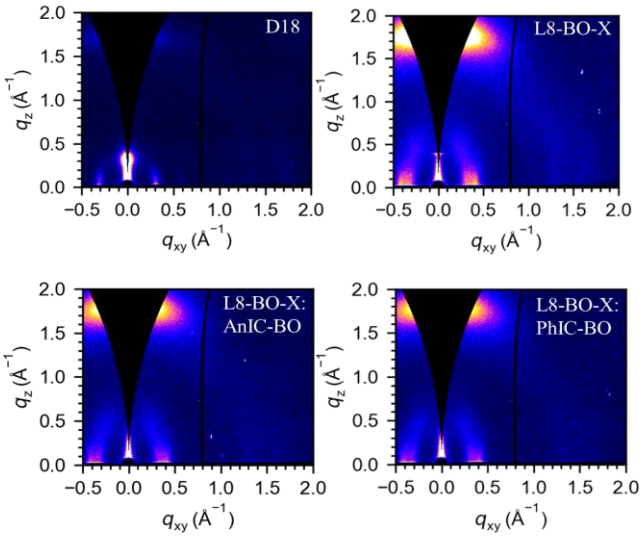

Figure 5. 33 2D GIWAXS patterns of the neat and mixed acceptor films.

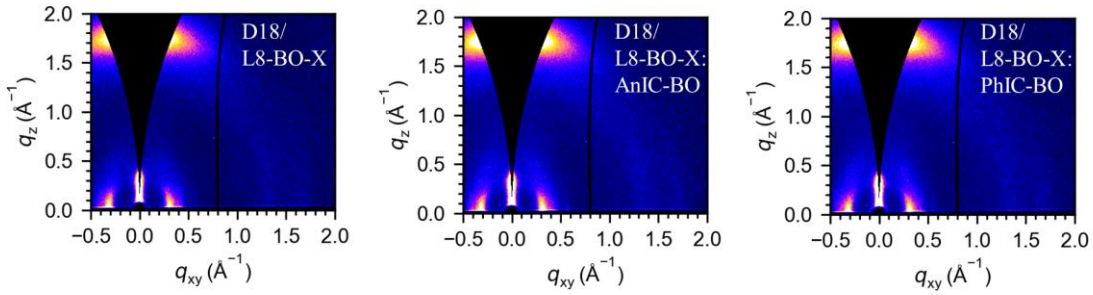

Figure 5. 34 2D GIWAXS patterns for the binary and AnIC-BO- and PhIC-BO-based ternary blend films.

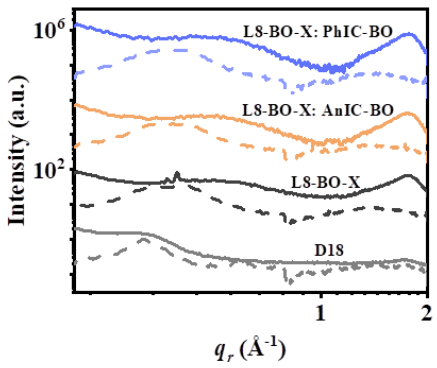

Figure 5. 35 The GIWAXS 1D line profiles of the neat and mixed acceptor films.

Table 5. 11 Summarized GIWAXS parameters of the (010) peak along the OOP direction of neat and mixed acceptor films.

Neat film - (010) peak	q_z (Å^{-1})	***d*-spacing (Å)**	**FWHM (Å^{-1})**	**Coherence length (Å)**
L8-BO-X	1.77	3.55	0.29	19.52
L8-BO-X: AnIC-BO	1.75	3.58	0.31	18.46
L8-BO-X: PhIC-BO	1.77	3.54	0.27	20.98

Table 5. 12 Summarized GIWAXS parameters of the (010) peak along OOP direction for the binary and AnIC-BO- and PhIC-BO-based ternary blend films.

blend film - (010) peak	q_z (Å^{-1})	***d*-spacing (Å)**	**FWHM (Å^{-1})**	**Coherence length (Å)**
L8-BO-X	1.76	3.58	0.30	18.74
L8-BO-X: AnIC-BO	1.75	3.60	0.30	19.12
L8-BO-X: PhIC-BO	1.75	3.58	0.28	20.15

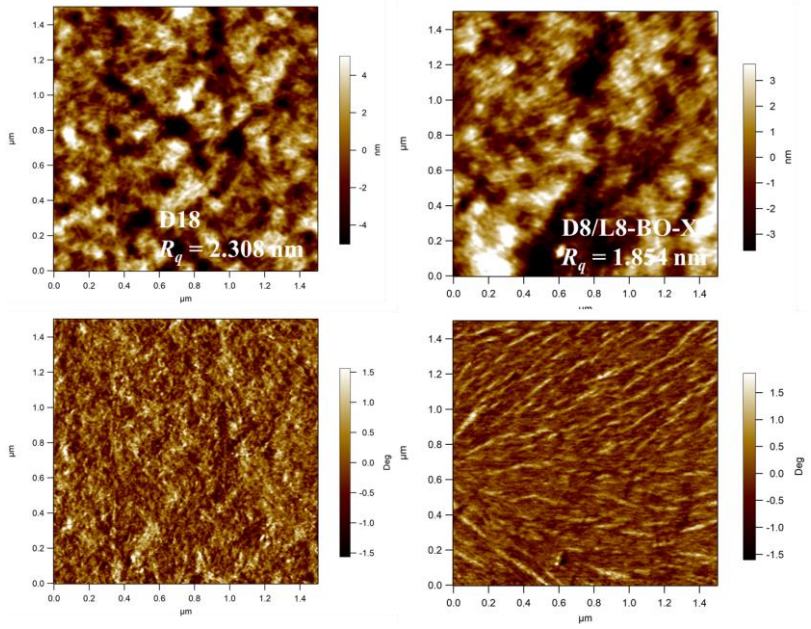

Figure 5. 36 AFM images for D18 neat film and binary control blend film.

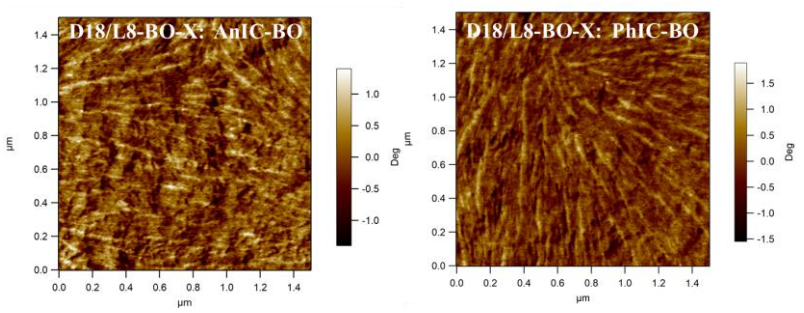

Figure 5. 37 AFM phase images for D18/L8-BO-X: AnIC-BO and D18/L8-BO-X: PhIC-BO blend film.

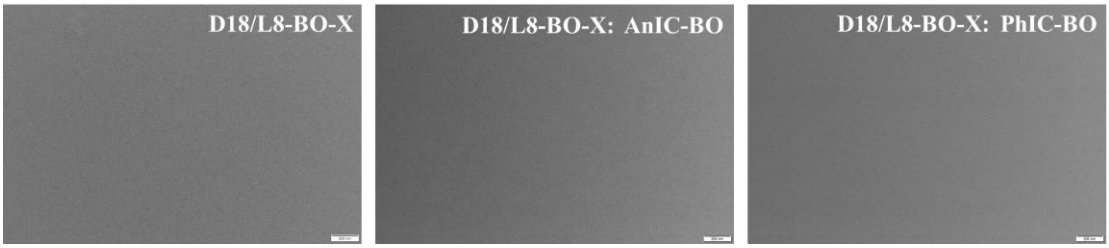

Figure 5. 38 TEM images for the binary and AnIC-BO- and PhIC-BO-based ternary blend films.

The tapping-mode AFM and TEM measurement was performed to detect the surface and bulk morphology of blends. The D18 neat film exhibited a distinctive fibril structure (Figure 5. 36), which was preserved in the blend films and largely profited charge separation and transport. The PhIC-BO-based blend gave a slightly decreased R_q of 1.838 nm than D18/L8-BO-X blends (R_q = 1.854 nm), indicating the optimal and smooth morphology in PhIC-BO ternary blends (Figure 5. 32h-i). Conversely, the increased R_q was detected in D18/L8-BO-X: AnIC-BO blends (1.900 nm), indicating the formation of relatively large aggregates. The TEM images showed the bulk morphology of the blends, where all blends gave fine and favorable nanoscale domains without obvious agglomerates, indicating the favorable film morphology of these blends (Figure 5. 38), especially the PhIC-BO-based ternary blend, where the improved molecular crystallinity and optimal film microstructure are synchronous achieved, implying the effectiveness of PhIC-BO in regulating film morphology, explaining its highest FF and device efficiency.

5.4 Conclusion

In summary, two highly crystalline 2D acceptors PhIC-BO and AnIC-BO were synthesized and employed to constructed the long-term operational highly efficient QHJ OSCs. The anthracene-extended AnIC-BO showed a linear molecular packing to form a quasis-3D crystal structure and the phenanthrene-extended PhIC-BO with multiple intermolecular interaction afforded a typical 3D network structure with an elliptical framework. Their difference in crystal structures induced distinct crystallization kinetics, degrees of crystallinity, and charge carrier dynamics in the ternary blends. The third component was found to function in the middle BHJ region of a p-i-n OSC, where they facilitate the exciton generation, energy and charge transfer, charge dissociation and transport, and suppression of recombination loss, improving device performance. Their high degree of crystallinity and rigid molecular conformation affords higher material stability by inhibiting molecular photo-oxidation degradation and higher morphological stability by optimizing domain purity and impeding molecular migration. As a result, the PhIC-BO-based devices achieved an outstanding PCE of 19.44% with the prominent operational stability (a T_{80} of 388h for thermal stability and 1040h for photostability, and a T_{99} of 3000 h for storage stability), lining in the top-ranking long-term stable ternary OSCs. This work unveils the working mechanism of improving device performance and stability by a third component in quasi-bilayer structure, guiding the further research on constructing long-term operational high-performance OSCs.

Chapter 6 Summary and Prospective

6.1 Summary

The OSCs' commercialization faces the problems of large radiative and nonradiative recombination loss, hard-controllable film aggregation kinetics and morphology in upscaling manufacturing, lagged device efficiency in the environmentally friendly nonhalogenated solvent, and inferior material and device stability. In this thesis, several works were conducted to provide possible strategies to address these issues.

In chapter 3, we developed a solubility-tuning strategy via multi-component to manipulate crystallization kinetics and aggregate sizes to achieve well-behaved phase separation in blade-coated blends. By incorporating BTP-4Cl, both ex-situ and in-situ investigations illustrated that the twisted molecular backbone of BTP-4Cl facilitates a dispersed and loose molecular distribution in the ternary solution. This leads to the formation of dispersed nuclei seeding sites and pre-aggregates, thereby advancing the crystallization process and achieving fine nanoscale phase domains. As a result, the blade-coated small-area OSCs achieved an outstanding PCE of 19.67% (19.76% for SC devices), which is the top-ranking efficiency among reported blade-coated OSCs. Overall, this work gave a new insight into the material selection criteria from the point of solubility control, and established the correlation between solubility, crystallization kinetics, and solid film microstructure, providing valuable guidance for achieving stable and high-performance eco-OSCs via open-air coating.

In chapter 4, two acenaphthene-expanded 2D acceptors were synthesized and systematically studied. The ATIC acceptors demonstrated high crystallinity, particularly ATIC-BO, which, despite its bulky-branched side chain, unexpectedly adopted a more planar conformation. Their distinct chemical structure led to unique molecular packing modes and crystal structures, with ATIC-C11 forming an elliptical framework and ATIC-BO displaying a rectangular one. The ATIC acceptors exhibited low reorganization energy and Urbach energy, which are beneficial for suppressing sub-gap absorption and nonradiative recombination losses. Through detailed investigation into

carrier kinetics and morphologies, it was found that the ATIC acceptors underwent the parallel-like model, providing additional pathways for charge separation and transport. However, the strong aggregation and poor compatibility of ATIC-BO led to large aggregates that hindered CT and dissociation, resulting in lower FF and JSC.In contrast, ATIC-C11, with its optimal crystallinity and compatibility, effectively regulated crystalline kinetics to achieve more ordered molecular packing and nanoscale phase separation. This, combined with the reduced energetic disorder, improved CT and dissociation, and enhanced carrier lifetime, allowed ATIC-C11based ternary devices to achieve a high efficiency of 19.28%, with great potential for scalability and stability. To the best of our knowledge, this is the top-ranking efficiency among nonhalogenated solvent-processed OSCs. This work not only presents an outstanding halogen-free solvent-processed OPV based on the "structure–performance–property" relationship but also offers new insights into material design and selection criteria for achieving highly efficient and stable OPVs, paving the way for OPV industrialization.

In chapter 5, two highly crystalline 2D expanded acceptors PhIC-BO and AnIC-BO were synthesized and studied by characterizing their physiochemical and photovoltaic properties. It was found that the anthracene-extended AnIC-BO showed a linear-packed crystal structure and phenanthrene-extended PhIC-BO showed a typical 3D network structure with an elliptical framework. It was found that their different crystal structures induced different crystallization kinetics and degrees of crystallinity of the other active layer components. Additionally, the high crystallinity of the two acceptors facilitates more ordered and structured molecular packing, leading to the suppression of radiative and nonradiative recombination. More importantly, they were found to improve material stability and device operational stability by inhibiting materials' oxidation degradation and morphology change via optimizing vertical phase distribution, improving domain purity, suppressing defects, and impeding molecular migration. As a result, simultaneously improved thermal, photo, and storage stability were achieved in the highly crystalline acceptor-based devices. Accompanied with the promoted exciton generation and charge transfer by two guest acceptors, a higher PCE was achieved in the ternary blends, among which the D18/L8-BO-X: PhIC-BO Q-PHJ

devices achieved a PCE of 19.44%, which was one of the state-of-the-art PCEs with the T_{80} of light stability larger than 1000h, indicating the simultaneously improved efficiency and stability by the regulation of the highly crystalline acceptor. This work not only guides the material design and material selection in ternary devices but also unveils the possible reasons for stability improvement by a ternary strategy, displaying the large potential of long-term operational high-performance OSCs.

6.2 Prospective

This thesis proposed several strategies to achieve highly efficient and stable OSCs. However, there are still many challenges and a long way to go to obtain practically used long-term high-performance OSCs.

First, inferior material stability is detrimental to long-term stable OSCs. Current polymeric donors are prone to photo-oxidation to singlet oxygen and superoxide anions and current high-performance small molecular non-fullerene acceptors with indanone end groups are susceptible to vinylidene oxidation to break the core and end groups. Thus, it is significant to explore new material structures to resist light-induced chemical deterioration.

Second, poor device operational stability largely impeded the application of OSCs. On one hand, the active layer morphological change resulting from molecular migration, for example, D/A interdiffusion to form extremely small phase separation or D/A demixing to form severe segregation in the aging films, leading to an inferior morphology and largely lowering the device performance. On the other hand, the degradation of the interlayer and electrodes is an important factor in lowering device stability. Additionally, the influence of moisture, heating, and oxygen accelerates device deterioration. Thus, a trade-off between miscibility and crystallinity to resist molecular migration, reasonable designation of interlayer and electrodes, proper inverted device structures, and preferable encapsulation methods to resist external detrimental factors are important to achieve good device stability.

Third, OSCs face a large energy loss of radiative recombination resulting from the existence of a charge transfer state and the large nonradiative recombination loss originating from OSCs' amorphous morphology that induces many traps and defects in blends. Thus, reasonable material structure designation and morphological manipulation strategies should be carefully considered to suppress energy loss.

Fourth, the flexible and semitransparent OSCs have great potential in wearable/portable devices and solar-powered see-through windows, showing future applications in agriculture and building-integrated photovoltaics. However, current flexible OSCs face challenges in balancing between mechanical and photovoltaic properties and a lack of proper resilient electrodes, and semitransparent OSCs face challenges in balancing between light harvesting and device transmittance and proper optical design for the light reflector. Therefore, appropriate material development and device structure design are important to achieve high-performance flexible and semitransparent OSCs.

Last but not least, large-area production is the prerequisite for practical application. Current upscaling manufacturing of OSCs faces multiple problems, including hard-to-control molecular aggregation behavior, nonuniform film morphology with tiny pinholes, and a lack of printable interlayer materials etc. Therefore, large efforts should be made to address these issues towards practically used long-term high-performance OSCs.

Reference

[1] Y. Jiang, S. Sun, R. Xu, F. Liu, X. Miao, G. Ran, K. Liu, Y. Yi, W. Zhang, X. Zhu, *Nat Energy* **2024**, *9*, 975.

[2] S. Guan, Y. Li, Z. Bi, Y. Lin, Y. Fu, K. Wang, M. Wang, W. Ma, J. Xia, Z. Ma, Z. Tang, X. Lu, L. Zuo, H. Li, H. Chen, *Energy Environ. Sci.* **2024**, 10.1039.D4EE03778B.

[3] B. Cheng, W. Hou, C. Han, S. Cheng, X. Xia, X. Guo, Y. Li, M. Zhang, *Energy Environ. Sci.* **2024**, DOI 10.1039/D4EE04623D.

[4] Z. Chen, J. Ge, W. Song, X. Tong, H. Liu, X. Yu, J. Li, J. Shi, L. Xie, C. Han, Q. Liu, Z. Ge, *Advanced Materials* **2024**, *36*, 2406690.

[5] L. Zhu, M. Zhang, G. Zhou, Z. Wang, W. Zhong, J. Zhuang, Z. Zhou, X. Gao, L. Kan, B. Hao, F. Han, R. Zeng, X. Xue, S. Xu, H. Jing, B. Xiao, H. Zhu, Y. Zhang, F. Liu, *Joule* **2024**, DOI 10.1016/j.joule.2024.08.001.

[6] 张春福, 习鹤, 陈, 有机太阳能电池材料与器件, **n.d.**

[7] “国 民 经 济,” can be found under https://www.gov.cn/test/2005-07/27/content_17464_8.htm, **n.d.**

[8] “Blackbody | Definition, Color, & Facts | Britannica,” can be found under https://www.britannica.com/science/blackbody, **2025**.

[9] *IJBPAS* **2018**, *7*, DOI 10.31032/IJBPAS/2018/7.6.4469.

[10] E. Technology, “Difference Between Conductor, Semiconductor and Insulator,” can be found under https://www.electricaltechnology.org/2019/10/difference-between-conductor-semiconductor-insulator.html, **2019**.

[11] “Formation of P - type semiconductor,” **2010**.

[12] victor-robles, “Doping of Semiconductors,” can be found under https://www.slideserve.com/victor-robles/doping-of-semiconductors, **2014**.

[13] S. Dam, “What is the Role of the Depletion Region in a Semiconductor PN Junction?,” can be found under https://www.azom.com/article.aspx?ArticleID=22739, **2023**.

[14] Himanshu, “Energy Band of pn junction in thermal equilibrium (Zero bias),” **2020**.

[15] C.-G. Lee, W.-G. Shin, J. R. Lim, H.-M. Hwang, oung-C. Ju, Y.-S. Jung, G.-H. Kang, H.-S. Chang, S.-W. Ko, *J Korean Solar Energy* **2019**, *39*, 15.

[16] B. M. E, *Comptes Rendus Hebdomadaires des Seances de L’Academie des Sciences* **1839**, *9*, 561.

[17] J. Huang, Z. Ren, Y. Zhang, K. Liu, H. Zhang, H. Tang, C. Yan, Z. Zheng, G. Li, *Advanced Functional Materials* **2021**, *31*, 2010172.

[18] A. Chellakhi, S. El Beid, Y. Abouelmahjoub, *International Journal of Photoenergy* **2022**, *2022*, 2133294.

[19] G. Uddin, Development of Simplified In Situ Processing Routes for Rear-Side Patterning of Silicon Heterojunction Interdigitated Back Contact (SHJ-IBC) Solar Cells, **2018**.

[20] W. Shockley, H. J. Queisser, *Journal of Applied Physics* **1961**, *32*, 510.
[21] H. Zhang, *Loss Mechanisms In Non-Fullerene Organic Solar Cells*, Linköping University Electronic Press, Linköping, **2021**.
[22] R. Das Adhikari, M. J. Patel, H. Baishya, D. Yadav, M. Kalita, M. Alam, P. K. Iyer, *Chem. Soc. Rev.* **2025**, 10.1039.D4CS01231C.
[23] J. Mei, F. Yan, *Advanced Materials* **n.d.**, *n/a*, 2418622.
[24] T. Kirchartz, G. Yan, Y. Yuan, B. K. Patel, D. Cahen, P. K. Nayak, *Nat Rev Mater* **2025**, DOI 10.1038/s41578-025-00784-4.
[25] J.-F. Guillemoles, T. Kirchartz, D. Cahen, U. Rau, *Nat. Photonics* **2019**, *13*, 501.
[26] L. Tous, **n.d.**
[27] R. Williams, *The Journal of Chemical Physics* **2004**, *32*, 1505.
[28] C. E. Fritts, *American Journal of Science* **1883**, *s3-26*, 465.
[29] "This Month in Physics History," can be found under http://www.aps.org/publications/apsnews/200904/physicshistory.cfm, **n.d.**
[30] B. Liang, X. Chen, X. Wang, H. Yuan, A. Sun, Z. Wang, L. Hu, G. Hou, Y. Zhao, X. Zhang, *J. Mater. Chem. A* **2025**, *13*, 2441.
[31] "2025-2030 年全球及中国光伏行业市场现状调研及发展前景分析报告_报告大厅," can be found under https://www.chinabgao.com/report/16546540.html, **n.d.**
[32] "Best Research-Cell Efficiency Chart | Photovoltaic Research | NREL," can be found under https://www2.nrel.gov/pv/cell-efficiency, **n.d.**
[33] **N.d.**
[34] Newton, "Periodic Elements: Electron Shells, SubShells, and Orbitals - Chemistry," **2021**.
[35] "What is a Jablonski Diagram (Perrin-Jablonski Diagram)? - Edinburgh Instruments," can be found under https://www.edinst.com/resource/what-is-a-jablonski-diagram-perrin-jablonski-diagram/, **n.d.**
[36] G. Li, R. Zhu, Y. Yang, *Nature Photon* **2012**, *6*, 153.
[37] Z. Zheng, J. Wang, P. Bi, J. Ren, Y. Wang, Y. Yang, X. Liu, S. Zhang, J. Hou, *Joule* **2022**, *6*, 171.
[38] Y. Han, J. Fu, Z. Ren, J. Yu, Q. Liang, Z. Xu, X. Xie, D. Li, R. Ma, M. Cao, Y. Sun, C. Yang, J. He, X. Chang, K. Liu, P. W. K. Fong, J. Huang, H. Liu, Z. Liu, D. Xu, L. Cheng, J. Zhang, G. Yang, X. Lu, Y. Zhu, Q. Tai, Q. Lin, H. Hu, Y. Yang, G. Li, *Nat Energy* **2025**, DOI 10.1038/s41560-025-01742-8.
[39] X. Liu, Z. Zhong, R. Zhu, J. Yu, G. Li, *Joule* **2022**, *6*, 1918.
[40] D. Wang, Y. Li, G. Zhou, E. Gu, R. Xia, B. Yan, J. Yao, H. Zhu, X. Lu, H.-L. Yip, H. Chen, C.-Z. Li, *Energy Environ. Sci.* **2022**, 10.1039.D2EE00977C.
[41] Z. Wang, D. Zhang, L. Yang, O. Allam, Y. Gao, Y. Su, M. Xu, S. Mo, Q. Wu, Z. Wang, J. Liu, J. He, R. Li, X. Jia, Z. Li, L. Yang, M. D. Weber, Y. Yu, X. Zhang, T. J. Marks, N. Stingelin, J. Kacher, S. S. Jang, A. Facchetti, M. Shao, *Science* **2025**, *387*, 381.

[42] J. Huang, Z. Lu, J. He, H. Hu, Q. Liang, K. Liu, Z. Ren, Y. Zhang, H. Yu, Z. Zheng, G. Li, *Energy Environ. Sci.* **2023**, *16*, 1251.

[43] H. Chen, Y. Huang, R. Zhang, H. Mou, J. Ding, J. Zhou, Z. Wang, H. Li, W. Chen, J. Zhu, Q. Cheng, H. Gu, X. Wu, T. Zhang, Y. Wang, H. Zhu, Z. Xie, F. Gao, Y. Li, Y. Li, *Nat. Mater.* **2025**, DOI 10.1038/s41563-024-02062-0.

[44] Y. Jiang, X. Dong, L. Sun, T. Liu, F. Qin, C. Xie, P. Jiang, L. Hu, X. Lu, X. Zhou, W. Meng, N. Li, C. J. Brabec, Y. Zhou, *Nat Energy* **2022**, DOI 10.1038/s41560-022-00997-9.

[45] G. Wang, F. S. Melkonyan, A. Facchetti, T. J. Marks, *Angewandte Chemie International Edition* **2019**, *58*, 4129.

[46] R. Ma, H. Li, T. A. Dela Peña, X. Xie, P. W.-K. Fong, Q. Wei, C. Yan, J. Wu, P. Cheng, M. Li, G. Li, *Advanced Materials* **n.d.**, *n/a*, 2304632.

[47] Y. Wang, H. Yu, D. Zhao, W. Liu, B. Liu, X. Wu, D. Gao, D. Zhang, S. Zhang, X. Sun, C. Zhang, C. Zhao, Y. Fu, W. Song, S. Gong, Y. Fu, C. H. Kwok, Z. Ge, X. Lu, X. Chen, S. Xiao, W. Wong, Y. Chai, H. Yan, Z. Zhu, *Advanced Energy Materials* **2025**, 2404499.

[48] R. Sun, T. Wang, Q. Fan, M. Wu, X. Yang, X. Wu, Y. Yu, X. Xia, F. Cui, J. Wan, X. Lu, X. Hao, A. K.-Y. Jen, E. Spiecker, J. Min, *Joule* **2023**, *7*, 221.

[49] W. Gao, R. Ma, T. A. Dela Peña, C. Yan, H. Li, M. Li, J. Wu, P. Cheng, C. Zhong, Z. Wei, A. K.-Y. Jen, G. Li, *Nat Commun* **2024**, *15*, 1946.

[50] T. Xu, J. Lv, D. Zheng, Z. Luo, M. H. Jee, G. Ran, Z. Chen, Z. Huang, J. Ren, Y. Li, C. Zhang, H. Hu, T. Pauporté, W. Zhang, H. Y. Woo, C. Yang, *Energy Environ. Sci.* **2023**, *16*, 5933.

[51] T. Xu, *Environmental Science* **2021**.

[52] Z. Chen, W. Song, K. Yu, J. Ge, J. Zhang, L. Xie, R. Peng, Z. Ge, *Joule* **2021**, *5*, 2395.

[53] R. Zeng, J. Deng, X. Xue, S. Tan, L. Kan, Y. Lin, W. Zhong, L. Zhu, F. Han, Y. Zhou, X. Gao, M. Zhang, Y. Zhang, S. Xu, F. Liu, *Angew Chem Int Ed* **2025**, *64*, e202420453.

[54] H. Xia, Y. Zhang, W. Deng, K. Liu, X. Xia, C.-J. Su, U.-S. Jeng, M. Zhang, J. Huang, J. Huang, C. Yan, W.-Y. Wong, X. Lu, W. Zhu, G. Li, *Advanced Materials* **2022**, *34*, 2107659.

[55] H. Xia, Y. Zhang, K. Liu, W. Deng, M. Zhu, H. Tan, P. W. K. Fong, H. Liu, X. Xia, M. Zhang, T. A. Dela Peña, R. Ma, M. Li, J. Wu, Y. Lang, J. Fu, W.-Y. Wong, X. Lu, W. Zhu, G. Li, *Energy Environ. Sci.* **2023**, 10.1039.D3EE02984K.

[56] "One-Pot Synthesis of Conjugation-Extended Isomeric Dimer Acceptors for High-Performance Q-PHJ Solar Cells," DOI 10.1002/adfm.202419453can be found under https://advanced.onlinelibrary.wiley.com/doi/epdf/10.1002/adfm.202419453, **n.d.**

[57] "Highly Planar Oligomeric Acceptor Enables Efficiency over 18% with Synergistically Enhanced VOC and Light Absorption," DOI 10.1002/adfm.202404919can be found under

https://advanced.onlinelibrary.wiley.com/doi/epdf/10.1002/adfm.202404919, **n.d.**

[58] X. Shen, F. He, *ACS Appl. Mater. Interfaces* **2024**, *16*, 50061.

[59] G. Feng, J. Li, Y. He, W. Zheng, J. Wang, C. Li, Z. Tang, A. Osvet, N. Li, C. J. Brabec, Y. Yi, H. Yan, W. Li, *Joule* **2019**, *3*, 1765.

[60] S. Liang, B. Liu, S. Karuthedath, J. Wang, Y. He, W. L. Tan, H. Li, Y. Xu, N. Li, J. Hou, Z. Tang, F. Laquai, C. R. McNeill, C. J. Brabec, W. Li, *Angewandte Chemie International Edition* **2022**, *61*, e202209316.

[61] Z. Zhang, J. Miao, Z. Ding, B. Kan, B. Lin, X. Wan, W. Ma, Y. Chen, X. Long, C. Dou, J. Zhang, J. Liu, L. Wang, *Nat Commun* **2019**, *10*, 3271.

[62] N. S. Sariciftci, L. Smilowitz, A. J. Heeger, F. Wudl, *Science* **1992**, *258*, 1474.

[63] N. S. Sariciftci, D. Braun, C. Zhang, V. I. Srdanov, A. J. Heeger, G. Stucky, F. Wudl, *Applied Physics Letters* **1993**, *62*, 585.

[64] G. Yu, J. Gao, J. C. Hummelen, F. Wudl, A. J. Heeger, *Science* **1995**, DOI 10.1126/science.270.5243.1789.

[65] S. E. Shaheen, C. J. Brabec, N. S. Sariciftci, F. Padinger, T. Fromherz, J. C. Hummelen, *Applied Physics Letters* **2001**, *78*, 841.

[66] P. Schilinsky, C. Waldauf, C. J. Brabec, *Appl. Phys. Lett.* **2002**, *81*, 3885.

[67] G. Li, V. Shrotriya, J. Huang, Y. Yao, T. Moriarty, K. Emery, Y. Yang, *Nature Mater* **2005**, *4*, 864.

[68] G. Koßmehl, P. Beimling, G. Manecke, *Die Makromolekulare Chemie* **1983**, *184*, 627.

[69] E. E. Havinga, W. ten Hoeve, H. Wynberg, *Polymer Bulletin* **1992**, *29*, 119.

[70] J. Hou, M.-H. Park, S. Zhang, Y. Yao, L.-M. Chen, J.-H. Li, Y. Yang, *Macromolecules* **2008**, *41*, 6012.

[71] L. Huo, J. Hou, S. Zhang, H. Chen, Y. Yang, *Angew Chem Int Ed* **2010**, *49*, 1500.

[72] L. Huo, S. Zhang, X. Guo, F. Xu, Y. Li, J. Hou, *Angewandte Chemie International Edition* **2011**, *50*, 9697.

[73] Y. Liang, D. Feng, Y. Wu, S.-T. Tsai, G. Li, C. Ray, L. Yu, *J. Am. Chem. Soc.* **2009**, *131*, 7792.

[74] Y. Liang, Z. Xu, J. Xia, S. Tsai, Y. Wu, G. Li, C. Ray, L. Yu, *Advanced Materials* **2010**, *22*, DOI 10.1002/adma.200903528.

[75] S.-H. Liao, H.-J. Jhuo, Y.-S. Cheng, S.-A. Chen, *Advanced Materials* **2013**, *25*, 4766.

[76] D. Qian, L. Ye, M. Zhang, Y. Liang, L. Li, Y. Huang, X. Guo, S. Zhang, Z. Tan, J. Hou, *Macromolecules* **2012**, *45*, 9611.

[77] M. Zhang, X. Guo, W. Ma, H. Ade, J. Hou, *Advanced Materials* **2015**, *27*, 4655.

[78] W. Zhao, S. Li, H. Yao, S. Zhang, Y. Zhang, B. Yang, J. Hou, *J. Am. Chem. Soc.* **2017**, *139*, 7148.

[79] A. Dhanabalan, J. K. J. van Duren, P. A. van Hal, J. L. J. van Dongen, R. a. J. Janssen, *Advanced Functional Materials* **2001**, *11*, 255.

[80] H. Zhou, L. Yang, A. C. Stuart, S. C. Price, S. Liu, W. You, *Angewandte Chemie International Edition* **2011**, *50*, 2995.

[81] D. Mo, H. Wang, H. Chen, S. Qu, P. Chao, Z. Yang, L. Tian, Y.-A. Su, Y. Gao, B. Yang, W. Chen, F. He, *Chem. Mater.* **2017**, *29*, 2819.
[82] M. Wang, X. Hu, P. Liu, W. Li, X. Gong, F. Huang, Y. Cao, *J. Am. Chem. Soc.* **2011**, *133*, 9638.
[83] Q. Liu, Y. Jiang, K. Jin, J. Qin, J. Xu, W. Li, J. Xiong, J. Liu, Z. Xiao, K. Sun, S. Yang, X. Zhang, L. Ding, *Science Bulletin* **2020**, *65*, 272.
[84] J. Qin, L. Zhang, C. Zuo, Z. Xiao, Y. Yuan, S. Yang, F. Hao, M. Cheng, K. Sun, Q. Bao, Z. Bin, Z. Jin, L. Ding, *J. Semicond.* **2021**, *42*, 010501.
[85] D. Liu, W. Zhao, S. Zhang, L. Ye, Z. Zheng, Y. Cui, Y. Chen, J. Hou, *Macromolecules* **2015**, *48*, 5172.
[86] C. Sun, F. Pan, B. Qiu, S. Qin, S. Chen, Z. Shang, L. Meng, C. Yang, Y. Li, *Chem. Mater.* **2020**, *32*, 3254.
[87] C. Zhu, L. Meng, J. Zhang, S. Qin, W. Lai, B. Qiu, J. Yuan, Y. Wan, W. Huang, Y. Li, *Advanced Materials* **2021**, *33*, 2100474.
[88] Y. Xu, Y. Cui, H. Yao, T. Zhang, J. Zhang, L. Ma, J. Wang, Z. Wei, J. Hou, *Advanced Materials* **2021**, *33*, 2101090.
[89] Y. Cui, Y. Xu, H. Yao, P. Bi, L. Hong, J. Zhang, Y. Zu, T. Zhang, J. Qin, J. Ren, Z. Chen, C. He, X. Hao, Z. Wei, J. Hou, *Advanced Materials* **2021**, *33*, 2102420.
[90] M. M. Wienk, J. M. Kroon, W. J. H. Verhees, J. Knol, J. C. Hummelen, P. A. van Hal, R. A. J. Janssen, *Angewandte Chemie International Edition* **2003**, *42*, 3371.
[91] Y. He, H.-Y. Chen, J. Hou, Y. Li, *J. Am. Chem. Soc.* **2010**, *132*, 1377.
[92] Q. Yan, Y. Zhou, Y.-Q. Zheng, J. Pei, D. Zhao, *Chem. Sci.* **2013**, *4*, 4389.
[93] "High-Performance Solution-Processed Non-Fullerene Organic Solar Cells Based on Selenophene-Containing Perylene Bisimide Acceptor | Journal of the American Chemical Society," can be found under https://pubs.acs.org/doi/10.1021/jacs.5b11149, **n.d.**
[94] Y. Lin, J. Wang, Z.-G. Zhang, H. Bai, Y. Li, D. Zhu, X. Zhan, *Advanced Materials* **2015**, *27*, 1170.
[95] S. Li, L. Ye, W. Zhao, S. Zhang, S. Mukherjee, H. Ade, J. Hou, *Advanced Materials* **2016**, *28*, 9423.
[96] Y. Lin, Z.-G. Zhang, H. Bai, J. Wang, Y. Yao, Y. Li, D. Zhu, X. Zhan, *Energy Environ. Sci.* **2015**, *8*, 610.
[97] H. Yao, Y. Chen, Y. Qin, R. Yu, Y. Cui, B. Yang, S. Li, K. Zhang, J. Hou, *Advanced Materials* **2016**, *28*, 8283.
[98] H. Yao, Y. Cui, R. Yu, B. Gao, H. Zhang, J. Hou, *Angewandte Chemie International Edition* **2017**, *56*, 3045.
[99] Z. Xiao, F. Liu, X. Geng, J. Zhang, S. Wang, Y. Xie, Z. Li, H. Yang, Y. Yuan, L. Ding, *Science Bulletin* **2017**, *62*, 1331.
[100] Z. Xiao, X. Jia, D. Li, S. Wang, X. Geng, F. Liu, J. Chen, S. Yang, T. P. Russell, L. Ding, *Science Bulletin* **2017**, *62*, 1494.
[101] J. Yuan, Y. Zhang, L. Zhou, G. Zhang, H.-L. Yip, T.-K. Lau, X. Lu, C. Zhu, H. Peng, P. A. Johnson, M. Leclerc, Y. Cao, J. Ulanski, Y. Li, Y. Zou, *Joule* **2019**, *3*, 1140.

[102] Y. Cui, H. Yao, J. Zhang, T. Zhang, Y. Wang, L. Hong, K. Xian, B. Xu, S. Zhang, J. Peng, Z. Wei, F. Gao, J. Hou, *Nat Commun* **2019**, *10*, 2515.
[103] Y. Cui, H. Yao, L. Hong, T. Zhang, Y. Tang, B. Lin, K. Xian, B. Gao, C. An, P. Bi, W. Ma, J. Hou, *National Science Review* **2020**, *7*, 1239.
[104] Y. Cui, H. Yao, J. Zhang, K. Xian, T. Zhang, L. Hong, Y. Wang, Y. Xu, K. Ma, C. An, C. He, Z. Wei, F. Gao, J. Hou, *Advanced Materials* **2020**, *32*, 1908205.
[105] H. Lai, Q. Zhao, Z. Chen, H. Chen, P. Chao, Y. Zhu, Y. Lang, N. Zhen, D. Mo, Y. Zhang, F. He, *Joule* **2020**, *4*, 688.
[106] C. Li, J. Zhou, J. Song, J. Xu, H. Zhang, X. Zhang, J. Guo, L. Zhu, D. Wei, G. Han, J. Min, Y. Zhang, Z. Xie, Y. Yi, H. Yan, F. Gao, F. Liu, Y. Sun, *Nat Energy* **2021**, *6*, 605.
[107] L. Feng, J. Yuan, Z. Zhang, H. Peng, Z.-G. Zhang, S. Xu, Y. Liu, Y. Li, Y. Zou, *ACS Appl. Mater. Interfaces* **2017**, *9*, 31985.
[108] J. Yuan, T. Huang, P. Cheng, Y. Zou, H. Zhang, J. L. Yang, S.-Y. Chang, Z. Zhang, W. Huang, R. Wang, D. Meng, F. Gao, Y. Yang, *Nat Commun* **2019**, *10*, 570.
[109] C. Zhu, J. Yuan, F. Cai, L. Meng, H. Zhang, H. Chen, J. Li, B. Qiu, H. Peng, S. Chen, Y. Hu, C. Yang, F. Gao, Y. Zou, Y. Li, *Energy Environ. Sci.* **2020**, *13*, 2459.
[110] W. Liu, J. Zhang, S. Xu, X. Zhu, *Science Bulletin* **2019**, *64*, 1144.
[111] Z. Zhou, W. Liu, G. Zhou, M. Zhang, D. Qian, J. Zhang, S. Chen, S. Xu, C. Yang, F. Gao, H. Zhu, F. Liu, X. Zhu, *Advanced Materials* **2020**, *32*, 1906324.
[112] F. Liu, L. Zhou, W. Liu, Z. Zhou, Q. Yue, W. Zheng, R. Sun, W. Liu, S. Xu, H. Fan, L. Feng, Y. Yi, W. Zhang, X. Zhu, *Advanced Materials* **2021**, *33*, 2100830.
[113] L. Zhu, M. Zhang, J. Xu, C. Li, J. Yan, G. Zhou, W. Zhong, T. Hao, J. Song, X. Xue, Z. Zhou, R. Zeng, H. Zhu, C.-C. Chen, R. C. I. MacKenzie, Y. Zou, J. Nelson, Y. Zhang, Y. Sun, F. Liu, *Nat. Mater.* **2022**, *21*, 656.
[114] L. Zhan, S. Yin, Y. Li, S. Li, T. Chen, R. Sun, J. Min, G. Zhou, H. Zhu, Y. Chen, J. Fang, C.-Q. Ma, X. Xia, X. Lu, H. Qiu, W. Fu, H. Chen, *Advanced Materials* **2022**, *34*, 2206269.
[115] P. Bi, J. Wang, Y. Cui, J. Zhang, T. Zhang, Z. Chen, J. Qiao, J. Dai, S. Zhang, X. Hao, Z. Wei, J. Hou, *Advanced Materials* **2023**, *35*, 2210865.
[116] L. Zhu, M. Zhang, J. Xu, C. Li, J. Yan, G. Zhou, W. Zhong, T. Hao, J. Song, X. Xue, Z. Zhou, R. Zeng, H. Zhu, C.-C. Chen, R. C. I. MacKenzie, Y. Zou, J. Nelson, Y. Zhang, Y. Sun, F. Liu, *Nat. Mater.* **2022**, *21*, 656.
[117] C. Chen, L. Wang, W. Xia, K. Qiu, C. Guo, Z. Gan, J. Zhou, Y. Sun, D. Liu, W. Li, T. Wang, *Nat Commun* **2024**, *15*, 6865.
[118] Y. Lang, Y. Zhang, H. Xia, K. Liu, Y. Fu, L. Han, P. W. K. Fong, D. Li, M. Zhang, W.-Y. Wong, X. Lu, T. Yang, F. He, Y. Yang, G. Li, *Advanced Materials* **n.d.**, *n/a*, 2420096.
[119] P. Zhang, Z. Zhang, H. Sun, J. Li, Y. Chen, J. Wang, C. Zhan, *Chinese Chemical Letters* **2024**, *35*, 108802.
[120] C. Li, G. Yao, X. Gu, J. Lv, Y. Hou, Q. Lin, N. Yu, M. S. Abbasi, X. Zhang, J. Zhang, Z. Tang, Q. Peng, C. Zhang, Y. Cai, H. Huang, *Nat Commun* **2024**, *15*, 8872.

[121] "20.6% Efficiency Organic Solar Cells Enabled by Incorporating a Lower Bandgap Guest Nonfullerene Acceptor Without Open-Circuit Voltage Loss," DOI 10.1002/adma.202500282can be found under https://advanced.onlinelibrary.wiley.com/doi/epdf/10.1002/adma.202500282?saml_referrer=, **n.d.**

[122] Y. Lang, H. Lai, Y. Fu, R. Ma, P. W. K. Fong, H. Li, K. Liu, X. Yang, X. Lu, T. Yang, G. Li, F. He, *Advanced Materials* **2024**, 2413270.

[123] Y. Sun, L. Wang, C. Guo, J. Xiao, C. Liu, C. Chen, W. Xia, Z. Gan, J. Cheng, J. Zhou, Z. Chen, J. Zhou, D. Liu, T. Wang, W. Li, *J. Am. Chem. Soc.* **2024**, *146*, 12011.

[124] C. Li, J. Song, H. Lai, H. Zhang, R. Zhou, J. Xu, H. Huang, L. Liu, J. Gao, Y. Li, M. H. Jee, Z. Zheng, S. Liu, J. Yan, X.-K. Chen, Z. Tang, C. Zhang, H. Y. Woo, F. He, F. Gao, H. Yan, Y. Sun, *Nat. Mater.* **2025**, DOI 10.1038/s41563-024-02087-5.

[125] H. Xu, J. Han, A. Sharma, S. H. K. Paleti, S. Hultmark, A. Yazmaciyan, C. Müller, D. Baran, *Advanced Materials* **2025**, *37*, 2407119.

[126] A. Kumar, R. Devine, C. Mayberry, B. Lei, G. Li, Y. Yang, *Advanced Functional Materials* **2010**, *20*, 2729.

[127] J. Huang, J. Fu, B. Yuan, H. Xia, T. Chen, Y. Lang, H. Liu, Z. Ren, Q. Liang, K. Liu, Z. Guan, G. Zou, H. T. Chandran, T. W. B. Lo, X. Lu, C.-S. Lee, H.-L. Yip, Y.-K. Peng, G. Li, *Nat Commun* **2024**, *15*, 10565.

[128] H. Xu, J. Han, M. Babics, L. Huerta Hernandez, D. Rosas Villalva, M. Sanviti, J. Bertrandie, Y. Zhang, Y. Liu, H. Chen, L. Zhao, J. Troughton, J. Martin, F. Laquai, S. De Wolf, D. Baran, *Nat. Photon.* **2025**, *19*, 415.

[129] Y. Che, M. R. Niazi, R. Izquierdo, D. F. Perepichka, *Angew Chem Int Ed* **2021**, *60*, 24833.

[130] P. Ding, D. Yang, S. Yang, Z. Ge, *Chem. Soc. Rev.* **2024**, *53*, 2350.

[131] S. Jung, Y. Cho, S.-H. Kang, S.-J. Yoon, C. Yang, *Solar RRL* **2022**, *6*, 2100819.

[132] Z.-X. Liu, Z.-P. Yu, Z. Shen, C. He, T.-K. Lau, Z. Chen, H. Zhu, X. Lu, Z. Xie, H. Chen, C.-Z. Li, *Nat Commun* **2021**, *12*, 3049.

[133] P. Jiang, L. Hu, L. Sun, Z. Li, H. Han, Y. Zhou, *Chem. Sci.* **2022**, *13*, 4714.

[134] B. Liu, O. J. Sandberg, J. Qin, Y. Liu, S. Wilken, N. Wu, X. Yu, J. Fang, Z. Li, R. Huang, W. Zha, Q. Luo, H. Tan, R. Österbacka, C.-Q. Ma, *Nat. Photon.* **2025**, *19*, 195.

[135] Y. Li, B. Huang, X. Zhang, J. Ding, Y. Zhang, L. Xiao, B. Wang, Q. Cheng, G. Huang, H. Zhang, Y. Yang, X. Qi, Q. Zheng, Y. Zhang, X. Qiu, M. Liang, H. Zhou, *Nat Commun* **2023**, *14*, 1241.

[136] Y. Wang, Z. Zheng, J. Wang, X. Liu, J. Ren, C. An, S. Zhang, J. Hou, *Advanced Materials* **2023**, *35*, 2208305.

[137] K. An, W. Zhong, F. Peng, W. Deng, Y. Shang, H. Quan, H. Qiu, C. Wang, F. Liu, H. Wu, N. Li, F. Huang, L. Ying, *Nat Commun* **2023**, *14*, 2688.

[138] P. Wang, J. Zhang, D. Luo, J. Xue, L. Zhang, H. Mao, Y. Wang, C. Yu, W. Ma, Y. Chen, *Advanced Functional Materials* **2024**, *34*, 2402680.

[139] Z. Fu, J.-W. Qiao, F.-Z. Cui, R.-H. Gui, P. Lu, H. Yin, X.-Y. Du, X.-T. Hao, *Advanced Materials* **n.d.**, *n/a*, 2413317.

[140] M. Ghasemi, N. Balar, Z. Peng, H. Hu, Y. Qin, T. Kim, J. J. Rech, M. Bidwell, W. Mask, I. McCulloch, W. You, A. Amassian, C. Risko, B. T. O'Connor, H. Ade, *Nat. Mater.* **2021**, *20*, 525.

[141] T. Jia, T. Lin, Y. Yang, L. Wu, H. Cai, Z. Zhang, K. Lin, Y. Hai, Y. Luo, R. Ma, Y. Li, T. A. Dela Peña, S. Liu, J. Zhang, C. Liu, J. Chen, J. Wu, S. Liu, F. Huang, *Nat Commun* **2025**, *16*, 871.

[142] Y. Liang, D. Zhang, Z. Wu, T. Jia, L. Lüer, H. Tang, L. Hong, J. Zhang, K. Zhang, C. J. Brabec, N. Li, F. Huang, *Nat Energy* **2022**, *7*, 1180.

[143] S. Jung, Y. Cho, S.-H. Kang, S.-J. Yoon, C. Yang, *Solar RRL* **2022**, *6*, 2100819.

[144] B. Zou, W. Wu, T. A. Dela Peña, R. Ma, Y. Luo, Y. Hai, X. Xie, M. Li, Z. Luo, J. Wu, C. Yang, G. Li, H. Yan, *Nano-Micro Lett.* **2024**, *16*, 30.

[145] Z. Chen, J. Zhu, D. Yang, W. Song, J. Shi, J. Ge, Y. Guo, X. Tong, F. Chen, Z. Ge, *Energy Environ. Sci.* **2023**, *16*, 3119.

[146] X. Liu, Z. Zhang, C. Wang, C. Zhang, S. Liang, H. Fang, B. Wang, Z. Tang, C. Xiao, W. Li, *Angewandte Chemie* **2024**, *136*, e202316039.

[147] Y. Zhang, W. Deng, C. E. Petoukhoff, X. Xia, Y. Lang, H. Xia, H. Tang, H. T. Chandran, S. Mahadevan, K. Liu, P. W. K. Fong, Y. Luo, J. Wu, S.-W. Tsang, F. Laquai, H. Wu, X. Lu, Y. Yang, G. Li, *Joule* **2024**, *8*, 509.

[148] "Manipulating Film Formation Kinetics Enables Organic Photovoltaic Cells with 19.5% Efficiency," DOI 10.31635/ccschem.023.202302907can be found under https://www.chinesechemsoc.org/doi/epdf/10.31635/ccschem.023.202302907, **n.d.**

[149] Y. Zhang, W. Deng, C. E. Petoukhoff, X. Xia, Y. Lang, H. Xia, H. Tang, H. T. Chandran, S. Mahadevan, K. Liu, P. W. K. Fong, Y. Luo, J. Wu, S.-W. Tsang, F. Laquai, H. Wu, X. Lu, Y. Yang, G. Li, *Joule* **2024**, DOI 10.1016/j.joule.2023.12.009.

[150] J. Fu, Q. Yang, P. Huang, S. Chung, K. Cho, Z. Kan, H. Liu, X. Lu, Y. Lang, H. Lai, F. He, P. W. K. Fong, S. Lu, Y. Yang, Z. Xiao, G. Li, *Nature Communications* **2024**, *15*, 1830.

[151] C. Liao, X. Xu, T. Yang, W. Qiu, Y. Duan, R. Li, L. Yu, Q. Peng, *Advanced Materials* **n.d.**, *n/a*, 2411071.

[152] B. Cheng, W. Hou, C. Han, S. Cheng, X. Xia, X. Guo, Y. Li, M. Zhang, *Energy & Environmental Science* **2025**, DOI 10.1039/D4EE04623D.

[153] G. Li, V. Shrotriya, J. Huang, Y. Yao, T. Moriarty, K. Emery, Y. Yang, *Nature Mater* **2005**, *4*, 864.

[154] Y. Zhang, K. Liu, J. Huang, X. Xia, J. Cao, G. Zhao, P. W. K. Fong, Y. Zhu, F. Yan, Y. Yang, X. Lu, G. Li, *Nat Commun* **2021**, *12*, 4815.

[155] J. Yuan, Y. Zhang, L. Zhou, G. Zhang, H.-L. Yip, T.-K. Lau, X. Lu, C. Zhu, H. Peng, P. A. Johnson, M. Leclerc, Y. Cao, J. Ulanski, Y. Li, Y. Zou, *Joule* **2019**, *3*, 1140.

[156] Y. Cui, H. Yao, J. Zhang, K. Xian, T. Zhang, L. Hong, Y. Wang, Y. Xu, K. Ma, C. An, C. He, Z. Wei, F. Gao, J. Hou, *Advanced Materials* **2020**, *32*, 1908205.

[157] Y. Cui, H. Yao, J. Zhang, T. Zhang, Y. Wang, L. Hong, K. Xian, B. Xu, S. Zhang, J. Peng, Z. Wei, F. Gao, J. Hou, *Nat Commun* **2019**, *10*, 2515.
[158] H. Lai, Q. Zhao, Z. Chen, H. Chen, P. Chao, Y. Zhu, Y. Lang, N. Zhen, D. Mo, Y. Zhang, F. He, *Joule* **2020**, *4*, 688.
[159] M. Zhang, X. Guo, W. Ma, H. Ade, J. Hou, *Advanced Materials* **2015**, *27*, 4655.
[160] "18% Efficiency organic solar cells | Elsevier Enhanced Reader," DOI 10.1016/j.scib.2020.01.001can be found under https://reader.elsevier.com/reader/sd/pii/S2095927320300013?token=75A452F574A323BA409AB586DC46C315DB61CFDC1D9B0C4847EE45E6DDAE4A7D8C58C55EDD176935B0BC540C833E8CBD&originRegion=us-east-1&originCreation=20220330033048, **n.d.**
[161] Y. Cui, Y. Xu, H. Yao, P. Bi, L. Hong, J. Zhang, Y. Zu, T. Zhang, J. Qin, J. Ren, Z. Chen, C. He, X. Hao, Z. Wei, J. Hou, *Advanced Materials* **2021**, *33*, 2102420.
[162] J. Fu, P. W. K. Fong, H. Liu, C.-S. Huang, X. Lu, S. Lu, M. Abdelsamie, T. Kodalle, C. M. Sutter-Fella, Y. Yang, G. Li, *Nat Commun* **2023**, *14*, 1760.
[163] P. Bi, J. Wang, Y. Cui, J. Zhang, T. Zhang, Z. Chen, J. Qiao, J. Dai, S. Zhang, X. Hao, Z. Wei, J. Hou, *Advanced Materials* **2023**, 2210865.
[164] J. Wan, Y. Wu, R. Sun, J. Qiao, X. Hao, J. Min, *Energy Environ. Sci.* **2022**, 10.1039.D2EE03134E.
[165] S. Liu, D. Chen, X. Hu, Z. Xing, J. Wan, L. Zhang, L. Tan, W. Zhou, Y. Chen, *Advanced Functional Materials* **2020**, *30*, 2003223.
[166] J. A. Britten, I. M. Thomas, *Journal of Applied Physics* **1992**, *71*, 972.
[167] P. C. Sukanek, *J. Electrochem. Soc.* **1991**, *138*, 1712.
[168] X. Gu, L. Shaw, K. Gu, M. F. Toney, Z. Bao, *Nat Commun* **2018**, *9*, 534.
[169] H. Li, S. Liu, X. Wu, Q. Qi, H. Zhang, X. Meng, X. Hu, L. Ye, Y. Chen, *Energy Environ. Sci.* **2022**, *15*, 2130.
[170] J. Yuan, D. Liu, H. Zhao, B. Lin, X. Zhou, H. B. Naveed, C. Zhao, K. Zhou, Z. Tang, F. Chen, W. Ma, *Advanced Energy Materials* **2021**, *11*, 2100098.
[171] H. W. Ro, J. M. Downing, S. Engmann, A. A. Herzing, D. M. DeLongchamp, L. J. Richter, S. Mukherjee, H. Ade, M. Abdelsamie, L. K. Jagadamma, A. Amassian, Y. Liu, H. Yan, *Energy Environ. Sci.* **2016**, *9*, 2835.
[172] J. Xue, H. B. Naveed, H. Zhao, B. Lin, Y. Wang, Q. Zhu, B. Wu, Z. Bi, X. Zhou, C. Zhao, K. Zhou, W. Ma, *J. Mater. Chem. A* **2022**, *10*, 13439.
[173] L. Zhang, B. Lin, B. Hu, X. Xu, W. Ma, *Advanced Materials* **2018**, *30*, 1800343.
[174] W. Zhao, S. Zhang, Y. Zhang, S. Li, X. Liu, C. He, Z. Zheng, J. Hou, *Advanced Materials* **2018**, *30*, 1704837.
[175] Z. Peng, Y. Zhang, X. Sun, W. Zhao, F. Bian, Y. Geng, L. Ye, C. Yang, *Adv Funct Materials* **2023**, *33*, 2213248.
[176] D. Chen, S. Liu, B. Huang, J. Oh, F. Wu, J. Liu, C. Yang, L. Chen, Y. Chen, *Small* **2022**, *18*, 2200734.
[177] S. Dong, T. Jia, K. Zhang, J. Jing, F. Huang, *Joule* **2020**, *4*, 2004.
[178] W. Zhao, Y. Zhang, S. Zhang, S. Li, C. He, J. Hou, *J. Mater. Chem. C* **2019**, *7*, 3206.

[179] F. Liu, S. Ferdous, E. Schaible, A. Hexemer, M. Church, X. Ding, C. Wang, T. P. Russell, *Advanced Materials* **2015**, *27*, 886.
[180] H. Chen, R. Zhang, X. Chen, G. Zeng, L. Kobera, S. Abbrent, B. Zhang, W. Chen, G. Xu, J. Oh, S.-H. Kang, S. Chen, C. Yang, J. Brus, J. Hou, F. Gao, Y. Li, Y. Li, *Nat Energy* **2021**, *6*, 1045.
[181] H. Chen, W. Sun, R. Zhang, Y. Huang, B. Zhang, G. Zeng, J. Ding, W. Chen, F. Gao, Y. Li, Y. Li, *Advanced Materials* **2024**, *36*, 2402350.
[182] B. Zhang, W. Chen, H. Chen, G. Zeng, R. Zhang, H. Li, Y. Wang, X. Gu, W. Sun, H. Gu, F. Gao, Y. Li, Y. Li, *Energy Environ. Sci.* **2024**, *17*, 2935.
[183] H. Bai, R. Ma, W. Su, T. A. D. Peña, T. Li, L. Tang, J. Yang, B. Hu, Y. Wang, Z. Bi, Y. Su, Q. Wei, Q. Wu, Y. Duan, Y. Li, J. Wu, Z. Ding, X. Liao, Y. Huang, C. Gao, G. Lu, M. Li, W. Zhu, G. Li, Q. Fan, W. Ma, *Nano-Micro Lett.* **2023**, *15*, 241.
[184] L. Zhan, S. Yin, Y. Li, S. Li, T. Chen, R. Sun, J. Min, G. Zhou, H. Zhu, Y. Chen, J. Fang, C.-Q. Ma, X. Xia, X. Lu, H. Qiu, W. Fu, H. Chen, *Advanced Materials* **n.d.**, *n/a*, 2206269.
[185] Y. Cui, H. Yao, L. Hong, T. Zhang, Y. Xu, K. Xian, B. Gao, J. Qin, J. Zhang, Z. Wei, J. Hou, *Advanced Materials* **2019**, *31*, 1808356.
[186] S. Rasool, D. V. Vu, C. E. Song, H. K. Lee, S. K. Lee, J.-C. Lee, S.-J. Moon, W. S. Shin, *Advanced Energy Materials* **2019**, *9*, 1900168.
[187] L. Hong, H. Yao, Z. Wu, Y. Cui, T. Zhang, Y. Xu, R. Yu, Q. Liao, B. Gao, K. Xian, H. Y. Woo, Z. Ge, J. Hou, *Advanced Materials* **2019**, *31*, 1903441.
[188] Y. Cui, H. Yao, L. Hong, T. Zhang, Y. Tang, B. Lin, K. Xian, B. Gao, C. An, P. Bi, W. Ma, J. Hou, *National Science Review* **2020**, *7*, 1239.
[189] B. Lin, X. Zhou, H. Zhao, J. Yuan, K. Zhou, K. Chen, H. Wu, R. Guo, M. A. Scheel, A. Chumakov, S. V. Roth, Y. Mao, L. Wang, Z. Tang, P. Müller-Buschbaum, W. Ma, *Energy Environ. Sci.* **2020**, *13*, 2467.
[190] X. Meng, L. Zhang, Y. Xie, X. Hu, Z. Xing, Z. Huang, C. Liu, L. Tan, W. Zhou, Y. Sun, W. Ma, Y. Chen, *Advanced Materials* **2019**, *31*, 1903649.
[191] X. Liu, Z. Zheng, J. Wang, Y. Wang, B. Xu, S. Zhang, J. Hou, *Advanced Materials* **2022**, *34*, 2106453.
[192] X. Song, Y. Song, H. Xu, S. Gao, Y. Wang, J. Li, J. Hai, W. Liu, W. Zhu, *Advanced Energy Materials* **n.d.**, *n/a*, 2203009.
[193] S. Dong, K. Zhang, T. Jia, W. Zhong, X. Wang, F. Huang, Y. Cao, *EcoMat* **2019**, *1*, e12006.
[194] R. Rai, B. K. Singh, **2013**.
[195] "16% efficiency all-polymer organic solar cells enabled by a finely tuned morphology via the design of ternary blend | Elsevier Enhanced Reader," can be found under https://reader.elsevier.com/reader/sd/pii/S2542435121000775?token=D988281CCF8F73DE6092A2A578D73C6D15C6FC500537CADE8DDC70FEE8DD04EB6B8A835611AB2BE01BFD9F86443FC12A&originRegion=us-east-1&originCreation=20221220072956, **n.d.**

[196] H. Lai, H. Chen, Z.-Y. Chen, Y. Lang, Y. Zhu, S.-T. Zhang, X. Lai, P. Tan, Y. Zhang, B. Yang, G. Li, F. He, *Energy Environ. Sci.* **2023**, *16*, 5944.
[197] W. Zhou, J. Liu, J. Xie, S. You, J. Deng, F. Yu, S. Y. Jeong, H. Y. Woo, F. Wu, L. Chen, *Angewandte Chemie International Edition* **n.d.**, *n/a*, e202415141.
[198] J. Song, C. Zhang, C. Li, J. Qiao, J. Yu, J. Gao, X. Wang, X. Hao, Z. Tang, G. Lu, R. Yang, H. Yan, Y. Sun, *Angewandte Chemie International Edition* **2024**, *63*, e202404297.
[199] X. Liao, Q. Xie, Y. Guo, Q. He, Z. Chen, N. Yu, P. Zhu, Y. Cui, Z. Ma, X. Xu, H. Zhu, Y. Chen, *Energy Environ. Sci.* **2022**, *15*, 384.
[200] R. Ma, C. Yan, P. W.-K. Fong, J. Yu, H. Liu, J. Yin, J. Huang, X. Lu, H. Yan, G. Li, *Energy Environ. Sci.* **2022**, *15*, 2479.
[201] R. Zeng, *Nature Energy* **n.d.**
[202] E. M. Speller, A. J. Clarke, J. Luke, H. K. H. Lee, J. R. Durrant, N. Li, T. Wang, H. C. Wong, J.-S. Kim, W. C. Tsoi, Z. Li, *J. Mater. Chem. A* **2019**, *7*, 23361.
[203] L. Arunagiri, Z. Peng, X. Zou, H. Yu, G. Zhang, Z. Wang, J. Y. Lin Lai, J. Zhang, Y. Zheng, C. Cui, F. Huang, Y. Zou, K. S. Wong, P. C. Y. Chow, H. Ade, H. Yan, *Joule* **2020**, *4*, 1790.
[204] H. Bai, R. Ma, W. Su, T. A. D. Peña, T. Li, L. Tang, J. Yang, B. Hu, Y. Wang, Z. Bi, Y. Su, Q. Wei, Q. Wu, Y. Duan, Y. Li, J. Wu, Z. Ding, X. Liao, Y. Huang, C. Gao, G. Lu, M. Li, W. Zhu, G. Li, Q. Fan, W. Ma, *Nano-Micro Lett.* **2023**, *15*, 241.
[205] J. Xue, H. Zhao, B. Lin, Y. Wang, Q. Zhu, G. Lu, B. Wu, Z. Bi, X. Zhou, C. Zhao, G. Lu, K. Zhou, W. Ma, *Advanced Materials* **2022**, *34*, 2202659.
[206] R. Sun, T. Wang, X. Yang, Y. Wu, Y. Wang, Q. Wu, M. Zhang, C. J. Brabec, Y. Li, J. Min, *Nat Energy* **2022**, DOI 10.1038/s41560-022-01140-4.
[207] L. Zhang, Y. He, W. Deng, X. Guo, Z. Bi, J. Zeng, H. Huang, G. Zhang, C. Xie, Y. Zhang, X. Hu, W. Ma, Y. Yuan, X. Yuan, *Discover Nano* **2024**, *19*, 39.
[208] G. Park, Y. Cho, S. Jeong, J. Park, S.-J. Yoon, C. Yang, *J. Mater. Chem. A* **2023**, *11*, 12185.
[209] L. Liu, B. Yu, L. Kang, W. Deng, X. Zhao, *Advanced Functional Materials* **2023**, *33*, 2214781.
[210] J. Zhang, L. Zhang, X. Wang, Z. Xie, L. Hu, H. Mao, G. Xu, L. Tan, Y. Chen, *Advanced Energy Materials* **2022**, *12*, 2200165.
[211] J.-Y. Fan, Z.-X. Liu, J. Rao, K. Yan, Z. Chen, Y. Ran, B. Yan, J. Yao, G. Lu, H. Zhu, C.-Z. Li, H. Chen, *Advanced Materials* **2022**, *34*, 2110569.
[212] Y. Yu, R. Sun, T. Wang, X. Yuan, Y. Wu, Q. Wu, M. Shi, W. Yang, X. Jiao, J. Min, *Advanced Functional Materials* **2021**, *31*, 2008767.
[213] J. Zhang, H. Mao, K. Zhou, L. Zhang, D. Luo, P. Wang, L. Ye, Y. Chen, *Advanced Materials* **n.d.**, *n/a*, 2309379.
[214] K. Weng, L. Ye, L. Zhu, J. Xu, J. Zhou, X. Feng, G. Lu, S. Tan, F. Liu, Y. Sun, *Nat Commun* **2020**, *11*, 2855.
[215] R. Sun, Q. Wu, J. Guo, T. Wang, Y. Wu, B. Qiu, Z. Luo, W. Yang, Z. Hu, J. Guo, M. Shi, C. Yang, F. Huang, Y. Li, J. Min, *Joule* **2020**, *4*, 407.

[216] Y. Li, H. Liu, J. Wu, H. Tang, H. Wang, Q. Yang, Y. Fu, Z. Xie, *ACS Appl. Mater. Interfaces* **2021**, *13*, 10239.

[217] H. Zhao, B. Lin, J. Xue, H. B. Naveed, C. Zhao, X. Zhou, K. Zhou, H. Wu, Y. Cai, D. Yun, Z. Tang, W. Ma, *Advanced Materials* **2022**, *34*, 2105114.

[218] Q. Wu, W. Wang, Y. Wu, Z. Chen, J. Guo, R. Sun, J. Guo, Y. (Michael) Yang, J. Min, *Advanced Functional Materials* **2021**, *31*, 2010411.

[219] W. Wei, C. Zhang, Z. Chen, W. Chen, G. Ran, G. Pan, W. Zhang, P. Müller-Buschbaum, Z. Bo, C. Yang, Z. Luo, *Angew Chem Int Ed* **2024**, e202315625.

[220] Y. Shi, Y. Chang, K. Lu, Z. Chen, J. Zhang, Y. Yan, D. Qiu, Y. Liu, M. A. Adil, W. Ma, X. Hao, L. Zhu, Z. Wei, *Nat Commun* **2022**, *13*, 3256.

[221] C. Li, J. Zhou, J. Song, J. Xu, H. Zhang, X. Zhang, J. Guo, L. Zhu, D. Wei, G. Han, J. Min, Y. Zhang, Z. Xie, Y. Yi, H. Yan, F. Gao, F. Liu, Y. Sun, *Nat Energy* **2021**, *6*, 605.

[222] F. Liu, Y. Jiang, R. Xu, W. Su, S. Wang, Y. Zhang, K. Liu, S. Xu, W. Zhang, Y. Yi, W. Ma, X. Zhu, *Angew Chem Int Ed* **2024**, *63*, e202313791.

[223] "Regioisomer-Free Difluoro-Monochloro Terminal-based Hexa-Halogenated Acceptor with Optimized Crystal Packing for Efficient Binary Organic Solar Cells," can be found under https://onlinelibrary.wiley.com/doi/epdf/10.1002/anie.202209454, **n.d.**

[224] G. Li, X. Zhang, L. O. Jones, J. M. Alzola, S. Mukherjee, L. Feng, W. Zhu, C. L. Stern, W. Huang, J. Yu, V. K. Sangwan, D. M. DeLongchamp, K. L. Kohlstedt, M. R. Wasielewski, M. C. Hersam, G. C. Schatz, A. Facchetti, T. J. Marks, *J. Am. Chem. Soc.* **2021**, *143*, 6123.

[225] Y. Gao, X. Yang, R. Sun, L.-Y. Xu, Z. Chen, M. Zhang, H. Zhu, J. Min, *Joule* **2023**, *7*, 2845.

[226] R. Sun, Y. Wu, X. Yang, Y. Gao, Z. Chen, K. Li, J. Qiao, T. Wang, J. Guo, C. Liu, X. Hao, H. Zhu, J. Min, *Advanced Materials* **n.d.**, *n/a*, 2110147.

[227] Z. Li, X. Li, J. Xue, J. Zhang, C. Zhu, J. Li, W. Ma, L. Meng, Y. Li, *ACS Energy Lett.* **2023**, *8*, 2488.

[228] F. Lin, K. Jiang, W. Kaminsky, Z. Zhu, A. K.-Y. Jen, *J. Am. Chem. Soc.* **2020**, *142*, 15246.

[229] Z. Luo, T. Liu, R. Ma, Y. Xiao, L. Zhan, G. Zhang, H. Sun, F. Ni, G. Chai, J. Wang, C. Zhong, Y. Zou, X. Guo, X. Lu, H. Chen, H. Yan, C. Yang, *Advanced Materials* **2020**, *32*, 2005942.

[230] C. Zhang, J. Song, L. Ye, X. Li, M. H. Jee, H. Y. Woo, Y. Sun, *Angew Chem Int Ed* **2024**, *63*, e202316295.

[231] H. Chen, T. Zhao, L. Li, P. Tan, H. Lai, Y. Zhu, X. Lai, L. Han, N. Zheng, L. Guo, F. He, *Advanced Materials* **2021**, *33*, 2102778.

[232] "Polymer Solar Cells with 18.74% Efficiency: From Bulk Heterojunction to Interdigitated Bulk Heterojunction - Xu - 2022 - Advanced Functional Materials - Wiley Online Library," can be found under https://onlinelibrary.wiley.com/doi/full/10.1002/adfm.202108797, **n.d.**

[233] J. Fu, P. W. K. Fong, H. Liu, C.-S. Huang, X. Lu, S. Lu, M. Abdelsamie, T. Kodalle, C. M. Sutter-Fella, Y. Yang, G. Li, *Nat Commun* **2023**, *14*, 1760.

[234] J. Wang, Y. Wang, P. Bi, Z. Chen, J. Qiao, J. Li, W. Wang, Z. Zheng, S. Zhang, X. Hao, J. Hou, *Advanced Materials* **n.d.**, *n/a*, 2301583.
[235] G. Zhang, Q. Chen, Z. Zhang, Z. Gao, C. Xiao, Y. Wei, W. Li, *Advanced Materials* **n.d.**, *n/a*, 2310630.
[236] X. Lai, S. Chen, X. Gu, H. Lai, Y. Wang, Y. Zhu, H. Wang, J. Qu, A. K. K. Kyaw, H. Xia, F. He, *Nat Commun* **2023**, *14*, 3571.
[237] Z. Jia, S. Qin, L. Meng, Q. Ma, I. Angunawela, J. Zhang, X. Li, Y. He, W. Lai, N. Li, H. Ade, C. J. Brabec, Y. Li, *Nat Commun* **2021**, *12*, 178.
[238] J. Yi, G. Zhang, H. Yu, H. Yan, *Nat Rev Mater* **2023**, DOI 10.1038/s41578-023-00618-1.
[239] J. Liu, S. Chen, D. Qian, B. Gautam, G. Yang, J. Zhao, J. Bergqvist, F. Zhang, W. Ma, H. Ade, O. Inganäs, K. Gundogdu, F. Gao, H. Yan, *Nat Energy* **2016**, *1*, 16089.
[240] A. Classen, C. L. Chochos, L. Lüer, V. G. Gregoriou, J. Wortmann, A. Osvet, K. Forberich, I. McCulloch, T. Heumüller, C. J. Brabec, *Nat Energy* **2020**, *5*, 711.
[241] F. D. Eisner, M. Azzouzi, Z. Fei, X. Hou, T. D. Anthopoulos, T. J. S. Dennis, M. Heeney, J. Nelson, *J. Am. Chem. Soc.* **2019**, *141*, 6362.
[242] X. Li, H. Lu, W. Zhu, *ChemPlusChem* **2021**, *86*, 700.
[243] H. Lai, X. Lai, Z.-Y. Chen, Y. Zhu, H. Wang, H. Chen, P. Tan, Y. Zhu, Y. Zhang, F. He, *CCS Chem* **2023**, *5*, 1118.
[244] D. He, F. Zhao, C. Wang, Y. Lin, *Advanced Functional Materials* **2022**, *32*, 2111855.
[245] H. Li, Y. Zhao, J. Fang, X. Zhu, B. Xia, K. Lu, Z. Wang, J. Zhang, X. Guo, Z. Wei, *Advanced Energy Materials* **2018**, *8*, 1702377.
[246] L. Nian, Y. Kan, K. Gao, M. Zhang, N. Li, G. Zhou, S. B. Jo, X. Shi, F. Lin, Q. Rong, F. Liu, G. Zhou, A. K.-Y. Jen, *Joule* **2020**, *4*, 2223.
[247] F. Bai, J. Zhang, A. Zeng, H. Zhao, K. Duan, H. Yu, K. Cheng, G. Chai, Y. Chen, J. Liang, W. Ma, H. Yan, *Joule* **2021**, *5*, 1231.
[248] J. Yuan, C. Zhang, B. Qiu, W. Liu, S. K. So, M. Mainville, M. Leclerc, S. Shoaee, D. Neher, Y. Zou, *Energy Environ. Sci.* **2022**, *15*, 2806.
[249] C. Zhang, S. Mahadevan, J. Yuan, J. K. W. Ho, Y. Gao, W. Liu, H. Zhong, H. Yan, Y. Zou, S.-W. Tsang, S. K. So, *ACS Energy Lett.* **2022**, *7*, 1971.
[250] H. Chen, D. Hu, Q. Yang, J. Gao, J. Fu, K. Yang, H. He, S. Chen, Z. Kan, T. Duan, C. Yang, J. Ouyang, Z. Xiao, K. Sun, S. Lu, *Joule* **2019**, *3*, 3034.
[251] X.-K. Chen, M. K. Ravva, H. Li, S. M. Ryno, J.-L. Brédas, *Advanced Energy Materials* **2016**, *6*, 1601325.
[252] J. Wang, H. Yao, Y. Xu, L. Ma, J. Hou, *Mater. Chem. Front.* **2021**, *5*, 709.
[253] M. Zhang, L. Zhu, C. Qiu, T. Hao, Y. Jiang, S. Leng, J. Chen, G. Zhou, Z. Zhou, Y. Zou, X. Su, Z. Shi, H. Zhu, Y. Zhang, T. P. Russell, X. Zhu, F. Liu, *Small Science* **2022**, *2*, 2100092.
[254] Y. W. Soon, S. Shoaee, R. S. Ashraf, H. Bronstein, B. C. Schroeder, W. Zhang, Z. Fei, M. Heeney, I. McCulloch, J. R. Durrant, *Advanced Functional Materials* **2014**, *24*, 1474.

[255] J. Luke, E. J. Yang, C. Labanti, S. Y. Park, J.-S. Kim, *Nat Rev Mater* **2023**, *8*, 839.
[256] Q. Liang, J. Han, C. Song, X. Yu, D.-M. Smilgies, K. Zhao, J. Liu, Y. Han, *J. Mater. Chem. A* **2018**, *6*, 15610.
[257] J. Xu, F. Lin, L. Zhu, M. Zhang, T. Hao, G. Zhou, K. Gao, Y. Zou, G. Wei, Y. Yi, A. K.-Y. Jen, Y. Zhang, F. Liu, *Advanced Energy Materials* **2022**, *12*, 2201338.
[258] H. Lai, H. Chen, Y. Zhu, H. Wang, Y. Li, F. He, *Macromolecules* **2022**, *55*, 3353.
[259] Y. Zhang, Y. Lang, G. Li, *EcoMat* **2023**, *5*, e12281.
[260] Y. Tamai, H. Ohkita, H. Benten, S. Ito, *J. Phys. Chem. Lett.* **2015**, *6*, 3417.
[261] L. Ma, S. Zhang, J. Wang, J. Ren, M. Gao, J. Zhang, T. Zhang, H. Yao, L. Ye, J. Hou, *ACS Materials Lett.* **2021**, *3*, 1276.
[262] S. Luo, C. Li, J. Zhang, X. Zou, H. Zhao, K. Ding, H. Huang, J. Song, J. Yi, H. Yu, K. S. Wong, G. Zhang, H. Ade, W. Ma, H. Hu, Y. Sun, H. Yan, *Nat Commun* **2023**, *14*, 6964.
[263] "Achieving 12.6% Efficiency in Single-Component Organic Solar Cells Processed from Nonhalogenated Solvents," can be found under https://onlinelibrary.wiley.com/doi/epdf/10.1002/solr.202101024, **n.d.**
[264] al C.-Y. L., "Processing Strategies for an Organic Photovoltaic Module with over 10% Efficiency | EndNote Click," can be found under https://click.endnote.com/viewer?doi=10.1016%2Fj.joule.2019.11.006&token=WzM2ODExODEsIjEwLjEwMTYvai5qb3VsZS4yMDE5LjExLjAwNiJd.KhaDoUR68CberuyuxN88wcOdL0g, **n.d.**
[265] J. Cheng, L. Zhang, H. Jiang, D. Yuan, Q. Wang, Y. Cao, J. Chen, *Organic Electronics* **2020**, *85*, 105871.
[266] "High-Performance Organic Solar Cells from Non-Halogenated Solvents," can be found under https://onlinelibrary.wiley.com/doi/epdf/10.1002/adfm.202107827, **n.d.**
[267] "Enabling High Efficiency of Hydrocarbon-Solvent Processed Organic Solar Cells through Balanced Charge Generation and Non-Radiative Loss," can be found under https://onlinelibrary.wiley.com/doi/epdf/10.1002/aenm.202101768, **n.d.**
[268] X. Xu, L. Yu, H. Yan, R. Li, Q. Peng, *Energy Environ. Sci.* **2020**, *13*, 4381.
[269] D. Wang, H. Liu, Y. Li, G. Zhou, L. Zhan, H. Zhu, X. Lu, H. Chen, C.-Z. Li, *Joule* **2021**, *5*, 945.
[270] C. Kim, S. Chen, J. S. Park, G.-U. Kim, H. Kang, S. Lee, T. N.-L. Phan, S.-K. Kwon, Y.-H. Kim, B. J. Kim, *J. Mater. Chem. A* **2021**, *9*, 24622.
[271] H. Liu, L. Wang, H. Liu, M. Guan, C.-J. Su, U.-S. Jeng, B. Zhao, C. Weng, K. You, X. Lu, *Chemical Engineering Journal* **2022**, *429*, 132407.
[272] T. Liu, Q. C. Burlingame, M. R. Ivancevic, X. Liu, J. Hu, B. P. Rand, Y.-L. Loo, *Advanced Energy Materials* **2023**, *13*, 2300046.
[273] T. Liu, Q. C. Burlingame, M. R. Ivancevic, X. Liu, J. Hu, B. P. Rand, Y. Loo, *Advanced Energy Materials* **2023**, *13*, 2300046.
[274] C. Labanti, M. J. Sung, J. Luke, S. Kwon, R. Kumar, J. Hong, J. Kim, A. A. Bakulin, S.-K. Kwon, Y.-H. Kim, J.-S. Kim, *ACS Nano* **2021**, *15*, 7700.

[275] J. Wu, *Environmental Science* **2020**.
[276] J. Luke, E. M. Speller, A. Wadsworth, M. F. Wyatt, S. Dimitrov, H. K. H. Lee, Z. Li, W. C. Tsoi, I. McCulloch, D. Bagnis, J. R. Durrant, J.-S. Kim, *Advanced Energy Materials* **2019**, *9*, 1803755.
[277] J. Xin, **n.d.**
[278] H. Chen, T. Zhao, L. Li, P. Tan, H. Lai, Y. Zhu, X. Lai, L. Han, N. Zheng, L. Guo, F. He, *Advanced Materials* **2021**, *33*, 2102778.
[279] Y. Wang, Y. Zhu, H. Lai, Y. Zhu, X. Lai, P. Tan, X. Shen, F. He, *ACS Materials Lett.* **2024**, *6*, 2506.
[280] C. Cao, H. Wang, D. Qiu, T. Zhao, Y. Zhu, X. Lai, M. Pu, Y. Li, H. Li, H. Chen, F. He, *Advanced Functional Materials* **2022**, *32*, 2201828.
[281] X. Lai, H. Lai, M. Du, H. Chen, D. Qiu, Y. Zhu, M. Pu, Y. Zhu, E. Zhou, F. He, *Chem. Mater.* **2022**, *34*, 7886.
[282] M. Pu, F. He, *Sci. China Chem.* **2023**, *66*, 3484.
[283] B. Li, X. Yang, S. Li, J. Yuan, *Energy Environ. Sci.* **2023**, *16*, 723.
[284] R. Sun, J. Guo, Q. Wu, Z. Zhang, W. Yang, J. Guo, M. Shi, Y. Zhang, S. Kahmann, L. Ye, X. Jiao, M. A. Loi, Q. Shen, H. Ade, W. Tang, C. J. Brabec, J. Min, *Energy Environ. Sci.* **2019**, *12*, 3118.
[285] H. Zhao, N. Prine, S. Kundu, G. Ma, X. Gu, *JACS Au* **2024**, *4*, 4334.
[286] H. Chen, H. Lai, Q. Jiang, X. Lai, Y. Zhu, J. Qu, Q. Wu, F. He, *Nano Energy* **2023**, *113*, 108593.
[287] Y. Zhang, K. Liu, J. Huang, X. Xia, J. Cao, G. Zhao, P. W. K. Fong, Y. Zhu, F. Yan, Y. Yang, X. Lu, G. Li, *Nat Commun* **2021**, *12*, 4815.
[288] S. Lai, Y. Cui, Z. Chen, X. Xia, P. Zhu, S. Shan, L. Hu, X. Lu, H. Zhu, X. Liao, Y. Chen, *Adv. Mater.* **2024**.
[289] H. Lai, Y. Zhu, Y. Ouyang, X. Lai, M. Ou, Z. Deng, Y. Wang, D. Qiu, C. Zhang, F. He, *Adv Funct Materials* **2024**, 2418106.
[290] F. Bai, J. Zhang, A. Zeng, H. Zhao, K. Duan, H. Yu, K. Cheng, G. Chai, Y. Chen, J. Liang, W. Ma, H. Yan, *Joule* **2021**, *5*, 1231.
[291] L. Nian, Y. Kan, K. Gao, M. Zhang, N. Li, G. Zhou, S. B. Jo, X. Shi, F. Lin, Q. Rong, F. Liu, G. Zhou, A. K.-Y. Jen, *Joule* **2020**, *4*, 2223.
[292] H. Li, Y. Zhao, J. Fang, X. Zhu, B. Xia, K. Lu, Z. Wang, J. Zhang, X. Guo, Z. Wei, *Advanced Energy Materials* **2018**, *8*, 1702377.
[293] H. Xia, Y. Zhang, K. Liu, W. Deng, M. Zhu, H. Tan, P. W. K. Fong, H. Liu, X. Xia, M. Zhang, T. A. D. Peña, R. Ma, M. Li, J. Wu, Y. Lang, J. Fu, W.-Y. Wong, X. Lu, W. Zhu, G. Li, *Energy Environ. Sci.* **2023**, *16*, 6078.
[294] Z. Zhou, J. Yang, S. Jin, Y. Zhao, C. Guan, W. Zhu, Y. Liu, *New J. Chem.* **2024**, *48*, 11420.
[295] T. Zhang, C. An, P. Bi, K. Xian, Z. Chen, J. Wang, Y. Xu, J. Dai, L. Ma, G. Wang, X. Hao, L. Ye, S. Zhang, J. Hou, *Energy Environ. Sci.* **2024**, *17*, 3927.
[296] J. Wang, H. Yao, Y. Xu, L. Ma, J. Hou, *Mater. Chem. Front.* **2021**, *5*, 709.
[297] M. Zhang, L. Zhu, C. Qiu, T. Hao, Y. Jiang, S. Leng, J. Chen, G. Zhou, Z. Zhou, Y. Zou, X. Su, Z. Shi, H. Zhu, Y. Zhang, T. P. Russell, X. Zhu, F. Liu, *Small Science* **2022**, *2*, 2100092.

[298] J. Luke, E. J. Yang, C. Labanti, S. Y. Park, J.-S. Kim, *Nat Rev Mater* **2023**, *8*, 839.

[299] "Material Crystallinity as a Determinant of Triplet Dynamics and Oxygen Quenching in Donor Polymers for Organic Photovoltaic Devices," DOI 10.1002/adfm.201302612can be found under https://advanced.onlinelibrary.wiley.com/doi/epdf/10.1002/adfm.201302612, **n.d.**

[300] H. Chen, D. Hu, Q. Yang, J. Gao, J. Fu, K. Yang, H. He, S. Chen, Z. Kan, T. Duan, C. Yang, J. Ouyang, Z. Xiao, K. Sun, S. Lu, *Joule* **2019**, *3*, 3034.

[301] X. Chen, M. K. Ravva, H. Li, S. Ryno, J. Brédas, *Advanced Energy Materials* **2016**, *6*, DOI 10.1002/aenm.201601325.

[302] Q. Liang, J. Han, C. Song, X. Yu, D.-M. Smilgies, K. Zhao, J. Liu, Y. Han, *J. Mater. Chem. A* **2018**, *6*, 15610.

[303] J. Xu, F. Lin, L. Zhu, M. Zhang, T. Hao, G. Zhou, K. Gao, Y. Zou, G. Wei, Y. Yi, A. K.-Y. Jen, Y. Zhang, F. Liu, *Advanced Energy Materials* **2022**, *12*, 2201338.

[304] J. Fu, P. W. K. Fong, H. Liu, C.-S. Huang, X. Lu, S. Lu, M. Abdelsamie, T. Kodalle, C. M. Sutter-Fella, Y. Yang, G. Li, *Nat Commun* **2023**, *14*, 1760.

[305] Y. Shi, **n.d.**

[306] P. Bi, J. Wang, Y. Cui, J. Zhang, T. Zhang, Z. Chen, J. Qiao, J. Dai, S. Zhang, X. Hao, Z. Wei, J. Hou, *Advanced Materials* **2023**, *35*, 2210865.

[307] S. Xia, J. Xu, Z. Wang, S. Lee, L. Wang, Y. Hu, X. Zhao, C. Yang, E. Zhou, Z. Yuan, *Angew Chem Int Ed* **2025**, e202501816.

[308] L. Zhan, S. Yin, Y. Li, S. Li, T. Chen, R. Sun, J. Min, G. Zhou, H. Zhu, Y. Chen, J. Fang, C.-Q. Ma, X. Xia, X. Lu, H. Qiu, W. Fu, H. Chen, *Advanced Materials* **2022**, *34*, 2206269.

[309] T. Liu, T. Yang, R. Ma, L. Zhan, Z. Luo, G. Zhang, Y. Li, K. Gao, Y. Xiao, J. Yu, X. Zou, H. Sun, M. Zhang, T. A. Dela Peña, Z. Xing, H. Liu, X. Li, G. Li, J. Huang, C. Duan, K. S. Wong, X. Lu, X. Guo, F. Gao, H. Chen, F. Huang, Y. Li, Y. Li, Y. Cao, B. Tang, H. Yan, *Joule* **2021**, *5*, 914.

[310] X. Sun, F. Wang, G. Yang, X. Ding, J. Lv, Y. Sun, T. Wang, C. Gao, G. Zhang, W. Liu, X. Xu, S. Satapathi, X. Ouyang, A. Ng, L. Ye, M. Yuan, H. Zhang, H. Hu, *Energy Environ. Sci.* **2025**, *18*, 2536.